A conceptual model of climate change using dynamical systems theory

Morupisi, Kgomotso

Award date:
2020

Awarding institution:
University of Bath

A study of a conceptual model of climate change using dynamical systems theory

submitted by

Kgomotso Susan Morupisi

for the degree of Doctor of Philosophy

of the

University of Bath

Department of Mathematical Sciences

December 2019

Declaration of any Previous Submission of the Work

The material presented here for examination for the award of a higher degree by research has not been incorporated into a submission for another degree.

.....

Kgomotso Susan Morupisi

Declaration of Authorship

I am the author of this thesis, and the work described therein was carried out by myself personally.

.....

Kgomotso Susan Morupisi

Summary

Conceptual climate models plays an important role in the study and understanding of the Earth climate system. They are mostly used to get insight on the processes or mechanism of the climate system. Therefore a rigorous study of a conceptual model developed to study a certain phenomena is crucial. An example of conceptual models of climate is the PP04 model for climate change, in particular the behaviour of the ice-ages [57]. This models the transition from a glacial to an inter-glacial state through a sudden release of oceanic Carbon Dioxide into the atmosphere. This process can be cast in terms of a Filippov dynamical system, with a discontinuous change in its dynamics. The work of this thesis is to perform a careful analysis of the PP04 model using the techniques from the theory of non-smooth dynamical systems. In particular, an analysis of this model is performed for cases of no forcing, periodic forcing and quasi-periodic forcing with both two and three modes. Earlier approaches to studying the PP04 model have used the theory of smooth dynamical systems. These approaches have limited the findings of the dynamics and bifurcations observed in this model. Therefore a thorough study of the model in a non-smooth dynamical systems framework is needed. This is the motivation for the research work in this thesis.

The thesis begins with a review on the development of simple conceptual models of climate and how dynamical systems theory was introduced in the construction of such models in showing response of ice sheets to astronomical forcing. A review on the literature of dynamical systems (both smooth and non-smooth systems) and in particular Filippov systems follows. The analyses of the PP04 model focuses on the presence of the discontinuity boundary due to sudden release of Carbon Dioxide. The results reveals that, the PP04 model has a rich and novel, dynamical structure. The PP04 model with no forcing has periodic solutions that are destroyed at discontinuity induced bifurcations. In addition, the periodically forced PP04 model, exhibits synchronised periodic solutions with subtle regions of existence which depend on the amplitude and frequency of the forcing. The orbits can be created or destroyed in both smooth and discontinuity induced bifurcations, in particular a grazing bifurcation. The changes in orbital stability at the bifurcations show behaviour similar to that observed at the Mid-Pleistocene Transition. The quasi-periodically forced PP04 model exhibits quasi-periodic time solutions that resemble those observed in paleoclimate records. The solutions are observed to depend on the phase of the forcing with possibility of chaotic response when the amplitude of the forcing is increased. The study of orbits and the transitions between them is done for all three types of forcing considered and comparisons made with actual climate dynamics. We conclude by stating further work to be done.

Acknowlegements

I would like to thank the God almighty for his abundant grace and infinite mercies upon my life. I am eternally grateful to my wonderful supervisor Prof. Chris Budd for the time he spent of this project, the constant guidance and endless support he gave me through out the course of my PhD. A special thank you goes to management of SAMBa for providing me with opportunities to expand my knowledge on applications of mathematics. I would not forget the support of my research group mates, more especially Shaerdan Shataer and Matthew Griffith who were always there for me when I needed help. I cannot forget Kebalebile and Sue who made my stay here in the UK memorable and easy, the last two years would not have been smooth without your company and friendship. Finally, to Maungo, Collen, Sadie and my husband Moeteledi, who provided me with support not only with my work but with all challenges of life. Thank you for your love, motivations and those phone calls. This project would not have been possible without funding from Botswana International University of Science and Technology.

Contents

Chapter 1

Introduction

Climate change potentially affects all aspects of life on the planet. The increase of temperatures observed on Earth these recent years has been linked to the increase in Carbon Dioxide released into the atmosphere. Carbon Dioxide is believed to act as an insulator preventing heat loss out of the Earth. Thereby causing high rise in temperatures leading to more severe impacts such as droughts and crop failure and hence increasing poverty. The melting of the ice sheets and glaciers due to increased temperature can lead to the rise in sea levels which might cause displacement of homes and problems like migration in large numbers will be encountered. These concerns and other severe impacts not mentioned above prompted the scientific community to come up with different ways such as modelling the climate system and its variabilities, in an attempt to understand causes of climate change.

The models are developed and evaluated by comparing their findings with the captured variations of past climate obtained from its proxies such as coral reefs and ice cores [42]. The simple conceptual climate models are mostly developed to understand how the climate system works. They are used to study some hypothesis that has been formulated by using laws of physics to study some processes and mechanism of the climate. One of the phenomenon that has been studied intensively, though not yet fully understood, is the glacial cycles.

The data reconstructed from the paleoclimate (past climate) records showed that the Earth climate has experienced oscillatory periods of the cold and warm conditions with periods which transitioned from $23kyrs$ to $41kyrs$ and of recent to $100kyrs$. The proxy record compiled by Lisiecki and Raymo [42] for global temperature using the benthic $\delta^{18}\,O$ records for 57 sites reflects these changes of the global climate (see Figure 2-4). The global temperature records shows the shift from $41kyrs$ oscillation to $100kyrs$ cycles occurring roughly about $1Myrs$ ago. This transition of the global climate from 41 to $100kyrs$ is known as the Mid Pleistocene Transition (MPT). The study of the MPT is one active area of research and different simple conceptual climate models have been developed to study this transition [67, 68, 54, 2, 56]. Some

of the simple conceptual models used to study the MPT were SM90, SM91, P98 and AD15 which were able to reproduce the transition using different hypothesis. They depicted the transition (MPT) as a result of significant changes in the dynamics of the climate system.

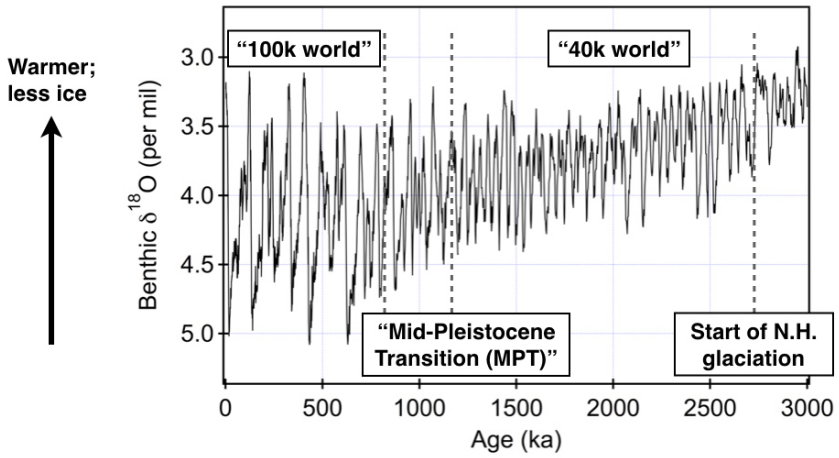

Figure 1-1: The graph showing compilation of benthic $\delta^{18}O$ records for last 3 Myrs showing different periods experienced by the Earth climate (image from Lisiecki and Raymo 2005).

The models are developed using mathematical equations to represent certain processes that typically occur over very different time scales. The processes that happen on short time scales can then be represented as almost instantaneous (discontinuous) when compared to others. One such simple conceptual climate model with processes on different time scales, and fast ones represented as discontinuous is the PP04 model of glacial cycles. This model is used to study the transition of the glacial cycles from a period of $41kyrs$ to $100kyrs$ and the driving force behind the $100kyrs$ cycles. The PP04 model postulates that the glacial state is ended by a very rapid (instantaneous) release of Carbon Dioxide from the oceans. The model was developed using the dynamical systems theory approach and has derivative discontinuities due to the equations for the Carbon Dioxide release. The system of equations with discontinuities are known as 'non-smooth dynamical systems' [19, 10, 38].

Non-smooth dynamical systems have been studied intensively in recent years [38] and are mostly observed in systems that has interrupted events or switches such as in medicine, electrical and mechanical engineering applications and climate. Therefore to study these systems we need to employ the techniques similar to those that are used in studying the smooth dynamical systems. The study of smooth dynamical systems involves the applications of bifurcation and qualitative topological theories, and the use of Poincaré maps as a vital tool to reduce dimensions of the systems and capture all possible transitions.

Since smooth dynamical systems theory is well studied and there is a lot of literature in this field, some researchers found it useful to approximate non-smooth dynamical

systems with the smooth dynamical systems in order to study them. The discontinuity in these systems are mostly regularised to give a smooth dynamical system. For instance the non-smooth dynamical systems model of climate change, the PP04 model, is widely studied through the use of smooth dynamical system theory [46, 47, 13]. This has led to only the dynamics and bifurcations that are only peculiar to smooth systems to be observed. However the non-smooth systems have subtle mathematics and novel results are expected in their analysis such as phenomena like switching, grazing and or sliding. Furthermore non-smooth systems are widely used in a range of applications, for example in development of machinery and a thorough analysis of such systems is needed to understand exactly how the machinery will work. This has however in part motivated this research. As a consequence we will consider the PP04 model of glacial cycles by reformulating it as a quasi-periodically forced piece-wise smooth dynamical system and then do a detailed study .The key results of this study are summarised at the end of this chapter. This is a novel approach both in the modelling of the glacial cycles and in the non-smooth dynamical systems.

The study of piece-wise smooth dynamical systems or any non smooth dynamical systems entails the study of dynamics to get an insight onto how the processes or variables of the system truly interacts. Because of the presence of discontinuity, the mathematical analysis cannot be done using the smooth dynamical systems tools but those relevant only to non-smooth dynamical systems. The analytical framework of systems with a single discontinuity boundary, involves studying the subsystems defined in a certain region of the state phase and merging the solutions to get the overall solution for the whole system. The results obtained are then compared with solutions of a numerical analysis. The analysis of each bifurcations of the system involving a periodic orbit is reduced to the study of an appropriate defined Poincaré map. Therefore the construction of the Poincaré map is needed though for physical systems construction of these maps is difficult.

The piece-wise smooth dynamical systems with degree of smoothness equal to one are known as Filippov systems. These are systems characterised with a discontinuous vector field. Therefore the PP04 model is a quasi-periodically forced Filippov system with a single discontinuity introduced by sudden release of Carbon Dioxide. According to our knowledge the quasi-periodically forced Filippov systems have not been studied before. Hence the study of the PP04 model in the framework of non-sliding Filippov system is a novel approach.

1.1 Outline of the Thesis

Chapter 2: Background

In Chapter 2, a brief introduction to general climate modelling is given. The general

approach behind construction of climate models, the processes and stages involved in validating the models using the past climate data are discussed. Different approaches in developing conceptual climate models in the framework of dynamical system theory and how each model taken as an example performed in depicting climate change are discussed.

We also give brief introduction to smooth dynamical systems and non-smooth dynamical systems and how they are introduced into climate modelling. The terminologies and definitions used in smooth systems and those particular to non-smooth dynamical systems are provided. The dynamics and bifurcations expected for both smooth dynamical and piece-wise smooth dynamical systems of Filippov type are discussed.

Chapter 3: Features of the PP04 model as a Filippov system

In this Chapter we introduce and motivate the PP04 model. The chapter then focuses on the reformulation of the PP04 model of glacial cycles as a quasi-periodically forced Filippov system with a single discontinuity surface. Then we give the analysis of the type of dynamics that are expected to be observed at the discontinuity boundary of the system and give a broad classification of the PP04 system within the Filippov framework. We observed that the PP04 system is a Filippov system without sliding, that is with transversally crossing orbits with a possibility of a grazing periodic orbit.

Chapter 4: Unforced System

In Chapter 4, we study the unforced Filippov system. The type of dynamics and bifurcations observed in this unforced PP04 model shows an existence of periodic solutions between the two sets of virtual fixed points. The bifurcation behaviours observed in this system are the Hopf bifurcation when considering the smooth system, and the Boundary Collision bifurcations for a non-smooth system.

Chapter 5: The Periodically forced system

Chapter 5 studies the periodically forced PP04 model. The system is studied analytically as a perturbation of the unforced PP04 model. The analysis showed the existence of $(1, n)$ periodic solutions and regions of synchronised periodic solutions. For small μ we observed that the boundary of the synchronised solutions are linear but become nonlinear as $\mu > 0.25$. When varying of the parameters ω and μ, we show that at the boundary of regions of synchronised periodic solutions, the periodic solutions are destroyed at a saddle node bifurcation. The numerical analysis of the model under a small forcing is studied by considering the Poincaré section and Monte Carlo plot which leads to observing different and or general periodic solutions. For

example when ω is varied we observed the (m, n) periodic solutions and regions of coexistence of multiple periodic solutions. The period $(1, 3)$ solution was observed to be stable. The stability and physicality of the periodic solutions also studied.

Chapter 6: The quasi-periodically forced system

In Chapter 6 we study the quasi-periodically forced PP04 model with two and or three modes of the forcing. The quasi-periodically forced system is studied analytically as a perturbation of the periodic forced system. For μ_2 small, we study the system using the linear map and the Poincaré map. The linear map is then derived using the perturbation of the point on the limit cycle and then used to study the system. The study of the system through the linear map has shown the existence of periodic n cycle solution for rational forcing and invariant curves for irrational forcing. The whole system was then studied numerically used the stroboscopic plots of the Poincaré map. When ω_2 is an irrational multiple of ω_1, using time series the quasi-periodic solution is observed and in the phase plane we observe tori. An increase in μ_2 showed the break up of the tori to apparent chaotic solutions for $\mu_2 \geq 1$.

Chapter 7: Grazing Bifurcations

Chapter 7 studies the grazing bifurcations, a transition observed for periodically forced system at a certain value of parameter μ or ω. The grazing bifurcation occurs when the part of the periodic orbit interacts with the discontinuity boundary and hence destabilising the solution. This transition is studied through the use of discontinuity maps. The domain of attraction that states which type of periodic solutions are expected for certain initial conditions is also studied.

Chapter 8: Links Back to climate

In Chapter 8 the results observed in the previous chapters $4, 5, 6$ and 7 are linked to what has been observed in the past climate system. The dynamics observed in the system are compared to the reconstructed data of the paleoclimate. Bifurcations observed are explained to have an understanding how they may relate to the transitions observed in the climate system.

Chapter 9: Conclusion and Remarks

In Chapter 9 the contents of the thesis are summarised and ideas for possible work are discussed.

1.2 Key results

The key results observed in the analyses of the $PP04$ model are:

- Proof of existence of a periodic solution for the $PP04$ model without forcing.
- For the periodically forced model we observed:
  - Perturbation of the periodic solution to give synchronised periodic solutions.
  - Proof of existence of ellipses on solutions and saddle node bifurcations.
  - Identification of the breakup of synchronised solutions ellipses and consequent expansion of the basin of attraction.
  - Identification of multiple existence of different periodic solutions and transitions between them.
  - Identification of grazing bifurcations.
- Possible explanation of the MPT via bifurcations (both smooth and non-smooth bifurcations).

Chapter 2

Background

2.1 General climate models

Climate can be described as being the statistics of the atmospheric, ocean state and including physical processes on the Earth surface (in particular Biosphere and Cryosphere) of a certain region over long periods of time. It is measured by assessing the patterns of variations in temperature, humidity, wind, precipitation, dryness and other variables. Subsequently when observing these different physical variables, it is apparent that variations in climate can be from month to month, year to year or any other longer time scales [41]. Furthermore, when the long term changes in the patterns of these variable elements persists over a longer period of time ranging from decades to millions of years, it is called climate change. Climate change can be limited to a certain region or it can be global. Consequently, this shows that the climate operates in different time and spatial scales. Moreover, the Earth climate is complex and difficult to understand hence the development of various models to simulate it.

Climate models are developed and/or used for variety of purposes which are :

(i) detection and establishing if climate is changing significantly and if so what are the causes.

(ii) studying climate dynamics in order to understand the past climate of the Earth.

(iii) projection or forecasting of the future climate and how it will change.

Furthermore, the climate models can be used to simulate the interaction between different components (subsystems) of climate such as oceans (Hydrosphere), land (Biosphere), ice (Cryosphere) and atmosphere which evolve on many time scales and spatial scales. These interactions are the causes of internally generated climate variability which can occur in different time scales. For example, the inter-annual

climate variability comprises of the phenomenon called El Ninõ Southern Oscillations and the Quaternary variability dominated by glaciation cycles [21]. In addition, these climate variabilities can be externally induced or influenced by different internal processes of climate components [21]. For example, according to Imbrie *et al.* [36], the glaciation cycles are believed to be driven by the 65^0N radiation cycle.

Therefore since the climate variabilities evolve in time and space, they can be represented mathematically through the use of systems of equations (mathematical model). These equations or mathematical representations of climate system are based on the basic laws of physics, fluid motion and chemistry to represent fundamental physical processes in the atmosphere, ocean, land surface and or Cryosphere associated with the climate variability [86]. The models are then run and verified by comparing their results against the information (data) reconstructed from past climate through use of ice cores and corals (called paleodata sources).

Like any mathematical model of a natural system, the climate models are a simplification of a complex and complicated system. The number of variables, processes and spatial and temporal scales that are involved in formulation of the model determines the degree of accepted simplification. Thus the complexity of the model determined by the physical,chemical and biological processes and the extent of Earth system interactions that are presented, vary and is used to classify them hence generating the hierarchy of models. Therefore, the hierarchy of models because of varying degrees of complexity and resolution of processes, gives us a range of models from the simple conceptual models (at the bottom) to the very complex Global Climate Models (GCM) at the top of the hierarchy (see Figure 2-1).

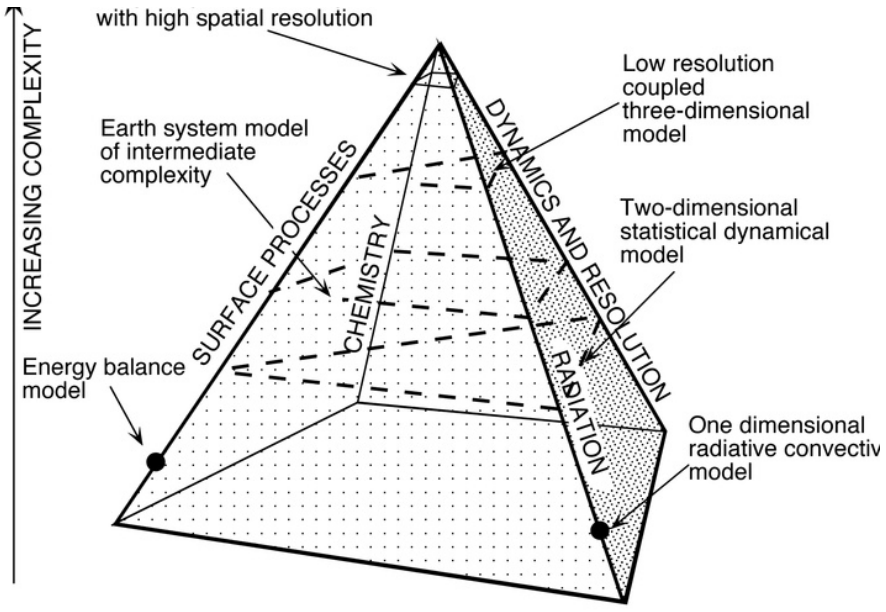

Figure 2-1: The graph showing the level of complexity of the climate models starting with the conceptual models at the bottom (image by Easterbrook[23])

The conceptual models are mainly used to test the hypothesis about a certain climate variability or phenomena in order to gain an understanding about it and for identifying the relevant physical processes within the system that influences that process. Therefore conceptual models considers a limited number of physical processes with limited resolutions and can assume zero or one dimensional resolution depending on whether they had addressed any spatial parameter. An example of a conceptual climate model which is zero dimensional ($0D$) is the Budyko's [6] or the Seller's [71] model of energy balance in which the Earth is represented as a point. That is, in this model there is no account for latitude, longitude or altitude (spatial resolution) and consequently averages the outgoing energy. However, this ($0D$) model can be extended to include either the latitude or vertical (altitude) dependence (increasing spatial resolution) in order to raise its dimension to a one dimensional($1D$) model. Therefore when the spatial resolution of the model is increased the complexity of the model is also increased.

Just above the simple conceptual climate models, for instance the Energy Balance models, are the Box models. These models represents different climate subsystems such as ocean, land and atmosphere as boxes which are connected through equations of energy transfer. Then we have the Intermediate Complexity model or the Earth systems models of Intermediate Complexity (EMICS) which are $3D$ models and accounts for the latitude, altitude and longitude dependence of the parameters. EMICS bridge the gap between conceptual and comprehensive models as they contain a sizeable number of physical processes.

The Global Climate models also known as General Circulation models (GCM) are of high dimensionality with billion degrees of freedom because many physical processes are considered and are also represented in their complex manner. GCMs incorporate the three dimensionality nature of the components of the climate considered such as ocean, atmosphere, sea ice, land surface (sometimes interaction with vegetation is considered), ocean biology, chemistry and ice sheets. In particular, GCMs have a large number of scales and consider high spatial and temporal resolutions and hence includes many feedback processes which increases the model complexity due to climate non-linearity. The GCMs are a compilation of what is already understood about the earth climate system hence a tool to be used to predict future climate. However, the processes that are not understood yet are parametrised and included into the model [86] and those that cannot be resolved are expressed in terms of the resolved quantities. The equations of this type of climate model are based on the conservation laws of mass, energy, momentum, Carbon Dioxide, water and so on. Therefore a fully coupled ocean-atmosphere GCM will need a high performing computing resource to be run and so experiment climate change. There are a number of GCMs that have been developed in the United Kingdom such as the UKLO, HadCM2, HadCM3 and of recent the HadGEM3 family which is still under development. The HadGEM3 family includes the NEMO ocean model which has

three major components and CICE sea-ice model components.

However, the GCMs cannot be run for the long periods associated with the glacial cycles. Hence, in order to obtain insight into the past climate phenomenon for instance the glacial cycles it is necessary to make use of simpler conceptual models which study variations of ice sheets and effects of astronomical forcing on these ice sheets.

The results from these models are then compared with the data reconstructed from proxies (such as ice cores and coral reefs) which provides the information about the long time behaviour of past climate. From these data sources, we observe that the Earth climate has been changing or varying but stable which implies that it has a mechanism of stabilising itself from extreme variabilities from the normal. The indicators (such as temperature, volume of ice, carbon dioxide) of climate observed from data clearly shows that there was alternating periods of cold and warm climate. Furthermore the oscillatory behaviour experienced in climate has been of different cyclic periods. All these behaviour of climate is believed to be influenced by various changing external forcing mechanisms, the most important of which is the sun [21].

2.1.1 Energy Balance Model

Considering the sun as the sole radiative energy provider to the Earth, there are a number of energy balance models developed in order to understand the glacial cycles of climate. Their equations are constructed such that they focus on the energy budget and the thermodynamics of the climate system assuming global radiation balance. The equations also describes the north south energy transport in terms of temperature gradients at the poles [4]. This is because the radiative energy is believed to be exchanged and distributed between Earth climate subsystems. The interactions and fluxes associated are called energy cycle. When the steady state of energy is affected or perturbed by internal or external forcing, change in climate occurs. Sellers [71] and Budyko [6] models were early attempts to understand the glacial cycles of climate by using energy balance methods. They independently, and using different approaches, arrived at the same model which is developed such that it represent zonally the averaged energy balance as a function of planetary albedo. The function of planetary albedo is proposed to depend on the extent of ice or snow cover and surface temperature. The Budyko-Seller's model [6, 71] is defined by:

$$A = Q(1 - \alpha) - I$$

where A represents the rate of gain or loss of heat (heat flux), Q solar radiation coming to the outer boundary of the atmosphere and I is outgoing radiation. The

planetary albedo, α is given as a two step function of surface temperature defined as:

$$\alpha = \begin{cases} b - 0.009T_g, & T_g < 283.16 \\ b - 2.548, & T_g > 283.16 \end{cases}$$

where T_g is average surface temperature and b is empirical coefficient given in [71].

Subsequently, most conceptual climate models were developed in order to improve the Sellers and Budyko's model by studying other different processes and mechanism but still using the notion of the radiative energy from the Sun. These are usually expressed in terms of low-dimensional dynamical systems. For instance Kgomotso Morupisi's master's project, extended the Budyko- Sellers model to address the lag in temperature changes as ice sheets increases or reduced . When the amount of ice sheets are increased, the ice-albedo effect lowers the amount of incoming solar radiation absorbed by the Earth system hence lowering temperature. However this process is not instantaneous. This is because the ice-albedo effect is delayed by a certain time period say τ which is the time it takes the ice sheets to accumulate (or reduced) from one level to the next level. Consequently the albedo at time t is dependent upon the temperature at some previous time $t - \tau$. Therefore the albedo function which was earlier defined as $\alpha(T)$ by Budyko and Sellers is now given by $\alpha(T(t - \tau))$. Therefore the equation for energy balance is defined

$$C\frac{dT}{dt} = Q(1 - \alpha(T(t - \tau))) - \sigma\epsilon(A + BT)$$

where C is heat capacity of the Earth surface, A and B represents empirical constants, Q mean annual incoming solar radiation, σ Stefan Boltzmann's constant, ϵ a constant accounting for greenhouse effect and T is surface temperature. The parameter τ is the time constant.

On the other hand, Widiasih [87] extended the Budyko model by coupling it with ice line dynamics. Walsh *et al.* [85] further extended the Budyko model by separating the introduced ice line to obtain two dynamic variables and hence introducing the two climatic states that corresponds to glacial advance and retreat. This reformulation yields a Filippov system with the switching governed by the ice extent and albedo line.

A Serbian geophysicist Milankovitch proposed that the changes in patterns of climatic cycles were initiated by variations in the Earth orbit parameters: eccentricity, obliquity and precession [45]. Thus the amount of radiation energy received by the Earth varies and is dependent on the shape of the Earth orbit and the orientation of the Sun from Earth axis (see Figure 2-2). He used the astronomical variations to explain the advancement and the retreat of polar ice cap. Furthermore, he proposed that the land gets heated at high summer insolation which makes glaciers ablate, and in contrast low summer radiation keeps land cool promoting growth of ice sheets

and also allowing persistence of ice sheets. That is, during summer period, if there is low Earth tilt and near circular shape of Earth orbit, the distance from Sun to Earth increases. Hence low solar radiation absorbed and promoting growth of ice sheets.

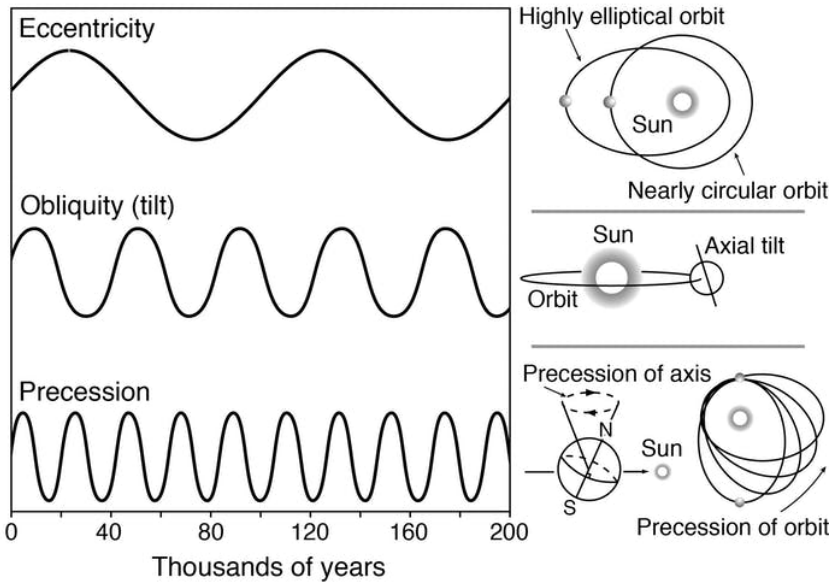

Figure 2-2: The graph showing the variations in the Earth orbit (image from Maslin [44]).

However, it has been established that the amount of energy received by the Earth system is also affected by other internal processes, mechanisms or feedbacks such as ice-albedo feedback and weathering [6, 71, 52, 41]. The albedo feedback helps in promotion of ice sheets growth or ice sheet waning. Consequently, during the period of more ice sheet, there will be reduction of temperature and during a period of less ice sheet there will be an increase of temperature. These two successive climatic conditions are labelled glacial (cold) and the interglacial (warm) climatic states respectively. Thus from beginning of history, the Earth climate has been characterised by periods of waxing and waning of ice sheets called ice ages (glaciation cycle) which persisted for thousands of years [88].

Imbrie *et al.* [36] states that scientists have recorded about five significant ice ages (see Figure 2-3) which includes the Quaternary: a period from 2.6 million years ago extending to the present day. Moreover, there is evidence from ice cores that suggests that as the earth climate slid in and out of the last ice age, at the end of each period of general cycle there was some abrupt changes. These abrupt events are characterised by large and rapid temperature fluctuations which were accompanied (followed) by transitions between cold stadials and warm stadials [1, 70] (see Figure 2-4). They are associated with the Dansgaard-Oeschger (DO) events which were found to occur at last glacial inception [13]. The general cyclic periods of glacial cycles observed from proxies are 23 000 years, 41 000 years and in the recent 500 000 years ago a period of 100 000 years [36, 9]. According to Raymo *et al.* [66] *a complete theory of ice ages is still elusive since there is still lack of understanding*

the causes of 100 000 year cycle.

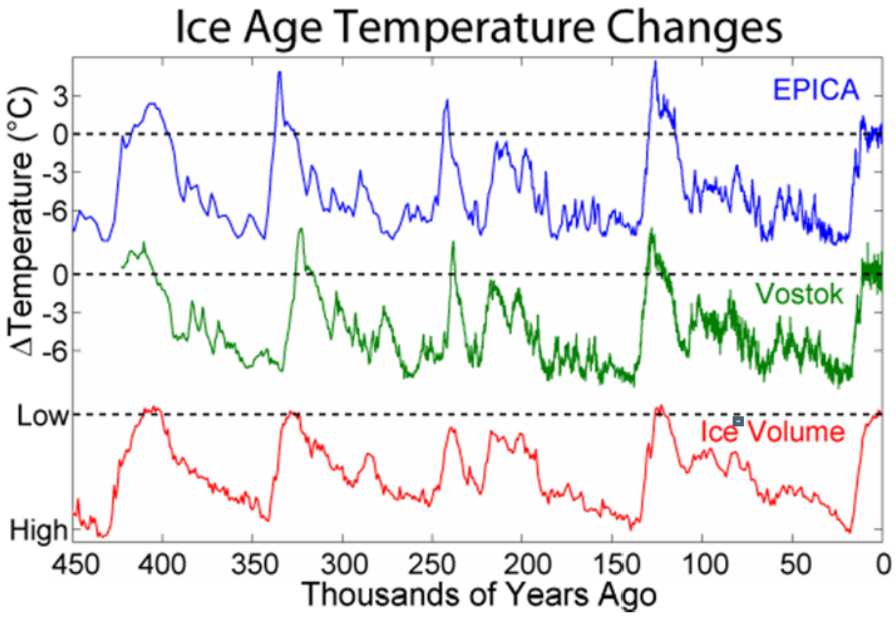

Figure 2-3: The graph shows the temperature and ice volume variations during the four major glaciations of the last 450 000 years reconstructed from the oxygen isotopes of Vostok and EPICA ice cores. From the graph we observe the slow growth of ice sheets and the fast waning of ice sheets including the periodicity of approximately 100,000 years. (image from: Global Warming Art; data is from Petit, J.R et al.,[60])

However, there is a consensus about other factors that are believed to be of importance in interpreting or understanding glacial cycles such as the astronomical forcing theory and the climatic variations: ocean circulation and atmosphere circulation patterns together with concentration of atmospheric Carbon Dioxide and methane [55, 33]. Hays *et al.* [32] attests that the glacial cycles are linearly correlated with Earth orbit. He showed that the 23 000 year cycle in the longitude of the perihelion (precession) and 40 000 years obliquity cycle are the same frequencies observed in the oxygen isotope ($\delta^{18}O$). Hence the proxy data supporting that the two periodic cycles observed are coherent with amplitude of insolation [36]. Consequently the variations in seasonal and spatial distribution of the solar radiation driven by orbital variations, are thought to be the fundamental drivers of the glacial and interglacial oscillations [73]. When applying Milankovitch's theory, the glacial cycles of 23 000 years and that of 41 000 years were able to be explained. However, this theory failed to explain the 100 000 year glacial cycle because the transition from the 41 000 year cycle to the 100 000 year cycle occurred in the absence of any significant change in the amplitude of orbital forcing.

The transition of the glacial cycles to the longer period of 100 000 is known as the Mid Pleistocene Transition (MPT). Since there was no significant change in orbital forcing to explain this dominant period, it was thought to be an indication that the transition can be due to climate responding to its internal changes. However, this is not yet

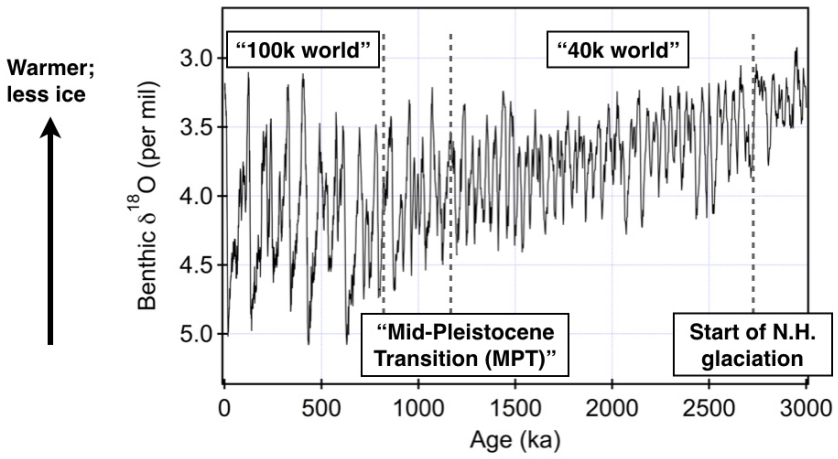

Figure 2-4: The graph showing different periods experienced by the Earth climate obtained from $\delta^{18}O$ isotope (image from Lisiecki and Raymo [42]).

justified as the physical mechanisms that drive the 100 000 year cycle are not yet fully known or understood [13, 36]. As a result a number of hypotheses were formulated in order to understand the causes of the MPT. One of such hypotheses was that the 100 000 year cycle is caused by an underlying change in the global carbon cycle [9]. This was brought about by the findings from proxies and other observational results, suggesting that during the Pleistocene period and before each glacial terminations, there was an increase on atmospheric carbon dioxide concentration several millenia before the melting of the Northern hemisphere ice sheets [5] and that this increase of Carbon Dioxide is parallel to the increase of temperature.

As a consequence, different mechanisms in the same time scale that can bring about this change were proposed: those involving the export of carbon to the deep ocean, those involving deep water ventilation of the Southern Ocean and those involving changes in the ocean chemistry and carbonate flow to the deep sea [28]. Imbrie *et al.* [36] supported this when he proposed that the ocean as carbon sink can provide part of the explanation (or reason) for this 100 000 year cycle. This is due to the fact that the ocean has the capability to store and release Carbon Dioxide in the longer time scales such as centuries to 10 000 years which is the time scale similar to that of glacial cycles. Nevertheless, Garcia-Olivares and Herrero [28], suggested that the 100 000 year periodicity of glacial cycles arises from the characteristic time of Antarctic ice sheet advance to the continental slope. Consequently, different hypothesis addressing specific mechanisms gave birth to different conceptual climate models.

Therefore in an attempt to explain the fluctuations of the climatic cycles and bi-stability of ice sheets, different concepts that originate from theory of dynamical systems were employed by different authors. The use of dynamical systems theory was introduced because the physical processes changes with respect to time. According to Crucifix [13], dynamical systems theory was first introduced to conceptual models

of paleo climate in order to show the response of the ice sheets to the astronomical forcing. One of such models was the experimental model by Oerlemans [52] using the bedrock and ice-sheet dynamics to explain the behaviour of Northern Hemisphere ice sheet during the 100 000 years glacial cycle.

The use of dynamical systems theory on conceptual models or low dimensional models has brought a lot of insightful information on how the complex Earth climate system behave. In particular through this approach, the dynamics of the complex system that are usually not easy to be captured in a General Circulation model or any complex model, are easily captured on conceptual models at some leading modes for a certain temporal and or spatial scales [13]. Moreover, the general understanding of climate as a dynamical system enables one to study the stability or instability of the system. Through this approach Calov *et al.* [7] was able to find a hysteresis responsive behaviour of the ice sheets to insolation, which indicated that the climate system has multi stability and hence may be able to explain the glacial cycles and changes in period of cycles. Furthermore, the approach was viewed as a tool that can help in identifying the bifurcation (tipping) points of the climate system or their neighbourhood, that can result in catastrophic climatic changes [13].

Saltzman and Maasch [67, 68] were one of the first scientists to address the hypothesis that the change in carbon cycle causes the MPT using dynamical system's theory. Consequently they developed two glacial models, the glacial model of 1990 (SM90) and the glacial model of 1991 (SM91) respectively. The SM90 and SM91 models couple the dynamics of ice volume, Carbon Dioxide concentration and deep ocean temperature and adopts the Milankovitch view that an increase in orbital forcing leads to a decrease in volume of ice sheets[13]. Both models consider that the ice mass responds to amount of Carbon Dioxide in the atmosphere and the changes in astronomical forcing $F_I(t)$. The dynamics of atmospheric Carbon Dioxide and the reaction of ocean temperature are obtained through the second and third equations respectively. The SM90 and SM91 models differs only in their equations of change in Carbon Dioxide, which have proven difficult (problematic) to be interpreted physically[13, 3].The equations of the model are such that there is no stochastic forcing and random forcing considered as the original model [67, 68, 13]. The equations of the Saltzman and Maasch Model (SM90) are given by

$$\begin{cases} \dot{I} = \alpha_1 - (c\alpha_2)\mu - \alpha_3 I - k_\theta \alpha_2 \theta - k_R \alpha_2 F_I(t) \\ \dot{\mu} = -\beta_1 - (\beta_2 - \beta_3\theta + \beta_4\theta^2)\mu - (\beta_5 - \beta_6\theta)\theta + F_\mu(t) \\ \dot{\theta} = \gamma_1 - \gamma_2 I - \gamma_3 \theta \end{cases}$$

and the Saltzman and Maasch model (SM91) is defined

$$\begin{cases} \dot{I} = \alpha_1 - (c\alpha_2)\mu - \alpha_3 I - k_\theta \alpha_2 \theta - k_R \alpha_2 F_I(t) \\ \dot{\mu} = -\beta_1 - (\beta_2 - \beta_3 \mu + \beta_4 \mu^2)\mu - \beta_5 \theta + F_\mu(t) \\ \dot{\theta} = \gamma_1 - \gamma_2 I - \gamma_3 \theta \end{cases}$$

where θ, I and μ represents mean ocean temperature in $^o c$, global ice mass and concentration of atmospheric Carbon Dioxide respectively. The other parameters α_1, β_1 and γ_1 represents the rates at which global ice mass, Carbon Dioxide and mean ocean temperature would increase respectively while $\alpha_2, \beta_2, \beta_3, \beta_4, \beta_5, \gamma_2$ are coefficients and γ_3 is inverse time constant for the response of deep ocean temperature.

The $SM90$ and $SM91$ models regard the change in period of glacial cycle from 41 kyr to the 100 kyr as a limit cycle synchronised with insolation due to the slow Carbon Dioxide feedback. They interpreted the Mid -Pleistocene Transition as a bifurcation from quasi-linear to nonlinear resonance regime of insolation [13] due to the gradual increase of ice sheet mass or slow Carbon Dioxide [67]. In particular the SM90 experienced a Hopf bifurcation [2] and assuming that the increase in insolation causes a decrease in ice sheet mass and therefore in a similar way, an increase in carbon dioxide causes decrease in ice mass.

In a similar way, other simple models of ice ages using the same approach were developed such as the Paillard 1998 model ($P98$) [54], Paillard and Parrenin 2004 model (PP04) [57], Crucifix 2013 model (VdP13) [14] and Ashwin and Ditlevsen 2015 model (AD15) [2]. However, Paillard [54] advocated for the use of thresholds and multiple states in developing model of glacial cycles.

He mentioned that threshold for different states introduces the non linearity observed in the response of global ice volume to forcing during the $100kyrs$ glacial cycle, and that there is evidence for existence of multiple states in the ocean. Hence he used an ocean box model to derive the threshold of the P98 model. The equation of the $P98$ model are defined by

$$\frac{dV}{dt} = \frac{(V_R - V)}{\tau_R} - \frac{F}{\tau_F} \tag{2.1}$$

where V is ice volume, R is current climate regime ($R = i,\ g,\ G$) and hence V_R is the reference ice volume for different climatic conditions. F is the forcing and τ_R and τ_F are the time constants. In this equation, the ice volume is relaxed to the reference ice volume and perturbed by the insolation forcing. The climate regimes are explained as i to refer to interglacial state, g the mild glacial state and G the deep glacial state.

Paillard proposed that the transition from 41kyrs to 100kyrs can be depicted as a bifurcation due to the gradual increase in total ice mass and that the climate

system can be represented by three quasi-steady states driven by astronomical forcing. Whereby the thresholds that triggers the transitions from one climatic state to another are driven by insolation forcing and ice volume and the climatic states are assumed to follow the sequence $i \to g \to G \to i$ according to the thresholds set. For instance the transition from $g \to G$ occurs if the threshold value of insolation has exceeded a certain value and the transition $g \to i$ is prohibited. The P98 model attributes the fast-slow dynamics. The multiple states used are derived from the study of Stommel's simplified model of the ocean [80].

Ashwin et al [2] motivated by the relaxation oscillator and threshold model proposed by Paillard [54] suggested the AD15 model of ice ages which is the regularisation of the P98 model with addition of the effect of noise. Though the study of this effect was never thoroughly done in the analyses of his model. Similar to the P98 model, AD15 model is a fast-slow system and couples the slow dynamics of ice volume $V(t)$ and the fast temperature variable $y(t)$. The model suggests that the Mid Pleistocene transition is due to the transcritical bifurcation. The equations of this model are defined

$$\frac{dV}{dt} = \frac{V_e(y) - V}{\tau_V(y)} - \frac{I(t)}{\kappa_f} + \sigma_v \eta_v \tag{2.2}$$

$$\frac{dy}{dt} = H(V, y, \lambda(t)) + \sigma_y \eta_y \tag{2.3}$$

where $V_e(y) = \beta(\alpha - y)$ represents the equilibrium state, V volume of ice and $H(V, y, \lambda(t))$ is the drift function that describes the nonlinear relationship between ice volume and some climate state with structural parameter $\lambda(t)$ that evolves slowly over the Pleistocene period. The insolation represented by $I(t)$, is the force that causes melt off of ice sheets during summer, $\tau_V(y)$ represents time variable assumed to be different in every climate state. Whilst $\sigma_{v,y}$ and $\eta_{v,y}$ are noise amplitude and additive noise respectively and κ_f the reaction time linked to ice sheet heat capacity [2].

Similarly the PP04 model was developed using the same principle of relaxation oscillators and thresholds to represent the ice ages and hence the concept of multi-stability of ice sheet volume. However in the PP04 model, thresholds are introduced by the Heaviside function in the equation for Carbon Dioxide represented by the step function describing the sudden release of Carbon Dioxide when the Southern Ocean is ventilated. In a further attempt Paillard [56] proposed other three different mechanisms involving insolation and ice sheets working together to possibly explain the 100 000 year periodic cycle: instability of base of large ice sheets, ice-albedo feedback in a dry and cold global climate and the effect of Antarctica ice sheet maximum extent to bottom water formation.

Clearly, all the models mentioned above perceived the climate system as a dynamical system hence were analysed by using the theory of dynamical systems. However,

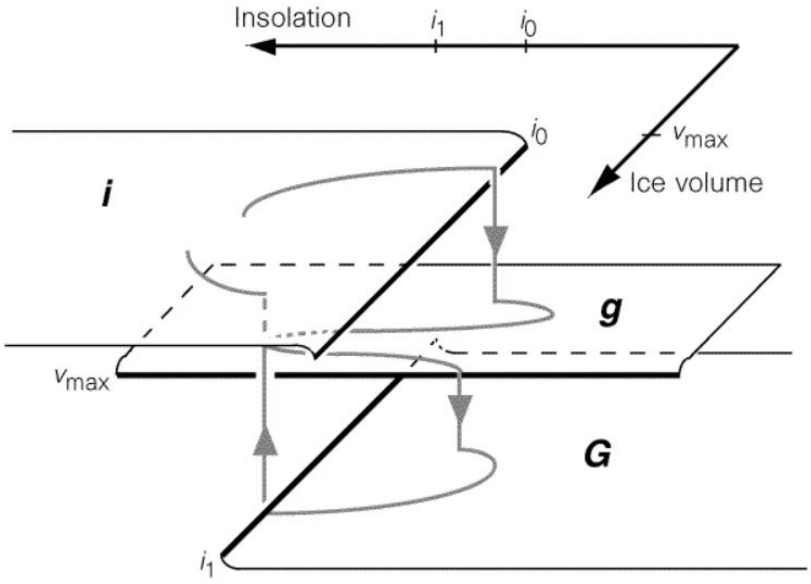

Figure 2-5: The graph showing the climate assumed three distinct regimes; i= interglacial, g = mild glacial state and G = deep glacial state. The transitions $i \to G$ is triggered by insolation threshold, $g \to G$ triggered by ice volume threshold and $G \to i$ occurs when the insolation threshold is reached [54].

smooth dynamical system theory was the one used for almost all the models mentioned above even those that are not smooth such as P98 and PP04. Therefore, the dynamics distinctive to smooth systems such as relaxation oscillators, strange non-chaotic attractors, hysteresis behaviour, Hopf bifurcations, transcritical bifurcations, synchronisation and Arnold tongues etc were observed [3, 13, 46, 47].

However the analysis of a non-smooth dynamical system through smooth dynamical systems theory limits the findings of the dynamics in the system. This is because only dynamics and bifurcations peculiar to smooth dynamical systems will be observed. For instance, if we consider a Filippov system, and study it using smooth dynamical systems theory, the dynamics such as grazing bifurcation (which is the primary bifurcation in our work relating to MPT) cannot be observed. This behaviour would only be observed if the system is studied using the non-smooth dynamical systems theory.

Evidently in the climate Filippov dynamics are common because of different time scales. Consequently Paillard *et al.* [57] when constructing a model of glacial cycles produced a Filippov system due to the consideration of ocean ventilation in the Carbon Dioxide equation. Similarly when Walsh *et al.* [85] extended the Budyko model of energy balance by separating the ice line into two dynamic variables and produced a Filippov system. When studying their model using non-smooth dynamical systems theory, they observed a periodic solution between two attracting virtual fixed points for each of the two climatic states. The behaviour we also observe in the PP04 model.

Therefore in order to be able to capture all the dynamics and the bifurcations even the complicated ones in the PP04 model, the study of the model using non-smooth dynamical system theory is imperative. Mitsui and Aihara [46] when studying this model, observed that the dynamics in the hybrid automata models or ones with complicated spatial dimensions are not clear if analysed using smooth dynamical systems theory, hence in part giving a strong motivation for this work.

Furthermore, it is desirable to include noise in the models of climate phenomenon as the climate system is complex system. Inasmuch as there are some chaotic processes and some uncertainties very evident in the atmosphere and oceans, which influences the climate. Therefore the inclusion of noise in the model of ice ages (AD15) was useful though in their analyses they never considered it. However, noise can have an effect known as phase dispersion on oscillators as glacial cycles [13].

However the principal climate models discussed in this chapter has some limitations and strengths. The weaknesses of these models are summarised in the Table 2.1. From the table, we could observe that most models have a weakness in explaining the Carbon Dioxide equation. However, the PP04 model captures the effect of the Carbon Dioxide on climate system and also provides the physical meaning of Carbon Dioxide changes in the atmosphere by considering processes occurring in the ocean. Most of the models are able to reproduce the results as captured in observational data (see Table 2.2) of the climate system but do not properly capture the sudden change in dynamics such as the MPT.

Table 2.1: Table summarising the weaknesses of main climate models discussed

Model	Weakness
Budyko	Uses energy balance and not consider the effect of Carbon Dioxide
SM90	Physical interpretation of CO_2 equation unclear
SM91	Physical interpretation of CO_2 equation unclear
P98	Physical meaning of the discrete variable
AD15	Physical interpretation of drift function $\lambda(t)$ and of climate state y

Table 2.2: Table summarising the strengths of main climate models discussed

Model	Strength
Budyko	Agreement of temperature results and observational data.
SM90	captures a close fit to Vostok data.
SM91	Gives a close fit to the SPECMAP and Vostok data.
P98	Gives a perfect fit to reconstructed data from Vostok records.
AD15	A good fit to observational data for over a period of 200 $kyrs$.

2.2 Dynamical systems

Differential equations are used widely in sciences to model systems that change with time in an attempt to provide the simple representation of the processes, mechanisms or phenomenon. If a differential equation is derived about the physical process, it is usually important to know the solutions and their behaviour both long and short time to gain an information about the process.

A general definition of a dynamical system written in terms of an $n-$dimensional state space $X \in \mathcal{R}^n$ and an evolution operator ϕ that takes elements x_0 of the phase space and evolves them through time t to a state x_t defined

$$\phi^t := X \to X, \quad x_t = \phi^t(x_0) \tag{2.4}$$

where t takes values in an index set T.

Definition 2.2.1. A state space X, index set $T \subset \mathcal{R}$ and the evolution operator ϕ^t are said to define a dynamical system if

$$\phi^0(x) = x, \quad for\ all \quad x \in X \tag{2.5}$$

$$\phi^{t+s}(x) = \phi^s(\phi^t(x)), \quad for\ all \quad x \in X,\ t, s \in T \tag{2.6}$$

The set of all points $\phi^t(x)$ for all $t \in T$ is called the orbit and the partitioning of the state space into orbits is called the phase portrait[19].

Definition 2.2.2. A dynamical system satisfying (2.5) and (2.6) is said to be smooth of index C^r if the first r derivatives of ϕ exists and are continuous at every point $x \in X$ [19].

Therefore a general dynamical system can be defined

$$\dot{\mathbf{x}} = \mathbf{f}(\mathbf{x}),\ \mathbf{x} \in \mathcal{R}^n \tag{2.7}$$

where $\mathbf{f}(\mathbf{x}) = \frac{\partial}{dt}(\phi^t(\mathbf{x}))$ is the vector field and can either be smooth or non-smooth. Therefore equation (2.7) is a system of ordinary differential equations.

Most nonlinear differential equation systems of the form (2.7) do not have explicit solutions. However the qualitative behaviour of the solutions can be studied geometrically, and this lies at the heart of the theory of dynamical systems. More especially the long term behaviour of the trajectories, as they provide more information about the invariant solutions of the system. Considering that systems of Ordinary differential equations exhibits different kinds of invariant sets such as equilibria and limit cycles and it is important to establish whether these are attracting or otherwise [29].

Definition 2.2.3. [19] An invariant set of a dynamical system (2.5- 2.6) is a subset $\Lambda \subset X$ such that $x_0 \in \Lambda$ implies that $\phi^t(x_0) \in \Lambda$ for all $t \in T$. An invariant set that is closed and bounded is called an attractor if :

1. for any sufficiently small neighbourhood $U \subset X$ of Λ, there exists a neighbourhood V of Λ such that $\phi^t(x) \in U$ for all $x \in V$ and all $t > 0$.
2. for all $x \in U$, $\phi^t(x) \to \Lambda$ as $t \to \infty$.

Definition 2.2.4. A closed and bounded invariant set Λ is called chaotic if it satisfies the two additional conditions and if :

1. it has sensitive dependence on initial conditions. That is there exists an $\epsilon > 0$ such that, for any $x \in \Lambda$ and any neighbourhood $U \subset \Lambda$ of x, there exists $y \in U$ and $t > 0$ such that $|\phi^t(x) - \phi^t(y)| > \epsilon$.
2. There exists a dense trajectory that eventually visits arbitrarily close to every point of the attractor[19].

However a dynamical system might have many competing attractors. Their importance is indicated by the size of the set of initial conditions that they attract. That is their domain or basin of attraction.

Definition 2.2.5. The domain of attraction of an attractor is the maximal set U for which $x \in U$ implies $\phi^t(x) \to \Lambda$ as $t \to \infty$ [19].

However, when the dynamical system has a discontinuous vector field, or if the evolution of the system with respect to time is discontinuous and or if the state reaches a discontinuous boundary, then the system is said to a non-smooth dynamical system [20, 10].

2.3 Non-smooth dynamical systems

A general unforced dynamical system is defined as

$$\dot{\mathbf{x}} = \mathbf{f}(\mathbf{x}), \ \ \mathbf{x} \in \mathcal{R}^n \tag{2.8}$$

where the vector field $\mathbf{f}(\mathbf{x})$ is piecewise smooth or discontinuous. This is known as piecewise smooth dynamical system as the trajectories of the solution may not be differentiable everywhere. The discontinuous dynamical systems have been used to model different processes or mechanisms. Considering that numerous physical processes and some machinery are characterised by periods of smooth evolutions and instantaneous interrupted events, they can be represented by non-smooth dynamical

system [19]. Notably non-smooth dynamical systems has been widely used in different scientific disciplines such as in vibro impacting mechanics, switching electronic circuits such as thermostats, vibration hammers e.t.c. Furthermore, Feigin [25] suggests that the piecewise continuous dynamical systems gives a good description of the behaviour of the broad class of machines such as relay, dry friction and vibroimpact machines. As a consequence, non-smooth dynamical systems were used in the model of a vertically bouncing ball on a sinusoidal vibrating plate [35]. Moreover, Shaw [72] employed the use of piecewise smooth systems when studying mechanical systems with components making intermittent contacts by representing the systems by a periodic forced piecewise linear oscillator. Likewise, Peterka [59] used the non-smooth systems when studying mechanical systems with impacts in particular those that have change in stability of periodic motion to a chaotic one. However, Barry *et al.* [4] extended the Budyko energy balance model of climate and considered the albedo to be dependent on the iceline and latitude. They introduced a step function which suggests that the change in iceline is dependent on latitude and greenhouse gas effect hence obtaining a non-smooth dynamical system.

Nevertheless different types of discontinuities captured in non-smooth dynamical systems gives birth to different classes of solutions. Thus the systems can be classified depending on the degree of their smoothness. According to Cortés [12] and di Bernardo *et al.* [19], the degree of smoothness depends on whether the system exposes jumps and or switches on its state, vector field or its Jacobian. Therefore the non smoothness behaviour can be represented by the piecewise smooth system.

For instance, the climate system experiences switches between different climatic states and some climate variabilities and therefore these switches can be modelled using non-smooth dynamical systems. For example the switch of the glacial cycles from glacial to interglacial states, in the PP04 model of glacial cycles was represented by a step (Heaviside) function, hence resulting into a piecewise smooth dynamical system [57]. In the study of the El Niño Southern Oscillation phenomenon, non-smoothness is represented by a delay equations in the classical delayed oscillator (ENSO) model [21].

2.3.1 Piecewise smooth systems

Piecewise smooth systems are characterised by having dynamics that are determined by different equations depending on the region of phase space the trajectory is passing through. In each region, the evolution of trajectories are defined by the smooth dynamical system which changes to a different defining system across the discontinuity boundary [29]. Therefore they can be classified into three classes: maps, flows and hybrids systems [19].

Definition 2.3.1. *Piecewise smooth map*
A piecewise smooth map consists of a finite set of smooth maps [19]

$$\mathbf{x} \mapsto F_i(\ \mathbf{x}), \qquad \mathbf{x} \in S_i \tag{2.9}$$

where each function $F_i(\mathbf{x})$ is smooth in state $\mathbf{x}$ and defined for any open subset U of S_i. The map has a switching boundary or discontinuity boundary (Σ) which is $n-1$ dimensional and separates the regions of the phase space S_i where different smooth maps apply.

Definition 2.3.2. *Piecewise smooth flow*
A piecewise smooth flow is given by a finite set of ordinary differential equation [19]

$$\dot{\mathbf{x}} = \mathbf{F}_i(\mathbf{x}) \qquad \mathbf{x} \in S_i \subset R^n \tag{2.10}$$

where each subspace or region S_i has a non-empty interior, and $\cup_i S_i = D \subset R^n$. Each vector field $\mathbf{F}_i(\mathbf{x})$ is smooth in the state $\mathbf{x}$ and defines a smooth flow $\Phi_i(t)$ within the disjoint open regions S_i. The intersection $\Sigma_{ij} := \bar{S}_i \cap \bar{S}_j$ is either an R^{n-1} dimensional manifold included in the boundaries ∂S_i and ∂S_j or is an empty set.

A non empty border or intersection between any two or more regions Σ_i is called discontinuity boundary or switching manifold. The switching manifold consists of finitely many smooth manifolds intersecting transversely, and the union of Σ_i and all S_i covers the whole state space $D \subseteq R^n$ [19, 11]. In studying the behaviour of the flow at the switching manifold, the degree of smoothness of the boundary and the discontinuity of boundary is considered.

Definition 2.3.3. *Degree of smoothness*
The degree of smoothness at a point $x_0 \in \Sigma_{ij}$ of a piecewise smooth ordinary differential equation with a single boundary, is the highest order r such that the Taylor expansions of $\Phi_i(x_0, t)$and $\Phi_j(x_0, t)$ with respect to time evaluated at $t = 0$ agree up to terms of $\mathcal{O}(t^{r-1})$ [19].

Definition 2.3.4. *Uniform discontinuity*
A discontinuous boundary Σ_{ij} is said to be uniformly discontinuous in some domain D if the degree of smoothness is the same for all points $\mathbf{x} \in \Sigma_{ij} \cap D$. If the first non-zero partial derivative of $F_i - F_j$ evaluated on the boundary is of order $m-1$ we say the discontinuity is uniform with degree m. That is, degree of smoothness is one if $F_i(\mathbf{x}, \mu) - F_j(\mathbf{x}, \mu) \neq 0$ for $\mathbf{x} \in \Sigma_{ij} \cap D$[19].

Climate models takes the form of smooth flows with changes in rate of a certain quantity. Many of the dynamical systems models in climate including the PP04 model which we will study in detail, have a discontinuity included in the evolution of the flow that makes it a piecewise smooth dynamical system. In particular, the

PP04 is an example of piecewise smooth system, of the Filippov system type because $F_i(\mathbf{x}, \mu) \neq F_j(\mathbf{x}, \mu)$.

2.3.2 Filippov systems

The Filippov systems are the particular examples of piecewise smooth systems characterised by ordinary differential equations defined in a certain region, where the discontinuity boundary is defined by a smooth scalar function $H(\mathbf{x})$ such that $\Sigma_{ij} := \{\mathbf{x} \in R^n |\ H(\mathbf{x}) = 0\}$. When we consider a single boundary Filippov system, then the regions can then be expressed as

$$S_i = \{\mathbf{x} \in R^n |\ H(\mathbf{x}) < 0\}$$
$$S_j = \{\mathbf{x} \in R^n |\ H(\mathbf{x}) > 0\},$$

Therefore a Filippov system with two states can be written as

$$\dot{\mathbf{x}} = \begin{cases} \mathbf{F}_1(\mathbf{x}, \mu) & \text{if} \quad H(\mathbf{x}) < 0 \\ \mathbf{F}_2(\mathbf{x}, \mu) & \text{if} \quad H(\mathbf{x}) > 0 \end{cases} \tag{2.11}$$

where $\mathbf{F}_1(\mathbf{x}, \mu)$ generates a flow $\Phi_1(\mathbf{x}, \mu)$ defined on the region S_1 and $\mathbf{F}_2(\mathbf{x}, \mu)$ generates a flow $\Phi_2(\mathbf{x}, \mu)$ defined on the region S_2. The discontinuity manifold $\Sigma_{12} := H(\mathbf{x})$ is between the two regions and μ is a parameter [11, 19, 17]. The switching manifold is considered to be as smooth as the flow. Thus flow Φ_1 can be defined as the quantity that satisfy

$$\frac{\partial}{dt}\Phi_1(\mathbf{x}, t) = \ \mathbf{F}_1(\Phi_1(\mathbf{x}, t)),\ \ \Phi(\mathbf{x}, 0) = \mathbf{x}.$$

According to Piiroinen *et al.* [61], the most important feature of the Filippov systems is the possibility of motion to be constrained to some region of the state space. If the vector fields $\mathbf{F}_1(\mathbf{x}, \mu)$ and $\mathbf{F}_2(\mathbf{x}, \mu)$ are locally both pointing away or towards the discontinuity surface $\Sigma_{12}(\mathbf{x})$, the dynamics are assumed to be locally constrained to the surface. Therefore when the trajectories of the Filippov system are confined to the boundary, they can be described by three basic forms of dynamics that would occur at the switching manifold: crossing , sliding and escaping, which depends on the orientation of the vector field on either side of the switching manifold[11]. To find out what happens to the trajectory of the flows when they reach the switching manifold from either region, we assess the components of the vector fields $\mathbf{F}_1(\mathbf{x}, \mu)$ and $\mathbf{F}_2(\mathbf{x}, \mu)$ orthogonal to the switching manifold Σ_{12}. That is, we find

$$\mathbf{W}_1(\mathbf{x}) = \nabla^T H(\mathbf{x}) \mathbf{F}_1(\mathbf{x}, \mu)$$

and $\mathbf{W}_2(\mathbf{x})$ which defines the forward time orbits.

Definition 2.3.5. *Crossing region*
The crossing region of a system (2.11) with uniform degree of smoothness one and having the phase space region divided into two regions, is given by that portion of the boundary of $H_{12}(\mathbf{x})$ for which

$$\mathbf{W}_1(\mathbf{x}) \cdot \mathbf{W}_2(\mathbf{x}) > 0.$$

The crossing regions are classified into the negative and positive crossing regions. Negative crossing is obtained for $\mathbf{x} \in \Sigma_{12}$ such that both $\mathbf{W}_1(\mathbf{x}) < 0$ and $\mathbf{W}_2(\mathbf{x}) < 0$. While the positive crossing is obtained for $\mathbf{x} \in \Sigma_{12}$ such that $\mathbf{W}_1(\mathbf{x}) > 0,\ \mathbf{W}_2(\mathbf{x}) > 0$. On the other hand, when the normal component of the vector field switches direction and the vector field is directed away from the manifold, we obtain escaping[11]. Otherwise when the trajectory or limit cycles may tangentially hits the switching manifold in the phase space, this is called grazing (see Figure 2-6b) and may result in non-unique solutions [17].

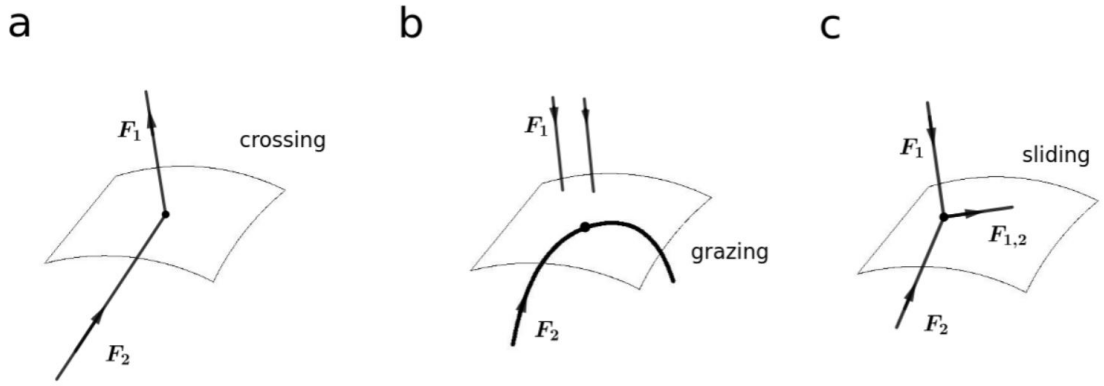

Figure 2-6: Trajectories of the vector field $\mathbf{F}(\mathbf{x})$ which switches between $\mathbf{F}_1$ above the surface and $\mathbf{F}_2$ below it. a) trajectory crosses the switching manifold. b) trajectory of $\dot{\mathbf{x}} = \mathbf{F}_2$ grazes the switching manifold. c) sliding trajectory constrained to evolve along the switching manifold. That is, both trajectories of $\mathbf{F}_1$ and $\mathbf{F}_2$ got attracted to the switching manifold and the combined trajectory $\mathbf{F}_{1,2}$ and $\mathbf{F}_2$ slide on the manifold.

Generally it is not possible to obtain analytical solutions of Filippov systems and thus their solutions cannot be expressed in terms of elementary functions. Consequently, the most notions of smooth dynamical systems cannot be directly applied to Filippov system but needs some updating first [31]. For example, in piecewise smooth systems concepts such as orbits need to account for finite time effects while the definition for topological equivalence needs to consider that many different trajectories can arrive at the discontinuity boundary and slide. Furthermore, since the solutions of these systems are not guaranteed, to obtain their analytical solutions, reformulation has to be done to construct a Filippov set valued map. The map then aids in transforming the differential equation into differential inclusion called the Filippov regularisation

[34]. That is the system takes the form,

$$\dot{\mathbf{x}} \in \mathbf{F}(\mathbf{x}(t)), \quad t \in [0, T]$$

where $\mathbf{F}(\mathbf{x}(t))$ is a set valued map. Complementary systems methods are another way that Filippov systems can be studied analytically. Other than these, a Filippov system can be studied by a geometric approach where the solutions are obtained analytically for two regions and then merged together. This approach allows for the determination of important characteristics of the solution which are the stability and bifurcations of the invariant sets.

In dynamical systems, the presence of periodic solutions implies that the system has some kind of an attractor. In particular, there are different kinds of attractors the most common being fixed points (equilibrium points), periodic (limit cycles) and chaotic attractors [83, 84]. Nevertheless, under parameter variations there is a possibility of destroying or changing the long time dynamics of dynamical system or affecting the stability of the invariant sets (attractors). When the qualitative appearance of dynamics of the system has changed, it is said to have a bifurcation. The parameter values at which the bifurcation occurs is called bifurcation point. However, according to di Bernardo *et al.* [19], the definition of bifurcation used in smooth dynamical systems is not used in non-smooth dynamical systems. Furthermore, in smooth systems, bifurcations can be defined by using the analytical or topological approach which are problematic in non smooth dynamics [20].

2.4 Bifurcations

Non-smooth dynamical systems can experience two types of bifurcations. That is, they can experience both smooth (where the local bifurcation occurs when one or more eigenvalues of the system crosses the imaginary axis of the system) and non-smooth (Discontinuity Induced Bifurcations) bifurcations. For instance, the smooth bifurcations that describe the evolution of attractors and are familiar and can be observed in non-smooth systems includes the saddle-node, Hopf and period doubling.

Notably, in piecewise smooth systems, the presence of the discontinuity boundary leads to complicated dynamical behaviour and bifurcations which are not possible in smooth systems. Feigin was one of the first to study bifurcation phenomena in non-smooth dynamical systems in detail, whereby he considered the case where the fixed point or period point changes stability when it collides with the switching manifold. He termed the resulting bifurcations C- bifurcations [26, 18]. Nusse and Yorke [51] later described these kind of bifurcations as the Border Collision Bifurcations a term commonly used today. However some of the main results by Feigin were remodelled

into the framework of modern bifurcation theory by di Bernado *et al.* [18] . On the same note, Filippov contributed immensely into the study of non-smooth dynamical systems by providing a detailed qualitative behaviour of these systems near or at the discontinuity boundary using regularised Filippov systems [34].

According to Simpson [74], the discontinuity boundary often causes changes in the system's response. For this reason, the bifurcation phenomena unique to piecewise smooth systems is where an invariant set interacts with the discontinuity boundary called Discontinuity Induced Bifurcation (DIB). This situation can exhibit dramatic transitions whereby periodic solutions suddenly transition to large scale chaotic attractors [17]. The behaviour of the invariant sets when interacting with switching manifold gives the type of DIB: Border collisions of maps, boundary equilibrium bifurcations, grazing bifurcation of limit cycles, sticking and sliding bifurcation or boundary intersection crossing or corner collision [19, 20].

Definition 2.4.1. *Discontinuity Induced Bifurcation*
A system of the form (2.11) is said to undergo a discontinuity induced bifurcation at a parameter value $\mu = \mu_0$ if there exists an arbitrarily small perturbation that leads to a loss of piecewise topological equivalence [17].

According to di Bernardo *et al.* [19], the common DIB occurring in codimension one systems such as the Filippov systems are Boundary Equilibrium Bifurcation (BEB) and Border Collision Bifurcation (BCB). Boundary Equilibrium Bifurcation is the type of DIB that occur when an equilibrium point lies on the discontinuity boundary and is associated with flows. Similarly, Border collision bifurcation are related to maps and corresponds to a fixed point (or periodic point) perturbed away from the switching manifold of the map.

Definition 2.4.2. *Boundary equilibrium bifurcation* [19]
A Filippov system (2.11) is said to undergo a boundary equilibrium bifurcation at $\mu = \mu^*$ if there exists a point x^* such that, for both $i = 1$ and 2:

1. $\mathbf{F}_i(x^*, \mu^*) = 0$
2. $H(x^*, \mu^*) = 0$
3. $\mathbf{F}_{i,x}(x^*, \mu^*)$ is invertible or equivalently $det(\mathbf{F}_{i,x}) \neq 0$.
4. $H_\mu(x^*, \mu^*) - H_x(x^*, \mu^*)[\mathbf{F}_{i,x}^{-1}\mathbf{F}_{i,\mu}](x^*, \mu^*) \neq 0$

In a piecewise smooth dynamical system, the complicated dynamics are often generated by the grazing bifurcation. A grazing bifurcation corresponds to the interaction of a periodic orbit with the boundary of the discontinuity surface (switching manifold) or where a periodic orbit touches the switching manifold [76, 74, 50]. Thus the limit cycles of the flow becomes tangential with the switching manifold under parameter perturbation.

Definition 2.4.3. *Grazing bifurcation of limit cycles*
A Filippov system (2.11) undergoes a grazing bifurcation at $\mu = \mu^*$ with respect to vector field $\mathbf{F}_1$ if there exists a point x^* such that

1. $\mathbf{F}_1(x^*, \mu^*) = 0$ but $\mathbf{F}_2(x^*, \mu^*) \neq 0$
2. $H(x^*, \mu^*) = 0$
3. $\mathbf{F}_{1,x}(x^*, \mu^*) = 0$ is invertible or equivalently $det(\mathbf{F}_{1,x}(x^*, \mu^*)) \neq 0$ [19]

Although the grazing bifurcations are local bifurcations: that is bifurcation that occur only at the switching manifold, the resulting motion of the orbit can be complex as this bifurcation destabilises the solution. Consequently, when studying dynamics of a system, it is important to not only know the location and type of solutions for the system, but also their basin of attraction [27]. This will enable us to know the behaviour of an orbit for certain initial conditions and also the regions of the phase plane that will give solutions that will be attracted to a certain equilibrium.

In our study of the $PP04$ model, we will find the evidence of Boundary Equilibrium bifurcations in the case of the unforced model. Whilst for the periodically forced PP04 model, we will observe the grazing bifurcations.

2.4.1 Relaxation oscillators and excitable systems

When considering periodic solutions governed by a parameter λ, we usually see changes in the stability as λ is varied. Periodic solutions and other attractors have various forms of stability: asymptotic and global. Asymptotic stable attractors have the trajectories of nearby orbits attracting towards them whereas, for globally stable attractors, all the trajectories in the phase plane are attracted towards them. As a result, a limit cycle is formed.

Definition 2.4.4. *Asymptotic stability* [19]
The equilibrium solution $x = \phi(t)$ of the system (2.8) at the origin is said to be asymptotically stable if :

1. For all $\epsilon > 0$, there exists $\delta > 0$ such that for any other solution $x = \psi(t)$ satisfying $||\psi(t_0) - \phi(t_0)|| < \delta$ then $||\psi(t) - \phi(t)|| < \epsilon$ for all $t > t_0$
   and
2. There exists δ_0 such that whenever $||\psi(t) - \phi(t)|| < \delta_0$ then $\psi(t) \to \phi(t)$ as $t \to \infty$.

According to Soliman [78] there can be several attractors that may coexist at a fixed set of parameter value where each attractor is embedded in its basin of attraction. In nonlinear systems, multiple attractors are common and there might be a coexistence

of chaotic and periodic attractors. Coexistence of solutions means that there is a possibility of existence of two periodic states at the same parameter value [77].

Relaxation oscillators are examples of limit cycles with global stability which have orbits with two time scales. That is, the oscillator is characterised by a consecutive extremely slow build up followed by a sudden discharge of motions (see Figure 2-7) and hence the orbit have segments of fast growth or reduction and segments of slow decay or growth and resetting at the threshold [62].

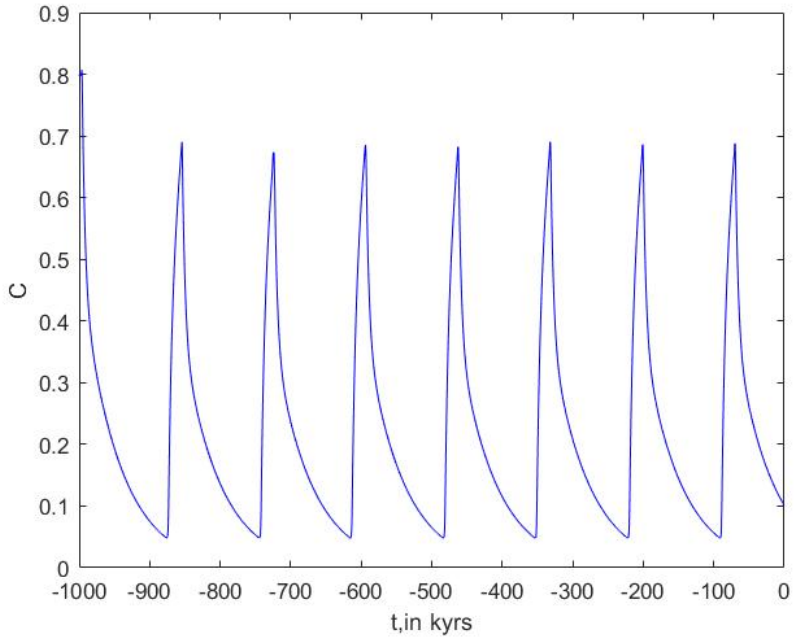

Figure 2-7: The graph showing the saw tooth behaviour of Carbon Dioxide depicting the sudden release of Carbon Dioxide into the atmosphere and its slow absorption by the ocean. The graph was obtained by solving the smoothed unforced PP04 model with $\eta = 80$ and initial conditions $V = 0.25, A = 0.55, C = 0.8$

However, a relaxation oscillator's oscillations are based upon the behaviour of a physical system's return to equilibrium after being disturbed. The period of the oscillations are determined by the time that it takes the system to relax from every perturbed state to the threshold that triggers the next disturbance [90]. According to Crucifix [13], there are three main types of relaxation oscillators based on their structure:

1. relaxation founded on slow-fast dynamics. That is whereby the vector space is organised by a slow manifold with several stable branches with all points of state space attracted towards the stable branches of the slow manifold (see Figure 2-8 (a) and (d)).

2. relaxation structured by a homoclinic orbit. In this type of relaxation oscillation, trajectories are quickly attracted towards a region of the phase plane influenced by a saddle point. However as the trajectory comes near to the saddle point, it

take a longer time before escaping in the direction of the unstable manifold (also known as bottleneck effect) (see Figure 2-8 (b)).

3. relaxation structured around a focus an unstable (see Figure 2-8 (c)).

If we refer to Figure 2-3, we can see that ice ages have the apparent form of relaxation oscillators. Ice ages depict a period of slow ice build up and a period of fast loss of ice sheets. A period of ice loss is initiated by a threshold mechanisms which involves the thermohaline circulation at the South Ocean that triggers ocean ventilation, thus releasing carbon dioxide into the atmosphere and hence observing two types of climate states (glacial and interglacial) in one glacial cycle. Therefore a number of scientists have used this knowledge to come up with different models [2, 54, 57, 67]. All these models envisaged that this climate phenomenon as an oscillator precisely a relaxation oscillator. A good review of models that use the notion of relaxation oscillation is given in a paper by Crucifix [13] and most of these models captures the smooth behaviour of the climate dynamics. However there are some models which also captures the non-smooth behaviour such as the P98 and PP04 models.

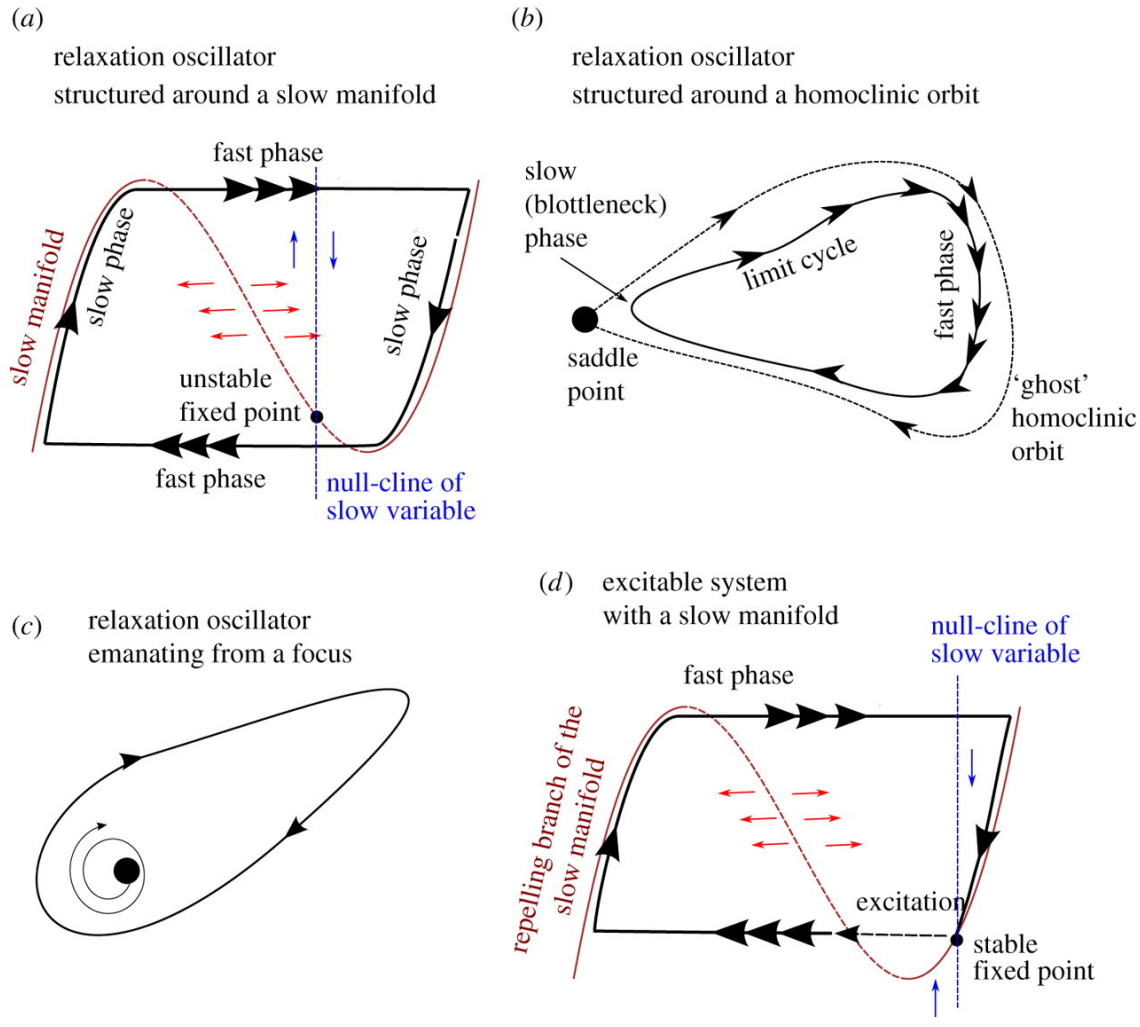

Figure 2-8: The graph showing different schematic forms of relaxation oscillators (image from Crucifix [13]).

A nonlinear dissipative dynamical systems which has the capacity to produce periodic oscillations such as a relaxation oscillator without an external drive is called a natural oscillator. These oscillators with self sustained oscillations can be excited by external perturbations [13]. However, their natural rhythm can be restored after perturbation of their oscillations [62] and therefore are called excitable systems. On the other hand, a dissipative natural oscillators when periodically forced or coupled to another oscillator, their frequencies may lock at different ratios through a phenomenon called synchronisation [43].

Synchronisation and resonance

When two oscillators with different natural frequencies have synchronised, their rhythms or frequencies are adjusted due to weak interaction such that they start to oscillate with a common frequency [39]. While in contrast, resonance is the phenomenon where an oscillator will oscillate with greater amplitude when forced near its natural frequency [81, 43]. However, when the dissipative self sustained oscillator is forced at a frequency that is the rational fraction of its natural frequency, it can phase lock and then can oscillate with the frequency near its natural frequency [43]. Furthermore, Strogatz [81] and Mike Schaus [69] assert that phase locking (synchronisation) can also occur when the coupled system's response oscillates at either the frequency of forcing or with a ratio of the forcing frequency. This can be determined by the strength of forcing as well as, how far from its natural frequency the system is forced. On the other hand, when the forced system assumes the frequency of the forcing or the ratio of forcing frequency, it is said to have entrained to the forcing frequency. However, synchronisation depends on the coupling strength and the difference between the two natural frequencies of the coupled system but not on the initial conditions [62]. That is, weak force or coupling can only influence the phase. We will see this behaviour in the PP04 model.

Arnold tongues and resonance tongues

When two coupled self sustained oscillatory systems interact, they can create regions on the phase plane, for which the frequencies of the coupled system are phase-locked. These are known as Arnold tongues. These regions provide information about the stability change and different dynamics obtained on the phase plane as the parameters of the forcing are varied. Moreover, inside these stability regions, forcing cycles and the resulting forced oscillations have ratios, in specific ratio of $n : m$. That is, the synchronous regimes with n cycles of forcing within m cycles of system oscillation can be observed [69]. This $n : m$ synchronisation phenomena for $n, m \in \mathbb{N}$ gives a relationship between phase of natural oscillator $\psi(t)$ and forcing phase $\phi(t) = \omega t$ such that $0 < |m\phi(t) - n\psi(t)| \leq 2\pi$. That is, the phase difference

across the synchronisation region changes between zero and π with phase difference of zero at the centre of the tongue. Hence obtain the relation $\frac{n}{m} = \frac{\omega}{\Omega}$ where Ω is frequency of the synchronised oscillations [43].

In most cases, the synchronisation of order $n : m$ can be observed with the tongues touching the ω axis of the parameter space and the regions becoming very narrow for large values of n and m [62]. That is having a tip at $\mu = 0$ and $\omega = \frac{m\omega_0}{n}$, for ω_0 being natural frequency of system. In addition, as μ is increased the tongues widen up and might overlap when a certain critical value of amplitude μ_c is reached which indicates the breaking up of the invariant tori [43] or coexistence of frequencies. According to Thompson *et al.* [84] and Montoya [48], outside the periodic mode locked regimes, there is drift (movement) corresponding to either chaotic or quasi-periodic motion. A quasi-periodic motion is achieved when the dynamic behaviour is characterised by the coexistence of two or more incommensurate frequencies [79]. Nevertheless, the change from synchronised regimes to unsynchronised ones corresponds to a saddle node bifurcation [43]. We will observe this in the periodically forced PP04 model.

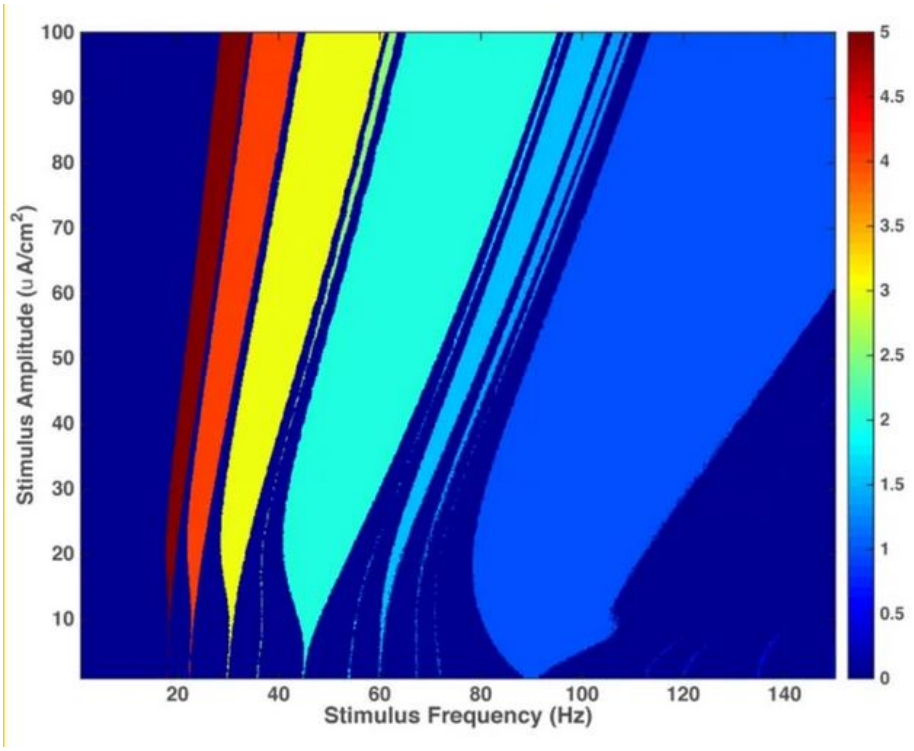

Figure 2-9: The diagram showing Arnold tongues representing the mode-locked regions as a function of the amplitude and frequency of this periodic forcing (image from A. Farokhniaee and E.W.Large [24]).

On a different note, resonance occurs when there is a noticeable increase in the amplitude of the periodic forcing near some frequencies. Therefore the resonance tongues which are regions in parameter space within which particular periodic solutions exists and are attracting, obtained by keeping the amplitude μ of forcing constant, and plotting the amplitude of periodic solutions as a function of the forcing frequency ω [82]. However, when the forcing frequency approach as certain fraction

or multiple of natural frequency of the system, there will be additional sub-harmonic resonances. Resonance occur for sufficiently large amplitude forcing [43]. The overlapping of resonance regions imply multi stability or coexistence of multiple stable periodic solutions or resonance states [77, 78]. However, according to Simpson [74], the resonance tongues of piecewise smooth continuous maps are commonly characterised by sausage-like geometry where stable and unstable periodic solutions exists throughout the tongue. Furthermore, for smooth maps, the codimension one boundaries of tongues may be analogous to familiar smooth bifurcations such as saddle node and period doubling [75], while for piecewise smooth systems the tongue boundaries may be due to boundary collision bifurcations [74].

The climate system comprises processes and phenomena for instance, glacial cycles, which are natural oscillators. If this oscillator is then forced by the other self sustained oscillation system, such as astronomical forcing, we expect to see resonance and synchronisation phenomena. That is, both resonance and synchronisation can be observed in glacial cycles. In this thesis to do the calculations to obtain resonance regions, the stroboscopic technique in particular a Poincaré map is used.

Natural Poincaré map

In order to study the dynamics near the limit cycle associated with the glacial cycles, we often make use of a Poincaré section and an associated map.

The Poincaré section is an $n-1$ dimensional surface Π that contains a point x_p such that x_p is a point on the limit cycle that is transverse to the flow at x_p. The notation of the Poincaré section is given as

$$\Pi := \{x \in \mathbb{R}^n : \pi(x) = 0\} \tag{2.12}$$

for some smooth scalar function π. The transversality condition is given by the normal vector $\pi_x(x_p)$ to Π at x_p having a non-zero component in the direction of the $\phi_t(x_p, 0) = f(x_p)$ [19]. That is, we have

$$\pi_x(x_p) f(x_p) \neq 0.$$

A Poincarè map is a mapping from Π to itself. This is obtained by following the trajectories from one intersection with the Poincaré section to the next, which is defined for, say x, sufficiently close to x_p contained in Π [19]. Thus Poincaré map reduces the dimension of the system by one and simplifies the study of a system of Ordinary Differential Equations (ODE) to the analysis of discrete difference equations or maps.

However to construct the Poincaré map analytically is not an easy task, and for practical problems, numerical methods are generally needed. Since the Poincaré map

is an exact method, the topology of phase space of the Poincaré map is identical with the topology of the phase space of the original non-averaged system. Consequently, they are useful in studying swirling flows such as flows near a periodic orbit [81] and hence Taylor [83] states that the bifurcation analysis of nonlinear continuous models is somewhat based on the ideas of Poincaré map. For non-smooth system with discontinuity on set Σ it is natural to set the Poincaré section to be equal to the discontinuity boundary more especially for crossing flows.

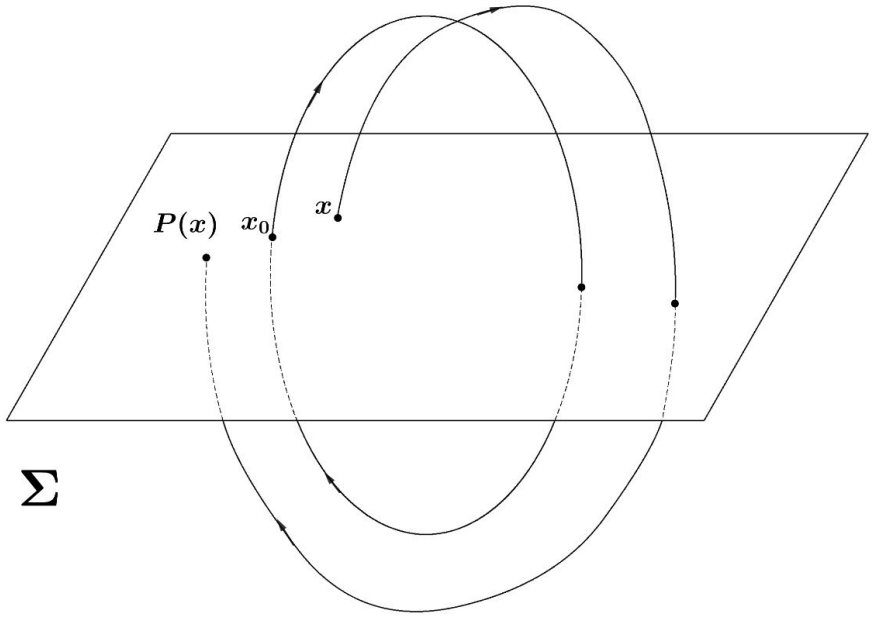

Figure 2-10: The graph showing the trajectories of the system as they intersect the discontinuity boundary (Poincaré section) creating a Poincaré map.

Suppose we consider an ice age model of climate, simplified to $n-$ dimensional systems of ODEs. The Poincaré section of this system should have $n-1$ dimensions. Consequently we should consider a natural Poincaré map

$$P_s : \mathbb{R}^{n-1} \to \mathbb{R}^{n-1} \tag{2.13}$$

If the forcing on the system is periodic, with frequency ω a natural and Poincaré map to be considered is the stroboscopic map defined by

$$P_S : \mathbf{x}(t) \to \mathbf{x}\left(t + \frac{2\pi\ k}{\omega}\right) \tag{2.14}$$

$$P_S\ \mathbf{x}(t) \equiv \mathbf{x}\left(t + \frac{2\pi\ k}{\omega}\right),\ \ for\ \ some\ \ \ k \in \mathbb{N}. \tag{2.15}$$

Using this map we can construct a set of points $\mathbf{x}_m$ defined by the iteration

$$\mathbf{x}_{m+1} = P_S\ \mathbf{x}_m. \tag{2.16}$$

If $\mathbf{x}_m \to \mathbf{x}^*$ then this corresponds to a periodic solution of the ODE system. If, asymptotically $\mathbf{x}_m$ lie on a closed (invariant) curve this corresponds to a torus in the original system.

We have already established that for a nonlinear dissipative dynamical system forced by a periodic oscillator, tongue like structures of phase-locked regions on the parameter space are observed. Furthermore, when considering the simplest nonlinear dynamical system, for example a circle map (a one dimensional map which maps a circle onto itself), different dynamics such as chaotic, quasi-periodic and strange non-chaotic attractor are observed if the map is forced by a rigid rotation with irrational frequency [53]. However, for quasi-periodically forced smooth dynamical systems, strange non-chaotic attractors are one of the mostly expected dynamics to be observed [22]. Therefore, when considering a smooth model for climate, we expect to also observe non-chaotic strange attractors since the model is quasi-periodic forced.

Strange non-chaotic attractor

Since the attractors of a dynamical systems can be classified by observing the dynamics of typical orbits, the ones characterised by fractal structure are said to have "strange attraction". Moreover, those with fractal structure and non differentiability (strangeness) but with no exponential sensitivity to initial conditions are called Strange non-chaotic attractors (SNA) [8]. Therefore a system has an SNA, when the typical orbits on the attractor have generally non-positive non-trivial largest Lyapunov exponents and when its geometrically strange [30, 37]. Thus typical nearby orbits do not diverge exponentially with time but stay correlated.

As a consequence, a small change to the systems' initial state have a proportionally small effect on the fractal journey of the orbit hence making its evolution relatively predictable and stable. Grebogi *et al.* [30] are the first to observe SNA's from a system defined by a two dimensional map

$$x_{n+1} = 2\sigma(\cos 2\pi\theta_n + \alpha)\tanh x_n$$

$$\theta_{n+1} = \theta_n + \omega \quad mod\, 1$$

where $(\theta, x) \in [0,1]$ x $\mathbb{R}$, $n \in \mathbb{Z}$, ω irrational, with α and σ as non-negative parameters [30, 47, 46]. The map defines a non-linear forced system with the type of forcing determined by ω: if ω is rational, we will have a periodic forced system whereas if ω is irrational, we have a quasi-periodically forced system. However, Prasad *et al.* [65] and Pikovsky *et al.* [63], states that strange non-chaotic attractors are generic in non-linear quasi-periodically forced systems and are not at all rare. As a consequence, SNA's are found in the neighbourhood of periodic, quasi-periodic attractors as well as the strange chaotic attractors in parameter space. Thus, SNA's can occur over a

finite range in parameter space [30]. From the Figure 2-11 and Figure 2-12, we could observe that the qualitative appearance of trajectories are dependent on the value of α. Furthermore, the SNA exists only for $|\sigma| > 1$ [63].

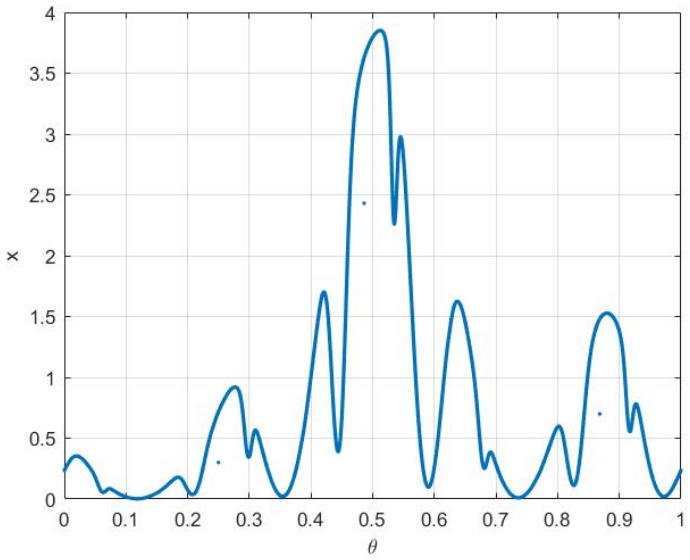

Figure 2-11: The graph showing the phase portrait of the circle map exhibiting a quasi-periodic attractor obtained for initial values $\theta = 0.25$, $x = 0.3$ with $\omega = (\sqrt{5} - 1)/2$ and parameters $\alpha = 1.001$ and $\sigma = 1.2$.

According to Prasad *et al.* [65] the distinct route or mechanism for SNA's formation is not yet clear. However, there are some already known situations that make their formation possible: the wrinkled double torus formed due to period doubling bifurcation ocollides with its unstable parent torus in a dense set of θ (torus collision), fractalisation, intermittency or blowout bifurcation. Of all the mentioned mechanisms above, the torus collision is the most common [65]. However, a sequence of torus doubling bifurcations depends upon the nonlinearity parameter of the model when the amplitude of forcing is fixed. Nevertheless, when the amplitude is large, smooth torus transform into an SNA thereby number of torus doubling bifurcation in a sequence depends on the amplitude [37].

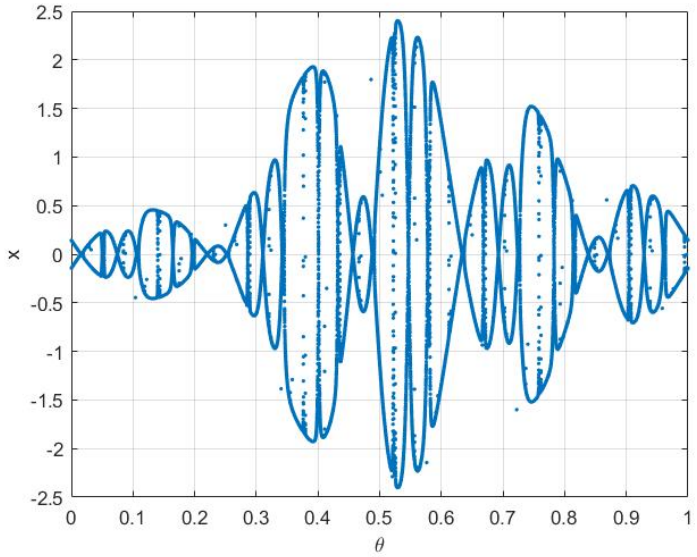

Figure 2-12: The graph showing the phase portrait results of the circle map exhibiting a strange non-chaotic attractor obtained for initial values $\theta = 0.25$, $x = 0.3$ with $\omega = (\sqrt{5}-1)/2$ and parameters $\alpha = 0.8$ and $\sigma = 1.2$.

2.5 The PP04 model of climate dynamics

The model for the glacial cycles that we are studying in this thesis, was introduced by Paillard and Parrenin in 2004. Before the introduction of this conceptual ice age model, there has been a number of conceptual models of glacial cycles introduced, that were employed to explain the observed behaviour of glacial cycles, more especially, the fast or rapid loss of ice sheets followed by the slow growth of ice sheets and MPT. In order to explain the glacial cycles and MPT, the researchers used the notion of interplay between variations of ice, temperature, Carbon Dioxide all coupled together by various feedback loops. The scientists proposed that there is a mechanism between internal cyclicity of earth climate system and astronomical variations that make them to be synchronised. At the same time, the data reconstructed from the Vostok ice core, identified a correlation between temperature and Carbon Dioxide suggesting that Carbon Dioxide drives the glacial cycles [60].

The PP04 is one simple glacial cycle model which captures the physics behind the initiation and termination of the ice ages and the pacing with astronomical forcing. This makes it an interesting model to study and a number of researchers such as Crucifix [13], Mitsui et al. [46] and Ashwin et al. [3] did some study of this model, but considered it a smooth system. This approach, hence limited the findings of the dynamics and bifurcations to be observed in the model. Therefore a thorough study of the model in a non-smooth dynamical systems framework is needed. This is the motivation for the research work.

During the later period of the 20th century, Paillard [54], introduced the model P98, to explained the glacial cycles and abrupt changes of climatic state from glacial

to interglacial using the concepts of relaxation and thresholds. He represented the climate system by the three quasi steady states (deep glacial, mild glacial and interglacial) given by the relaxation processes driven by the astronomical forcing. However in this model, Paillard failed to provide a physical meaning of the discrete variable involved in the threshold criteria. Subsequently, Paillard and Parrenin [57], introduced a relaxation model of ice ages (known as the PP04 model) which incorporates the physical mechanism involving the influence of Antarctica ice sheets extent on bottom water formation. The threshold in the bottom water formation in the Atlantic ocean, induces a switch between the glacial and interglacial states. This transition influences the sudden changes in amount of atmospheric Carbon Dioxide during the glacial-interglacial transitions. Therefore the fast transition from the glacial to the interglacial states is caused by a sudden release of Carbon Dioxide from the ocean into the atmosphere and the slow transition from interglacial to glacial can be explained through Milankovitch theory.

According to Ashwin *et al.* [3], when the surface water rich with oxygen has density which is sufficiently high, it allows for this water to sink to great depths. Thus the bottom water in the deep ocean is strongly stratified with cold salty water which has the capability of storing a lot of carbon. On the other hand, when the Antarctic ice sheet reach its maximum, brine rejection makes salty water formation difficult, and then stratification weakens leading to the release of Carbon Dioxide into the atmosphere. The formulation of the model as a relaxation oscillator is due to multiple states of the glacial cycles evident from records of deep ocean temperature, Carbon Dioxide or Southern Ocean temperature suggesting a link between Northern ice sheets, atmospheric Carbon Dioxide and deep ocean temperature [57].

On a different note, it was observed from geological records that at the end of every glacial cycle, the temperature change leads Carbon Dioxide decrease and that both Antarctica air temperature and atmospheric Carbon Dioxide concentration lagged global ice volume changes. This showed that the temperature change drives atmospheric Carbon Dioxide. Therefore mechanisms occurring at the Southern Ocean were proposed as significant role players in the long term changes of atmospheric Carbon Dioxide changes [60]. Furthermore, similarities between insolation at 65^0N and data from $\delta^{18}O$ isotope helped in establishing a link between atmospheric temperature and astronomical forcing [40, 60].

2.5.1 The model

The PP04 model describes the evolution of ice sheets and feedback mechanisms associated with global ice volume V, atmospheric Carbon Dioxide content C and the extent of Antarctica ice sheet A. The glacial cycle model is defined

$$\frac{dV}{dt} = \frac{(V_r - V)}{\tau_V,} \tag{2.17}$$

$$\frac{dA}{dt} = \frac{(V - A)}{\tau_A}, \tag{2.18}$$

$$\frac{dC}{dt} = \frac{(C_r - C)}{\tau_C}, \tag{2.19}$$

where variables V, A, C are considered to be functions of time t. From equations (2.17 - 2.19), the first equation shows that the growth of global volume of ice depends upon the quantity of V_r defined

$$V_r = -xC - yI_{65}(t) + z,$$

where the parameters x, y, z are constants and are summarised in Table 2.3. In particular, (2.17) expresses that the global ice volume depends on the amount of Carbon Dioxide in the atmosphere and is driven by the astronomical forcing $I_{65}(t)$. An increase of Carbon Dioxide in the atmosphere as a result of mechanism happening in the Southern Ocean, such as upwelling, cause an increase of the global temperature because Carbon Dioxide is a greenhouse gas, and hence cause the melting of ice caps. The water from melting of the ice caps, is added into the ocean hence affecting the salinity of ocean water. Thereby weakening the upward and downward movement of water and air in the ocean surface, which in turn triggers the absorption of dissolved inorganic carbon on ocean surface. Therefore equation for change in atmospheric Carbon Dioxide concentration is given by (2.19) and C_r defined as

$$C_r = \alpha I_{65}(t) - \beta V + \gamma H(-F) + \delta,$$

where the parameters $\alpha, \beta, \gamma, \delta$ are constants and are also summarised in Table 2.3. According to Garcia-Olivares *et al.* [28], δ can be interpreted as the Carbon Dioxide reference level and β represents the positive feedback between temperature and Carbon Dioxide through the ice volume V and A. The function $I_{65}(t)$ is insolation at the latitude of 65^0N during summer solstice, and is provided in Mitsui *et al.* [46, 16]. The equation (2.19) describes that the growth in the amount of atmospheric Carbon Dioxide is dependent on the volume of global ice and an increase of insolation received, as well as the contribution of the Southern Ocean. The ocean contribution is represented by a Heaviside function which is dependent on the stratification parameter F. Thus the ocean contribution is such that when more fresh water is added into the ocean, causing salinity stratification, in turn makes absorption of carbon on ocean surface possible. When more carbon is absorbed, consecutively the amount or concentration of Carbon Dioxide in the atmosphere is reduced and thereby initiating slow ice sheet growth. When the stratification parameter reach a certain value, the ocean ventilates and through an upwelling of Carbon Dioxide, it is

released into the atmosphere and subsequently causing deglaciation.

Therefore the ocean contribution is parametrised as $H(-F)$ with stratification parameter F acting as a switch when its threshold value is reached and suddenly triggering the release of Carbon Dioxide from the ocean. Consequently there is no ocean contribution during glacial periods until another release of Carbon Dioxide from the ocean is initiated. However, the ocean ventilates when $F < 0$ and the stratification parameter is defined

$$F = aV - bA - cI_{60}(t) + d, \tag{2.20}$$

where the parameters a, b, c and d are constants and provided in the Table 2.3. The stratification parameter increases with global ice volume and decreases with Antarctica ice sheet and Southern Hemisphere insolation. However the parameter d controls the threshold switching for the model from glacial to interglacial states and Southern Hemisphere insolation $I_{60}(t)$, is the daily insolation 60^0S. Therefore the ocean contribution is defined

$$H(-F) = \begin{cases} 1 & \text{if} \quad F < 0 \\ 0 & \text{if} \quad F \geq 0 \end{cases}$$

The parameters τ_V, τ_A and τ_C in equations (2.17- 2.19) are time constants and are also summarised in the table. They are provided in thousands of years units as it is believed that the process for ice volume and Antarctica ice sheet build up before melting take an estimated lag time of $10^3 - 10^4$ years. Therefore the time scale for Antarctica ice sheet and volume of global ice are coupled together with the very faster one for Carbon Dioxide release.

Therefore due to the disparity in the time scales for the climate driven events, it is natural to describe some processes or events as instantaneous when compared to others, for example, the ocean contribution in this model. As a result, the sudden release of Carbon Dioxide into the atmosphere, a fast process compared to ice growth or loss, represented by a step function (representing ocean contribution) introduces the discontinuity in the equation for Carbon Dioxide. Hence making the model a piecewise smooth dynamical system. Consequently the PP04 model becomes a non-smooth dynamical system.

2.6 Astronomical forcing

The astronomical forcing terms are obtained by using a Fourier representation by Berger(1978) for the detection of Northern Hemisphere summer solstice insolation at

higher latitude (65^0N) and is defined by

$$I_{65}(t) = \frac{1}{e}\sum_{i=1}^{35} s_i \sin(w_i\, t) + c_i \cos(w_i\, t) \tag{2.21}$$

where w_i are different frequencies, s_i and c_i coefficients provided in [16, 46, 47]. However the coefficients c_i and s_i are found through linear regression of the insolation on the frequencies ω_i and the function is valid for the period of about the past one million years to present [16]. The parameter e is a scale factor used to make the function for astronomical forcing dimensionless though different researchers seem to take different values of e for different models and the value seem to be dependent on the number of components of the astronomical forcing considered. For instance Ashwin and Dietlevsen [2] considered $e = 1$ for the AD15 model. However Mitsui and Aihara [46] considered $e = 11.77\ Wm^{-2}$ for the Crucifix-De Saedeleer model and $e = 18.3\ Wm^{-2}$ for the SM90, SM91 and PP04 models, basing the value on the three frequency components of astronomical forcing that they considered to be significant. In contrary Mitsui *et al.* [47] considered the parameter $e = 23.58\ Wm^{-2}$ for the PP04 model. According to Mitsui *et al.* [46] the three astronomical forcing components: precession terms at $i = 1$ (23.7 kyr) and $i = 3$ (19.1 kyr) as well as obliquity term at $i = 4$ (41.0 kyr) constitute 78 percent of original insolation forcing. Since the

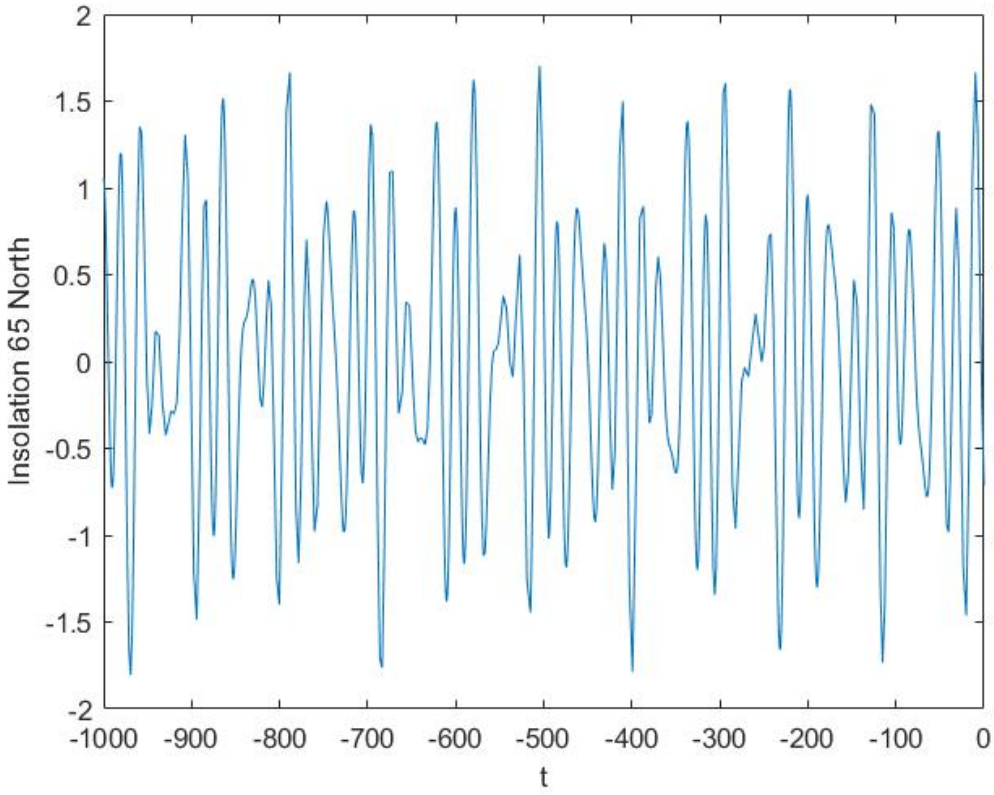

Figure 2-13: The graph showing the quasi-periodicity nature of the astronomical forcing using only three modes of the forcing given by $i = 1, 3$ and 4 reproduced for the past 1000 $kyrs$

insolation forcing has high degrees of freedom, and has obliquity and precesion as the dominant frequencies, it is thus reasonable to consider the simplified astronomical forcing as a quasi-periodic function comprising of the two or three harmonics that includes precession at (19 $kyrs$ *or* 23$kyrs$) and the (dominant) obliquity at 41$kyrs$ or $\omega_4 = 0.153$ (Figure 2-13 is produced using these three modes). The approach we will follow in this thesis.

We observe that the amplitude of the forcing obtained by taking coefficient $s_4 \approx -11$ and dividing it by $e = 23.58$ is approximately

$$\mu = 0.467. \tag{2.22}$$

For the remainder of this thesis we will use the above frequencies and coefficients as in [46, 16].

Paillard *et al.* [57] considered values given in Table 2.3 to produce the figures in their paper. In the absence of forcing they observed a self sustained relaxation oscillator with a periodicity of 132 $kyrs$. The results of the model was able to reproduce most of the glacial-interglacial cycles and also predicted the correct termination times.

We also consider the same values for our analysis of the model, except that we consider $\gamma = 0.7$ a consideration made after personal communications with Paillard. We also do not consider the contribution of $I_{60}(t)$ in the system by taking $c = 0$ since the absence of $I_{60}(t)$ does not affect the initiation and termination of ice ages, the parameter values in the model were considered from first principles and obtained experimentally [57].

Table 2.3: Model parameter values used

Variables	Values	Range	Units
a	0.3	0.26-0.39	
b	0.7	0.63-0.74	
c	0	0-0.15	
d	0.27	0.253-0.302	
x	1.3	1.23-1.44	
y	0.5	0.4-0.64	
z	0.8	0.77-0.82	
α	0.15	0-0.35	
β	0.5	0.46-0.54	
γ	0.7	0.37 - 0.7	
δ	0.4	0.39 - 0.42	
τ_V	15	13.2 - 18.1	kyrs
τ_C	5	3.1 - 15	kyrs
τ_A	12	9.5 - 26	kyrs

The PP04 model is a discontinuous system because of the threshold described above,has been studied so far as smooth dynamical system, See for example [3, 46, 15, 47].

However, the unforced system was found to exhibit the dynamics of a relaxation oscillator [14, 57] and when quasi-periodically forced, the strange non-chaotic attractors were observed [46, 47]. According to Mitsui *et al.* [46],the simulated model for over 700 000years exhibited solutions that agreed with the data obtained from the $\delta^{18}O$ isotope of LR04 stack and that they synchronised after transient time.

Nevertheless, the only types of dynamics peculiar to smooth dynamical systems were observed. Discontinuous dynamical systems are non-smooth systems and should be studied using non-smooth dynamical systems theory in order to find all the dynamics present in the system. Therefore, we propose that non-smooth dynamical system theory should be employed in studying the discontinuous dynamical systems models. Therefore in the remainder of this thesis, we will study the PP04 model through employing the non-smooth dynamical system's theory.

Chapter 3

Features of the PP04 model as a Filippov system

In this chapter we will prove some basic results on the PP04 model, showing that it is a Filippov system without sliding. The PP04 model can be formulated as a Filippov system principally because of the presence of the switching mechanism (due to the Heaviside function) representing the ventilation of the ocean which is influenced by stratification of the water in the Southern Ocean. The ventilation of the ocean brings about the transition from one climatic state to the other and hence the stratification parameter F is considered as a transition surface Σ across which the dynamics of the system changes. When $F < 0$ the ocean switch is triggered and Carbon Dioxide is released into the atmosphere and the climate system experience a warm climate (interglacial state). However, when $F > 0$ the switch is off and Carbon gets absorbed by the ocean hence reducing Carbon Dioxide in the atmosphere as a result the climate system experiences cold climate (glacial state).

We can formulate the PP04 model as a forced Filippov System. To do this we introduce a state vector

$$\mathbf{X} = (V, A, C)^T.$$

According to Paillard *et al.* [57], the inclusion of the $I_{60}(t)$ term in the definition of F does not affect the times when the glacial cycles terminates or the qualitative form of the overall dynamics. Setting it to zero significantly simplifies the resulting analysis of the PP04 model and we will do this for the remainder of this thesis. With this simplification, it then follows from (2.20) that

$$F(\mathbf{X}) = (a, -b, 0)^T \mathbf{X} + d \equiv \mathbf{c}^T \mathbf{X} + d. \tag{3.1}$$

In this thesis we will use the notation in the PP04 paper whereby we consider $F(\mathbf{X}) = H(\mathbf{x})$ corresponding to the discontinuity surface Σ of the PP04 model. Therefore in the Filippov framework the discontinuity surface Σ is given by the

simple linear relation

$$\Sigma = \{\mathbf{X} : \mathbf{c}^T\mathbf{X} + d = 0, \}. \tag{3.2}$$

This transition surface is the important aspect of this system as it governs which region of the plane is the orbit observed. That is, from which type of climatic state are the dynamics observed.

Now we define the two climatic states corresponding to the glacial and inter-glacial states

$$S^+ = \{\mathbf{X} : \mathbf{c} \cdot \mathbf{X} + d > 0\}, \quad S^- = \{\mathbf{X} : \mathbf{c} \cdot \mathbf{X} + d < 0\}. \tag{3.3}$$

Therefore in the PP04 model the dynamics in $S^{\pm}$ is given by

$$\dot{\mathbf{X}} = L\mathbf{X} + \mathbf{b}^{\pm} + I_{65}(t)\ \mathbf{e} \tag{3.4}$$

where the linear operator L and vector $\mathbf{e}$ are defined by

$$L = \begin{pmatrix} -1/\tau_V & 0 & -x/\tau_V \\ 1/\tau_A & -1/\tau_A & 0 \\ -\beta/\tau_C & 0 & -1/\tau_C \end{pmatrix}, \quad \mathbf{e} = \begin{pmatrix} -y/\tau_V \\ 0 \\ \alpha/\tau_C \end{pmatrix}. \tag{3.5}$$

and these do not depend upon the system state. In contrast the vectors $\mathbf{b}^{\pm}$ depend upon which region $\mathbf{X}$ lies in and are given by:

$$\mathbf{b}^+ = \begin{pmatrix} z/\tau_V \\ 0 \\ \delta/\tau_C \end{pmatrix}, \quad \mathbf{b}^- = \begin{pmatrix} z/\tau_V \\ 0 \\ (\gamma+\delta)/\tau_C \end{pmatrix}. \tag{3.6}$$

From this formulation, it is clear that the PP04 model has a piecewise-linear Filippov structure. We can thus expect it to have similar dynamics to a typical Filippov problem and to show both 'smooth' and 'discontinuity induced' bifurcations (for example grazing bifurcations) as parameters are varied. When now looking at the generic structure of this formulation, we observe that the degree of discontinuity of the system is given by

$$(L\mathbf{X} + \mathbf{b}^+ + I_{65}(t)\ \mathbf{e}) - (L\mathbf{X} + \mathbf{b}^- + I_{65}(t)\ \mathbf{e}) \neq 0. \tag{3.7}$$

We now look at the structure of this formulation.

Lemma 3.1 *The degree of discontinuity of the PP04 model is one.*

Proof It is clear from the formulation that $\mathbf{X}$ is continuous on Σ, but that $\dot{\mathbf{X}}$ has a jump discontinuity. The result then follows. □

The following results show that we do not have sliding solutions.

Lemma 3.2 *The value of* $\frac{dF}{dt}$ *is continuous across* Σ.

Proof

If

$$F(\mathbf{X}) = \mathbf{c} \cdot \mathbf{X} + d$$

then it follows immediately that

$$\frac{d}{dt}F = \mathbf{c} \cdot \frac{d}{dt}\mathbf{X} \ = \mathbf{c} \cdot L\mathbf{X} + \mathbf{c} \cdot \mathbf{b}^{\pm} + \mathbf{c} \cdot \mathbf{e}I_{65}(t). \tag{3.8}$$

Then if we define

$$\mathbf{h} = \mathbf{c} \cdot L, \quad \mathbf{r}^{\pm} = \mathbf{c} \cdot \mathbf{b}^{\pm}, \quad g(t) = \mathbf{c} \cdot \mathbf{e}\ I_{65}(t), \tag{3.9}$$

then we have

$$\frac{d}{dt}F = \mathbf{h} \cdot \mathbf{X} + r^{\pm} + g(t). \tag{3.10}$$

However, it follows directly from (3.1) and (3.6) that

$$r^{-} = r^{+} \equiv r.$$

So

$$\frac{d}{dt}F = \mathbf{h} \cdot \mathbf{X} + \mathbf{r} + g(t). \tag{3.11}$$

It is clear that $\frac{dF}{dt}$ is then continuous across the discontinuity surface (3.2). □

If we approach Σ from S^{+} it follows that $\frac{dF}{dt} \leq 0$. In particular if $\frac{dF}{dt} < 0$ on Σ then from Lemma 3.2 it follows immediately that the corresponding trajectory must immediately enter the region S^{-} and does not slide on Σ.

It is possible for *grazing* to occur on Σ. This arises when $F = 0$ **and** $\frac{dF}{dt} = 0$. In the case of an unforced system this will arise when

$$\mathbf{c} \cdot \mathbf{X} + d = 0 \quad \text{and} \quad \mathbf{h} \cdot \mathbf{X} + r = 0.$$

It follows immediately that in this case grazing on Σ occurs along a straight line, the *grazing set* $\mathcal{G}$, which is parallel to the vector $\mathbf{c} \times \mathbf{h}$.

We note further that in this case we have

$$\frac{d^2F}{dt^2} = \mathbf{h} \cdot (L\mathbf{X} + \mathbf{b}^{\pm}).$$

Hence the surface $\frac{d^2F}{dt^2} = 0$ is another plane in each region $S^{\pm}$. This can intersect $\mathcal{G}$ at most one point. This rules out the possibility of sliding. Moreover, we could observe from the model that the release of a Carbon Dioxide induces the big change in climatic conditions. Therefore the stratification parameter of the ocean cannot remain in one level or condition without the threshold for either absorption of carbon or release of Carbon Dioxide being triggered. Since the release of Carbon Dioxide takes a certain period of time before the ocean stratification threshold reached, intuitively no sliding of solutions could be observed.

Chapter 4

The unforced PP04 system

In this chapter, we study the unforced PP04 model, that is the case where $I_{65}(t) = 0$. We will consider the non-smooth system case where we solve the system through non-smooth dynamical system's theory and a smoothed system case where we solve the system numerically. The purpose of this is to show that the unforced (non-smooth) model has periodic solutions of approximately 140 kyr period, which arise at border collision bifurcations from fixed points, and that in the smooth system these are Hopf bifurcations.

4.1 Non-smooth system

In this section we are going to consider the solutions of two ordinary differential equations merged together to give solution of the system. That is, we are studying the system

$$\dot{\mathbf{X}} = \begin{cases} L\mathbf{X} + \mathbf{b}^+ & \text{if} \quad F(\mathbf{X}) > 0 \\ L\mathbf{X} + \mathbf{b}^- & \text{if} \quad F(\mathbf{X}) < 0 \end{cases} \tag{4.1}$$

where the discontinuity boundary Σ_{12} between the two regions of the phase plane is defined as

$$F(\mathbf{X}) = \mathbf{c} \cdot \mathbf{X} + d = 0,$$

while the two regions are given by $S^+ = F(\mathbf{X}) > 0$ and $S^- = F(\mathbf{X}) < 0$.

4.1.1 Fixed points

The general unforced PP04 model has two fixed points corresponding to the two systems of ordinary differential equations and obtained by solving the right hand

side of (4.1) and hence given by

$$\mathbf{Z}^{\pm} = -L^{-1}\mathbf{b}^{\pm}. \tag{4.2}$$

The linear operator L is given by

$$L = \begin{pmatrix} -1/\tau_V & 0 & -x/\tau_V \\ 1/\tau_A & -1/\tau_A & 0 \\ -\beta/\tau_C & 0 & -1/\tau_C \end{pmatrix},$$

and the vectors depending on the two climatic states are given by

$$\mathbf{b}^{+} = \begin{pmatrix} z/\tau_V \\ 0 \\ \delta/\tau_C \end{pmatrix}, \quad \mathbf{b}^{-} = \begin{pmatrix} z/\tau_V \\ 0 \\ (\gamma+\delta)/\tau_C \end{pmatrix}.$$

Consequently the two fixed points are given by

$$\mathbf{Z}^{+} = \begin{pmatrix} (z-x\delta)/(1-x\beta) \\ (z-x\delta)/(1-x\beta) \\ (\delta-z\beta)/(1-x\beta) \end{pmatrix}, \quad \mathbf{Z}^{-} = \begin{pmatrix} (x(\gamma+\delta)-z)/(1-x\beta) \\ (x(\gamma+\delta)-z)/(1-x\beta) \\ (\gamma+\delta-z\beta)/(1-x\beta) \end{pmatrix}.$$

If we now consider the tabulated values for the PP04 model, we then have linear operator given by

$$L = \begin{pmatrix} -1/15 & 0 & -1.3/15 \\ 1/12 & -1/12 & 0 \\ -0.5/5 & 0 & -1/5 \end{pmatrix}$$

with the eigenvalues of the linear operator as

$$\begin{pmatrix} \lambda_1 \\ \lambda_2 \\ \lambda_3 \end{pmatrix} = \begin{pmatrix} -0.08033 \\ -0.0188 \\ -0.2478 \end{pmatrix}.$$

It follows that since eigenvalues of the linear operator L are negative, both fixed points are attractors.

If the fixed point $\mathbf{Z}^{+}$ lies in S^{+} then it is *physical*. Since the linear operator L has negative eigenvalues, it follows that orbits will be attracted to it, and the system will evolve towards a steady state. This arises if

$$F(\mathbf{X}) > 0. \tag{4.3}$$

In contrast, if $\mathbf{Z}^+$ lies in S^- then the fixed point is called a *virtual* fixed point. Although it does not strictly exist as part of the dynamics, it still has a stable manifold in S^+ and attracts trajectories towards it. An exactly similar situation arises for the fixed point $\mathbf{Z}^-$. A *Border Collision Bifurcation (BCB)* arises when one of the virtual fixed points crosses the discontinuity set $\Sigma \equiv \{F(\mathbf{X}) = 0\}$.

4.1.2 The existence of periodic solutions of the unforced system.

Now when considering the motion of the whole unforced system. We have to describe the trajectory of the system between the two fixed points. Therefore we establish the following results which will aid in describing the motion of the system.

Lemma 4.1 *Let* $\mathbf{Z}^{\pm}$ *be defined as above*

(i) If $F(\mathbf{Z}^+) \equiv d - L^{-1}b^+ > 0$ *then the system trajectory starting in* S^+ *evolves to* $\mathbf{Z}^+$.

(ii) If $F(\mathbf{Z}^-) \equiv d - L^{-1}b^- < 0$ *then the system trajectory starting in* S^- *evolves to* $\mathbf{Z}^-$.

(iii) If $F(\mathbf{Z}^-) \equiv d - L^{-1}b^- > 0$ *and if* $F(\mathbf{Z}^+) \equiv d - L^{-1}b^+ < 0$ *then the system has a periodic solution* $P(t)$.

Proof
Parts (i) and (ii) of this lemma are already considered above, whereby we found out that for each case the orbit will be attracted to their respective fixed points. So we now only consider part (iii). Consider the situation illustrated in the Figure (4-1). In this figure a periodic trajectory starts at the regionS^+ and evolves towards its virtual fixed point crossing the discontinuity boundary Σ before trying to reach it. That is if the flow starts at point $\mathbf{X}_0$ in Σ it then evolves in the region S^+ before reaching the discontinuity boundary Σ again. As the unforced system is autonomous it can be assumed to start from $\mathbf{X}_0$ at time $t = 0$. Then the flow $\mathbf{X}(t)$ in S^+ is then given by the exact expression

$$\mathbf{X}(t) = e^{Lt}(\mathbf{X}_0 - Z^+) + Z^+. \tag{4.4}$$

If we consider the quantity $y = c \cdot x + d$, we know that as the flow is initially in S^+ then $y > 0$ for small $t > 0$. Similarly, as L has negative eigenvalues and we are in case (iii) then for large $t > 0$ we must have $y < 0$. Then there must be a first time $t = t_1$ at which $y = 0$ and the trajectory intersects Σ at the point $\mathbf{X} = \mathbf{X}_1$ then the

flow now crosses over into S^-. The resulting flow is then given by

$$\mathbf{X}(t) = e^{L(t-t_1)}(\mathbf{X}_1 - Z^-) + Z^-. \tag{4.5}$$

By the same argument, it follows that there is a first time $t_2 > t_1$ such that $y = 0$ and the trajectory intersects Σ from S^- at the point $\mathbf{X}_2$. The condition for a periodic solution is that

$$\mathbf{X}_0 = \mathbf{X}_2 \equiv \mathbf{N}(\mathbf{X}_0) \tag{4.6}$$

This can be considered to be a fixed point condition for the nonlinear map $\mathbf{N} : \Sigma \to \Sigma$ defined above. However, as Σ is finite dimensional, and, as L has negative eigenvalues, $\mathbf{N}$ must map a finite region of Σ to itself. It follows from the Brouwer fixed point theorem that $\mathbf{N}$ has a fixed point, and hence there is a periodic solution to the Filippov system. □

If we now consider the tabulated values of the PP04 model, the two fixed points are $\mathbf{Z}^+ = (0.8, 0.8, 0)$ and $\mathbf{Z}^- = (-1.8, -1.8, 2)$ then the trajectories of $F(\mathbf{X})$ between $F(\mathbf{Z}^+)$ and $F(\mathbf{Z}^-)$ in the regions S^+ and S^- gives a periodic solution (see illustration in Figure 4-2). The time series of the components of the resulting solution is then illustrated in Figure 4-1. From the results, we observe that the system spends most of its time on the glacial period (where $\mathbf{N} > 0$)and less time on the interglacial state. Furthermore, the results show that when Carbon Dioxide is suddenly released into the atmosphere, the system switches to the interglacial state as the Antarctica ice sheet and global ice volume extent wanes. Thus the results show a saw-tooth like structures similar to those evident in the geological reconstructed data. Therefore these results suggest that without insolation the climate will always alternate regularly between the interglacial and the glacial states. Hence a relaxation oscillator has been obtained and has a period of $147kyr$ in this case. This phenomenon was also observed in the original PP04 paper without any mathematical analysis. Note that the period of this unforced oscillation is higher than the observed period of $100kyr$ but it is not dissimilar. This indicates that in this model the natural timescales of the Earth play a major role in determining the frequency of the ice ages.

4.1.3 Border Collision bifurcations of the periodic solution.

If one of the parameters of the system, say d, is varied, then the periodic solution can lose existence at a border collision bifurcation (BCB), when either one of the two virtual fixed points $Z^{\pm}$ intersects Σ. As a consequence, we see a change from a periodic solution to a fixed point. As the BCB is approached, the period of the periodic solution increases, rising to infinity when the fixed point lies on Σ.

To illustrate this, for example, we consider the flow in S^+, where $F(\mathbf{X}) = \mathbf{c}\cdot\mathbf{X} + d > 0$

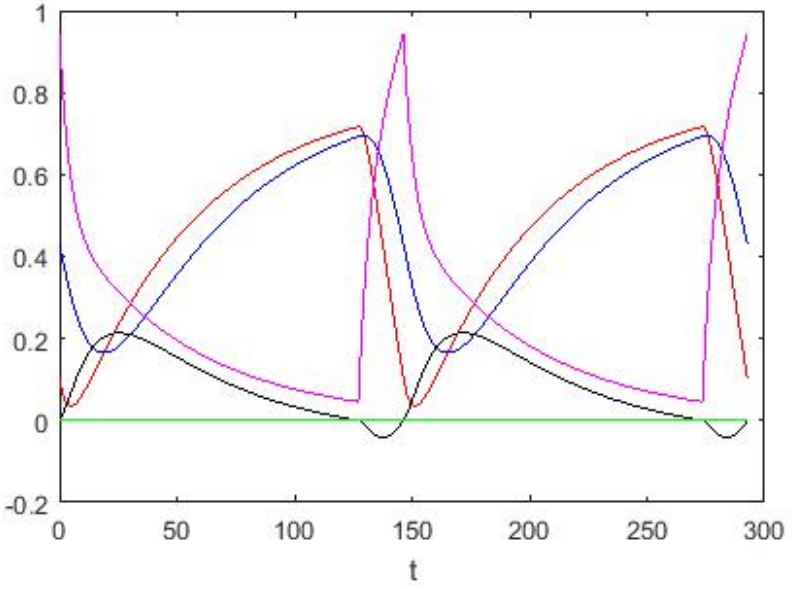

Figure 4-1: Unforced periodic solution of the non-smooth system showing V (red), A (blue) and C (magenta), F (black) as well as $I_{65}(t)$(green) obtained by merging the solutions of two systems (that is, considering a non-smooth system).

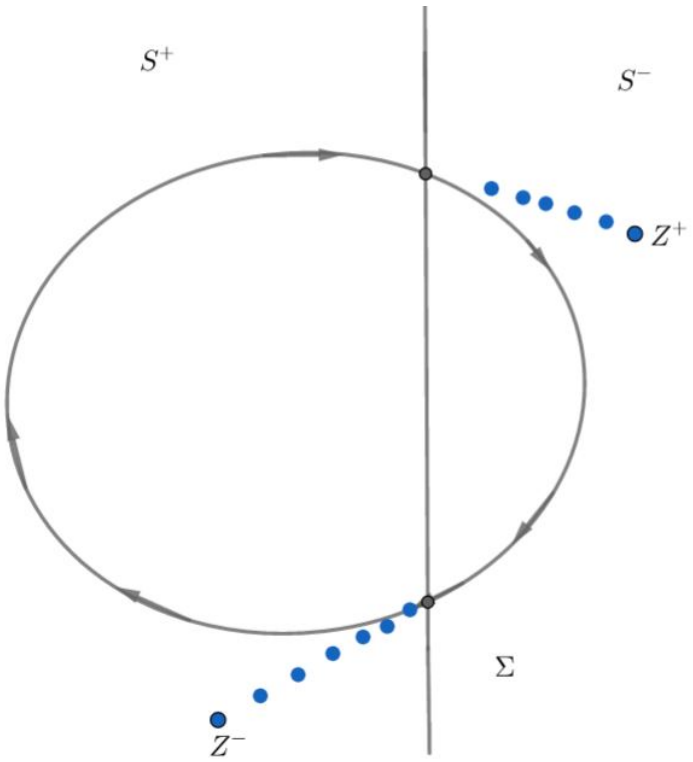

Figure 4-2: Schematic diagram showing the existence of a periodic solution as the orbit evolves between two virtual fixed points.

and follow its evolution in this region until it crosses Σ as it approaches $\mathbf{Z}^+$ in S^-. Similarly we consider the flow in S^- where $F(\mathbf{X}) = \mathbf{c}\cdot\mathbf{X}+d < 0$ as it evolves towards $\mathbf{Z}^-$ in S^+.

Lemma 4.2

(i) The solutions of PP04 system remain bounded for all time.

(ii) There is an attracting region $\mathbf{B}$ in the $\mathbf{X}-$ phase space into which all trajectories enter.

Proof
As L has all negative real eigenvalues, it can be written as $L = U\Lambda U^{-1}$ where $\Lambda = diag(\lambda_1, \lambda_2, \lambda_3)$. If we set $Y = U^{-1}\mathbf{X}$, $\mathbf{p}^{\pm} = u^{-1}\mathbf{b}^{\pm}$ and $q = U^{-1}\mathbf{e}$ then

$$\dot{\mathbf{Y}} = \Lambda\mathbf{Y} + \mathbf{p}^{\pm} + \mathbf{q}I_{65}(t).$$

Now consider $\mathbf{N} = \mathbf{Y}^T\mathbf{Y}/2$ then it is immediate that if $\mathbf{N}$ is sufficiently large then

$$\dot{\mathbf{N}} = \mathbf{Y}^T\Lambda\mathbf{Y} + \mathbf{Y}^T(\mathbf{p}^{\pm} + \mathbf{q}I_{65}(t)) < -min(\lambda_i)\mathbf{Y}^T\mathbf{Y} + \mathbf{Y}^T(\mathbf{p}^{\pm} + \mathbf{q}I_{65}(t)) < 0.$$

Hence $\mathbf{N}$, and thus $|\mathbf{X}|$ is bounded.

To prove (ii) we note (from inspection of the actual matrix) that the matrix U^TU is positive definite. It follows that the bounded sets in $\mathbf{Y}$ correspond to bounded sets in $\mathbf{X}$ and vice versa. Hence the $\mathbf{N}-$ ball in the $\mathbf{Y}$ space corresponds to a bounded set $\mathbf{B}$ in the $\mathbf{X}$ space. □

If we consider a trajectory starting from a point $\mathbf{X}$ on the discontinuity boundary Σ and entering S^+. This will be attracted to Z^+ which is in S^-. Therefore the trajectory must intersect the discontinuity boundary again and enter S^-. It is then attracted to the point Z^- which is in S^+. Therefore it must cross the discontinuity boundary at a point $F(\mathbf{X})$. By construction the map $\mathbf{X} \to F(\mathbf{X})$ is continuous from Σ to itself. By Lemma 4.2 it also maps the region Σ intersect $\mathbf{B}$ to itself. Therefore by the Brouwer fixed point theorem it must have a fixed point $\mathbf{X}^*$ on Σ, so that $F(\mathbf{X}^*) = \mathbf{X}^*$. Therefore any trajectory starting from $\mathbf{X}^*$ must be a periodic orbit.

The values of $d^{\pm}$ at which we have a BCB are given by solving the following equation

$$d^{\pm} = -\mathbf{c}\cdot\mathbf{Z}^{\pm} \tag{4.7}$$

Using the tabulated values we obtain

$$d^- = -0.72, \quad d^+ = 0.32,$$

with periodic solutions obtained when $-0.72 < d < 0.32$. In Figure 4-3 we show the period of the periodic solution as a function of d in which we can see the two BCBs.

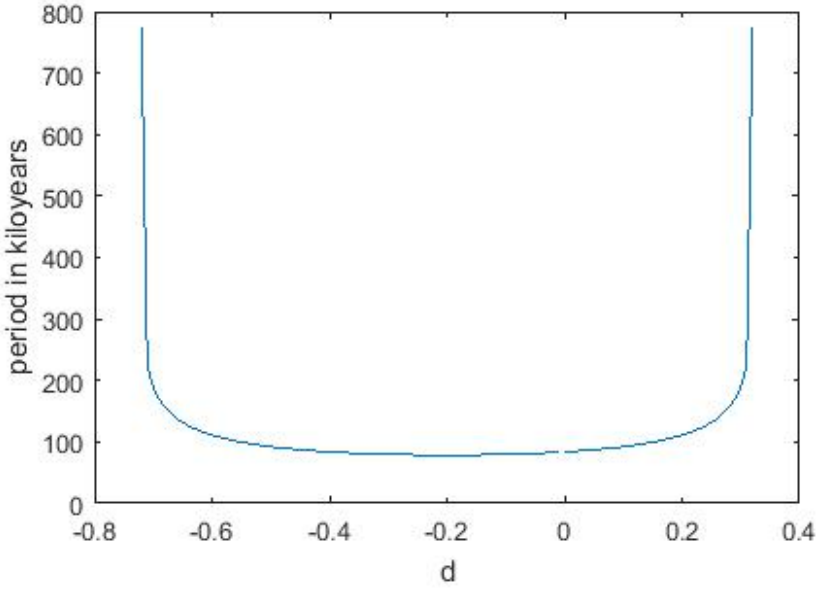

Figure 4-3: Graph showing the period of solution as parameter d is varied and the Border Collision Bifurcations at $d = -0.72$ and $d = 0.32$.

It is of interest to consider how this bifurcation structure arises if we replace the non-smooth system by a smooth one. A convenient way to do this is to replace the (non-smooth) Heaviside function, by the regularized function.

4.2 Numerical methodology

We now consider the PP04 model with the Heaviside function replaced by the function

$$H_\eta(z) = \frac{1}{2}(1 + \tanh(\eta z)). \tag{4.8}$$

The advantage of this formulation is that we can solve the system numerically forward in time using Matlab code `ode45`. By varying the values of η in the Function (4.8) we can simulate both a smooth or a non smooth system. For $\eta \geq 100$, the Function (4.8) closely approximates the Heaviside function. Therefore using this approximation we can easily integrate the system (2.17-2.19) forward in time and explore its varied dynamics.

4.2.1 Periodic solutions

When using this approximation and consider $\eta \geq 100$, we observe a system approximately equivalent to the non smooth system. This is illustrated by using the periodic solutions observed for $\eta = 80$ and $\eta = 1000$. In Figure 4-4 and Figure 4-5 where $\eta = 80$, the time solution shows periodic solutions that looks more sinusoidal. However in Figure 4-6 and Figure 4-7 where $\eta = 1000$, the time solutions shows a saw-tooth dynamic behaviour similar to the one observed in ice age records. For instance, the time solution for V, shows the trajectory with alternately exponentially growing part and fast reduction parts. Similarly the time solutions for Carbon Dioxide clearly shows the sudden increase of Carbon Dioxide and slow reduction. Thus we have a period of rapid decay and of slow growth of ice sheets and Carbon Dioxide as evidently shown by saw tooth kind of time series obtained for non-smooth system (see Figure 4-1) and these depicts what is expected on the climate system (see Figure 2-3).

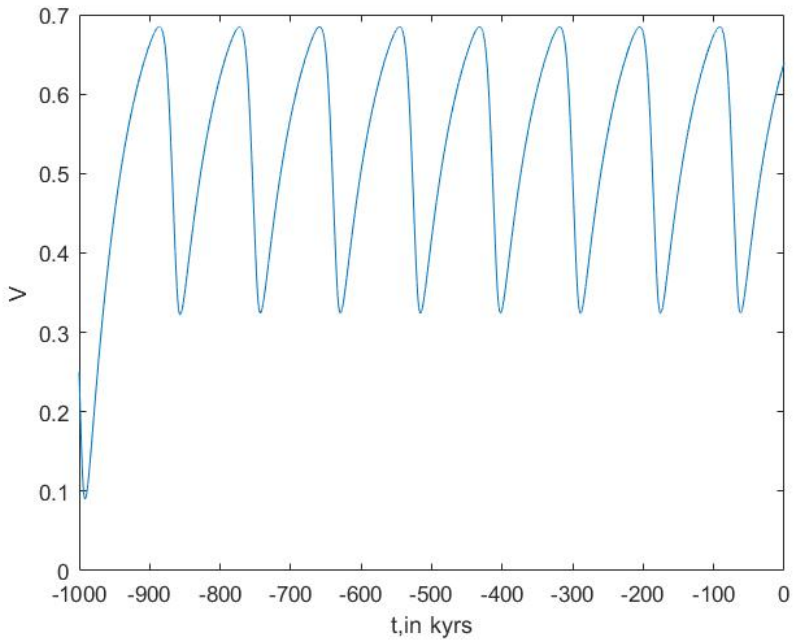

Figure 4-4: Graph showing the periodic solutions of global volume of ice V for the smoothed system with $\eta = 80$ and initial conditions $V = 0.25, A = 0.55, C = 0.8$.

In Figure 4-8, we observe a relaxation oscillator in the phase plane and the unforced system has a period of about $140kyr$. When considering the time solution for the stratification parameter F (see Figure 4-9), we observe the periodic solutions similar to those observed in Figure 4-1.Thus the solutions for the smoothed system when $\eta = 1000$ and the non smooth system are consistent. Notably when we vary the parameter d, we observe that the periodic solution of the system gets destroyed and then the system gets attracted to the fixed point. That is the climate system gets locked into one climatic state (see Figure 4-11). For $d = 0.4$, we observe the system

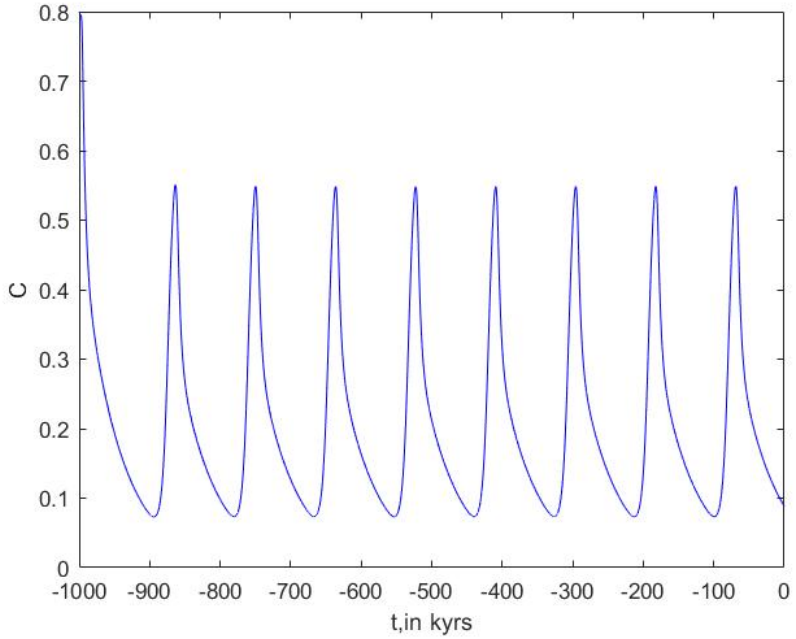

Figure 4-5: Graph showing the periodic solutions of Carbon Dioxide C for the smoothed system with $\eta = 80$ and initial conditions $V = 0.25, A = 0.55, C = 0.8$.

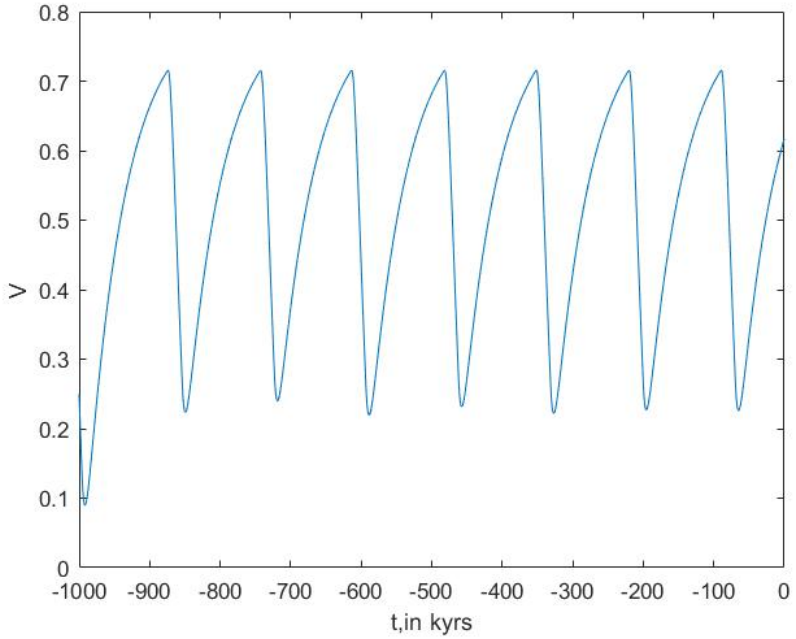

Figure 4-6: Graph showing the periodic solutions of global volume of ice V for the non smooth approximated system with $\eta = 1000$ for initial conditions $V = 0.25, A = 0.55, C = 0.8$ when $d = 0.4$.

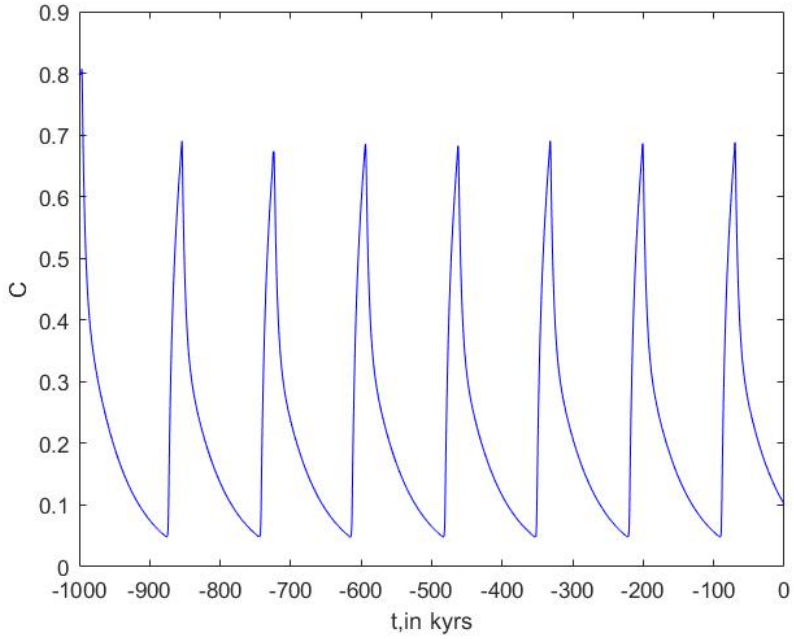

Figure 4-7: Graph showing the periodic of solutions of Carbon Dioxide C for the non smooth approximated system with $\eta = 1000$ and initial conditions $V = 0.25, A = 0.55, C = 0.8$

locked onto the glacial state of climate where there is little to no Carbon Dioxide in the atmosphere but a high amount of ice sheets globally.

4.2.2 Hopf bifurcations of periodic solutions

To determine the dynamics of the solutions of both the smooth and non-smooth approximated system, we start with a random set of initial conditions and integrate forward in time until the solution converges onto its $\Omega-$limit set. To record this we then plot the maximum and minimum values of the solution on this set. If this is done for a set of values of d then we can determine the complete bifurcation picture for the solutions. This is given in Figure 4-12 to 4-14. In Figure 4-13 we take $\eta = 100$ and this represents a smooth system and in Figure 4-14 we take $\eta = 1000$ and represents a non-smooth system. In Figure 4-12 we can clearly see a smooth Hopf Bifurcation. In Figure 4-13, which represents a smooth system, we see that the two fixed points lose stability, each at Hopf bifurcations, to a periodic solution. This type of solutions were also observed by Crucifix in [13]. In Figure 4-14, which much more closely represents the non-smooth system described above, we see the discontinuous change in the solution at the BCB.

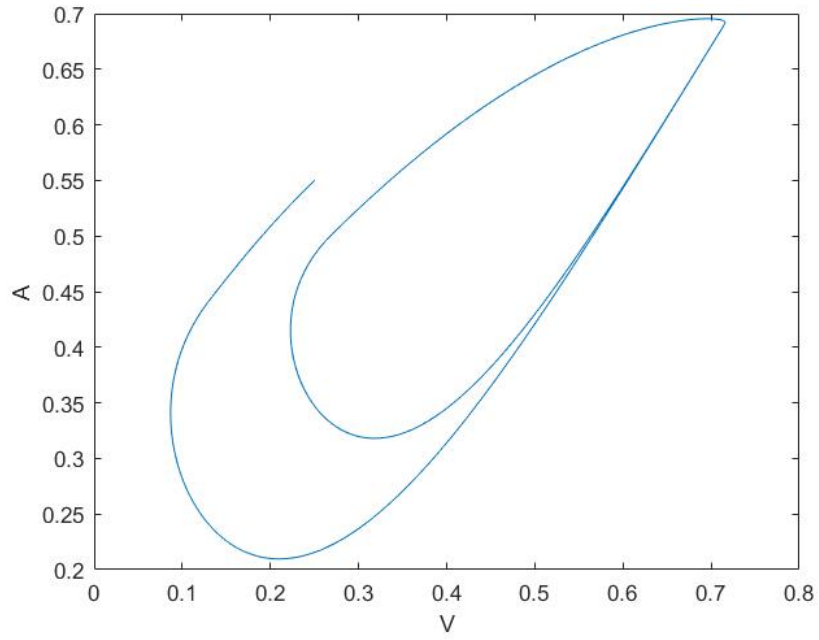

Figure 4-8: The graph showing the phase portrait of volume of global ice and Antarctica ice sheets

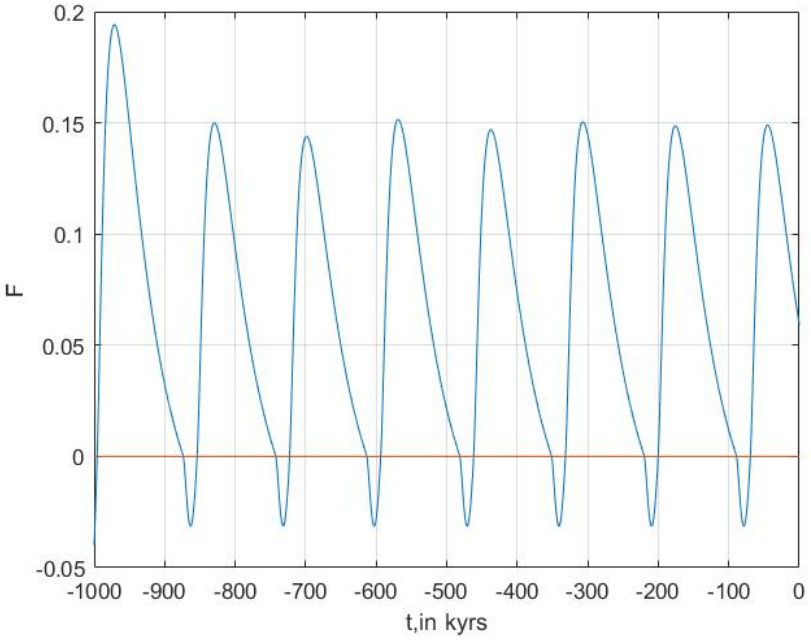

Figure 4-9: The graph showing time solution for the stratification parameter F plotted forward in time obtained by solving the smoothed PP04 model with $\eta = 1000$ and initial conditions $(V, A, C) = (0.25, 0.55, 0.8)$.

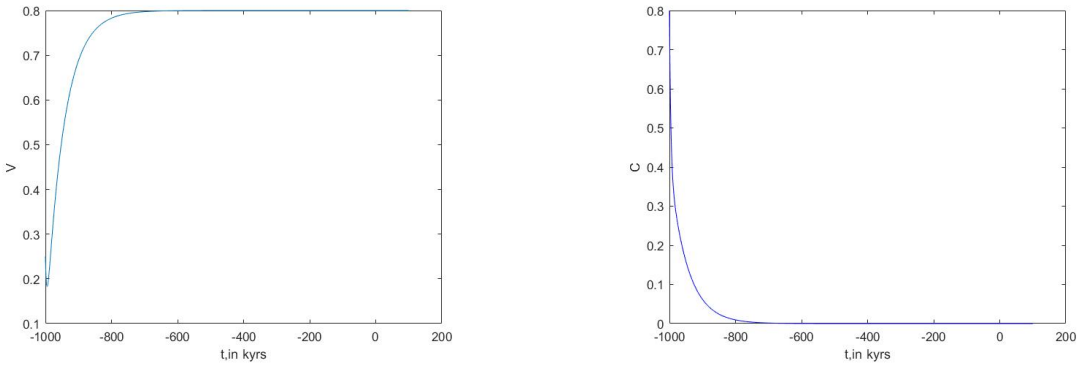

Figure 4-10: Graph showing the fixed points of the non-smooth approximated system with $\eta = 1000$ for initial conditions $V = 0.25, A = 0.55, C = 0.8$ and $d = 0.4$

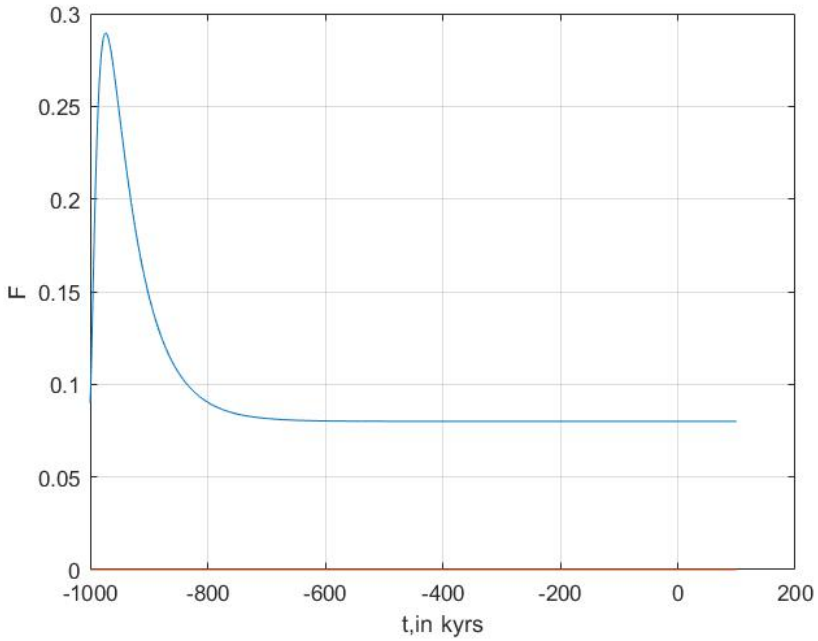

Figure 4-11: The graph showing time solution for the stratification parameter F plotted forward in time for $d = 0.4$

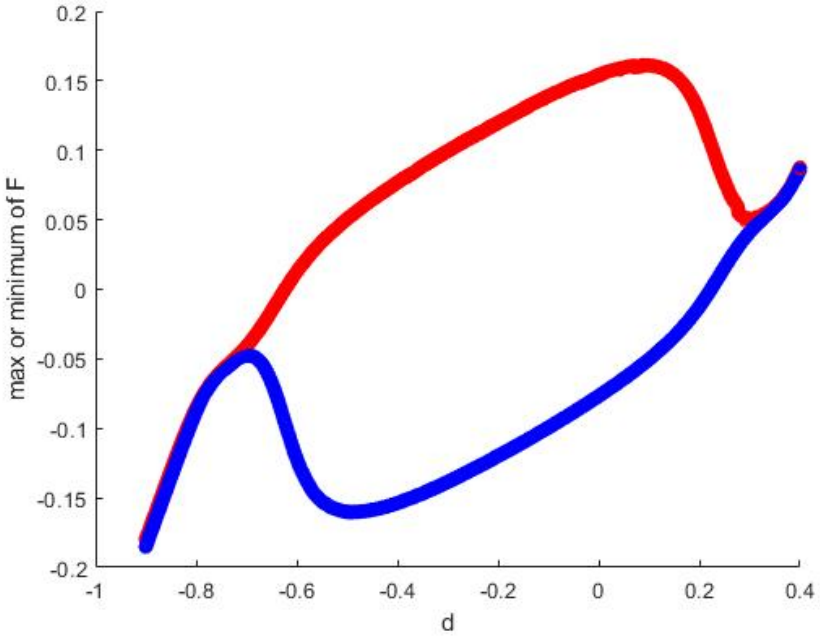

Figure 4-12: The graph showing the smooth bifurcations obtained when plotting the Omega limit set of minimum values (blue circles) of F and Omega limit set of maximum values (red circles) of F against d with $\eta = 30$.

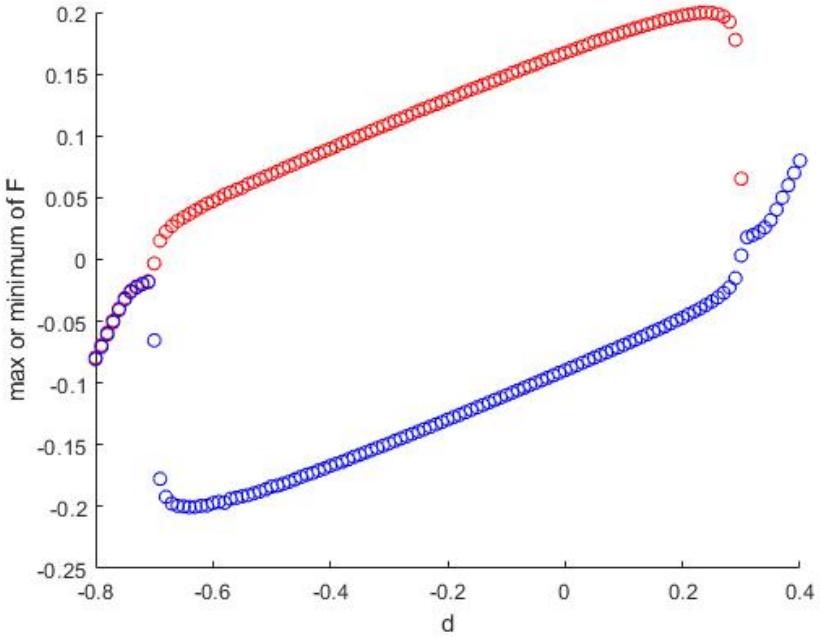

Figure 4-13: The graph showing the smooth Hopf bifurcations obtained when plotting the Omega limit set of minimum values (blue circles) F and Omega limit set of maximum values (red circles) F against d with $\eta = 100$.

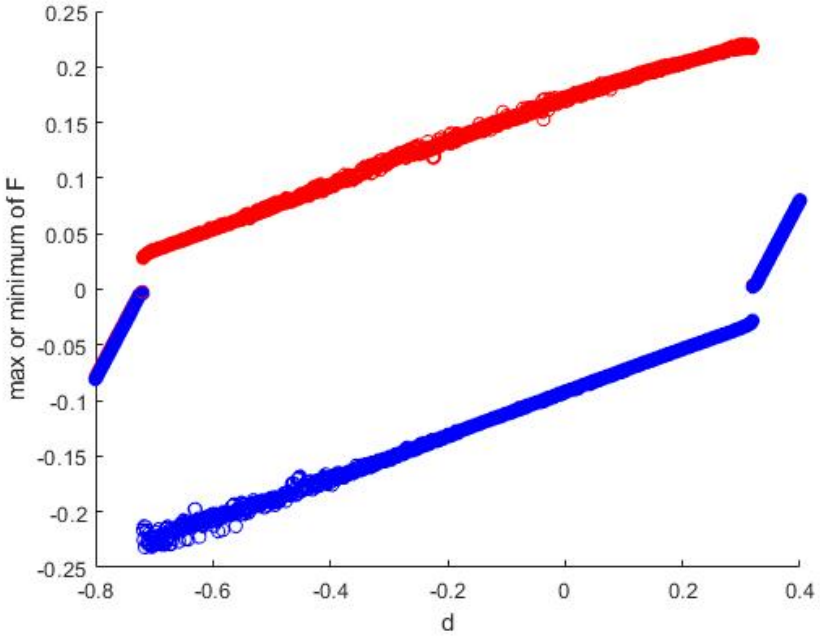

Figure 4-14: The graph showing the Hopf bifurcation , which is now very close to a Border Collision bifurcation. The graph is obtained by plotting the Omega limit set of minimum values (blue circles) of F and Omega limit set of maximum values(red circles) of F with parameter $\eta = 1000$.

4.3 Summary

In this chapter we have observed that the unforced PP04 model can have both fixed points and a periodic solution of a period of $147kyrs$. In non-smooth case it exchanges stability from a fixed point to a periodic solution through a border collision bifurcation when parameter d is varied. In smooth case the border collision bifurcation is replaced by the complex scenario including the Hopf bifurcation.

Chapter 5

The periodically forced system

This chapter studies the periodically forced PP04 model. That is we consider the model when insolation is considered to be a single mode forcing. Although this form of forcing is unrealistic from a physical point of view, studying such systems allows us to gain insight into the more general case of quasi-periodic forcing, especially when one frequency is dominant in the insolation. Therefore, we consider the system of the form

$$\dot{\mathbf{X}} = L\mathbf{X} + \mathbf{b}^{\pm} + I_{65}(t)\ \mathbf{e} \tag{5.1}$$

where

$$I_{65}(t) = \mu \sin(\omega t), \tag{5.2}$$

so that the period of the forcing is given by

$$T = \frac{2\pi}{\omega}. \tag{5.3}$$

5.1 Analytical solutions

When considering the forced system, we observe that for small μ this is a perturbation of the unforced Filippov System (4.1) which we have periodic solution. Therefore we might expect to observe periodic solutions of (5.1) that are bounded for certain parameters values and a perturbation of the periodic solution of the unforced system. As a consequence, we will investigate the effect of amplitude and or frequency of the forcing to determine their effect on the periodic solutions. Therefore, in general we might expect to see the following types of solution behaviour from the PP04 system

(a) Synchronised periodic solutions (both stable and unstable) of period $P = nT = \frac{2\pi n}{\omega}$ with $n = 1, 2, 3..$ which have precisely one glacial and one inter-glacial period (one glacial cycle) between repeats. We define these as $(1, n)$ periodic orbits.

(b) Synchronised periodic solutions with several (for example m) glacial cycles between repeats. We define these as (m, n) periodic orbits.

(c) Quasi-periodic solutions showing at least two distinct frequencies

(d) Chaotic solutions

In practice, for appropriate choices of parameters, we see all of these types of solutions, possibly co-existing. Some of these solutions arise through smooth bifurcations and others (as we have seen in the previous chapter) from non-smooth bifurcations as we vary parameters such as μ and ω. We note that in parametrically excited smooth dynamical systems we might expect to see *Arnold Tongues* which are curves of (say) parameters (μ, ω) which define the existence regions for synchronised periodic solutions [62, 74]. Moreover, these curves can be used to represent the regions of stability change of the solutions. Inside these stability regions, forcing cycles and the resulting forced oscillations have specific ratios of $n : m$. Thus n cycles of forcing which results in m cycles of system oscillation [69]. Outside of the phase locked regions,the quasi-periodic or chaotic motion of the solutions is expected [84] and similar behaviour is observed in this non-smooth system. Indeed we will now study the solutions of type (a) and (b) and will obtain analytic estimates for these tongues.

5.1.1 Conditions for the existence of the $(1, n)$ periodic solutions.

It is relatively easy to construct algebraic conditions which are necessary for the existence of the $(1, n)$ periodic orbits. Suppose that we have a periodic solution of period $P = \frac{2n\pi}{\omega}$, with one period existing in the range $t \in [t_0, t_2 = t_0 + P]$. We assume that this solution is *glacial* if $t \in [t_0, t_1]$ and *inter-glacial* if $t \in [t_1, t_2]$. We then assume that $\mathbf{X}(t_i) = \mathbf{X}_i$. It then follows that

$$\mathbf{X}_0 = \mathbf{X}_2 \quad \text{and} \quad F(t_i) \equiv \mathbf{c} \cdot \mathbf{X}_i + d = 0. \tag{5.4}$$

The differential equations satisfied by this system are then

$$\dot{\mathbf{X}} = L\mathbf{X} + \mathbf{b}^{\pm} + \mu\, \mathbf{e}\, \sin(\omega t). \tag{5.5}$$

when we consider a particular integral of this system given by

$$\mathbf{X}^{\pm}_{PI}(t) = \mathbf{Z}^{\pm} + \mu\, \mathbf{p}\, \cos(\omega t) + \mu\, \mathbf{q}\, \sin(\omega t), \tag{5.6}$$

it follows from (5.5) that

$$\dot{\mathbf{X}} = -\mu\, \omega\, \mathbf{p}\, \sin(\omega t) + \mu\, \omega\, \mathbf{q}\, \cos(\omega t). \tag{5.7}$$

and hence comparing coefficients of (5.5) and(5.7) it gives the following

$$\mathbf{Z}^{\pm} = -L^{-1}\mathbf{b}^{\pm}, \quad \mathbf{p} = -(L^2 + \omega^2 I)^{-1}\, \omega\, \mathbf{e}, \quad \mathbf{q} = -(L^2 + \omega^2 I)^{-1}\, L\, \mathbf{e}. \tag{5.8}$$

We can then integrate the whole system to give

$$\mathbf{X}_1 = e^{L\Delta_1}\left(\mathbf{X}_0 - \mathbf{X}^+_{PI}(t_0)\right) + \mathbf{X}^+_{PI}(t_1), \tag{5.9}$$

and similarly

$$\mathbf{X}_2 = e^{L\Delta_2}\left(\mathbf{X}_1 - \mathbf{X}^-_{PI}(t_1)\right) + \mathbf{X}^-_{PI}(t_2). \tag{5.10}$$

Here we set

$$\Delta_1 = t_1 - t_0, \quad \Delta_2 = t_2 - t_1 = P - \Delta_1. \tag{5.11}$$

Therefore the problem of existence of a periodic solution is then reduced to finding $\mathbf{X}_0$ together with the phase t_0 and t_1 so that the conditions (5.4) hold.

This nonlinear system may or may not have algebraic solutions, and we will consider this in the next sub-section. Furthermore the algebraic solutions, if they exist may or may not lead to physically relevant climate trajectories.

Definition 5.1.1. We define a periodic solution for the PP04 model to be *physical* if

$$V(t) > 0, \;\; A(t) > 0, \; C(t) > 0 \quad \forall t \tag{5.12}$$

and

$$F(\mathbf{X}^+(t)) > 0, \quad t_0 < t < t_1, \quad \text{and} \quad F(\mathbf{X}^-(t)) < 0 \quad t_1 < t < t_2. \tag{5.13}$$

Typically solutions lose algebraic existence through smooth (saddle-node) bifurcations, and lose physicality through non-smooth (grazing) bifurcations. In the case of F changing sign the Filippov condition is violated and we expect to see a dramatic change in the solution as indicated in Chapter 7 of [19]. We will return to this situation in the next chapter.

5.1.2 Small μ synchronised $(1, n)$ periodic solutions

We consider first the question of the existence of the $(1, n)$ periodic solutions. To do this we use perturbation theory, and look for periodic solutions of the forced system which are perturbations of the periodic solution of the unforced system when μ is *small*. We have shown in the previous chapter that if $\mu = 0$ (the unforced system) there is a single glacial cycle periodic solution with frequency $\omega = \omega^*$ with period $P^* = \frac{2\pi}{\omega^*}$ and which takes values $X^* = (V^*, A^*, C^*)$ at the start of the glacial cycle.

Accordingly, for small μ we might expect to see a *synchronised* $(1, n)$ periodic orbit of period P provided that this period is closer to the period of the perturbed one. That is $P \approx P^*$ so that

$$P = \frac{2\pi n}{\omega} \approx P^* = \frac{2\pi}{\omega^*}.$$

Therefore by perturbation theory

$$\omega = n\omega^* + \mu\alpha + \mathcal{O}(\mu^2) \tag{5.14}$$

and it follows that for small values of μ

$$\omega \approx n\,\omega^*. \tag{5.15}$$

As a result, we propose that for small μ there is a range of ω values with $|\omega - n\,\omega^*| = \mathcal{O}(\mu)$ such that *two synchronised periodic solutions* exist within this range. Over the interval the phase t_0 of each such solution (defined as the phase of the forcing at the start of the glacial cycle) is well defined and varies over the whole range $[0, \frac{2\pi}{\omega^*}]$. One of these periodic solutions is stable and the other is unstable. Both solutions are perturbations of the unforced solution which is given when $\mu = 0$, and which has an arbitrary phase. Hence, both solutions are physical provided that μ is sufficiently small and the parameter d is not close to the value at which a border collision occurs for the free system. The boundaries of the regions of existence are determined by the existence of saddle-node bifurcations.

Therefore this result is an immediate consequence of the following

Lemma 5.1 (i) *For each n, if μ is* small *then there is a set of solutions $(\omega, \mathbf{x})$ to the algebraic system, which is parametrised by t_0.*

(ii) *If μ is small then the curves $(\omega, V(\omega))$,$(\omega, C(\omega))$ etc form ellipses which have for instance $(n\omega^*, V^*)$ at the centre.*

(iii) *The size (for example the semi-major axis) of the ellipses is (for sufficiently small μ) directly proportional to μ.*

(iv) *As we go once around the small elliptical curves, the phase t_0 increases by $\frac{2\pi}{\omega^*}$.*

Corollary 5.2 *If $\mu \ll 1$ then for each value of n, the synchronised periodic solutions of the PP04 model exhibit saddle node (SN) bifurcations at points $(\omega_{1,n}, \omega_{2,n})$. At which points they change to quasi-periodic orbits. Synchronised periodic solutions exist in the interval $\omega \in (\omega_{1,n}, \omega_{2,n})$. We have that*

$$|\omega_{i,n} - n\omega^*| = \mathcal{O}(\mu), \quad i = 1, 2.$$

We illustrate the conclusions of Lemma 5.1 and Corollary 5.2 in Figure 5-1, in which we plot the ellipses of solutions $(\omega, V(t_0))$ for $\mu = 0.05, 0.1, 0.2$ and $n = 3$.

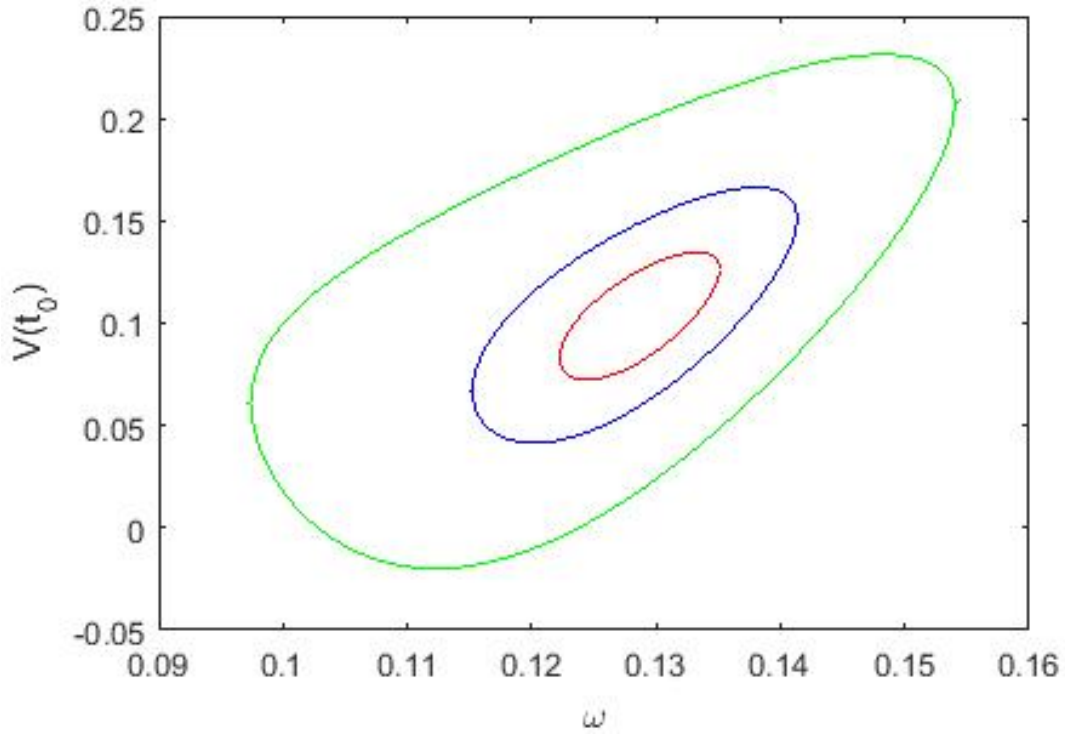

Figure 5-1: The variation of $V(t_0)$ with ω for $\mu = 0.05$ (red), $\mu = 0.1$ (blue) and $\mu = 0.2$ (green) for $n = 3$ showing the (elliptical) curve of the solutions and the two SN bifurcation points. It is clear that the size of the curve increases in proportion to μ and that it has a true elliptical shape for the smaller values of μ.

In Figure 5-2 we plot t_0 for the case of $\mu = 0.1$ and $n = 3$ as we go around the ellipse. For the problem considered we have $\omega^* = 0.128$ we can see that t_0 increases by $\frac{2\pi}{\omega^*} = 49.0874$ over this cycle.

Proof

If $\mu = 0$ we have a periodic solution $X^*(t)$ of the autonomous system. This can have an *arbitrary time* t_0^* at the start of the glacial cycle for which $F(X^*(t_0^*)) = 0$. We have a well defined set of time differences Δ_1^* and Δ_2^* so that the glacial period is in the interval $[t_0^*, t_0^* + \Delta_1^*]$ and the inter-glacial period in the time interval $[t_0^* + \Delta_1^*, t_0^* + \Delta_1^* + \Delta_2^*]$ with $\Delta_1^* + \Delta_2^* = \frac{2\pi}{\omega^*}$. In the forced case, with $\mu > 0$, the system will exhibit *phase-locking* so that we expect to see a well defined time t_0 in this case and finding t_0 will be part of the solution procedure. Setting as before

$$\mathbf{X} = (V, A, C)^T$$

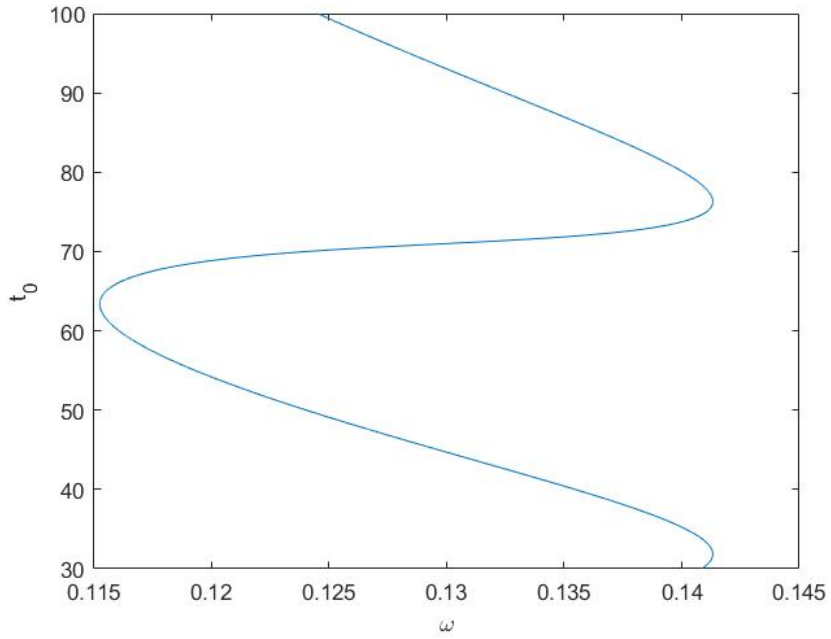

Figure 5-2: The variation of t_0 with ω for $\mu = 0.1$ ($n = 3$) showing that it increases by approximately $\frac{2\pi}{\omega^*} = 49.0874$ over this cycle.

we have that

$$\dot{\mathbf{X}} = L\mathbf{X} + \mathbf{b}^{\pm} + \mu \mathbf{e}\cos(\omega t).$$

Suppose that we consider a periodic orbit of period $T = \frac{2\pi n}{\omega} \approx \frac{2\pi}{\omega^*}$, so that $\omega \approx n\omega^*$, with a glacial state in the interval $t \in (t_0, t_1)$ and an inter-glacial state for $t \in (t_1, t_2)$ so that

$$t_2 = t_0 + \frac{2\pi n}{\omega}.$$

We define $\mathbf{X}_i = \mathbf{X}(t_i)$. Thus to have a periodic solution we must satisfy the following three conditions

$$\mathbf{X}_0 = \mathbf{X}_2 \quad \text{and} \quad F(\mathbf{X}_i) = \mathbf{c} \cdot \mathbf{X}_i + d = 0. \tag{5.16}$$

We now consider a solution which is a perturbation of the unforced case so that to order $\mathcal{O}(\mu)$ we have

$$\omega = n\omega^* + \mu\alpha, \quad \Delta_1 = \Delta^* + \mu\delta, \quad \mathbf{X}_0 = \mathbf{X}_0^* + \mu\mathbf{x}.$$

It follows immediately that

$$\Delta_2 = \frac{2\pi}{\omega} - \Delta_1 = \Delta_2^* - \mu\delta - \mu\frac{2\pi\alpha}{(\omega^*)^2}.$$

It follows from (5.5) that

$$\mathbf{X}_1 = e^{L\Delta_1}(\mathbf{X}_0 + -\mathbf{Z}^+ - \mu\ \mathbf{p}\ \cos(\omega t_0) - \mu\ \mathbf{q}\ \sin(\omega t_0)) + \mathbf{Z}^+ + \mu\ \mathbf{p}\ \cos(\omega t_1) + \mu\ \mathbf{q}\ \sin(\omega t_1).$$

which is simplified

$$\mathbf{X}_1 = e^{L(\Delta_1+\mu\delta)}(\mathbf{X}_0^* + \mu\mathbf{x} - \mathbf{Z}^+ + \mu\mathbf{r}(t_0)) + \mathbf{Z}^+ + \mu\mathbf{r}(t_1).$$

Hence, after some manipulation

$$\mathbf{X}_1 = \mathbf{X}_1^* + \mu\left(e^{L\Delta_1^*}\left(\delta L\mathbf{X}_0^* + \mathbf{x} + \mathbf{r}(t_0)\right) + \mathbf{r}(t_1)\right) + \mathcal{O}(\mu^2).$$

Thus

$$\mathbf{X}_1 = \mathbf{X}_1^* + \mu\mathbf{y} + \mathcal{O}(\mu^2),$$

where

$$\mathbf{y} = e^{L\Delta_1^*}\left(\delta L\mathbf{X}_0^* + \mathbf{x} - \mathbf{r}(t_0)\right) + \mathbf{r}(t_1)$$

Similarly,

$$\mathbf{X}_2 = \mathbf{X}_2^* + \mu\mathbf{z} + \mathcal{O}(\mu^2),$$

where

$$\mathbf{z} = e^{L\Delta_2^*}\left(-(\delta + \frac{2\pi\alpha}{(\omega^*)^2})L\mathbf{X}_1^* + \mathbf{y} - \mathbf{r}(t_1)\right) + \mathbf{r}(t_0).$$

The conditions $F(\mathbf{X}_i) = 0$ are then satisfied provided that

$$\mathbf{x} = \mathbf{z} \quad \text{and} \quad \mathbf{c}\cdot\mathbf{x} = 0, \quad \mathbf{c}\cdot\mathbf{y} = 0.$$

We define the linear operators A_1 and A_2 by:

$$e^{L\Delta_1} = A_1, \quad e^{L\Delta_2} = A_2.$$

It follows that

$$\mathbf{y} = A_1(\delta L\mathbf{X}_0^* + \mathbf{x} - \mathbf{r}(t_0)) + \mathbf{r}(t_1), \quad \mathbf{z} = A_2(-(\delta+\gamma\alpha)L\mathbf{X}_1 + \mathbf{y} - \mathbf{r}(t_1)) + \mathbf{r}(t_0).$$

Hence, as $\mathbf{z} = \mathbf{x}$ we have

$$\mathbf{x} = A_2(-(\delta+\gamma\alpha)L\mathbf{X}_1 + A_1(\delta L\mathbf{X}_0 + \mathbf{x} - \mathbf{r}(t_0)) + \mathbf{r}(t_0), \tag{5.17}$$

$$\mathbf{c}\cdot\mathbf{x} = 0, \quad \mathbf{c}\cdot\mathbf{y} = 0. \tag{5.18}$$

Now we look at the structure of the equations (5.17,5.18). We note that to leading order, as $t_1 = t_0 + \Delta_1^*$ that there are vectors $\mathbf{p}_0, \mathbf{q}_0, \mathbf{p}_1, \mathbf{q}_1$ so that

$$\mathbf{r}(t_0) = \mathbf{p}_0\cos(n\,\omega^* t_0) + \mathbf{q}_0\sin(n\,\omega^* t_0), \quad \mathbf{r}(t_1) = \mathbf{p}_1\cos(n\,\omega^* t_0) + \mathbf{q}_1\sin(n\,\omega^* t_0).$$

It follows that there is a linear operator M and vectors $\mathbf{a}$ and $\mathbf{b}$ so that (5.17,5.18)

can be put into the form

$$M \begin{bmatrix} \mathbf{x} \\ \delta \\ \alpha \end{bmatrix} + \mathbf{a}\cos(n\,\omega^* t_0) + \mathbf{b}\sin(n\,\omega^* t_0) = \mathbf{0}. \tag{5.19}$$

The linear operator M and the vectors $\mathbf{a}, \mathbf{b}$ can all be constructed explicitly. We will make the assumption that M is invertible. If this is the case then for each value of t_0 the system (5.19) can be solved uniquely to give the values of $\mathbf{x}, \delta$ and α in the form

$$\begin{bmatrix} \mathbf{x} \\ \delta \\ \alpha \end{bmatrix} = \mathbf{f}\cos(n\,\omega^* t_0) + \mathbf{g}\sin(n\,\omega^* t_0)$$

for appropriate (constant) vectors $\mathbf{f}$ and $\mathbf{g}$. In particular there will be unique values f_5 and g_5 so that

$$\alpha = f_5\cos(n\,\omega^* t_0) + g_5\sin(n\,\omega^* t_0).$$

As t_0 varies over the whole range of $[0, 2\pi/(n\,\omega^*)]$ so α will range over the interval.

$$\alpha \in \left[-\sqrt{f_5^2 + g_5^2}, \sqrt{f_5^2 + g_5^2}\right]. \tag{5.20}$$

This interval sets the limits of existence of the solutions of (5.17,5.18) and hence the width of the tongues over which we will see synchronised periodic solutions. Clearly if $W_\alpha = \sqrt{f_5^2 + g_5^2}$ then there is a phase ϕ_α so that

$$\alpha = W_\alpha\cos(n\,\omega^* t_0 - \phi_\alpha). \tag{5.21}$$

If we set $[V\,A\,C] = \mathbf{X}^T$, then an identical argument implies that there are amplitudes W_V, W_A and W_C, and phases ϕ_V, ϕ_A and ϕ_C so that

$$v = W_V\cos(n\,\omega^* t_0 - \phi_V), \quad a = W_A\cos(n\,\omega^* t_0 - \phi_A), \quad c = W_C\cos(\omega^* t_0 - \phi_c). \tag{5.22}$$

It follows immediately that the curves $(\alpha, V), (\alpha, A)$ and (α, C) are all ellipses centred on the origin. □

The nature of the solution ellipses

The values of the coefficients of the vectors $\mathbf{f}$ and $\mathbf{g}$ are determined explicitly by the calculation above, but are hard to estimate from this. However, the basic calculation of the $(1, n)$ periodic orbits is identical for all values of $n = 1, 2, 3, 4, ..$ although the precise values of the coefficients will change in each case. In particular, for small μ we expect to see small ellipses in each case, the size of which is directly proportional to μ. In Figure 5-3 we plot the resulting ellipses when $\mu = 0.1$ for $n = 1, 2, 3, 4$. These

ellipses are computed by numerically solving the nonlinear equations for V, A, C, ω and t_1. As these solutions are parametrised by t_0, it is convenient in this calculation to use t_0 as the path following variable. Each of these ellipses are centred on the values of $\omega_1 = 0.0426$ $\omega_2 = 0.0853$, $\omega_3 = 0.128$ and $\omega_4 = 0.1706$ respectively, corresponding to the integer multiples of the frequency of the periodic solution to the unforced problem.

We note that as n increases the minor axis of the ellipse appears to decrease, although the major axis stays approximately constant.

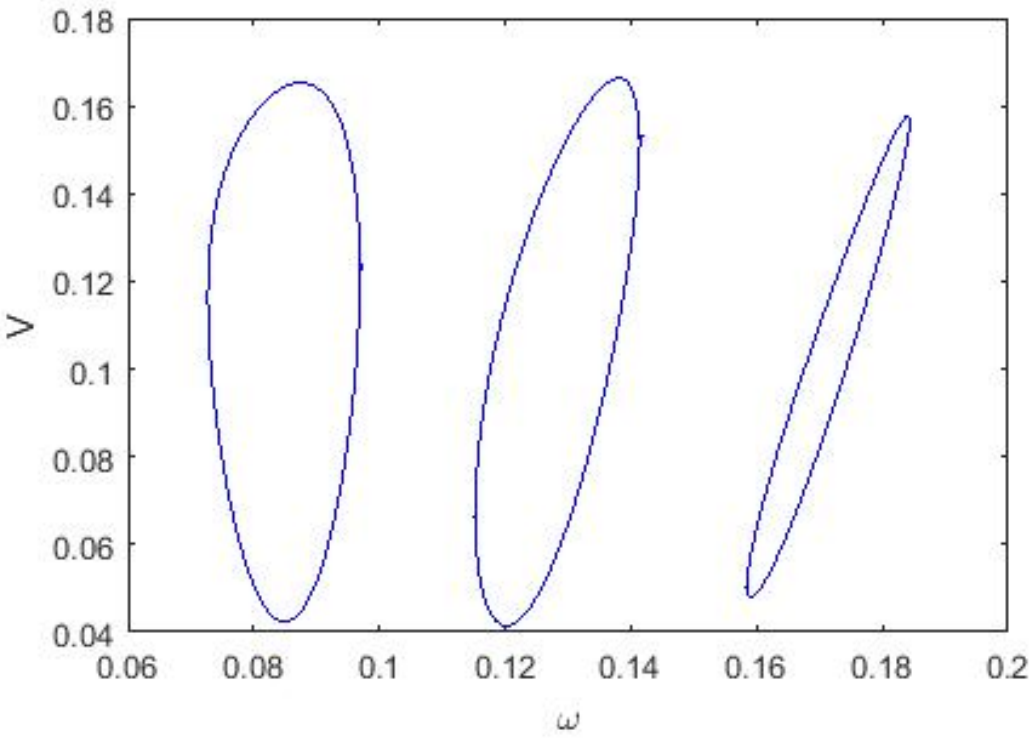

Figure 5-3: The variation of $V(t_0)$ with ω for $\mu = 0.1$ for (from left to right) the three cases of $n = 2, 3, 4$.

The value of t_0 varies over the interval $[0, \frac{2\pi}{(n\,\omega^*)}]$ as we travel around the ellipse. In particular, it follows from (5.20) that the value of t_0 changes by $\frac{\pi}{(n\,\omega^*)}$ between the two saddle node bifurcation points. This is of interest as it demonstrates that the phase of the response (V, A, C) to the insolation forcing, whilst locked to it for a particular periodic orbit, differs from it. This phenomenon has been observed in the record of the ice ages in which the Milankovitch cycles are not always seen to be in phase with the cooling and warming periods.

As an example we take the case $n = 3$ and $\mu = 0.1$. A numerical calculation in this case shows that solutions exist for $\omega \in [0.1152, 0.1413]$, $\frac{2\pi}{\omega} \in [44.46, 54.52]$, $T = \frac{6\pi}{\omega} = [133.37, 163.57]$ and $t_0 \in [8.7965, 31.882]$. In Figure 5-6 we plot two cycles of the resulting periodic orbits for the three cases $t_0 = 8.7965$, $t_0 = 20.3156$ and

$t_0 = 31.882$ representing the left and right limits and the middle of the range of values for which we see a solution.

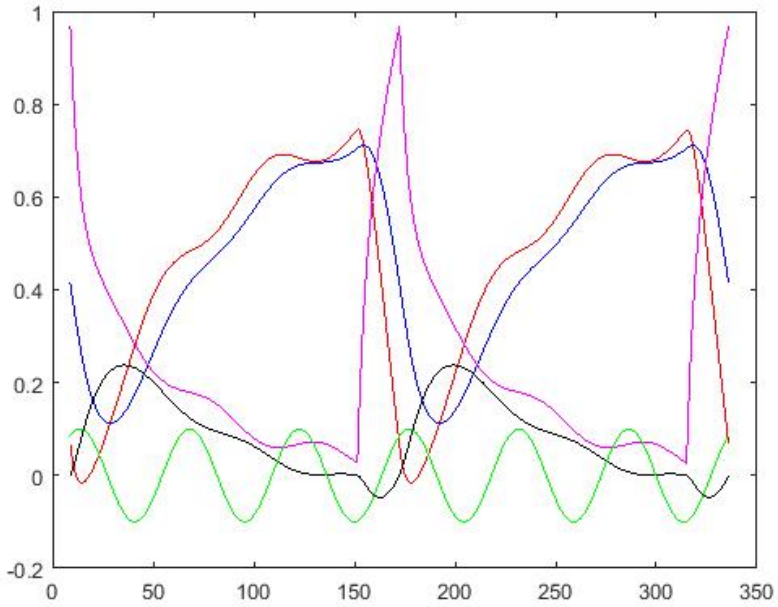

Figure 5-4: Two cycles of the periodic solutions when $n = 3$. In this plot we see V (blue), A (red), C (maroon), F (black), and the insolation (green) when $t_0 = 8.79$

We see that the periodic solutions observed in Figure 5-4 to Figure 5-6 are similar to the ones observed in Figure 4-1. However, the former have some oscillations added into the solutions.

Regions of existence for small μ

The previous analysis shows that $\omega^* = 0.0429$. Further numerical studies lead to the following approximations for small μ of the regions of existence of the $(1, n)$ orbits.

$$\begin{aligned} \omega_{1,1} &= \omega^* - 0.0905\mu \quad \omega_{2,1} = \omega^* + 0.0905\mu \\ \omega_{1,2} &= 2\omega^* - 0.1228\mu \quad \omega_{2,2} = 2\omega^* + 0.1228\mu \\ \omega_{1,3} &= 3\omega^* - 0.1348\mu \quad \omega_{2,3} = 3\omega^* + 0.1348\mu \\ \omega_{1,4} &= 4\omega^* - 0.1296\mu \quad \omega_{2,4} = 4\omega^* + 0.1296\mu \end{aligned} \tag{5.23}$$

In Figure 5-7 we give the graph of the regions of existence of the periodic solutions for $n = 1, 2, 3, 4$ for the linearised problem as described above. We can see that the regions of existence of periodic solutions for this linear problem start to overlap if $\mu > 0.15$.That is, for $\mu > 0.15$ we expect to see (as we in fact do see) the co-existence of periodic solutions with different values of n and hence of different periods $T = \frac{2n\pi}{\omega}$. In fact, as we shall see, the original (nonlinear) problem has rather larger regions of overlap of the existence regions or of coexistence of periodic solutions.

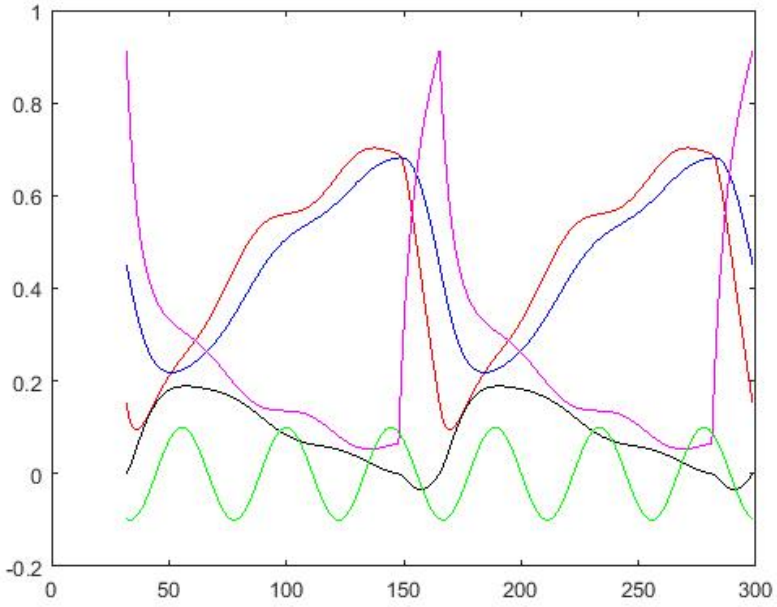

Figure 5-5: Two cycles of the periodic solutions when $n = 3$. In this plot we see V (blue), A (red), C (maroon), F (black), and the insolation (green) when $t_0 = 31.882$.

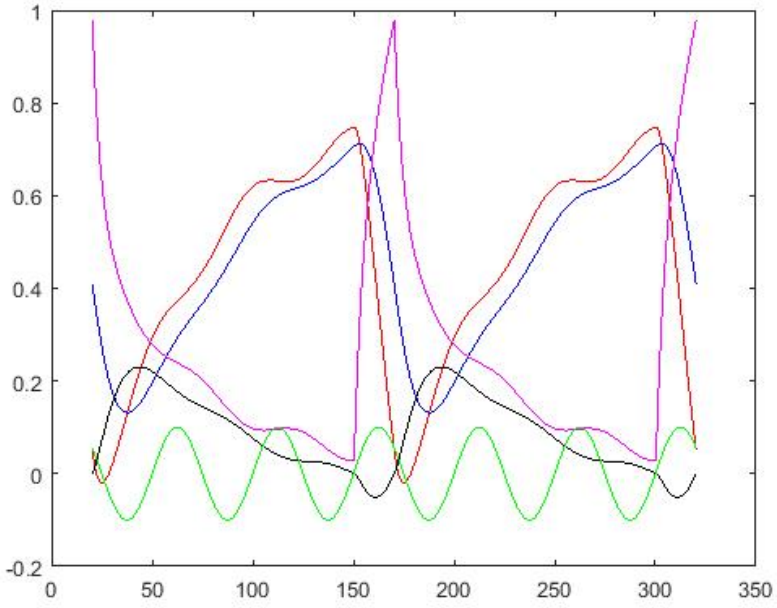

Figure 5-6: Two cycles of the periodic solutions when $n = 3$. In this plot we see V (blue), A (red), C (maroon), F (black), and the insolation (green) when $t_0 = 20.3156$.

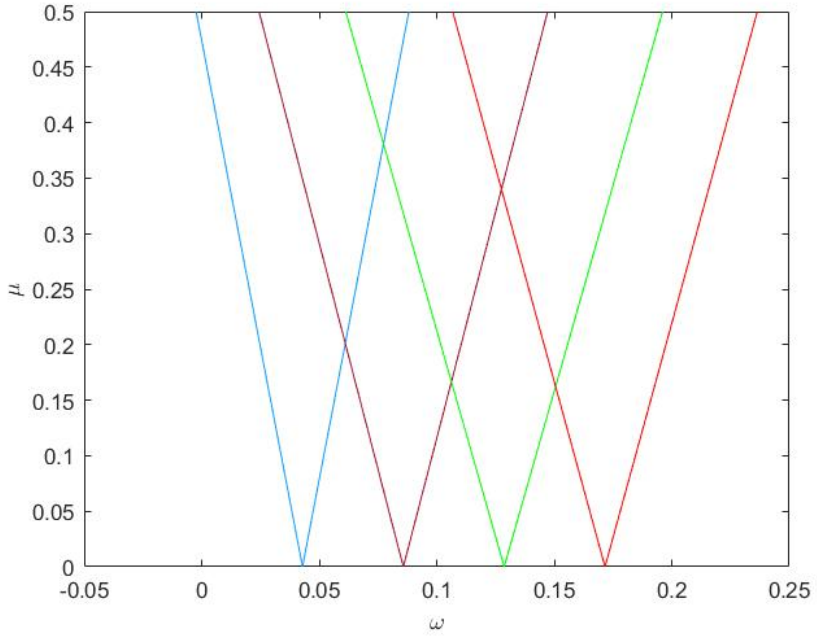

Figure 5-7: The existence regions for the linearised problem.

5.1.3 Larger values of μ.

The above calculation has given only a small μ analysis, showing that for small μ the width of the existence tongues increases directly proportionally to μ for all values of n. However, as μ increases, so this analysis will break down as further nonlinear effects become important. Indeed, we see a distortion, and indeed a break up, of the elliptical curves.

In Figure 5-8 we plot computed regions of existence of the $(1, n)$ periodic solutions. These regions are determined by first fixing the value of μ and solving the full algebraic system numerically for a set of values of $\omega = n\omega^* \pm \delta$ increasing δ from 0. The calculation was done using the Matlab solver `fsolve` with an initial guess given by $\mathbf{X}_0 = (5, 5, 5, 5, 5, 5, 100, 200)$. We then plot the first values of ω_{new} against μ for which the algebraic solver breaks down. As can be seen, the regions of existence are linear (as predicted) for small values of μ. They then expand significantly as μ increases. This is due to a break up of the solution ellipses.

We note that the physically interesting case of $(\mu, \omega) = (0.467, 0.1476)$ (as per the approximated values for the frequency and coefficient terms for obliquity provided in [46, 16]) lies in the region where there is only a $(1, 3)$ periodic solution.

In Figure 5-9 we see the set of elliptical curves for the cases of $n = 2, 3, 4$ taking larger values of μ than before. For $n = 2, 3$ we see a break up of the ellipses at $\mu = 0.25$. In the case of $n = 4$ the break up occurs for a larger value of μ. Indeed, we observe in general, that break up of the ellipses occurs for smaller values of μ

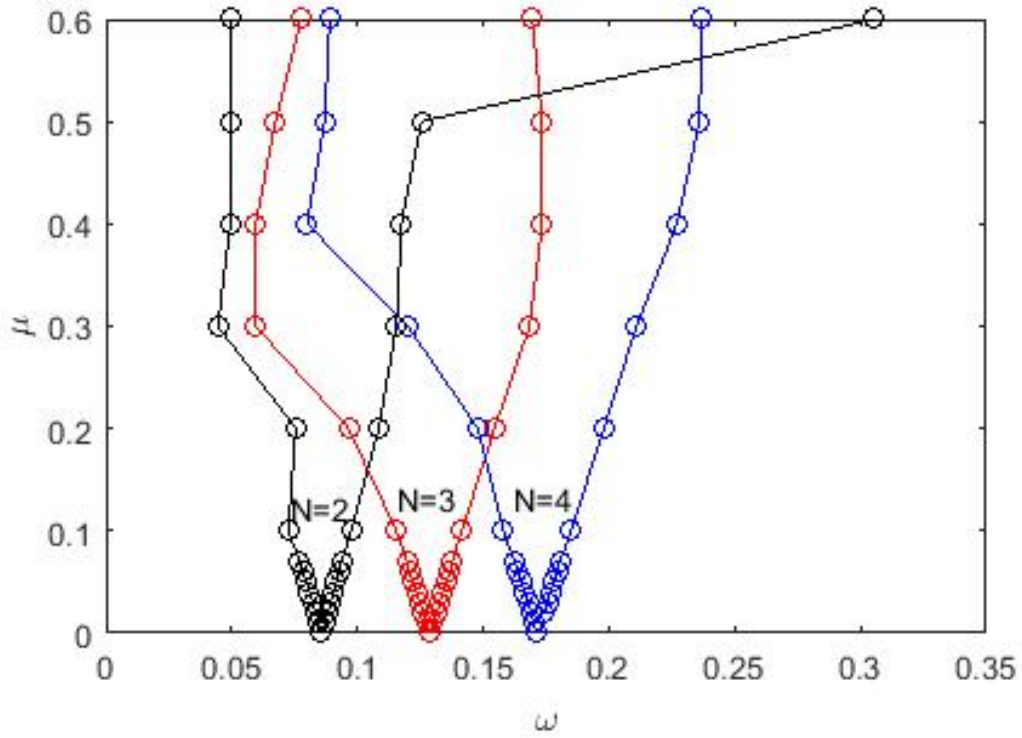

Figure 5-8: A set of graphs showing the regions of existence of the $(1, n)$ orbits when both μ and ω are varied. The red case $n = 2, 3, 4$ are illustrated.

as n decreases. We note further that if $\mu = 0.25$ then (as expected from the linear analysis) the regions of existence of the $n = 2$ and $n = 3$ periodic orbits overlap. As a consequence we might expect to see both $n = 2$ and $n = 3$ orbits in this case, with related domains of attraction for the initial data. If we take the larger, and physically relevant, value of $\mu = 0.467$ then we see a more complicated curve, and the range of existence of the solutions in this case is more difficult to predict. In Figure 5-10 we show the curves of the $(1, 3)$ orbit for a range of values of μ increasing from $\mu = 0.1$ to $\mu = 0.467$. In this figure we observe solution existence ellipses for $\mu < 0.245$. These then break up at around $\mu = 0.25$ and enlarge as μ increases. When $\mu = 0.467$ we see that the maximum value of $\omega = 0.194$. There is no minimum value shown on this graph, however we note that not all of the solutions of the algebraic solver are physical over this range. To see this we take $\mu = 0.467$ and consider the physically relevant value of $\omega = 0.1476$. For this value of ω it is apparent from Figure 5-10 that there are (at least) two solutions, $S_{1,2} \equiv [V(t_0), A(t_0), C(t_0), t_0, \Delta]$ to the algebraic equations, with S_1 on the upper side of the curve of solutions and S_2 on the lower. A careful calculation shows that these solutions are given by

$$S_1 = [0.3835, 0.5501, 0.7585, 37.3574, 113.8284],$$

and

$$S_2 = [0.0246, 0.3966, 0.9906, 23.2615, 109.9237].$$

The resulting functions $(V(t), A(t), C(t), F(t))$ are plotted in Figure 5-11 and Figure

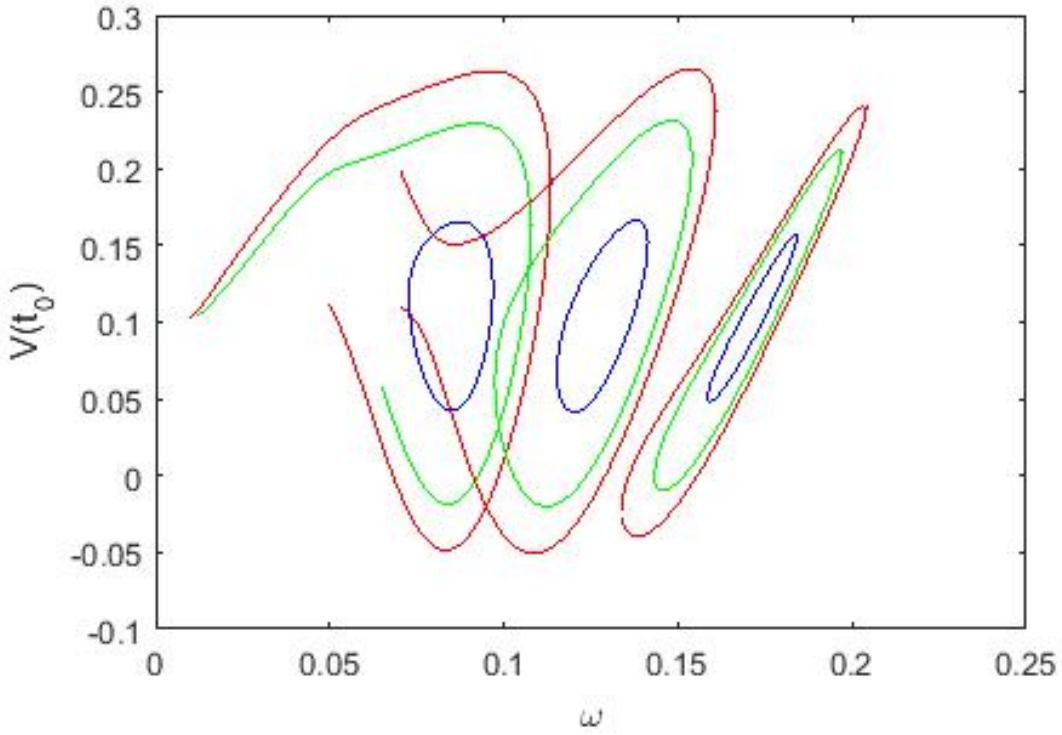

Figure 5-9: The variation of $V(t_0)$ with ω when $n = 2, 3, 4$ (from left to right respectively) for $\mu = 0.1$ (blue), $\mu = 0.2$ (green) and $\mu = 0.25$ (red) showing the break up of the elliptical curves as μ increases when $n = 2, 3, 4$.

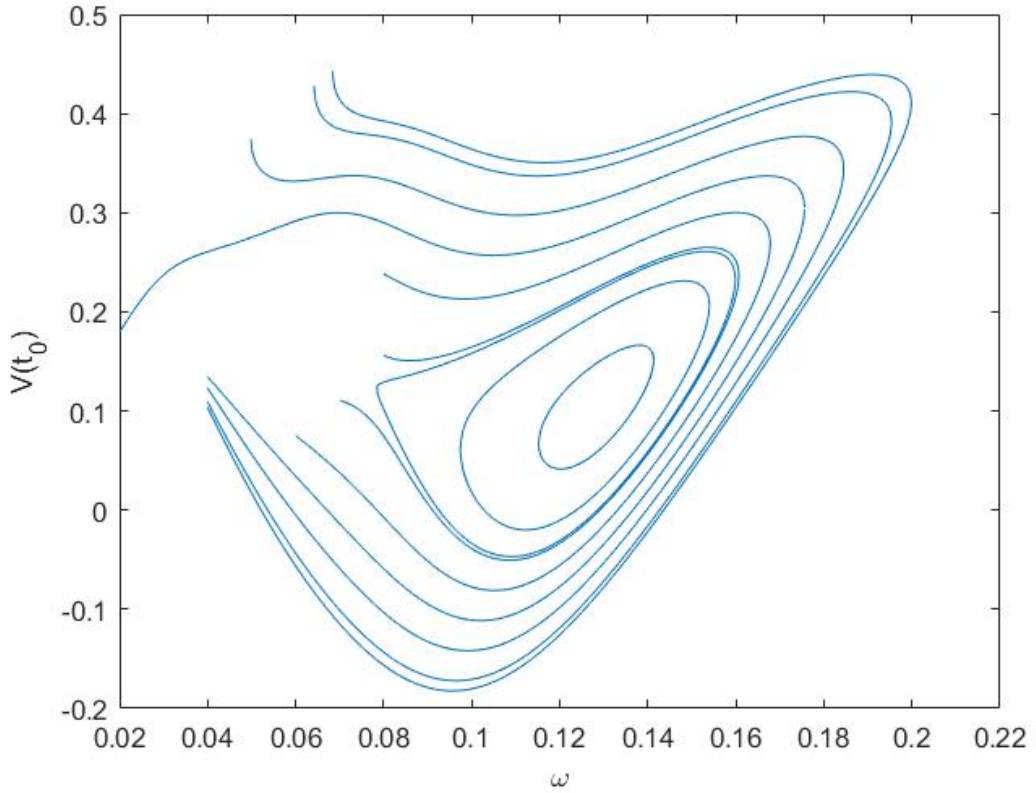

Figure 5-10: The variation of $V(t_0)$ with ω for the $(1, 3)$ orbit when μ increases from $\mu = 0.1$ to $\mu = 0.467$ showing the break up of the elliptical curve at $\mu = 0.25$

5-12, along with the forcing. It is clear from these figures that only the solution S_2 can be physical. This is because when we consider the solution S_1 it is clear from the graph that the function $F(t)$ does not keep a constant sign during either the glacial or the inter-glacial cycles.

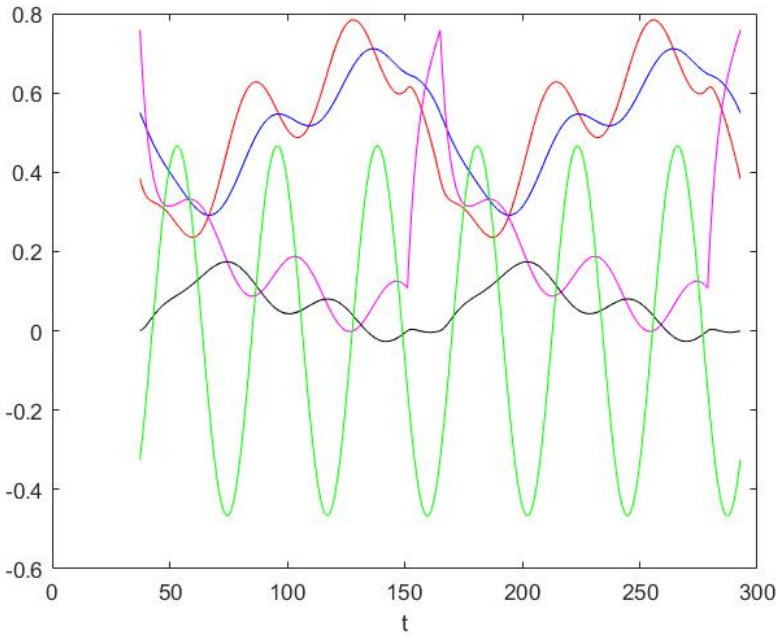

Figure 5-11: The solutions on the upper branch (S_1). In these graphs we plot (as functions of time) V (red), A (blue), C (purple), F (black) and the forcing (green). The solution S_1 is not physical as F changes sign during the cycles.

The solutions close to $\mu = 0.25$ are of some theoretical interest. In Figure 5-13 we show the solution existence curves for $\mu = 0.244$ (left) and $\mu = 0.245$ (right). The curve for $\mu = 0.244$ shows evidence for two separated solution branches, one of which is a distorted ellipse. These two branches then merge when $\mu = 0.25$ leading to a break up of the ellipse.

A plot of the curve of (t_0, ω) and of (t_0, V) for the case of $\mu = 0.25$ is given in Figure 5-14. We see in this case that, unlike in the case of small μ when t_0 could take arbitrary values, in this case we have an upper limit of $t_0 < 78$. We note, however, that the solutions on these curves are not necessarily physical.

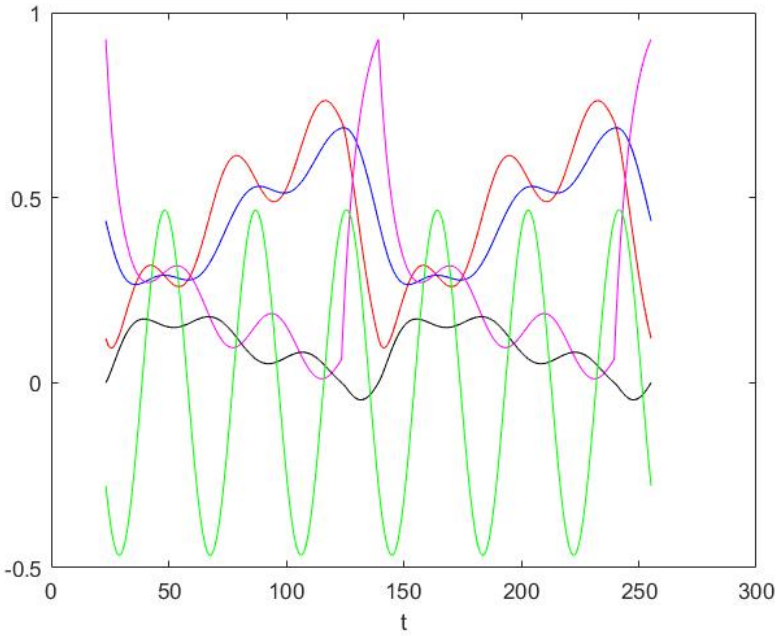

Figure 5-12: The solutions on the lower branch (S_2 right). In these graphs we plot (as functions of time) V (red), A (blue), C (purple), F (black) and the forcing (green).

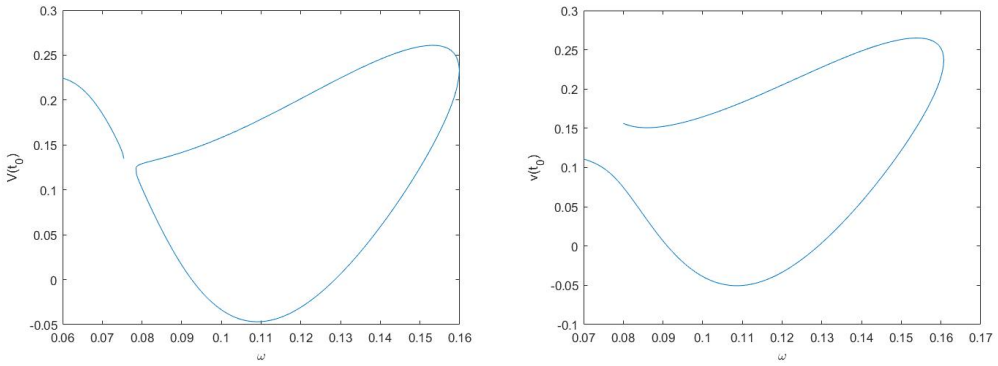

Figure 5-13: The variation of $V(t_0)$ with ω for the $(1,3)$ orbit for $\mu = 0.244$ (left) and $\mu = 0.25$ (right).

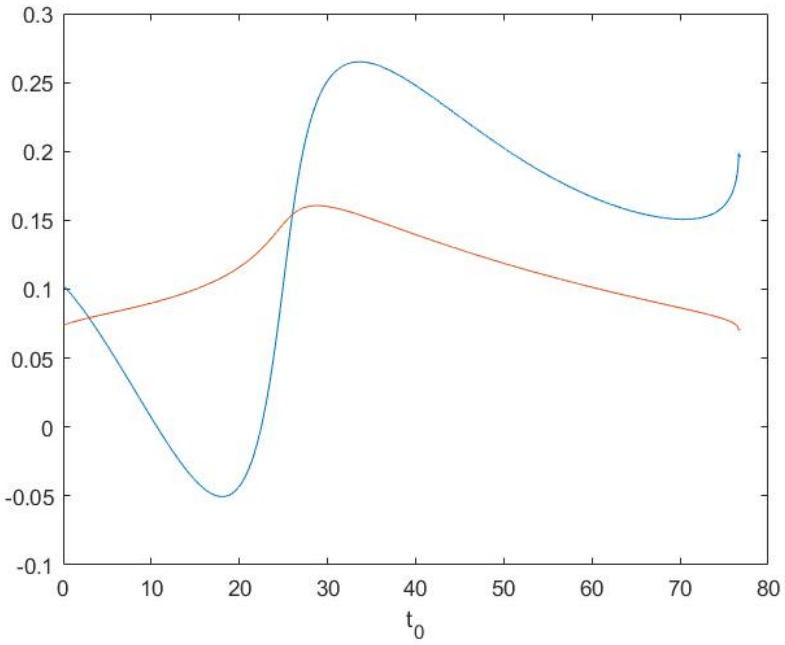

Figure 5-14: The variation of $V(t_0)$ (blue), and of ω with t_0 for the $(1,3)$ orbit for $\mu = 0.25$

5.2 Stability and physicality

As we have seen, not all of the orbits on the computed curves are physical, in the sense that the function F can change sign during a glacial or an inter-glacial cycle. We will consider the implications of this to the resulting dynamics in the Chapter 7.

Also of significant interest is the stability of the resulting orbits. The right extremes of the (ω, V) solution curves are in all cases marked by saddle-node bifurcations. In general such bifurcations are associated with changes in the *stability* of the solutions. It is difficult to determine the stability algebraically. However a large number of numerical experiments demonstrate clearly that it is the *lower branch of the curves* which is stable, and the *upper branch* is unstable.

When considering the curve for $\mu = 0.1$ as shown by Figure 5-15, we observe that the point $(\omega, V(t_0)) = (0.128, 0.0571)$ is on the lower branch while the point $(0.14, 0.1643)$ is on the top branch. In Figure 5-17 we observe that the lower branch of the curve gives stable solutions shown by the stroboscopic plots of F. Similarly when we consider the curve for $\mu = 0.2$ as shown by Figure 5-19 the point $(\omega, V(t_0)) = (0.15, 0.15003)$ is on the lower branch and $(0.15, 0.231)$ is on the top branch. In Figure 5-21 we observe that the lower branches of the curves for $\mu = 0.2$ give the stable solutions shown by the stroboscopic plots of F.

In Figures 5-18 and 5-16 we observe that the upper branch of the curve for $\mu = 0.1$ give the unstable solutions respectively as shown by the stroboscopic plots of F. The

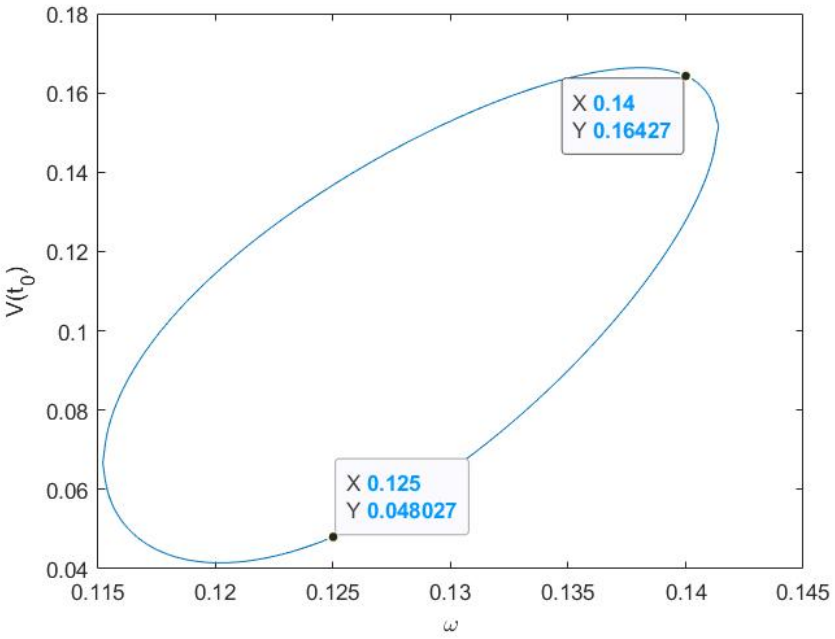

Figure 5-15: The variation of $V(t_0)$ with ω for $n = 3$ and $\mu = 0.1$.

solutions are unstable around the initial point and then converge to a period $(1, 3)$ solution.

We will see later that the solutions can also lose stability at *period-doubling bifurcations*, where a (m, n) orbit is replaced by a $(2m, 2n)$ orbit. A further loss of stability is associated with a *grazing bifurcation*, when a solution loses physicality with the function F changing sign within a glacial or an inter-glacial cycle.

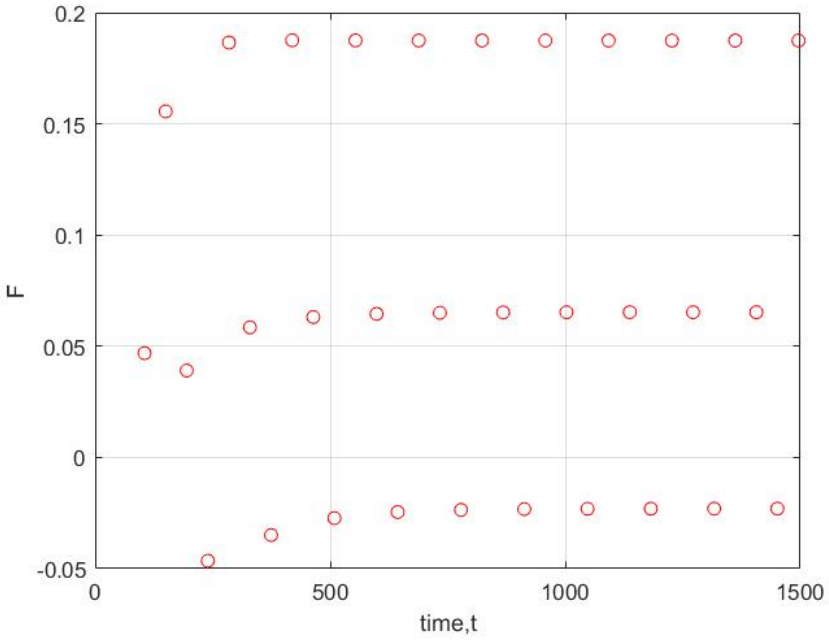

Figure 5-16: The stroboscopic plots of F showing the lack of stability of solutions. The solutions evolves from the upper branch to the lower branch of the curve when $\mu = 0.1$ and $\omega = 0.14$ with initial conditions $(V, A, C) = (0.1643, 0.4561, 0.9043)$ starting at $t_0 = 80.1320$.

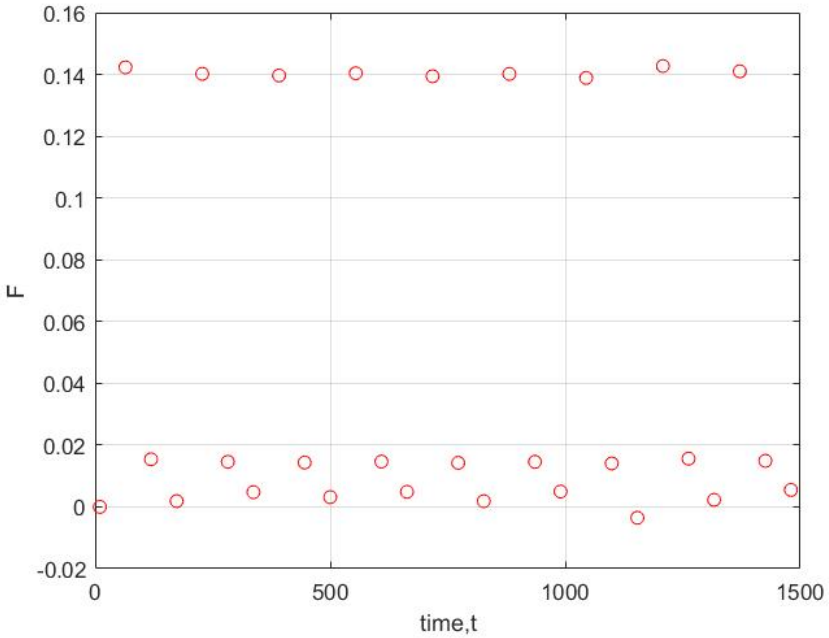

Figure 5-17: The stroboscopic plots of F showing the stability of solutions corresponding to the lower branch for $n = 3$ when $\mu = 0.1$ and $\omega = 0.1154$ with initial conditions $(V, A, C) = (0.0606, 0.4117, 0.9727)$ starting at $t_0 = 10$.

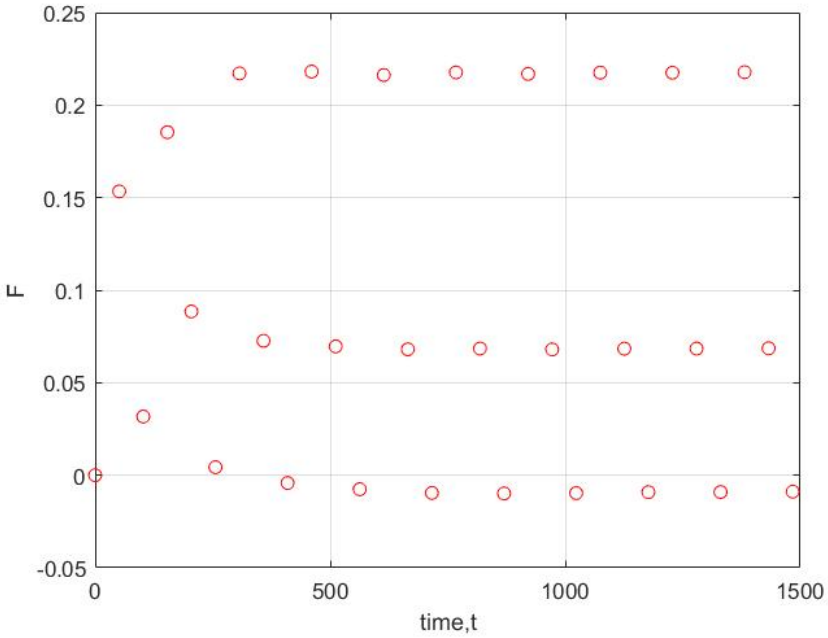

Figure 5-18: The stroboscopic plots of F showing unstable solutions for corresponding to the upper branch when $\mu = 0.1$ and $\omega = 0.1228$ with initial conditions $(V, A, C) = (0.1281, 0.4406, 0.9293)$ starting at $t_0 = 0$.

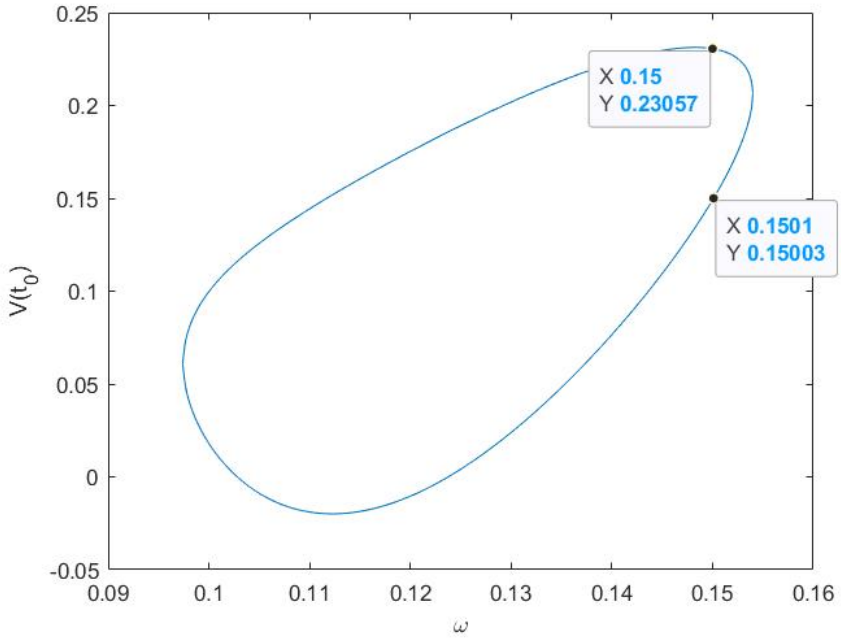

Figure 5-19: The variation of $V(t_0)$ with ω for $n = 3$ and $\mu = 0.1$.

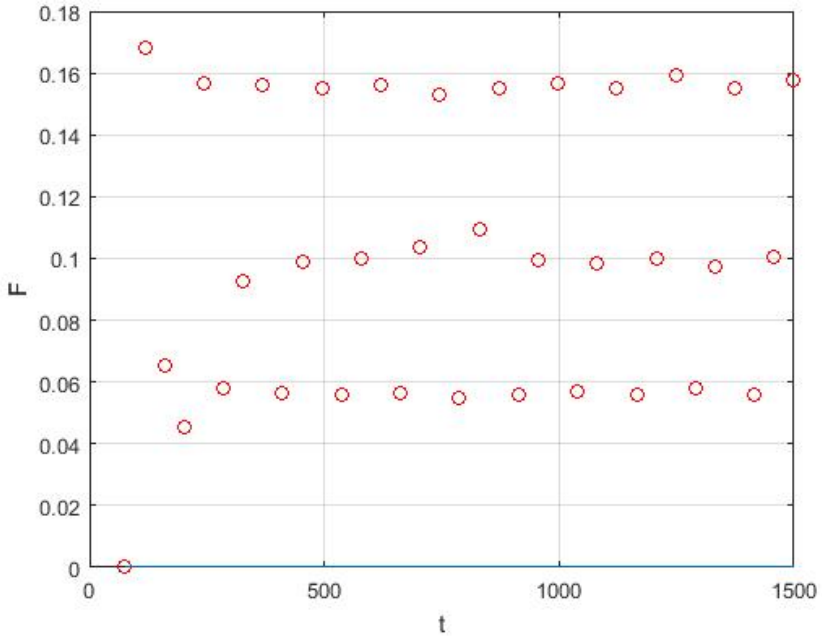

Figure 5-20: The stroboscopic plots of F showing unstable solutions on the upper branch when $\mu = 0.2$ and $\omega = 0.15$ with initial conditions $(V, A, C) = (0.2306, 0.4845, 0.8601)$ starting at $t_0 = 75.7907$.

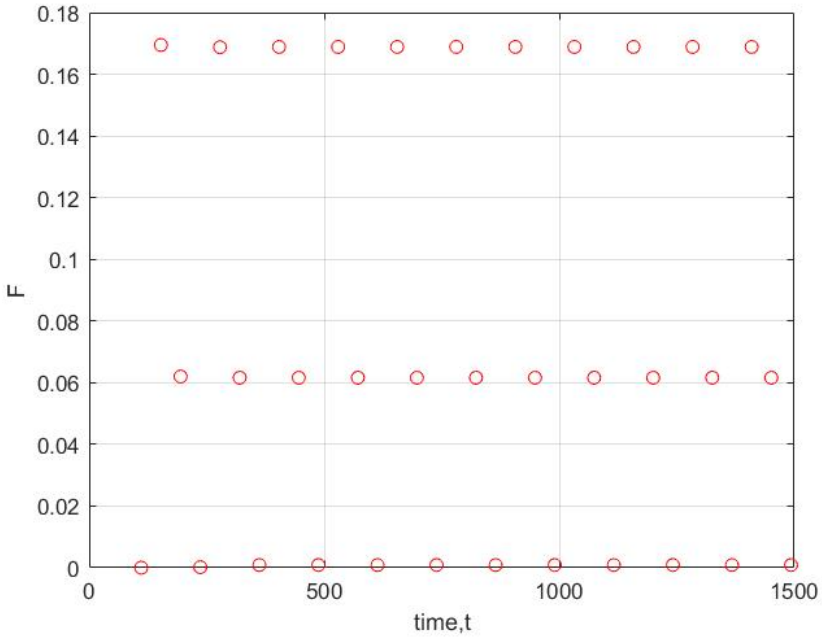

Figure 5-21: The stroboscopic plots of F showing the stability of solutions on the lower branch for $n = 3$ when $\mu = 0.2$ and $\omega = 0.15$ with initial conditions $(V, A, C) = (0.1491, 0.4496, 0.9122)$ starting at $t_0 = 110.7196$.

5.3 More general (m, n) periodic orbits

The analysis described above applies to $(1, n)$ orbits. An essentially similar analysis can be applied to the more general (m, n) orbits, which exhibit m glacial cycles. To construct, and analyse these, we introduce a series of m intervals $\Delta_{i,1}$ and $\Delta_{i,2}$ summing in total to $\frac{2\pi}{\omega}$, being the times between successive glacial and inter-glacial periods. Each such interval will start at a time $t_{i,1}$ or $t_{i,2}$, with $i = 0 \ldots m-1$, where each such $t_{i,1,2}$ can be computed from the initial time $t_{i,1}$ of the first cycle by adding the appropriate time periods $\Delta_{i,1,2}$. For small μ each $\Delta_{i,1}$, and $\Delta_{i,2}$ is then a perturbation $\delta_{i,1}$ or $\delta_{i,2}$ of the respective times for the unforced problem. Similarly, let $X_{i,1}$ and $X_{i,2}$ be the initial conditions at the start of the respective glacial and inter-glacial periods. These will be perturbations $x_{i,1}$ and $x_{i,2}$ of the unperturbed values. The equations for a $(1, n)$ orbit then extend to the following system for $i = 0 \ldots m-1$.

$$\begin{aligned}
\mathbf{X}_{i,2} &= \mathbf{E}(t_{i,1}, \Delta_{i,1}, \mathbf{X}_{i,1}), && (5.24)\\
\mathbf{X}_{i+1,1} &= \mathbf{E}(t_{i,2}, \Delta_{i,2}, \mathbf{X}_{i,2}) && (5.25)\\
F(\mathbf{X}_{i,1}) &= 0, && (5.26)\\
F(\mathbf{X}_{i,2}) &= 0, && (5.27)\\
\sum_{i=0}^{m-1} \Delta_{i,1} + \Delta_{i,2} &= \frac{2\pi n}{\omega}, && (5.28)\\
\mathbf{X}_{0,1} &= \mathbf{X}_{m,1}. && (5.29)
\end{aligned}$$

Here $\mathbf{E}(t_{i,1}, \Delta_{i,1}, \mathbf{X}_{i,1})$ is the evolutionary operator which we have constructed explicitly. If we specify the start time $t_{0,1}$ then the system (5.29) constitutes $8m + 4$ equations for the $8m + 4$ unknowns $\mathbf{X}_{i,1}, \mathbf{X}_{i,2}, \Delta_{i,1}, \Delta_{i,2}$, and ω.

As before, the complete system (5.29) can then be linearised about the solution when $\mu = 0$. The resulting system will be identical in form to that given in equation (5.19). Hence we expect to see small ellipses of solutions as before, scaling linearly with μ.

It is difficult to predict from the above analysis the size of the window of existence of the (m, n) solutions. It is tempting to relate the (m, n) orbits to the periodic orbits of circle maps of frequency ω with forcing proportional to μ. In these the theory of Arnold Tongues implies mode-locked regions close to rational frequencies $\omega = \frac{n}{m}$ the width of which scales as μ^m [62]. This means that the windows of existence are much smaller for the larger values of m. In the non-smooth problem we are considering the scaling of the (m, n) is *always linear in* μ. However, we will show by some numerical experiments, that it appears that the regions of existence are much smaller if $m > 1$ than for the case of $m = 1$.

5.4 More general dynamics of the PP04 model

The previous sections have allowed us to gain an analytical insight into the general behaviour of the periodic solutions of the PP04 model for small periodic forcing, but give less information about the general behaviour of the system. Of course this is of most interest in a general discussion of how well the model applies to climate dynamics for which μ takes larger values. We now make a systematic numerical analysis of this case which both confirms the predictions of the previous section, and allows us to explore the rich dynamics of the forced PP04 system.

5.4.1 Poincaré sections and Monte-Carlo plots

As we discussed in Chapter 2, a natural tool for analysing the PP04 climate model under periodic forcing is the *stroboscopic Poincaré map* P_S. This map is defined as follows

Definition 5.4.1. Let the PP04 model be forced by the insolation function $\mu \sin(\omega t)$, with state vector $\mathbf{X}(t)$ then

$$P_S\, \mathbf{X}(t) \equiv \mathbf{X}\left(t + \frac{2\pi}{\omega}\right). \tag{5.30}$$

Using this map we can construct a set of points $\mathbf{x}_m$ defined by the iteration

$$\mathbf{X}_{m+1} = P_S\, \mathbf{X}_m. \tag{5.31}$$

A (m, n) periodic orbit, as constructed above, then corresponds to an orbit which is an $n-$cycle $(\mathbf{X}_0, \mathbf{X}_1, \ldots, \mathbf{X}_{n-1})$ of P_S for which

$$\mathbf{X}_0 = P_S\, \mathbf{X}_{n-1}.$$

Such an orbit crosses the discontinuity manifold $2m$ times. The nature of such maps for Filippov flows has been studied some detail in [19] Chapter 7. In general the map P_S will be piecewise smooth. However it will lose smoothness if there is a grazing event in the interval $[t, t + \frac{2\pi}{\omega}]$. We will return to this in the Chapter 7.

The general dynamics of the PP04 system can now be studied by considering the iterations of the map P_S. To do this we use a Monte-Carlo approach in which we consider a set of randomly chosen initial conditions but we fix the strength of the forcing. The random initial conditions are considered so that the multiple attractors or all attractors of the system may be observed if they so exists. In this calculation we ignore the transient dynamics and plot the Omega limit set given by the final

set of iterations of the map in a long set of iterations. If this is done for a set of random initial data then we obtain a Monte-Carlo plot, which gives a significant insight into the overall dynamics of the system. It is convenient to represent the state of the whole system by plotting the single variable $F(\mathbf{X})$. We gradually increase the frequency of the forcing with each iteration to see the resulting dynamics as a function of ω.

Varying ω.

Initially we take fixed small values of μ (consistent with the earlier analysis) and vary the value of ω. In Figure 5-22 we take $\mu = 0.05$ and increase ω from 0.08 to 0.13, plotting the Omega-limit set of the resulting orbit in each case. It is convenient to represent these orbits by plotting the values of the function F. In this figure we can see a clear $(1, 2)$ orbit for smaller values of ω and an equally clear $(1, 3)$ orbit for the larger values. For $\omega \approx 0.107$ we see a small window of existence for the $(2, 5)$ periodic orbit. Away from these values we observe quasi-periodic behaviour. An

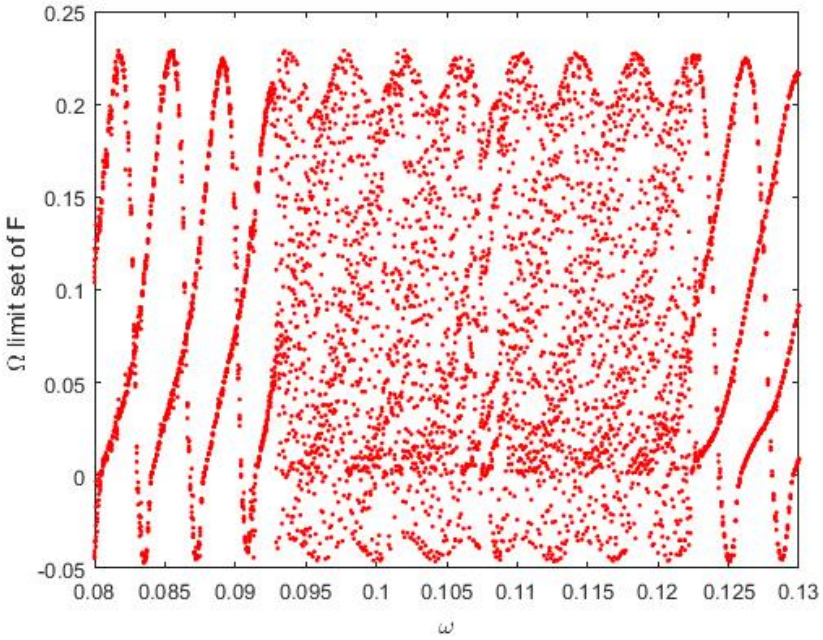

Figure 5-22: The Poincaré section points of F on the omega limit set, as a function of ω with $\mu = 0.05$ showing (as ω increases), a large window of existence for the $(1, 2)$ periodic orbit, a small window of existence for the $(2, 5)$ periodic orbit and then another large window for the $(1, 3)$ periodic orbit, all separated by intervals of quasi periodic motion

equivalent figure is presented in Figure 5-23 in which we take the larger value of the forcing $\mu = 0.1$. This figure shows, as we might expect, larger regions of existence for all of the above periodic orbits, with other emerging structures between the $(1, 2)$ and the $(1, 3)$ periodic orbits.

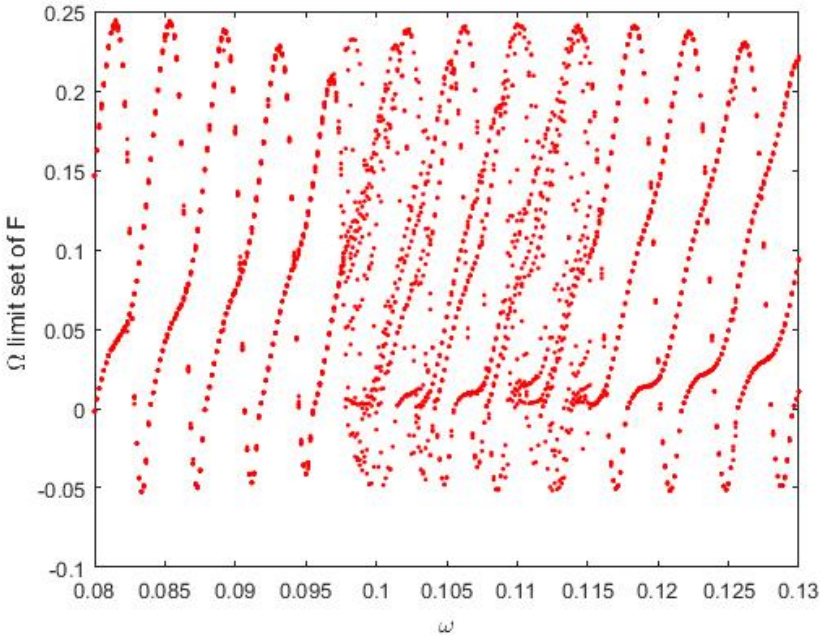

Figure 5-23: The Poincaré section points on the Omega limit set, as a function of ω with $\mu = 0.1$ showing the $(1,2), (2,5)$ and $(1,3)$ periodic solutions.

In Figures 5-24, and 5-25 we now study the $(1,3)$ orbit in more detail as this will turn out to be the most interesting orbit from a climate perspective. In Figure 5-24 we take $\mu = 0.03$ and see the transition from quasi-periodic motion when $\omega < 0.1245$ to period $(1,3)$ motion when $\omega > 0.1245$. Note the change of phase of the $(1,3)$ orbit as ω is increased. In Figure 5-25 we see the $(1,3)$ orbit changing to a quasi-periodic orbit when $\omega = 0.135$ followed by an interval of quasi-periodic motion, which then turns into a $(1,4)$ orbit when $\omega = 0.165$. This is fully consistent with the separation of the solution ellipses for these two orbits. There appears to be a very thin window of existence for a $(2,7)$ orbit between the $(1,3)$ and $(1,4)$ orbits. This is what might be expected from the related theory of Arnold Tongues of orbits of circle maps, in which we see a Farey sequence describing the periods of the various orbits.

Varying μ

As a second calculation, we fix ω at the physically relevant value of $\omega = 0.1467$ and increase μ from zero. The resulting Monté-Carlo calculation is presented in Figure 5-26. We see quasi-periodic behaviour for small values of μ and for large values of μ we see $(1,1)$ periodic orbits, completely locked to the forcing. At $\mu = 0.467$ we see only a $(1,3)$ periodic orbit. This figure is fully consistent with the regions of existence of the $(1,n)$ orbits plotted in Figure 5-8.

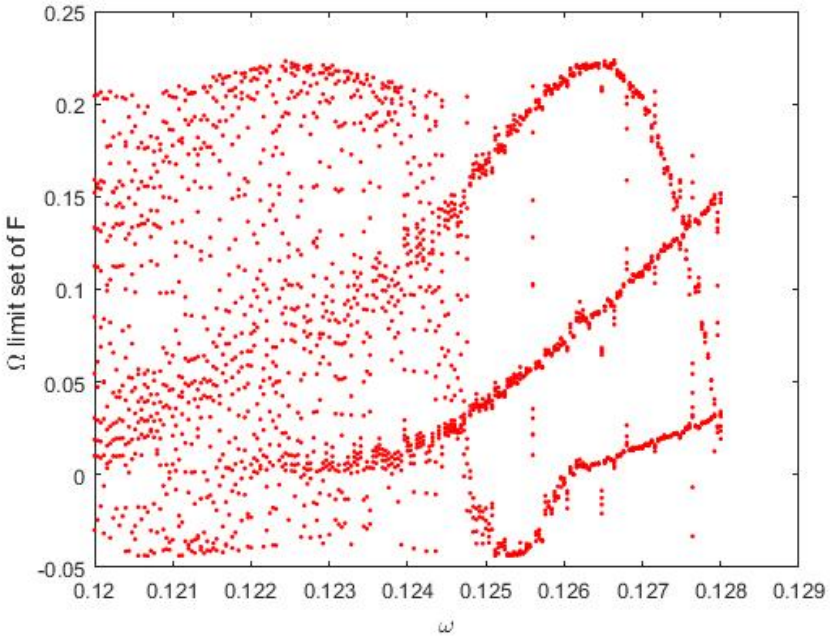

Figure 5-24: The Poincaré section points on the Omega limit set of F , as a function of ω with $\mu = 0.03$ showing quasi-periodic motion followed by period $(1, 3)$ motion

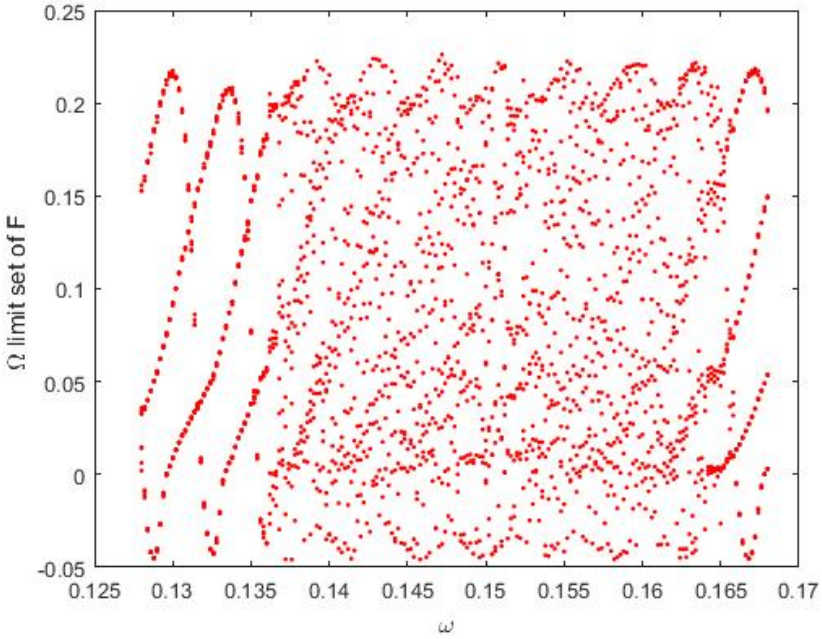

Figure 5-25: The Poincaré section of F on the Omega limit set, as a function of ω with $\mu = 0.05$ showing period $(1, 3)$ and period $(1, 4)$ motions separated by an interval of quasi periodic motion, with some evidence of a period $(2, 7)$ orbit between them.

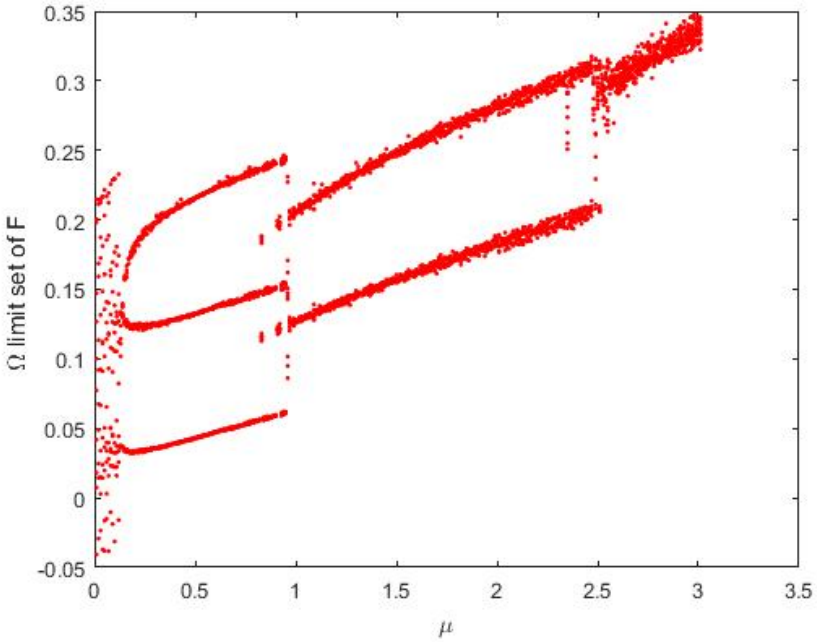

Figure 5-26: The Poincaré section points on the Omega limit set of F, as a function of μ with $\omega = 0.1476$ showing the different types of solutions as μ increases from quasi-periodic, to $(1,3)$,$(1,2)$ and then $(1,1)$ with regions of co-existence.

5.4.2 Period doubling and intermittent dynamics

For a final calculation we take $\mu = 0.467$ and vary ω from 0.121 to 0.129. The results are presented in Figure 5-27. As we would expect from the previous results for the smaller values of ω we see a $(1,2)$ orbit and for the larger values a $(1,3)$ obit. Two interesting transitions can be observed in this figure as ω increases. At $\omega = 0.122$ the $(1,3)$ orbit abruptly appears. The reason for this can be seen from studying the values of F. In particular $F = 0$ at the bifurcation point. This is a (non-smooth) grazing bifurcation at which the $(1,3)$ orbit starts to become physical. We will study this transition in more detail in a next chapter. A (smooth) super critical period-doubling bifurcation can be seen at $\omega = 0.127$. At this point the $(1,2)$ orbit loses stability to a nearby $(2,4)$ orbit. To support this calculation we take $\omega = 0.128$ which is just greater than the period-doubling value. The resulting intermittent dynamics resembles that at the mid-Pleistocene transition

5.4.3 Numerical calculations of the time dependent solutions

In fixing the values of μ and ω but varying the initial conditions, we expect to observe the $(1,n)$ time dependent orbits in accordance with Figure 5-8. In Figure 5-28, when fixing $\mu = 0.467$ and $\omega = 0.126$, and considering different initial conditions, the $(1,2)$ periodic orbit is observed. From the solution, it is established that the system spends

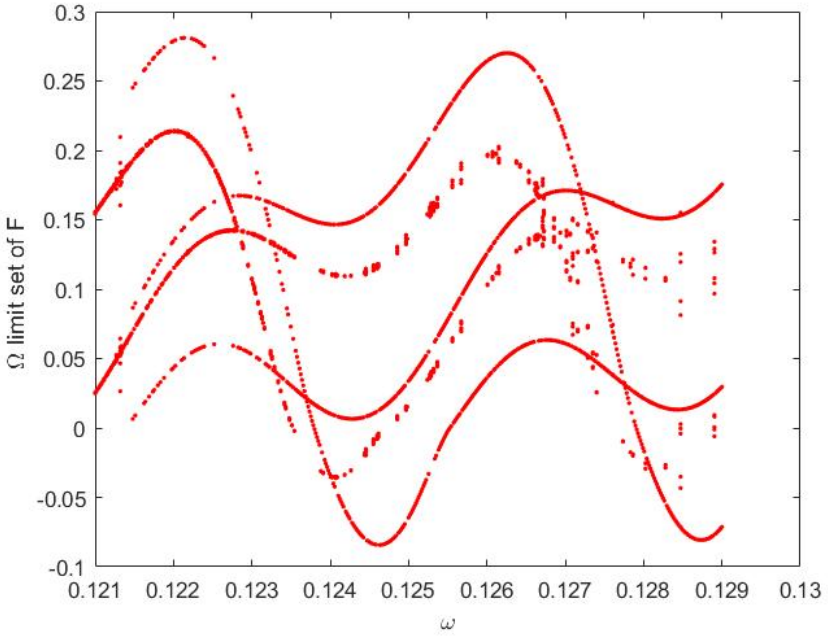

Figure 5-27: Monte-Carlo plot of F for $\mu = 0.467$. To the left we observe a $(1, 2)$ orbit and to the right a $(1, 3)$ orbit. Various transitions between these orbits can also be observed. These include a grazing bifurcation at $\omega = 0.1215$ and what appears to be a period-doubling bifurcation at $\omega = 0.1275$.

most of its time in the glacial state, as clearly seen in Figure 5-29 and in accordant with analytical calculations. However in Figure 5-30, for the same values of μ and ω, but with different set of different initial conditions, a period $(1, 3)$ solution is observed. These periodic solutions observed are consistent with Figure 5-27, where we observed the presence of both periodic solutions. This implies that for $\mu = 0.467$ and $\omega = 0.126$, the type of solution observed depends on the initial conditions.

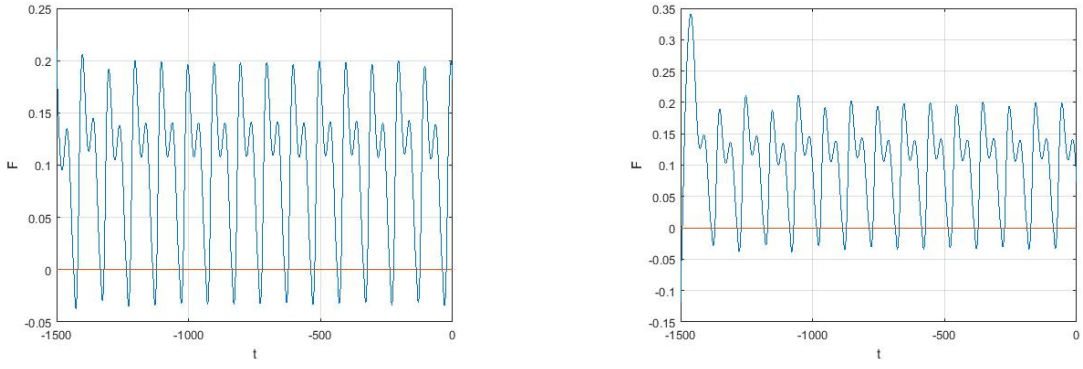

Figure 5-28: The time solution of the system showing a period $(1, 2)$ orbit of F for $\omega = 0.126$ and $\mu = 0.467$ for different initial conditions left: $(V, A, C) = (0.5, 0.3, 0.4)$ and right: $(V, A, C) = (0.1, 0.6, 0.9)$

Figure 5-32, shows a period $(2, 4)$ solution when the same value of μ is considered with $\omega = 0.128$, and initial conditions $(V, A, C) = (0.3, 0.55, 0.8)$. The transition from the $(1, 2)$ periodic solution to the $(2, 4)$ periodic solution is as a result of period

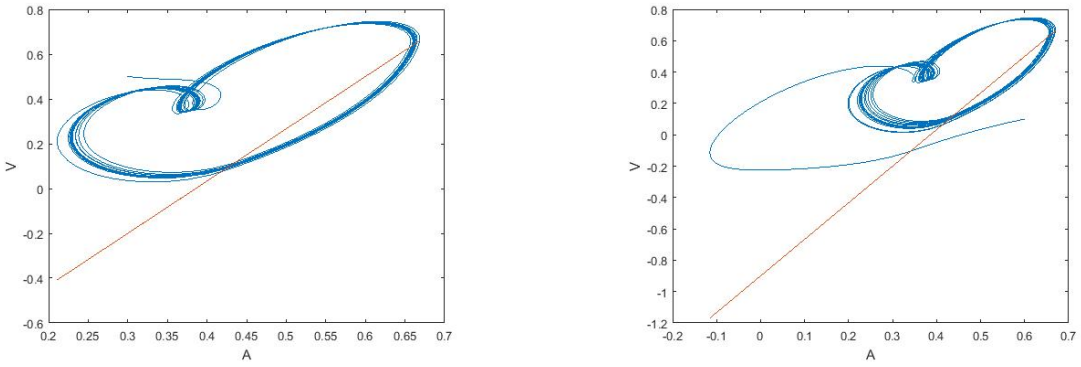

Figure 5-29: The phase plot showing different period $(1, 2)$ solutions with different initial conditions for left: $\omega = 0.126$ and right: $\mu = 0.467$

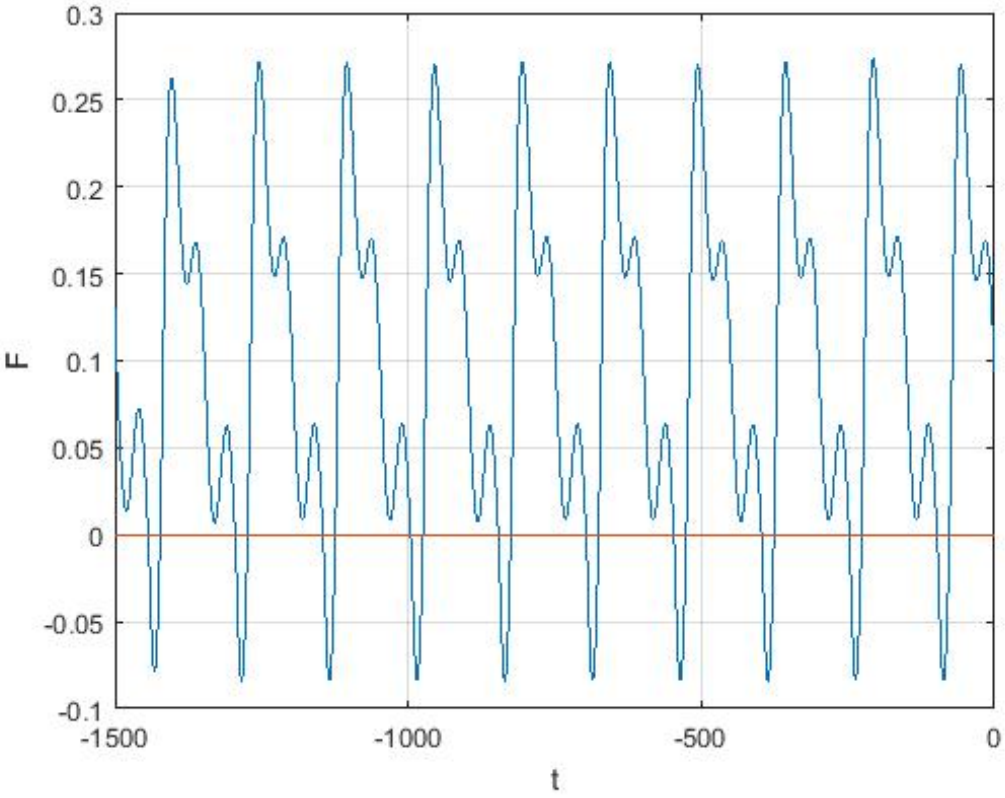

Figure 5-30: The time solution of the system showing a period $(1, 3)$ orbit of F for $\omega = 0.126$ and $\mu = 0.467$ for initial conditions $(V, A, C) = (0.7, 0.5, 0.2)$

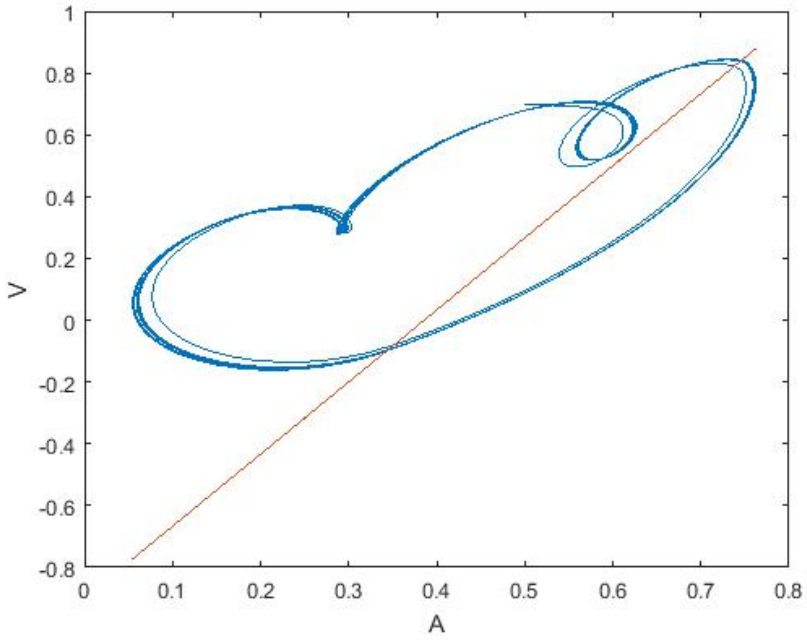

Figure 5-31: The phase plot V, A of the system showing a period $(1,3)$ orbit for $\omega = 0.126$ and $\mu = 0.467$ for initial conditions $(V, A, C) = (0.7, 0.5, 0.2)$

doubling that occurs at $\omega \approx 0.1275$. This solution is also consistent with what we expected.

However in Figure 5-31, we observe that there is possibility of the period $(1,3)$ orbit to interact with the discontinuity boundary if one of the parameters of the system say μ or ω are varied. When the periodic orbit interacts with the switching boundary, a *grazing bifurcation* is observed. We will do a detailed study of this transition in Chapter 7.

5.4.4 Existence and persistence of the $(1,3)$ orbit

A significant observation from these calculations under periodic forcing with the physically relevant values of $(\mu, \omega) = (0.467, 0.15)$ we see only a stable $(1,3)$ periodic orbit. This orbit has period $\frac{3*2\pi}{\omega} = 127.7kyr$ which is slightly longer than the observed period of $100kyr$. The $(1,3)$ orbit appears from our numerical calculations to be globally stable attracting flow for all initial conditions. An example of the system evolving towards this orbit is given in Figure 5-36.

This analysis has only been made for the case of *periodic forcing* and in practice the Milankovitch cycles introduce quasi-periodic forcing. However, the structural stability of the $(1,3)$ orbit constructed above means that this orbit persists, appropriately perturbed, when quasi-periodic forcing is introduced, with a small additional forcing at a different frequency. This motivates a detailed study of the quasi-periodic forced PP04 model which will be given in the next chapter.

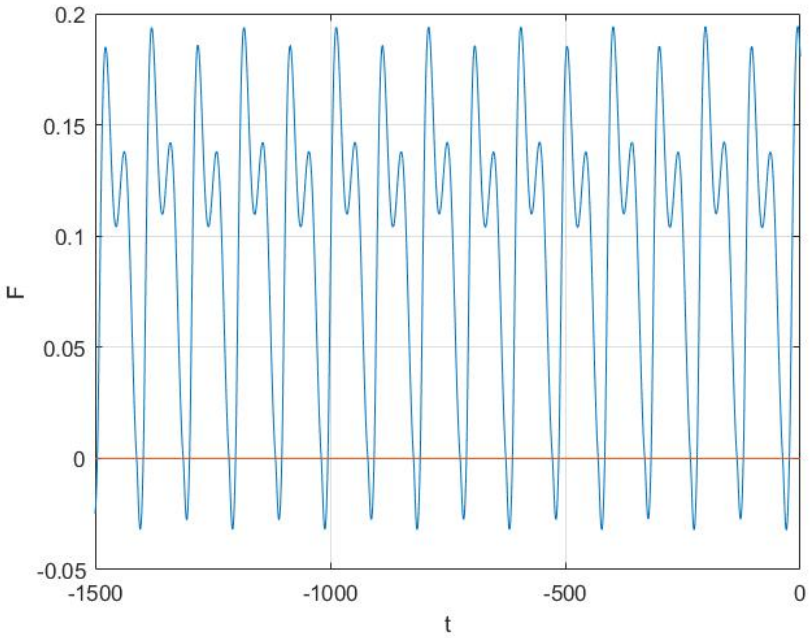

Figure 5-32: The time solution of the system showing a period $(2, 4)$ orbit of F which arises following the period doubling bifurcation from the (1,2) solution, for $\omega = 0.128$, $\mu = 0.467$ and initial conditions $(V, A, C) = (0.3, 0.55, 0.8)$.

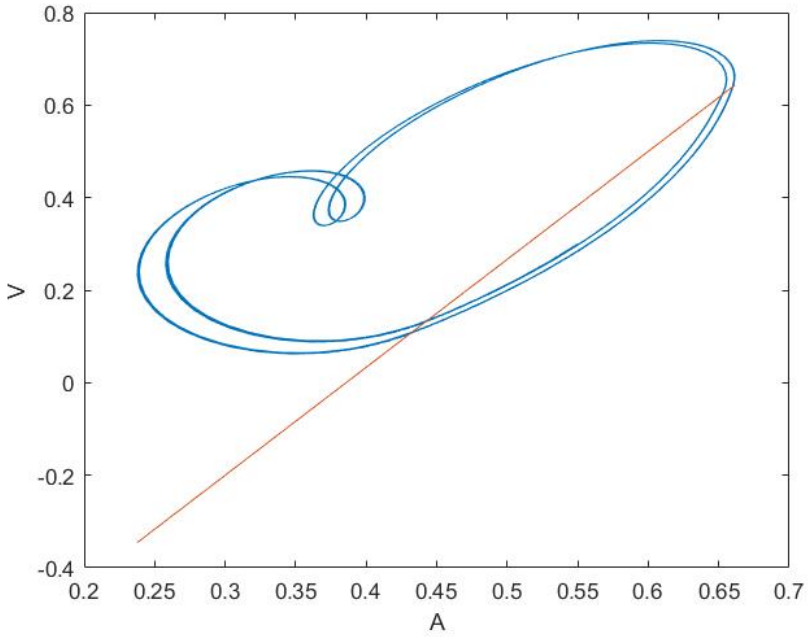

Figure 5-33: The phase plot showing period $(2, 4)$ solution for $\omega = 0.128$ and $\mu = 0.467$.

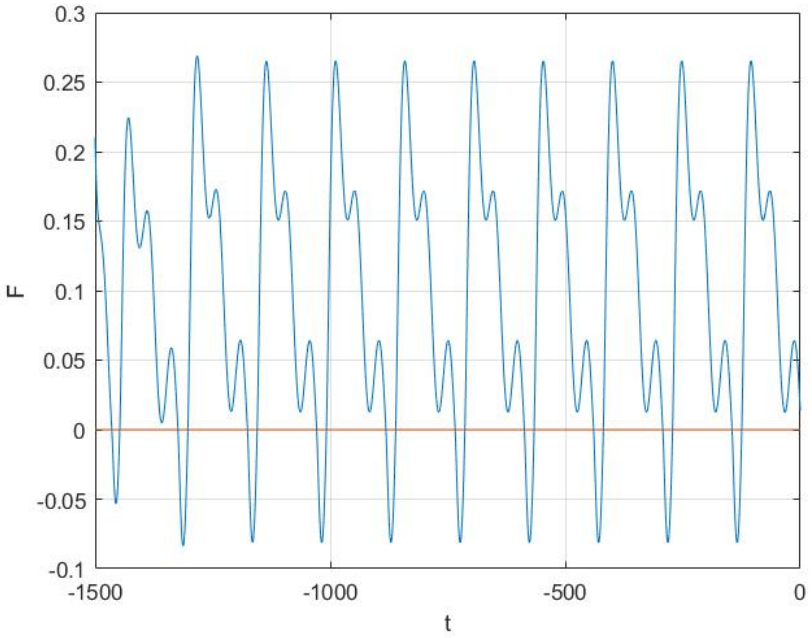

Figure 5-34: The time solution of the system showing a period $(1, 3)$ orbit of F for $\omega = 0.128$ and $\mu = 0.467$ for initial conditions $(V, A, C) = (0.5, 0.3, 0.4)$

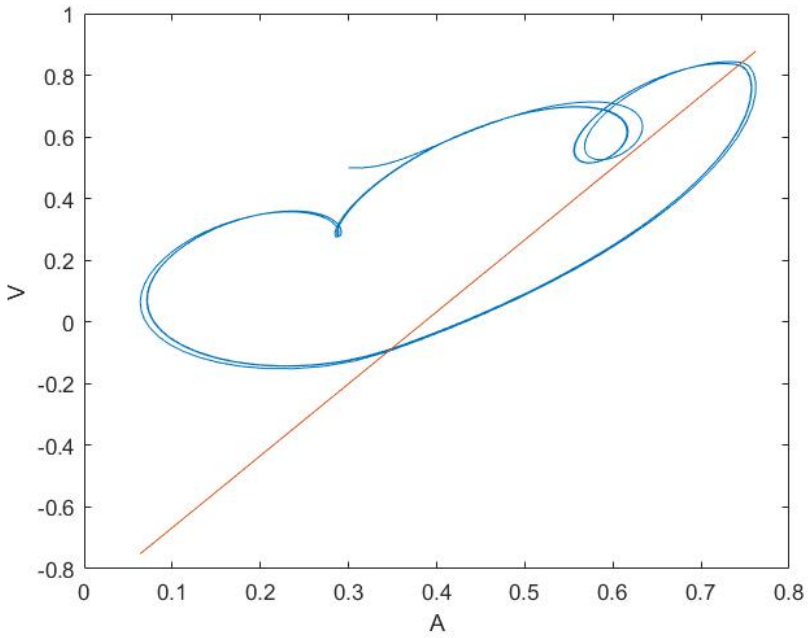

Figure 5-35: The phase plot showing period $(1, 3)$ solution for $\omega = 0.128,\ \mu = 0.467$

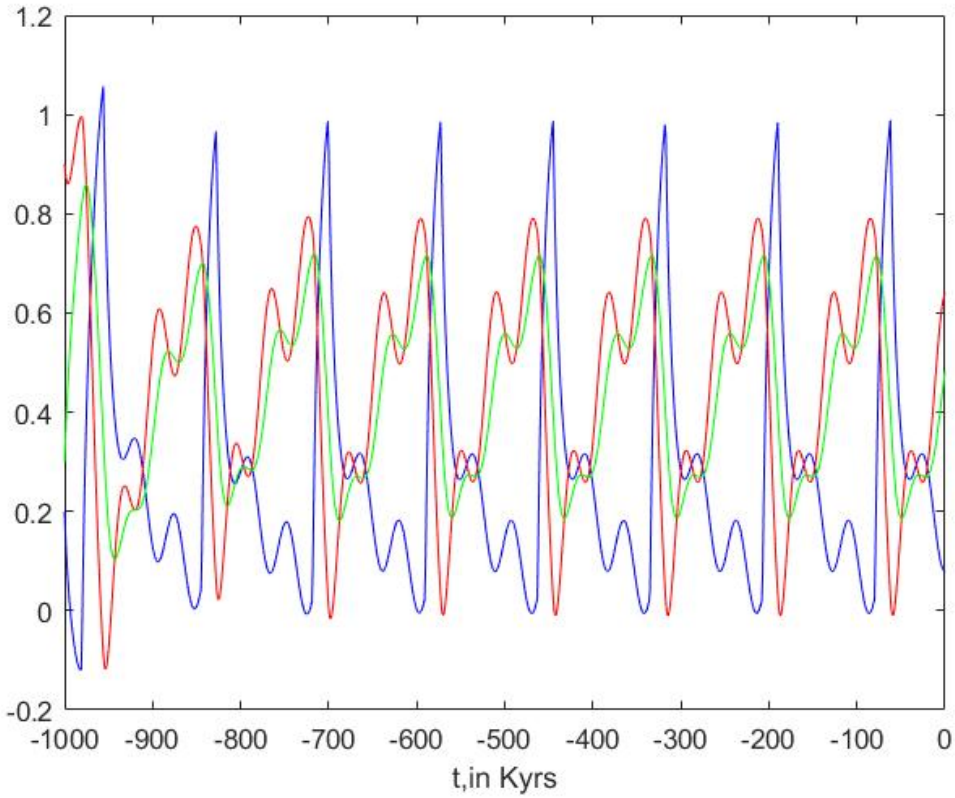

Figure 5-36: The time solution of the system when $(\mu, \omega) = (0.467, 0.1476)$ showing the evolution towards the $(1, 3)$ periodic solution.

5.5 Summary

In this chapter we have observed that the periodically forced PP04 model exhibits:

1. the existence of periodic solutions with a period of $127kyrs$.
2. the existence of periodic solutions with one or several glacial cycles between repeats.
3. the existence of a stable period $(1, 3)$ solution.
4. the existence of regions of synchronised periodic solution with their boundary determined by saddle node bifurcations.
5. the co-existence of multiple stable periodic.
6. Large amplitude of the forcing leads to loss of stability physicality of periodic solutions at grazing bifurcation.

Chapter 6

The quasi-periodically forced system

6.1 Overview

The original forcing of the PP04 model $I_{65}(t)$ is quasi-periodic with about $N = 35$ degrees of freedom and it is very challenging to do a thorough analysis using this forcing. Therefore this chapter studies the quasi-periodically forced PP04 model but with the simplified forcing

$$I_{65}(t) = \mu_1 \sin(\omega_1\, t) + \mu_2 \sin(\omega_2\, t)$$

considering two modes of the forcing or more. This allows us to investigate a more representative forcing model than the previous chapter, but still allows us to do some rigorous analysis.

In the previous chapter, we have found out that the periodically forced PP04 model has stable period $(1, 3)$ solutions. To extend this calculation we now study the quasi-periodically forced system as a perturbation of the periodically forced one, and the resulting orbit as an extension on the periodically forced system. The study of this system is to be done through the use of two maps, the linearised map and the stroboscopic map. The linearised map is used to study the perturbed periodic orbit if $\mu_2 \ll 1$ and to find the types of solutions observed for different ω_2. The stroboscopic map is be used to study the smoothed quasi-periodic system whereby the sampling time is considered $\tau = \frac{2\pi}{\omega_1}$ for different values of ω_2 and μ_2.

For the linear map we observed both the period k solutions, where k is dependent on the quotient $\frac{\omega_2}{\omega_1}$, and the existence of invariant curves. For the stroboscopic map, we observe the presence of the tori which break up as μ_2 is increased leading to a more complex behaviour e.g chaos.

6.2 Non-smooth quasi-periodic system

We consider the quasi-periodically forced PP04 model with simple two modes of insolation defined by

$$\dot{\mathbf{X}} = L\mathbf{X} + \mathbf{b}^{\pm} + \mathbf{e}_1\mu_1 \sin(\omega_1 t) + \mathbf{e}_2\mu_2 \sin(\omega_2 t), \tag{6.1}$$

To start the study of this system, we will consider the case when quasi-periodic forcing is small, that is when the values of μ_2 are small. We study this system by deriving approximate Poincaré map obtained by linearising about the periodic solution constructed in the earlier section when $\mu_2 = 0$

6.2.1 Derivation of a linearised map if $\mu_2 \ll 1$

To construct this map, we start by assuming that when $\mu_2 = 0$ the equation (6.1) has a stable period (m, n) solution of period nT. For example the $(1, 3)$ solution we found in the previous chapter, with period $T = \frac{2\pi}{\omega_1}$. Then we consider a case where μ_2 is very small i.e $\mu_2 \ll 1$ and seek a perturbation of the periodic orbit.

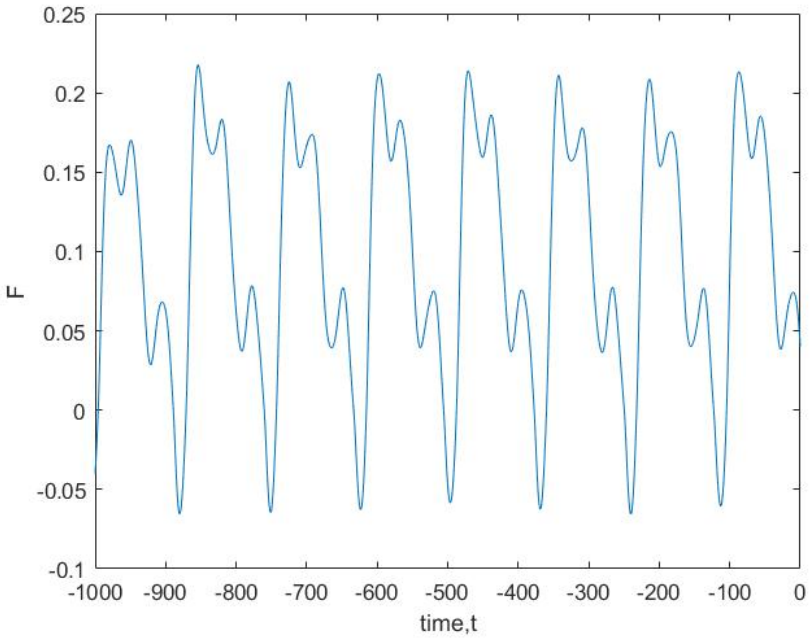

Figure 6-1: The solution as a function of time showing the $(1, 3)$ periodic solution for $\mu_1 = 0.467$, $\omega_1 = 0.1476$ and $\mu_2 = 0.1$, $\omega_2 = 0.331$.

In Figure 6-1, we take $\mu_2 = 0$, and observe a periodic orbit which intersects the discontinuity boundary, in particular the $(1, 3)$ periodic solution. Therefore the dynamics at the discontinuity boundary Σ will take the form illustrated in Figure

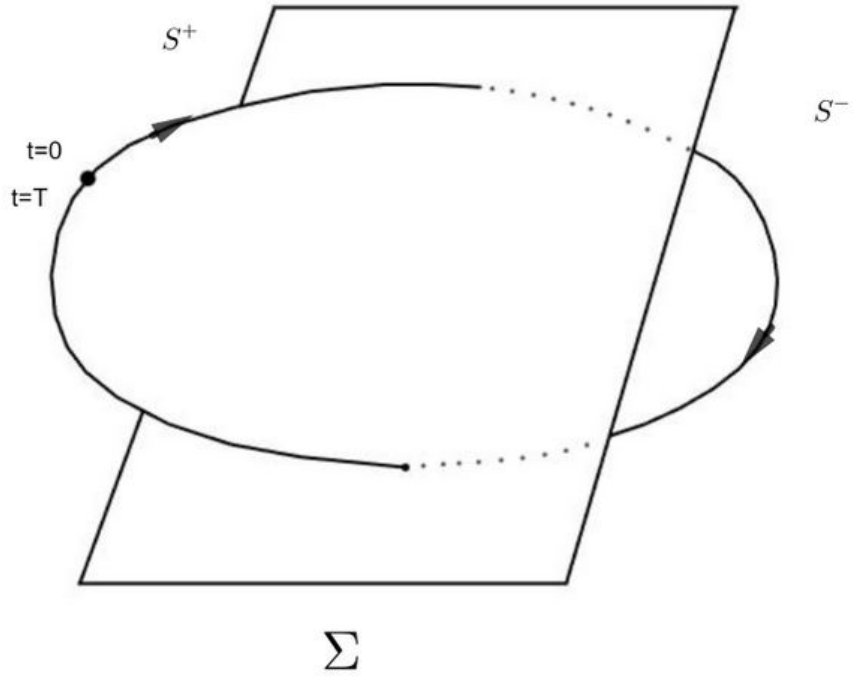

Figure 6-2: The graph showing the trajectory of the periodic orbit of the system with $\mu_2 = 0$ showing two intersections with Σ.

6-2. Now we let $\mu \ll 1$ and consider the Poincaré map of the system (6.1) the form

$$P : \mathbf{X}(t) \to \mathbf{X}(t+T) \tag{6.2}$$

where $T = \frac{2\pi\, n}{\omega_1}$ with $\mathbf{X}_k = \mathbf{X}(k\, T)$. Suppose that the periodic orbit is $\mathbf{X}^*(t)$ so that

$$\mathbf{X}^*(t_0) = \mathbf{X}^*(t_0 + \ T) = \mathbf{X}^*(t_0 + 2\ T) = \mathbf{X}^*(t_0 + 3\ T) = \cdots \tag{6.3}$$

Without loss of generality we take $t_0 = 0$. We assume that this periodic solution is stable so that if $\mu_2 = 0$ and $\mathbf{X}(t_0) = \mathbf{X}^*(t_0) + \mathbf{x}(t_0)$ with $\mathbf{x}(t_0)$ small, then

$$\mathbf{X}(t_0 + T) = \mathbf{X}^*(t_0 + T) + A\mathbf{x}(t_0 + T) \tag{6.4}$$

where A is a stability(contraction) matrix. That is, all eigenvalues of A are less than one in modulus. We will show that the map can be linearised about the periodic orbit and

Lemma 6.1 *Linearised form is*

$$\mathbf{X}(n+1) = A\ \mathbf{X}(n) + \mathbf{a}\ \cos(\omega_2 n\ T) + \mathbf{b}\ \sin(\omega_2 n T). \tag{6.5}$$

We will do this by perturbing the periodic orbit. This involves two calculations

(i) perturbation away from the intersections with Σ

(ii) perturbation of the intersection with Σ.

Proof
We consider the case where μ_2 is small in the equation (6.1) and the discontinuity surface $\Sigma = F(\mathbf{X}) = 0$.

The particular integral of the system (6.1) is given by

$$\mathbf{X}^{\pm}_{PI}(t) = \mathbf{Z}^{\pm} + \mu_1\ \mathbf{a}_1\ \cos(\omega_1 t) + \mu_1\ \mathbf{b}_1\ \sin(\omega_1 t) + \mu_2\ \mathbf{a}_2\ \cos(\omega_1 t) + \mu_2\ \mathbf{b}_2\ \sin(\omega_2 t), \tag{6.6}$$

it follows from (6.1) that

$$\begin{aligned}\dot{\mathbf{X}} = -\mu_1\ \mathbf{a}_1\ \omega_1\ \sin(\omega_1 t) + \mu_1\ \mathbf{b}_1\omega_1\ \cos(\omega_1 t) - \mu_2\ \mathbf{a}_2\ \omega_2\ \sin(\omega_2 t) + \\ \mu_2\ \mathbf{b}_2\ \omega_2\ \cos(\omega_2 t).\end{aligned} \tag{6.7}$$

When comparing the coefficients of (6.1) and (6.7) it gives the following vectors

$$\begin{aligned}\mathbf{Z}^{\pm} = -L^{-1}\mathbf{b}^{\pm}, \quad \mathbf{a}_1 = -(L^2 + {\omega_1}^2 I)^{-1}\ \mathbf{e}_1, \quad \mathbf{b}_1 = \frac{-(L^2 + {\omega_1}^2 I)^{-1}\ L\ \mathbf{e}_1}{\omega_1} \\ \mathbf{a}_2 = -(L^2 + \omega_2^2 I)^{-1}\ \mathbf{e}_2, \quad \mathbf{b}_2 = \frac{-(L^2 + \omega_2^2 I)^{-1}\ L\ \mathbf{e}_2}{\omega_2}.\end{aligned} \tag{6.8}$$

Then we obtain the following general solution of this system in each region given by

$$\begin{aligned}\mathbf{X}(t) = e^{L(t-t_i)}\left(\mathbf{X}(t_i) - L^{-1}\mathbf{b}^{\pm} - \mu_1\ \mathbf{a}_1\ \cos(\omega_1 t_i) - \mu_1\ \mathbf{b}_1\ \sin(\omega_1 t_i)\right) \\ -\mu_2\ \mathbf{a}_2\ e^{L(t-t_i)}\cos(\omega_2 t_i) - \mu_2\ e^{L(t-t_i)}\ \mathbf{b}_2\ \sin(\omega_2 t_i) - L^{-1}\mathbf{b}^{\pm} + \mu_1\mathbf{a}_1\ \cos(\omega_1 t) \\ +\mu_1\mathbf{b}_1\ \sin(\omega_1 t) + \mu_2\left(\mathbf{a}_2\ \cos(\omega_2 t) + \mathbf{b}_2\ \sin(\omega_2 t)\right)\end{aligned} \tag{6.9}$$

where the orbit intersects the discontinuity boundary at times $\mathbf{X}(t_i) = \mathbf{X}(t_1) = \mathbf{X}(t_2)\cdots$.

Now we let

$$\mathbf{X}(t_0) = \mathbf{X}^*(t_0) + \mathbf{x}(t_0) \tag{6.10}$$

where $\mathbf{x}$ is small. Then it follows from (6.9), that before the trajectory hits the discontinuity boundary we have

$$\begin{aligned}\mathbf{X}(t) = \mathbf{X}^*(t) + e^{L(t-t_0)}\mathbf{x}(t_0) - e^{L(t-t_0)}L^{-1}\mathbf{b}^{+} - \mu_1\ e^{L(t-t_0)}\mathbf{a}_1\ \cos(\omega_1 t_0) \\ -e^{L(t-t_0)}\mathbf{b}_1\ \sin(\omega_1 t_0) - \mu_2\ e^{L(t-t_0)}\left(\mathbf{a}_2\ \cos(\omega_2 t_0) + \ \mathbf{b}_2\ \sin(\omega_2 t_0)\right) \\ -L^{-1}\mathbf{b}^{+} + \mu_1\left(\mathbf{a}_1\ \cos(\omega_1 t) + \mathbf{b}_1\ \sin(\omega_1 t)\right) \\ +\mu_2\left(\mathbf{a}_2\ \cos(\omega_2 t) + \mathbf{b}_2\ \sin(\omega_2 t)\right).\end{aligned} \tag{6.11}$$

This can be written as

$$\begin{aligned}\mathbf{X}(t) = \mathbf{X}^*(t) + e^{L(t-t_0)}\mathbf{x}(t_0) - \mu_2\, e^{L(t-t_0)}\,(\mathbf{a}_2\ \cos(\omega_2 t_0) + \ \mathbf{b}_2\ \sin(\omega_2 t_0)) \\ +\mu_2\,(\mathbf{a}_2\ \cos(\omega_2 t) + \mathbf{b}_2\ \sin(\omega_2 t))\,.\end{aligned} \tag{6.12}$$

Equation (6.12) is simplified and represented as

$$\mathbf{X}(t) \equiv \mathbf{X}^*(t) + \mathbf{x}(t)$$

where $\mathbf{x}(t)$ is small. Now we assume that we hit the discontinuity boundary Σ at time t_1 with the periodic orbit $\mathbf{X}^*$. That is,

$$F(\mathbf{X}^*(t_1)) = 0$$

Then we can find the time $t_1+\delta$ when the perturbed orbit $\mathbf{X}^*+\mathbf{x}$ hits the discontinuity boundary Σ. To do this we solve

$$F(\mathbf{X}(t_1+\delta)) = 0$$

so that

$$\mathbf{c}\cdot(\mathbf{X}^* + \mathbf{x}) + d = 0.$$

Therefore we have to leading order

$$\begin{aligned} F(\mathbf{X}(t_1+\delta)) &= F(\mathbf{X}^*(t_1 + \ \delta) + \ \mathbf{x}(t_1+\delta)), \\ F(\mathbf{X}(t_1+\delta)) &= F(\mathbf{X}^*(t_1) + \delta X^{*'} + \mathbf{x}(t_1) + \delta \mathbf{x}'(t_1)) + H.O.T, \\ F(\mathbf{X}(t_1+\delta)) &= F(\mathbf{X}^*(t_1)) + \delta \mathbf{X}^{*'}(t_1)F'(\mathbf{X}^*(t_1)) + \mathbf{x}(t_1)F'(\mathbf{X}^*(t_1)) + H.O.T \end{aligned}$$

and it follows that

$$\delta = \frac{-\mathbf{x}(t_1)F_x(\mathbf{X}^*(t_1))}{\mathbf{X}^{*'}(t_1)F_x(\mathbf{X}^*(t_1))}$$

or equivalently

$$\delta = \frac{-\mathbf{c}\cdot\mathbf{x}}{\mathbf{c}\cdot\frac{d\mathbf{X}^*}{dt}}$$

which is well defined and $\mathbf{x}(t_1)$ a function of μ_2 as observed from (6.12). The intersection with the discontinuity boundary Σ is then at

$$\mathbf{X}^*(t_1) + \delta\frac{d\mathbf{X}^*}{dt}(t_1) + \mathbf{x}(t_1)$$

to leading order. So the perturbed orbit hit the discontinuity boundary Σ close to t_1, it then continues hitting the switching boundary again before returning at time $t_0 + T$ (see Figure 6-3).

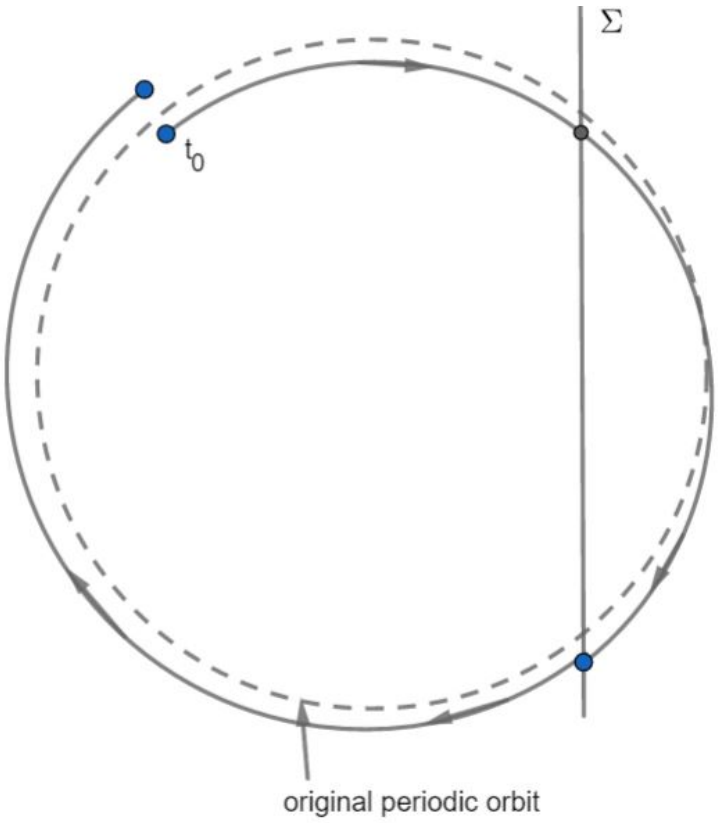

Figure 6-3: The schematic diagram showing the trajectory of the perturbed periodic orbit.

We now look at where the orbit has got to at the time $t_0 + T$. It follows from the stability and equation (6.12) that the orbit $\mathbf{X}(t_0 + T)$ is mapped into

$$\begin{aligned}\mathbf{X}^*(t_0) + A\,\mathbf{x}(t_0) - \mu_2\, e^{LT}\,(\mathbf{a}_2\ \cos(\omega_2 t_0) + \ \mathbf{b}_2\ \sin(\omega_2 t_0))\\ +\mu_2\,(\mathbf{a}_2\ \cos(\omega_2(t_0+T)) + \mathbf{b}_2\ \sin(\omega_2(t_0+T))) + H.O.T\end{aligned}$$

where A is the linearisation of the return map about the periodic solution. However the matrix A is hard to compute analytically because it involves calculating the intersection of the periodic orbit with the discontinuity boundary.

Thus the original perturbation $\mathbf{x}(t_0)$ mapping is simplified to

$$\begin{aligned}A\mathbf{x}(t_0) + \mu_2\,(\mathbf{a}_2\ \cos(\omega_2(t_0\ +\ T)) + \mathbf{b}_2\ \sin(\omega_2(t_0+T))) - \mu_2 e^{LT}\mathbf{a}_2\cos(\omega_2\ t_0) -\\ \mu_2 e^{LT}\ \mathbf{b}_2\sin(\omega_2\ t_0)\end{aligned}$$

and higher order terms are ignored and the contribution of μ_2 is to leading order. When expanding μ_2 term about t_0 we obtain

$$\begin{aligned}-\ e^{LT}\ \mu_2\,(\mathbf{a}_2\ \cos(\omega_2 t_0) + \mathbf{b}_2\ \sin(\omega_2 t_0)) + \ \ \mathbf{a}_2\ \mu_2\left(\cos(\omega_2 t_0) - \omega_2^2\ T\sin(\omega_2 t_0)\right)\\ +\ \mathbf{b}_2\ \mu_2\left(\sin(\omega_2 t_0) + {\omega_2}^2\ T\ \cos(\omega_2 t_0)\right) + H.O.T\end{aligned}$$

And simplified to

$$\mu_2 \ (\mathbf{c}_1 \ \cos(\omega_2 t_0) + \ \mathbf{c}_2 \ \sin(\omega_2 t_0))$$

for vectors $\mathbf{c}_1$ and $\mathbf{c}_2$ defined $\mathbf{c}_1 = e^{LT}\mathbf{a}_2 + \mathbf{a}_2 + \omega_2^2 T \ \mathbf{b}_2$ and $\mathbf{c}_2 = -e^{LT}\mathbf{b}_2 + \mathbf{b}_2 - \omega_2^2 T \ \mathbf{a}_2$. So if we start at time t_0 and orbit for T then

$$\mathbf{X}^*(t_0) + \mathbf{x}(t_0) \to \mathbf{X}^*(t_0) + A\mathbf{x}(t_0) + \mu_2 \ (\mathbf{c}_1 \ \cos(\omega_2 t_0) + \ \mathbf{c}_2 \ \sin(\omega_2 t_0)) \, .$$

Without loss of generality when we take $t_0 = 0$ for the first orbit, we then have $t_0 = T, \ t_0 = 2T, \ \cdots$. That is, $t_0 = n \ T$ for subsequent orbits. We deduce that if $\mathbf{X}_n \equiv \mathbf{x}(n \ T)$ then the linearised map takes the form

$$\mathbf{x}(n+1) = A \ \mathbf{x}(n) + \mu_2 \, (\mathbf{c}_1 \ \cos(\omega_2 n \ T) + \mathbf{c}_2 \ \sin(\omega_2 n T)) \, . \tag{6.13}$$

So we derived the approximate map

$$\mathbf{x}(n+1) = A \ \mathbf{x}(n) + \mu_2 \, (\mathbf{c}_1 \ \cos(\omega_2 n \ T) + \mathbf{c}_2 \ \sin(\omega_2 n T)) \, . \tag{6.14}$$

stated in the lemma (6.1) where $T = \frac{2\pi}{\omega_1}$. □

We now study the map.

6.2.2 Calculations of the dynamics of the linearised map

In order to determine the types of solutions to be expected, we consider the general case. That is, we take the map

$$\mathbf{x}(n+1) = A \ \mathbf{x}(n) + \mathbf{e}_1 \ \cos(\omega_2 n \ T) + \mathbf{e}_2 \ \sin(\omega_2 n T) \tag{6.15}$$

where $\mathbf{x}(n)$ is a vector and consider a solution of the from

$$\mathbf{x}(n) = \mathbf{p} \ \cos(\omega_2 n \ T) + \mathbf{q} \ \sin(\omega_2 n T). \tag{6.16}$$

When substituting (6.16) into equation (6.15) we have

$$\begin{aligned} \mathbf{p} \ \cos(\omega_2 (n+1) \ T) + \mathbf{q} \ \sin(\omega_2 (n+1) T) = A\mathbf{p} \ \cos(\omega_2 n \ T) + A\mathbf{q} \ \sin(\omega_2 n T) \\ + \mathbf{e}_1 \ \cos(\omega_2 n \ T) + \mathbf{e}_2 \ \sin(\omega_2 n T) \end{aligned}$$

$$\begin{aligned} \mathbf{p} \ \cos(\omega_2 \ n \ T + \omega_2 \ T) + \mathbf{q} \ \sin(\omega_2 n \ T + \omega_2 \ T) = A\mathbf{p} \ \cos(\omega_2 n \ T) + A\mathbf{q} \ \sin(\omega_2 n T) \\ + \mathbf{e}_1 \ \cos(\omega_2 n \ T) + \mathbf{e}_2 \ \sin(\omega_2 n T) \end{aligned}$$

which simplifies to

$$\begin{aligned}\mathbf{p}\ \cos(\omega_2\ n\ T)\cos(\omega_2\ T) - \mathbf{p}\ \sin(\omega_2\ n\ T)\sin(\omega_2\ T) + \mathbf{q}\ \sin(\omega_2 n\ T)\ \sin(\omega_2\ T) + \\ \mathbf{q}\cos(\omega_2\ n\ T)\cos(\omega_2\ T) \\ = A\mathbf{p}\ \cos(\omega_2 n\ T) + A\mathbf{q}\ \sin(\omega_2 nT) + \mathbf{e}_1\ \cos(\omega_2 n\ T) + \mathbf{e}_2\ \sin(\omega_2 nT).\end{aligned}$$

Comparing coefficients in $\cos(\omega_2 n\ T)$ and $\sin(\omega_2 n\ T)$ we have

$$\begin{aligned}\mathbf{p}\ \cos(\omega_2\ n\ T)\cos(\omega_2\ T) - A\mathbf{p}\ \cos(\omega_2 n\ T) + \mathbf{q}\cos(\omega_2\ n\ T)\cos(\omega_2\ T) \\ = \mathbf{e}_1\ \cos(\omega_2 n\ T)\end{aligned}$$

and

$$\begin{aligned}\mathbf{q}\sin(\omega_2 n\ T)\ \sin(\omega_2\ T) + \ -A\mathbf{q}\sin(\omega_2 nT) - \mathbf{p}\sin(\omega_2\ n\ T)\sin(\omega_2\ T) \\ = \mathbf{e}_2\ \sin(\omega_2 nT).\end{aligned}$$

Thus we have

$$\mathbf{p}\cos(\omega_2\ T) - A\mathbf{p}\ + \mathbf{q}\cos(\omega_2\ T) = \mathbf{e}_1$$

and

$$\mathbf{q}\ \sin(\omega_2\ T) - A\mathbf{q}\ - \mathbf{p}\sin(\omega_2\ T) = \mathbf{e}_2.$$

Hence we obtain

$$\mathbf{q} = \frac{\mathbf{e}_1 + A\mathbf{p} - \mathbf{p}\ \cos(\omega_2\ T)}{\cos(\omega_2\ T)}$$

and similarly

$$\mathbf{p} = \frac{\mathbf{e}_2 + A\mathbf{q} - \mathbf{q}\sin(\omega_2\ T)}{-\sin(\omega_2\ T)}$$

which gives the following expressions

$$\mathbf{p} = \frac{\mathbf{e}_1\ \sin(\omega_2\ T) - A\mathbf{e}_1 - \mathbf{e}_2\cos(\omega_2\ T)}{A^2\ + 2\sin(\omega_2\ T)\cos(\omega_2\ T) - A\ \sin(\omega_2\ T) - A\cos(\omega_2\ T)}$$

and

$$\mathbf{q} = \frac{\mathbf{e}_1\ \sin(\omega_2\ T) - A\mathbf{e}_2 + \mathbf{e}_2\cos(\omega_2\ T)}{A^2\ + 2\sin(\omega_2\ T)\cos(\omega_2\ T) - A\sin(\omega_2\ T) - A\ \cos(\omega_2\ T)}.$$

The solution of the linearised map can therefore be represented as

$$\mathbf{x}(n) = A^n\ C + \mathbf{p}\ \cos(\omega_2 n\ T) + \mathbf{q}\ \sin(\omega_2 nT) \tag{6.17}$$

where C is an arbitrary constant.

Corollary 6.2 *The $\Omega-$limit set of the linearised equation is*

(i) *an ellipse if $\omega_2 \times \frac{T}{2\pi}$ is irrational.*

(ii) discrete points if $\omega_2 \times \frac{T}{2\pi}$ is rational.

To illustrate this we take the special $2D$ case of $\mathbf{x} = \begin{bmatrix} x \\ y \end{bmatrix}$ and

$$x(n+1) = \lambda\ x(n) + \mu_2 \cos(\omega_2\ n\ T), \tag{6.18}$$

$$y(n+1) = \lambda\ y(n) + \mu_2 \sin(\omega_2\ n\ T), \tag{6.19}$$

Given if $z(n+1) = x(n) + i\ y(n)$ we have

$$z(n+1) = \lambda\ z(n) + \mu_2\ \exp(i\ \omega_2\ n\ T). \tag{6.20}$$

We can then find a solution quickly . If

$$\mathbf{z}(n) = a \exp(i\ \omega_2\ n\ T)$$

where a is a complex number of the form $r \exp(i\ \psi)$. Then we have

$$\begin{aligned} a \exp(i\ \omega_2(n+1)\ T) = \lambda\ a \exp(i\ \omega_2\ n\ T + \mu_2 a \exp(i\ \omega_2\ n\ T) \\ a \exp(i\ \omega_2\ T) = \lambda\ a + \mu_2 \\ a = \frac{\mu_2}{\exp(i\ \omega_2\ T) - \lambda}. \end{aligned}$$

We have $r = |a|$, so that r is the radius of the invariant curve. Then the general solution of (6.20) is

$$\mathbf{z}(n) = \lambda^n\ C + a \exp(i\ \omega_2\ n\ T) \tag{6.21}$$

where C is an arbitrary constant. We observe that for $\lambda < 1$ the first term decays to zero leaving the invariant curve.

Now the linear map is studied to find its solutions.

6.2.3 Solutions of the linear map

In order to study the map numerically, we need to calculate the stability matrix A. To find this matrix, we start by picking a point away from the discontinuity surface Σ and using it as an initial condition in the Matlab solver solving the smoothed periodic forced PP04 system for fixed value of μ_1 and ω_1. The solver is then run a number of times until we get an equilibrium point. Then the equilibrium point is perturbed and the resulting value is taken as the initial condition for the solver which is ran only once. The value of the equilibrium point is then subtracted from the new value obtained, then the difference is divided by the perturbation value to find the elements of the matrix A. The eigenvalues of the matrix A are then calculated, because both the eigenvalues and matrix A give us the information as to how each component of the model is affected by the perturbation. The eigenvalues of matrix A, are all observed to be always less than one.

For an example, if we consider $\mu_1 = 0.3$ and $\omega_1 = 0.1558$ we observe that the periodically forced PP04 system gives a physical period $(1, 3)$ solution (see Figure 6-4). We define X^* to be the point on the periodic orbit at a start time t_0 chosen such that the periodic orbit at this point is not close to the discontinuity surface. The point is then used as an initial condition on the smoothed periodic system and the system is solved numerically for a number of cycles until we obtain an stable equilibrium point. The stable equilibrium point is a point that lie on the periodic solution and is then perturbed using the vectors

$$\mathbf{e}_1 = \begin{pmatrix} 1 \\ 0 \\ 0 \end{pmatrix}, \quad \mathbf{e}_2 = \begin{pmatrix} 0 \\ 1 \\ 0 \end{pmatrix}, \quad \mathbf{e}_3 = \begin{pmatrix} 0 \\ 0 \\ 1 \end{pmatrix}.$$

The new value $\mathbf{X}_{in} = \mathbf{X}^* + \epsilon\, \mathbf{e}_i$ is then used as an initial condition for the Matlab solver, and the trajectory starting from $\mathbf{X}_{in}$ simulated for only one cycle $t_0 \to t_0 +$ Period (where Period is the period of the periodic orbit). We set $\mathbf{X}_{new} = \mathbf{X}(t_0 + Period) = P(\mathbf{X}_{in})$. The components of the column of the matrix A corresponding to $\mathbf{e}_i$ are found by dividing the difference $\mathbf{X}_{new} - \mathbf{X}^*$ by ϵ. For $\omega_1 = 0.1558$, and $\mu_1 = 0.3$ with initial time $t = 25$ we find the equilibrium point $\mathbf{X}(t = 25) \equiv \mathbf{X}^* = \begin{pmatrix} 0.1 \\ 0.4 \\ 0.9 \end{pmatrix}$ a point on the periodic solution $\mathbf{X}(t) = (V, A, C)^T$ which when perturbed gave

$$A = \begin{bmatrix} -0.7894 & -0.4977 & -0.7608 \\ 3.2029 & 1.9347 & -1.3238 \\ 0.3367 & 0.2086 & 0.1207 \end{bmatrix}$$

with eigenvalues

$$\begin{pmatrix} -0.6335 + 0.5808i \\ 0.6335 - 0.5808i \\ -0.0011 + 0.0000i \end{pmatrix}.$$

We could observe that the modulus of eigenvalues of this matrix are less than one therefore the first term of the map will decay to zero leaving the invariant curve as the $\omega-$ limit set.

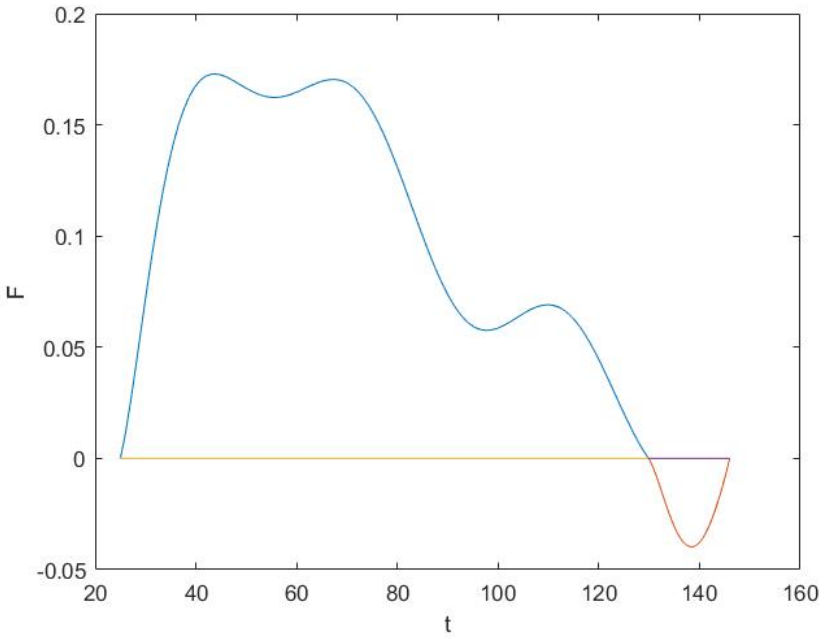

Figure 6-4: The graph showing a physical period $(1, 3)$ solution of the periodically forced PP04 model with $\mu_1 = 0.3$ and $\omega_1 = 0.1558$. The blue part of the orbit represents the solution $F(\mathbf{X})$ of the PP04 model obtained for when the amount of Carbon Dioxide in the system is increased, that is the glacial climatic state. The yellow line represent the state when the stratification parameter of the ocean has reached the threshold value for Carbon Dioxide to be released or when $F(\mathbf{X}) = 0$. The red orbit represent the solution of the quasi-periodically PP04 model when carbon is absorbed by the ocean.

The matrix A is then substituted into the linear map (6.14) and the map is evaluated numerically to get the next iterated point. In Figure 6-5 and Figure 6-6, we observe that if we start anywhere in the phase space and considering $\mu_2 = 0$, the trajectory of the iterated points of the linear map will eventually settles or decays to the stable periodic solution after about forty iterations . We now study the linear map taking $\mu_2 \ll 1$ with rational and irrational values of $\omega_2\, T$.

In Figure 6-7, we observe that for random initial values with $\mu_2 = 0.2$ and $\omega_2 = 1.6 \times \omega_1$ which implies that $\omega_2 T = \frac{16\pi}{5}$ a rational multiple of π, the linear map exhibits a period five cycle solution. In Figure 6-8, with the same random initial conditions with $\mu_2 = 0.6$ and $\omega_2 = 1.5 \times \omega_1$ where $\omega_2 T = \frac{3\pi}{2}$, we observe a period two cycle

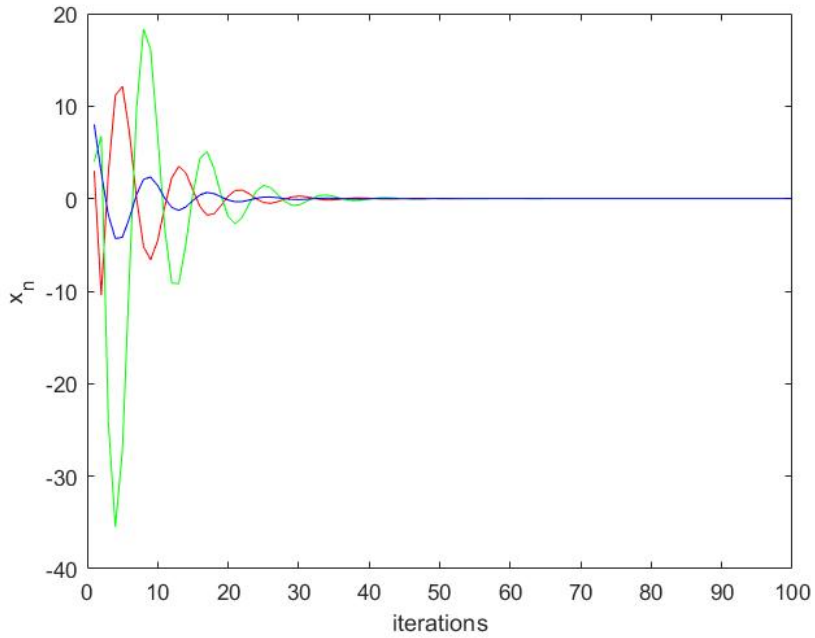

Figure 6-5: The graph showing the change in the iterated value of $\mathbf{x}_n$ of the linear map (6.14) with $\mu_2 = 0$ and $\omega_1 = 0.1558$. The red curve represents $\mathbf{x}_n(1)$, green curve represents $\mathbf{x}_n(2)$ and blue curve represents $\mathbf{x}_n(3)$.

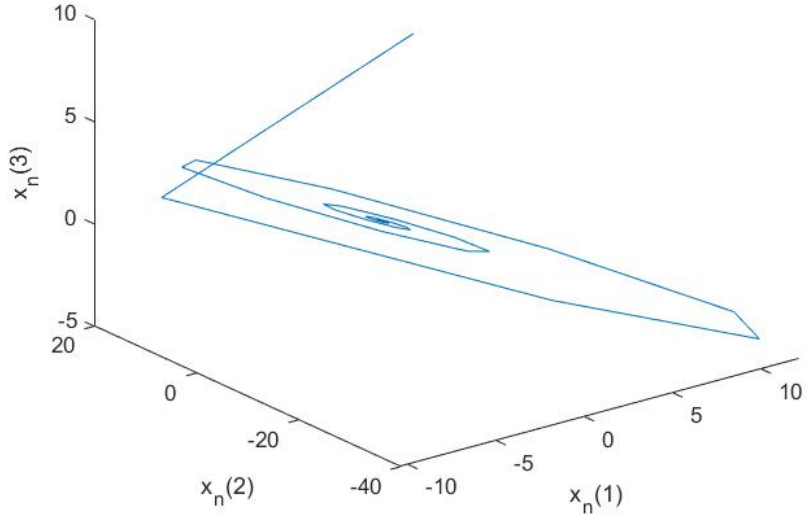

Figure 6-6: The graph showing the phase plane changes of the iterated points of the linear map (6.14) until it settles into a point in the periodic orbit for $\mu_2 = 0$ and $\omega_1 = 0.1558$.

solution of the linear map.

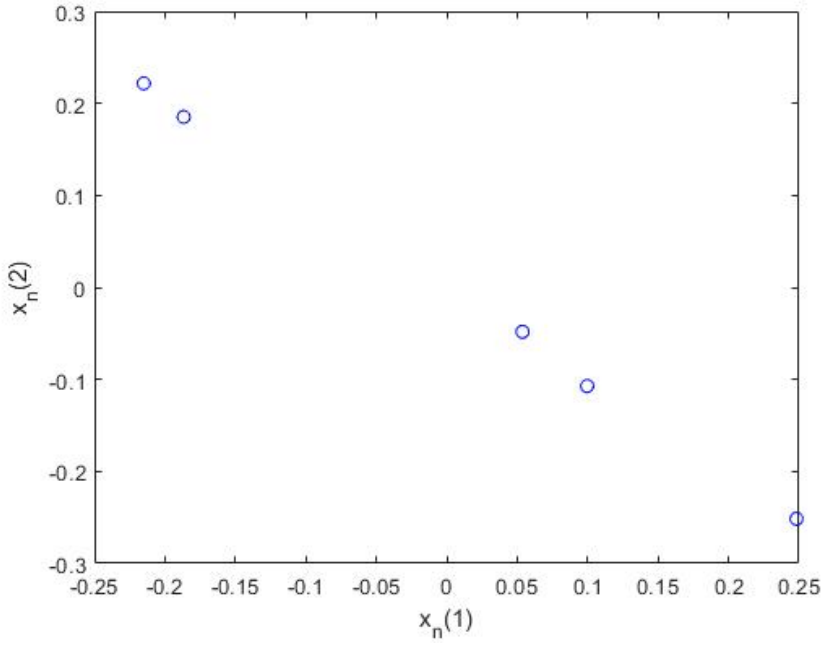

Figure 6-7: The stroboscopic Omega-limit set of the linear map (6.14) showing the period 5 cycle when $\mu = 0.2$, $\omega_1 = 0.1558$ and $\omega_2 = 1.6 \times \omega_1$ and this gives $\frac{\omega_2}{\omega_1} = \frac{8}{5}$

In Figure 6-9 and Figure 6-10, we observe that if we have $\omega_2 = 1.6180339888 \times \omega_1$ which gives $\omega_2\, T$ as an irrational multiple of π, invariant curves are solutions of the linear map. The size of the invariant curve are observed to be dependent on the value of μ_2 and hence can be expressed in terms of μ_2. These solutions observed are consistent with the theory of nonlinear systems, stating that the introduction of an external force on incommensurate frequency leads to complicating the dynamics with fixed points in maps becoming invariant curves [64].

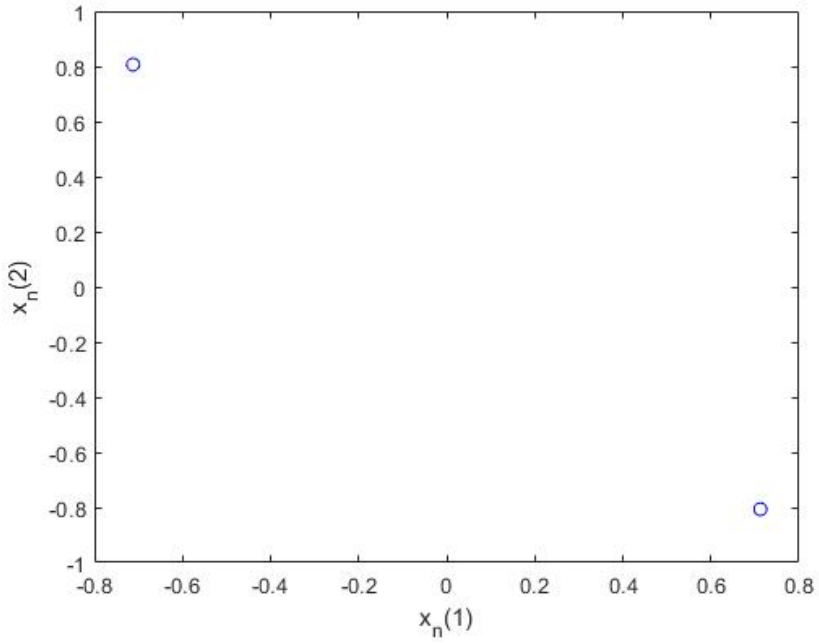

Figure 6-8: The stroboscopic Omega limit set of the linear map (6.14) showing the period 2 cycles solution when $\mu = 0.6$, $\omega_1 = 0.1558$ and $\omega_2 = 1.5 \times \omega_1$ and this gives $\frac{\omega_2}{\omega_1} = \frac{3}{2}$

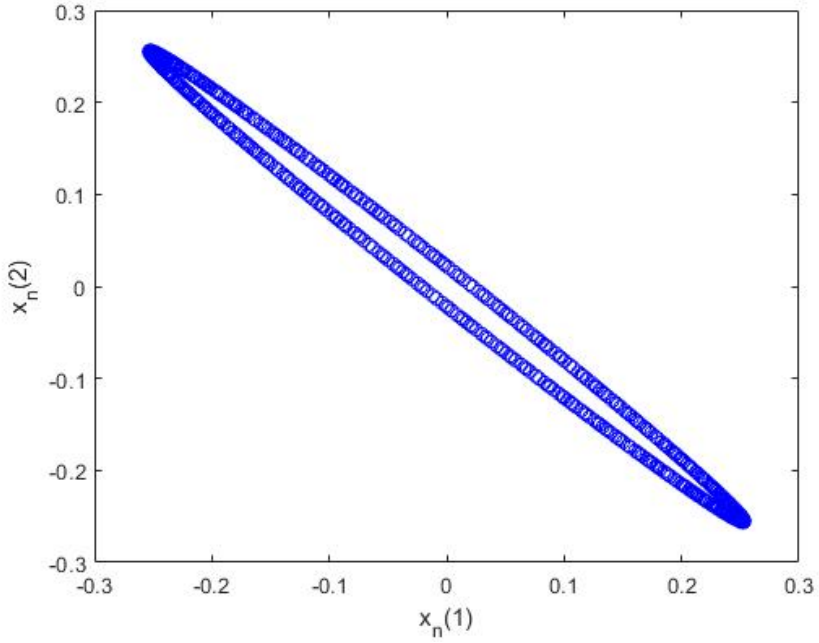

Figure 6-9: The stroboscopic Omega limit set of the linear map (6.14) showing the solution as a closed curve when $\mu = 0.2$, $\omega_1 = 0.1558$ and $\omega_2 = 1.6180339888 \times \omega_1$.

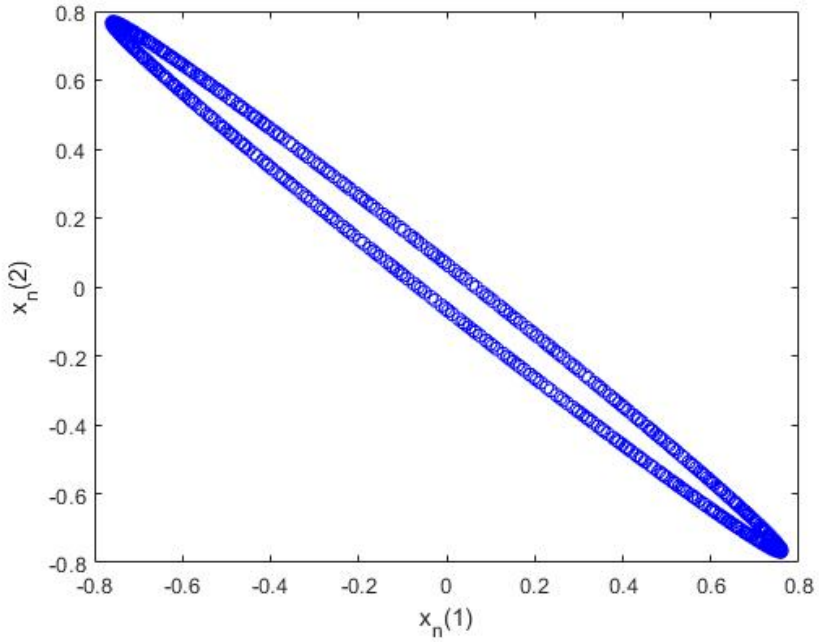

Figure 6-10: The stroboscopic Omega limit set of the linear map (6.14) showing the solution as a closed curve when $\mu = 0.6$, $\omega_1 = 0.1558$ and $\omega_2 = 1.6180339888 \times \omega_1$.

6.3 Numerical methodology: solution of the smoothed quasi-periodic system

The previous section helped us to gain an analytical insight into the behaviour of the solution of the PP04 model if forced with two modes of insolation (i.e quasi-periodically forced) and the amplitude of the second mode is very small ($\mu \ll 1$) in relation to the periodic solution observed for the periodic forced system. We observed that with periodic forcing ($\mu_2 = 0$), the system has a stable periodic solution, that is a $(1, 3)$ periodic solution.

Now we consider the smoothed PP04 quasi-periodically forced model where Heaviside function is represented by $\tanh(-\eta F)$. The dynamics of the system are then studied using the stroboscopic plots of the Poincaré map P defined by

$$P\mathbf{X}(t) \equiv \mathbf{X}(t + T) \tag{6.22}$$

where $T = \frac{2\pi}{\omega_1}$ the sampling time. Using this map we construct the set of points defined by the iteration

$$\mathbf{X}(m + 1) = P\mathbf{X}(m). \tag{6.23}$$

The stroboscopic map of the Omega limits sets of V and A are then plotted to obtain the dynamics. The stroboscopic plots are obtained by solving the smoothed quasi-periodic PP04 model with two or three modes of the forcing, with sampling frequency $T = \frac{2\pi}{\omega_1}$ and then plotting the last five hundred points of the variables V and A. We consider $\mu_1 = 0.467$ and $\omega_1 = 0.1476$ for all the figures with $T = \frac{2\,\pi}{\omega_1}$.

In Figure 6-11, we observe that if $\mu_2 = 0$ we have corresponding to the period $(1, 3)$ solution of the full system, the three equilibrium points of the map.

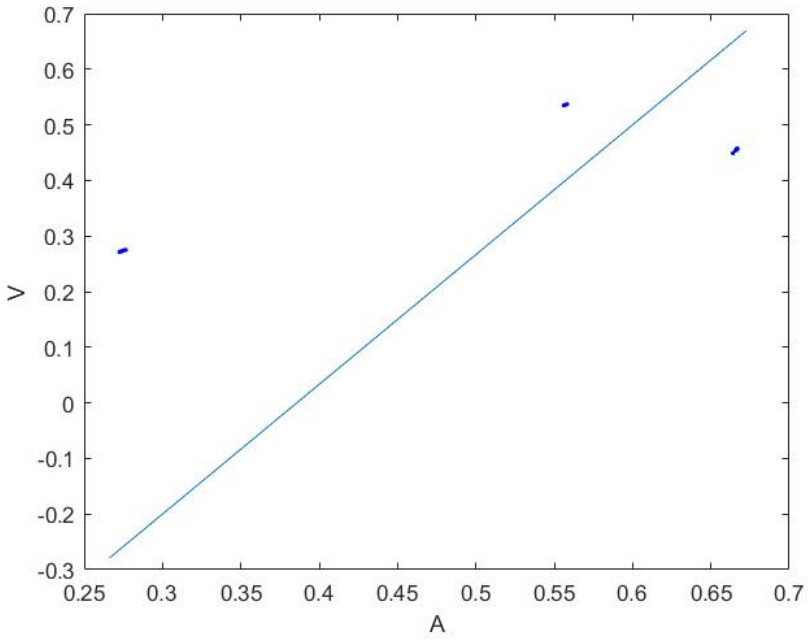

Figure 6-11: The stroboscopic map of V and A on the limit cycle with $\mu_2 = 0$ showing the three equilibrium points of the map corresponding to the $(1, 3)$ periodic orbit obtained after solving the quasi-periodic forced PP04 model with two modes. The blue line represent the discontinuity boundary Σ.

6.3.1 Small μ_2 and rational ω_2 comparison to linear case

Now we consider the stroboscopic map, where we fix $\mu_1 = 0.467$ and $\omega_1 = 0.1476$ and varied values of ω_2 such that $\omega_2\ T$ is rational with small values of μ_2. The stroboscopic plot of the limit cycle in the phase plane (V, A) is plotted taking the period of the map $T = \frac{2\,\pi}{\omega_1}$. For $\mu_2 = 0$, we have observed the three equilibrium solutions and for small values of μ_2, the three periodic solutions with the number of periodic cycles determined by the denominator of the relation $\frac{\omega_2}{\omega_1}$.

In Figure 6-12, we consider $\omega_2 = 1.6\ \omega_1$, and take $\mu_2 = 0.2$ and the stroboscopic plot of the Omega limit set shows the three invariant curves made up of five points. The five points observed are due to the relation $\frac{1.6}{1} \equiv \frac{8}{5}$.

In Figure 6-18 we consider $\omega_2 = 0.9\ \omega_1$ and $\mu_2 = 0.2$ the stroboscopic map on limit cycle shows three sets of invariant curves made of ten points as solutions consistent with the denominator of the relation $\frac{\omega_2}{\omega_1}$. We also observed that if the the relation $\frac{\omega_2}{\omega_1}$ is a proper fraction, when μ_2 is increased the three invariant curves are easily destroyed and only the points exactly equal to the denominator are observed. While if the relation is an improper fraction and μ_2 increased, the three invariant curves are destroyed and points spread out. This can be observed in for example Figure

6-20 which shows the case of the proper fraction, and Figure 6-14 showing the case of the improper fraction.

We then consider the Fast Fourier Transform (FFT) of the solutions of the system in order to find the periods present in the system and the one driving it.

If we have a function $U(t)$ and takes samples at Δt intervals to give $U(j) \equiv U(j\Delta t)$ for $j = 0, 1, \cdots N-1$. We set $T = N\Delta t$ as the total length of the time interval. The FFT algorithm, $W = fft(U)$ transforms the function in time domain into the frequency domain and is defined by

$$W(k) = \sum_{j=0}^{N-1} U_k e^{-2\,\pi\,i\,kj/N}. \tag{6.24}$$

Here $U(k) = U(k\Delta t)$ thus we have

$$W(k) = \frac{1}{\Delta t} \sum_{j=0}^{N-1} U(j\ \Delta\ t)\Delta\ t\ e^{-2\,\pi\,i\,kj\Delta t/N\Delta t} \tag{6.25}$$

$$W(k) = \sum_{j=0}^{N-1} U(t) e^{-2\,\pi\,i\,k\,t/N\Delta t} \tag{6.26}$$

and $t = j\Delta t$ for $k = 0, 1, \cdots N-1$. The frequency corresponding to $W(k)$, is then $f(k) = \frac{k}{N\Delta t} = \frac{k}{T}$ corresponding to a periodic signal of period $\frac{T}{k}$.

For the calculation of the FFT of the quasi-periodically forced system, we considered the time interval or the sampling length from $-n\ \ kyrs$ to $n\ \ kyrs$ which give $N = 2n+1$ and taking samples every $\Delta t = 10kyrs$. We know that the glacial cycles have a dominant period of $100kyr$, therefore we have the frequency

$$\frac{1}{100} = \frac{k}{2n+1}$$

which gives the frequency index at $k = \frac{2n+1}{100}$.

For instance if we considered the sampling length from $-720kyrs$ to $720kyrs$ we have $N = 1441$. Therefore we have the frequency

$$\frac{1}{100} = \frac{k}{1441}$$

which gives the frequency index at $k \approx 14$. Thus we expect a peak at $k \approx 14$ for the 100 $kyrs$ period to be present. We also know from literature that the climate have driving cycles of $40kyr$ and $23kyrs$ which if present will be observed at $k = 36$ and $k = 72$ respectively.

In Figures 6-13, 6-16, 6-19, and 6-22 we observe that the dominant frequency is

at index $k = 12$ which corresponds to the $120kyr$ period. This implies that the dominant or the fundamental period driving this system is the $120kyrs$. We also observe its harmonics at index $k = 24$ and $k = 36$ corresponding to $60kyrs$ and $40kyrs$ respectively.

In Figure 6-19 and Figure 6-22 we observe that there is a small peak at $k = 32$ corresponding to $45kyrs$ but is not one of the harmonics hence another frequency introduced by the forcing of the system. As a consequence we observe that the time dependent solutions in Figure 6-23 and Figure 6-21 the solutions are quasi-periodic. Furthermore in Figure 6-22, there are a number of components present introduced by an increase in amplitude μ_2.

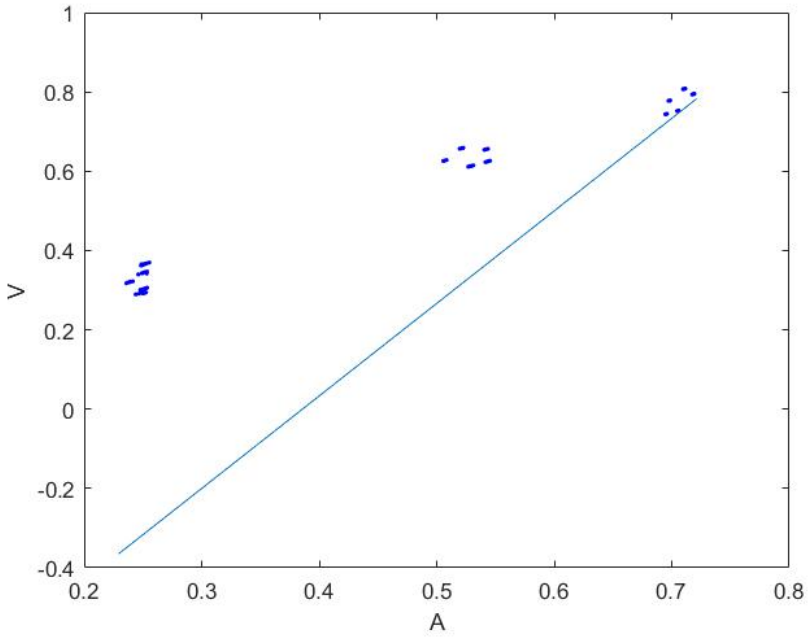

Figure 6-12: The stroboscopic map of V and A on the limit cycle with $\mu_2 = 0.2$ and $\frac{\omega_2}{\omega_1} = \frac{8}{5}$ showing the invariant curve of exactly 5 points.

6.3.2 Small μ_2 and irrational ω_2

We start by considering the irrational forcing that is $\omega_2 = \frac{1+\sqrt{5}}{2}\omega_1$ and $\frac{1+\sqrt{5}}{2}$ is known as the golden mean. We then vary the value of μ_2 starting with the very small value, that is considering $\mu_2 \ll 1$. In Figure 6-24, we observe that when μ_2 is gradually increased, the tori is observed and its size increases with μ_2.

In Figure 6-26 we observe that as μ_2 is increased further say when $\mu_2 = 0.6$, one of the tori breaks as it interacts with the discontinuity boundary. But the further increase say to $\mu_2 = 0.72$ another different torus is formed (see Figure 6-30). The tori is completely destroyed if $\mu_2 > 0.72$ and hence at this value of μ_2 the quasi-periodic solution is destroyed.

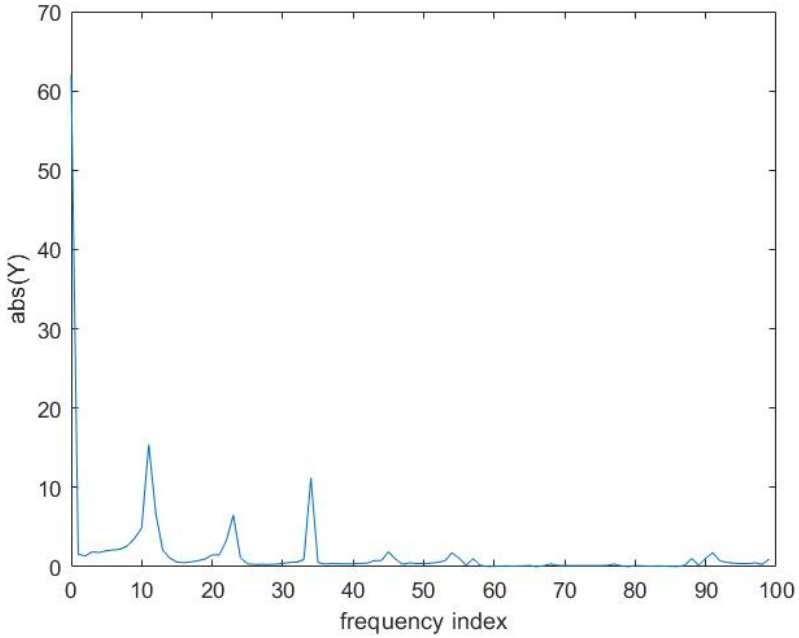

Figure 6-13: The graph showing the frequencies available in the system when $\mu_1 = 0.467$, $\omega_1 = 0.1476$, $\mu_2 = 0.2$ and $\omega_2 = 1.6 \times \omega_1$ with $\frac{\omega_2}{\omega_1} = \frac{8}{5}$.

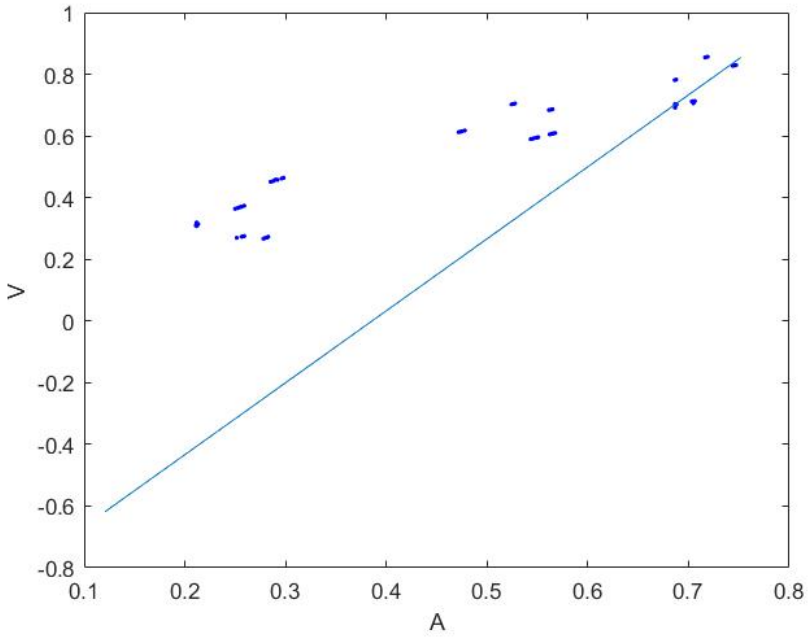

Figure 6-14: The stroboscopic map of V and A on the limit cycle with $\mu_2 = 0.5$ and $\frac{\omega_2}{\omega_1} = \frac{8}{5}$ showing the three invariant curves made up of 5 points destroyed and points spread on the plane intersection with Σ.

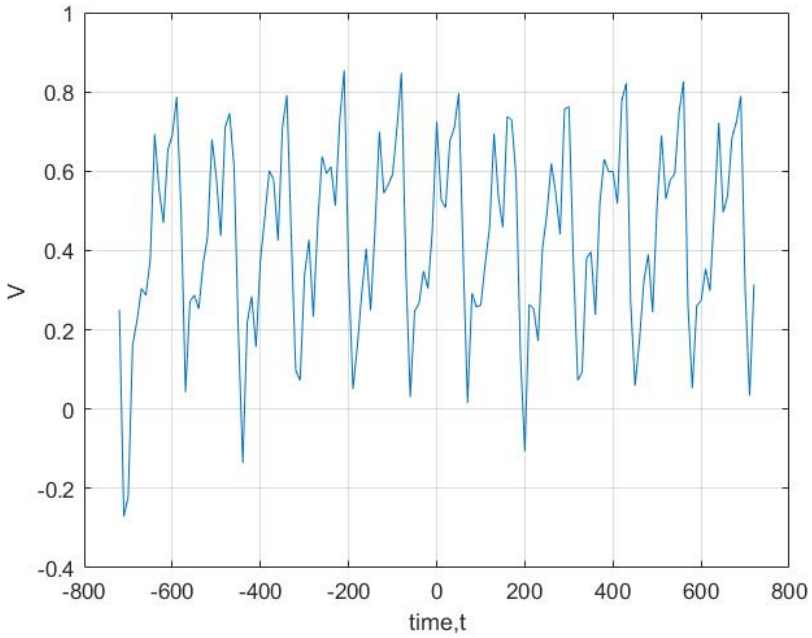

Figure 6-15: The graph showing the time dependent solution of V for $\mu_2 = 0.5$ and $\omega_2 = 1.6 \times \omega_1$.

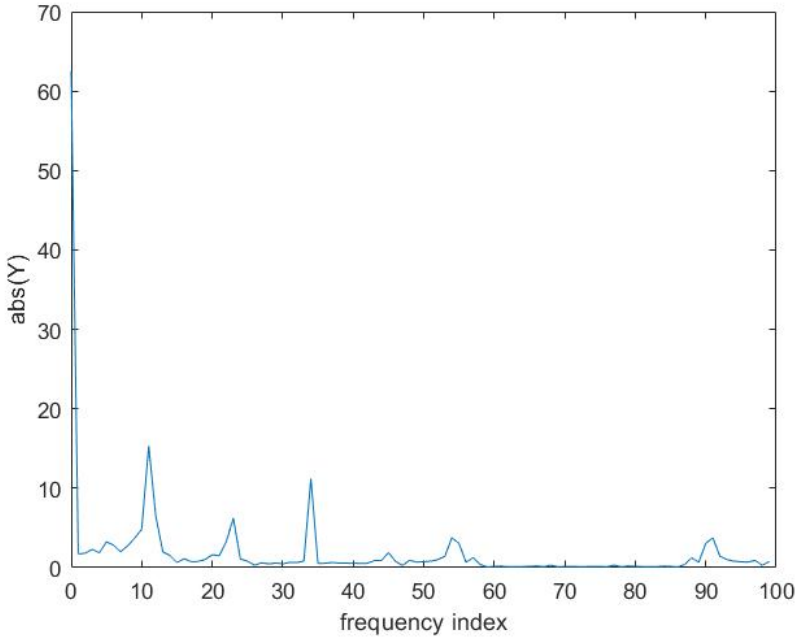

Figure 6-16: The graph showing the frequencies available in the system when $\mu_1 = 0.467$, $\omega_1 = 0.1476$, $\mu_2 = 0.5$ and $\omega_2 = 1.6 \times \omega_1$.

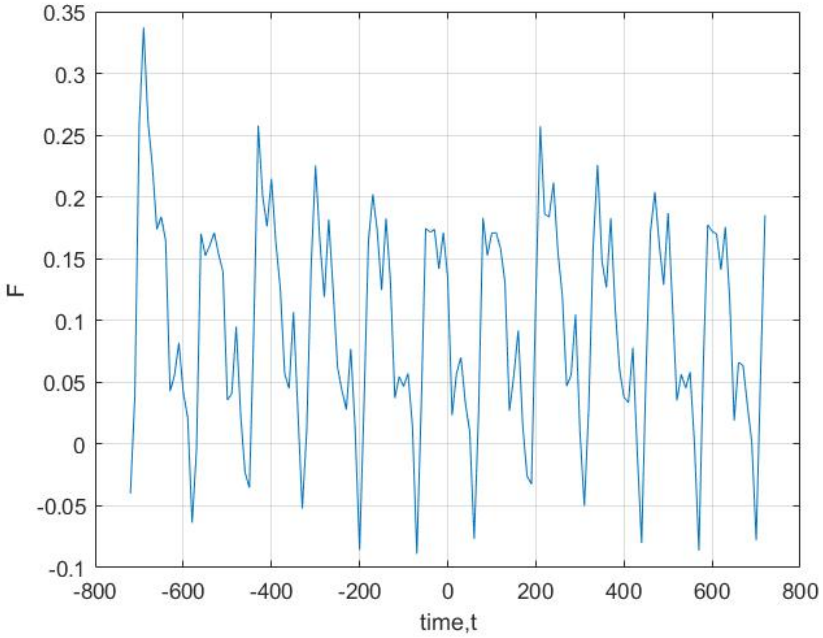

Figure 6-17: The graph showing the time dependent solution of F for $\mu_2 = 0.5$ and $\omega_2 = 1.6 \times \omega_1$.

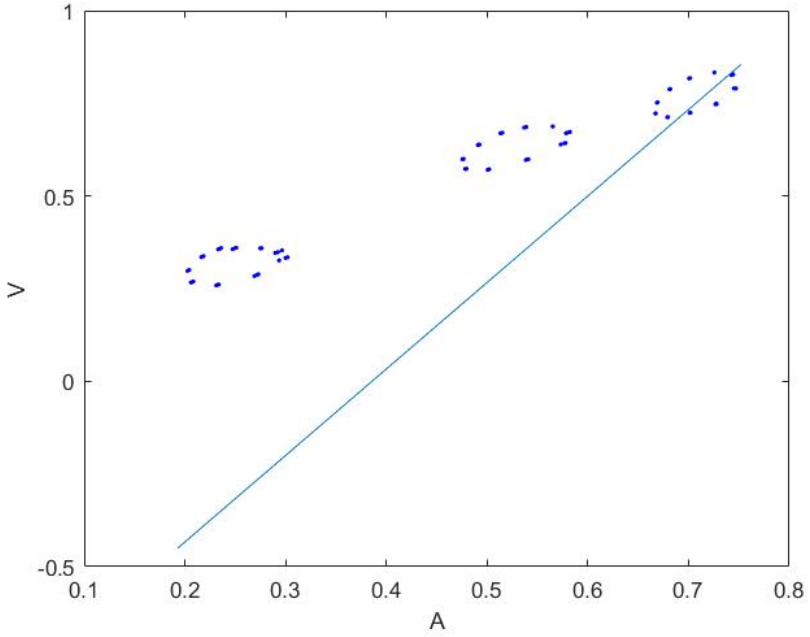

Figure 6-18: The stroboscopic map of V and A on the limit cycle with $\mu_2 = 0.2$ and $\frac{\omega_2}{\omega_1} = \frac{9}{10}$ showing the invariant curve made up of only 10 points intersection with Σ.

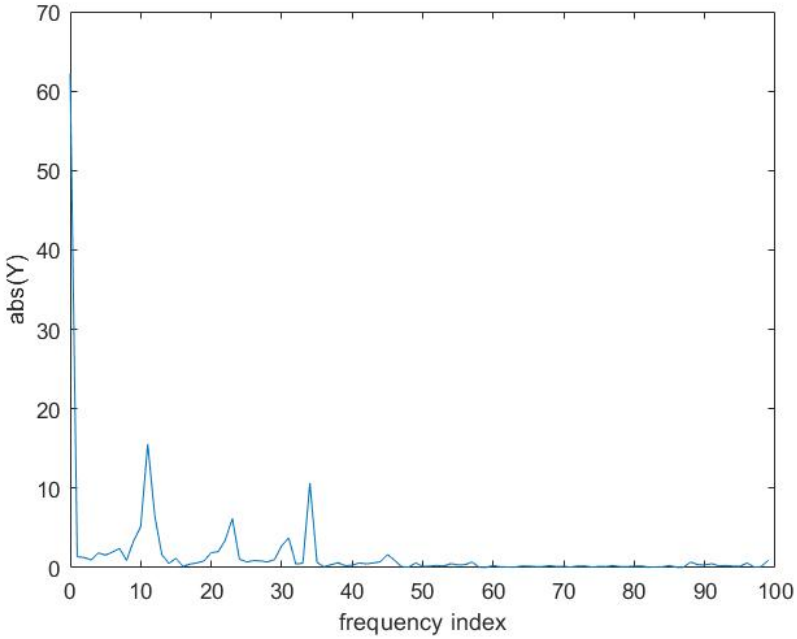

Figure 6-19: The graph showing the frequencies available in the system when $\mu_1 = 0.467$, $\omega_1 = 0.1476$, $\mu_2 = 0.2$ and $\omega_2 = 0.9 \times \omega_1$.

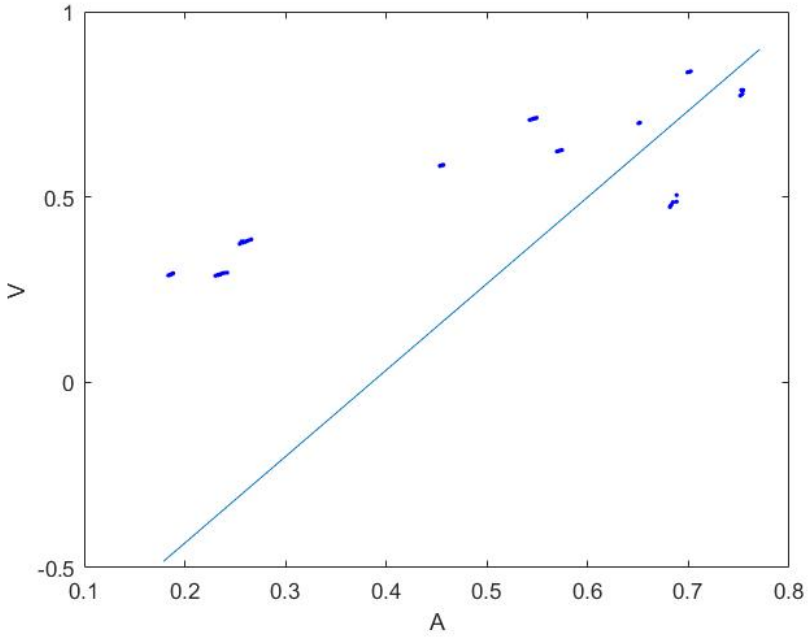

Figure 6-20: The stroboscopic map of V and A on the limit cycle with $\mu_2 = 0.29$ and $\frac{\omega_2}{\omega_1} = \frac{9}{10}$ showing exactly a total of the ten points spread out.

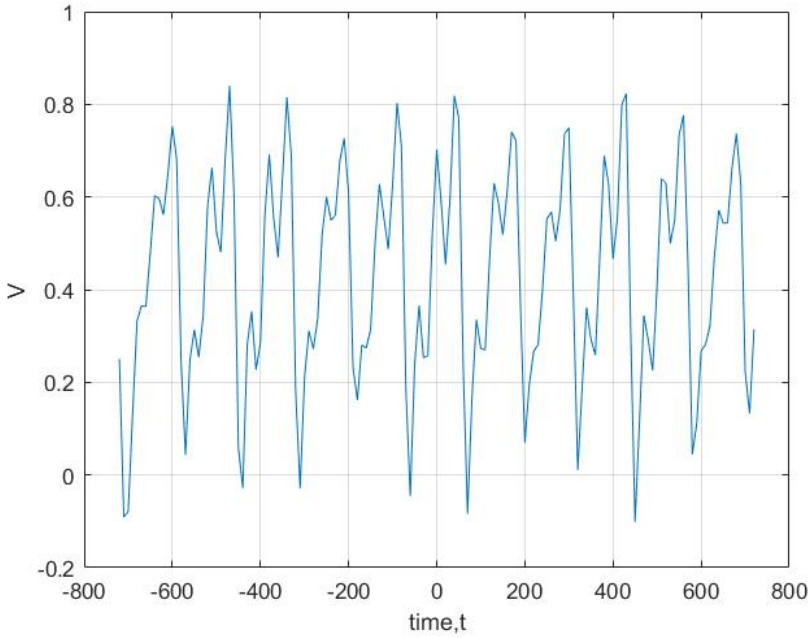

Figure 6-21: The graph showing the time dependent solution of V for $\mu_2 = 0.2$ and $\omega_2 = 0.9 \times \omega_1$.

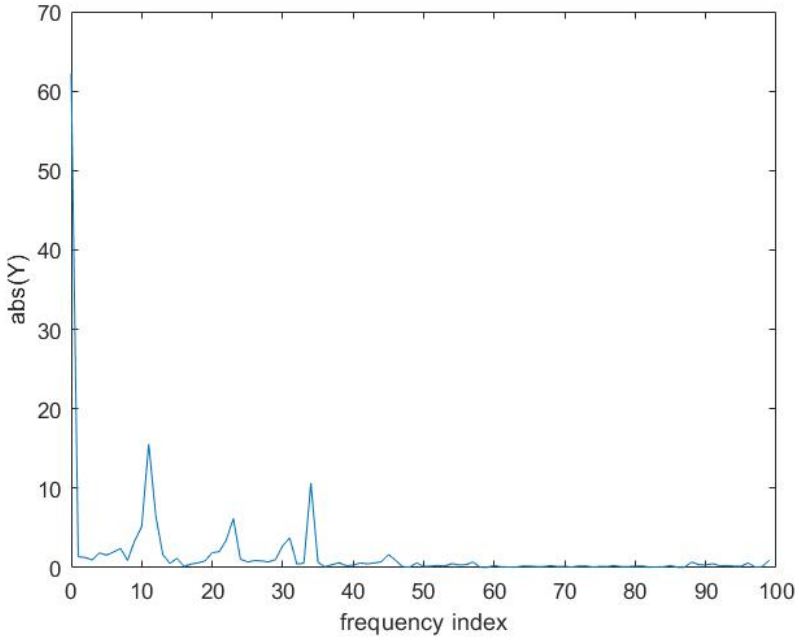

Figure 6-22: The graph showing the frequencies available in the system when $\mu_1 = 0.467$, $\omega_1 = 0.1476$, $\mu_2 = 0.29$ and $\omega_2 = 0.9 \times \omega_1$ with $\frac{\omega_2}{\omega_1} = \frac{9}{10}$.

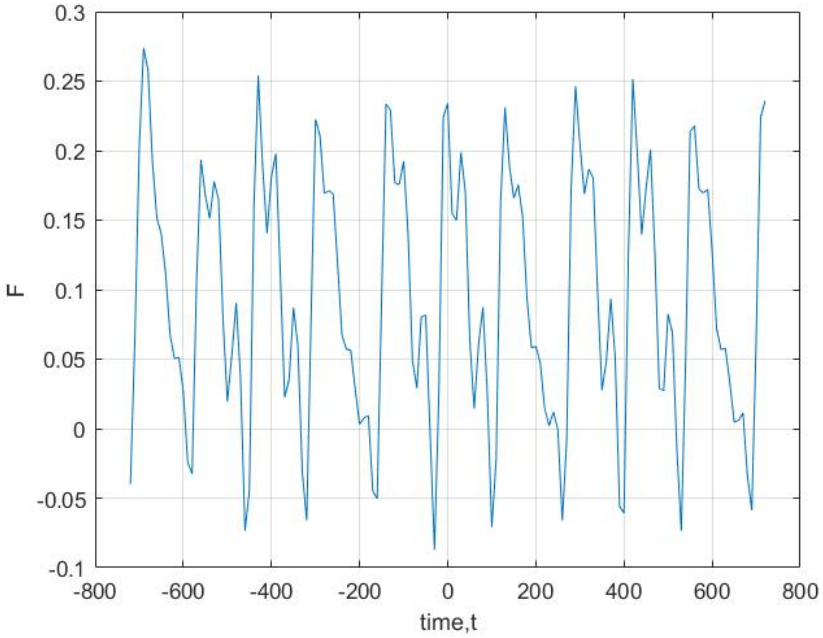

Figure 6-23: The graph showing the time series solution of F for $\mu_2 = 0.29$ and $\omega_2 = 0.9 \times \omega_1$.

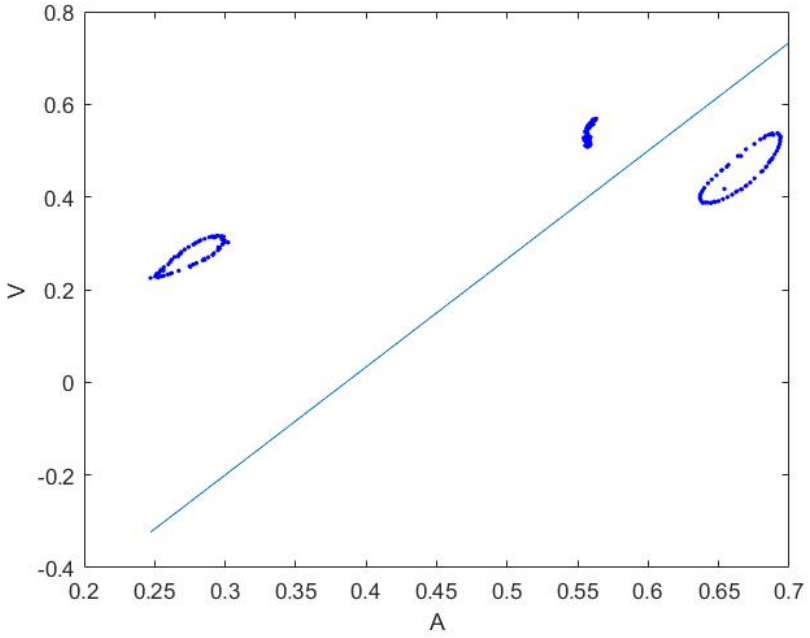

Figure 6-24: The stroboscopic map of V and A on the Omega limit set with $\mu_1 = 0.467$, $\omega_1 = 0.1476$, $\mu_2 = 0.2$ and $\omega_2 = 1.6180339888 \times \omega_1$ showing the invariant tori. These closed curves are centred on the period 3 limit cycle.

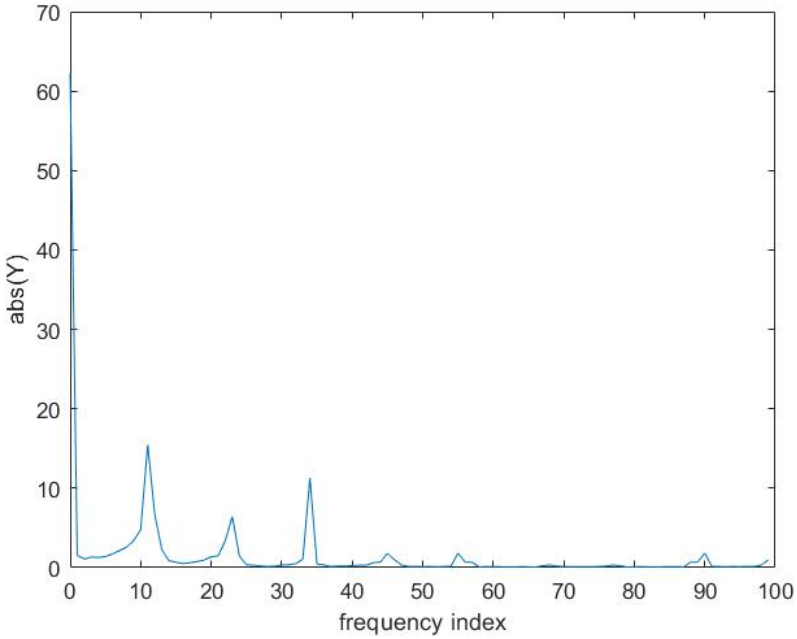

Figure 6-25: The graph showing the frequencies available in the system when $\mu_1 = 0.467$, $\omega_1 = 0.1476$, $\mu_2 = 0.2$ and $\omega_2 = 1.6180339888 \times \omega_1$.

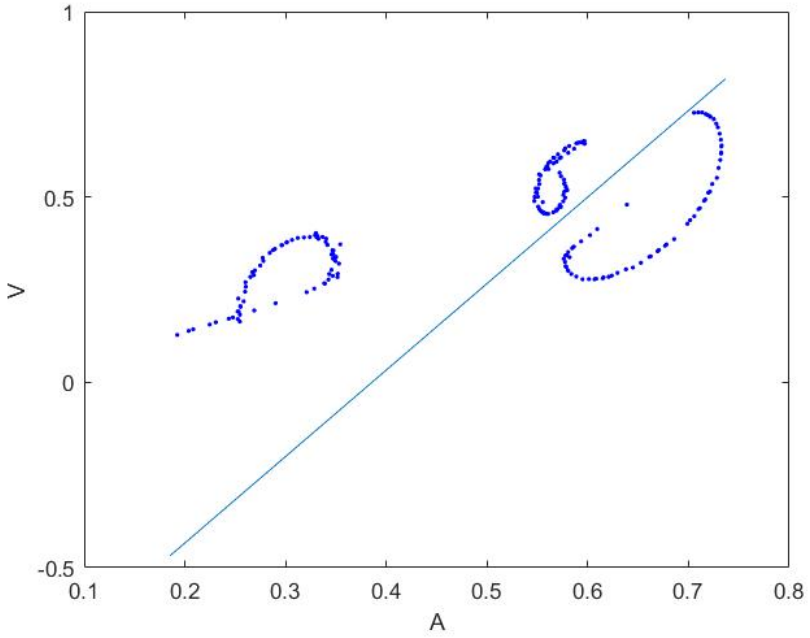

Figure 6-26: The stroboscopic map of V and A on the Omega limit set with $\mu_1 = 0.467$, $\omega_1 = 0.1476$, $\mu_2 = 0.6$ and $\omega_2 = 1.6180339888 \times \omega_1$ showing the breakup of the tori.

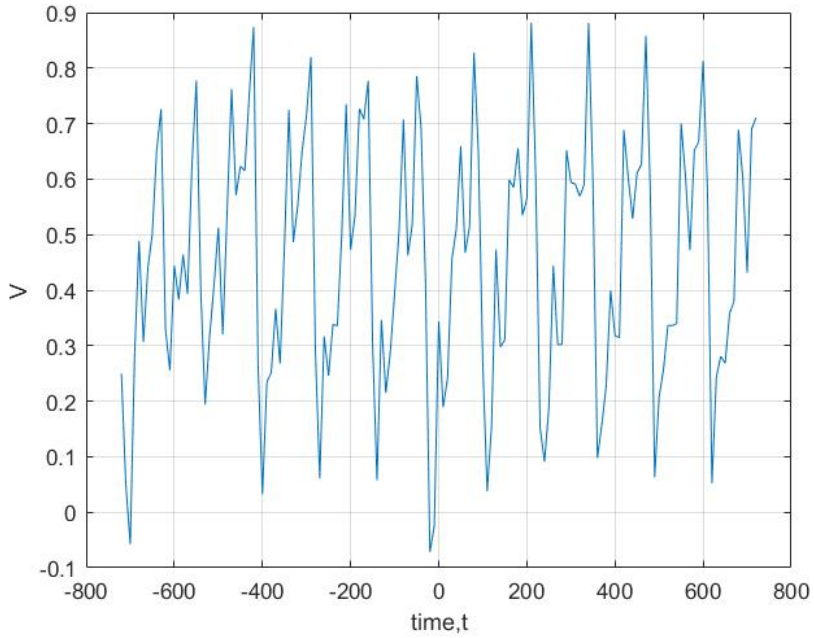

Figure 6-27: The graph showing the time series solution of V for $\mu_2 = 0.6$ and $\omega_2 = 1.6180339888 \times \omega_1$.

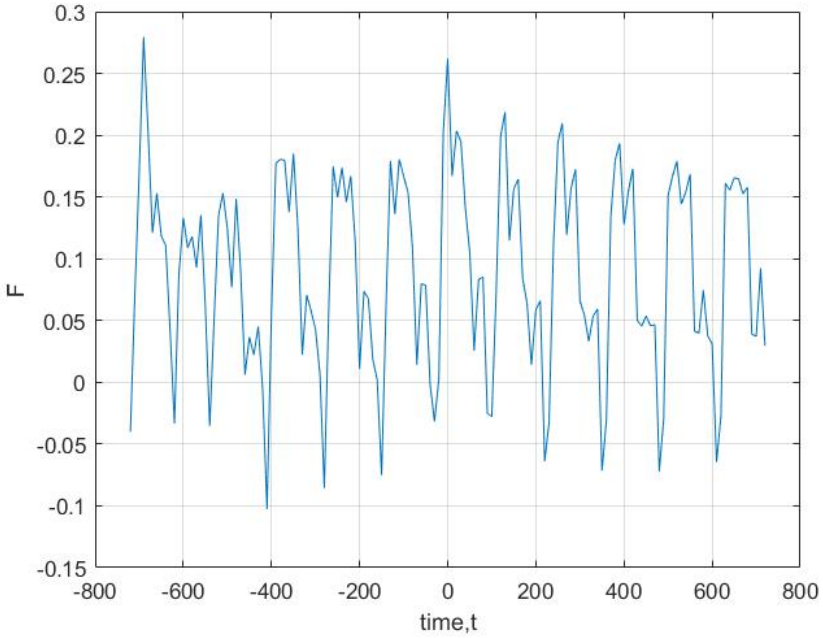

Figure 6-28: The graph showing the time dependent solution of F for $\mu_2 = 0.6$ and $\omega_2 = 1.6180339888 \times \omega_1$.

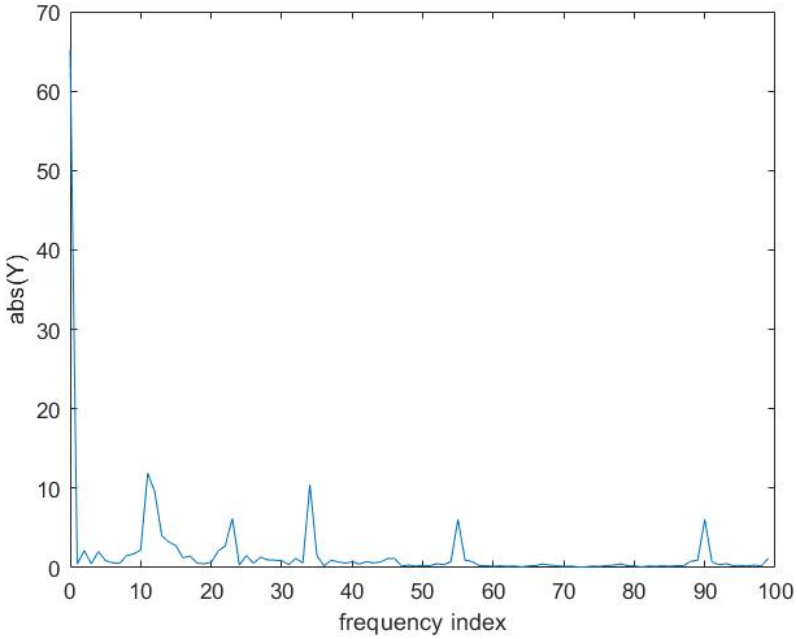

Figure 6-29: The graph showing the frequencies available in the system when $\mu_1 = 0.467$, $\omega_1 = 0.1476$, $\mu_2 = 0.6$ and $\omega_2 = 1.6180339888 \times \omega_1$.

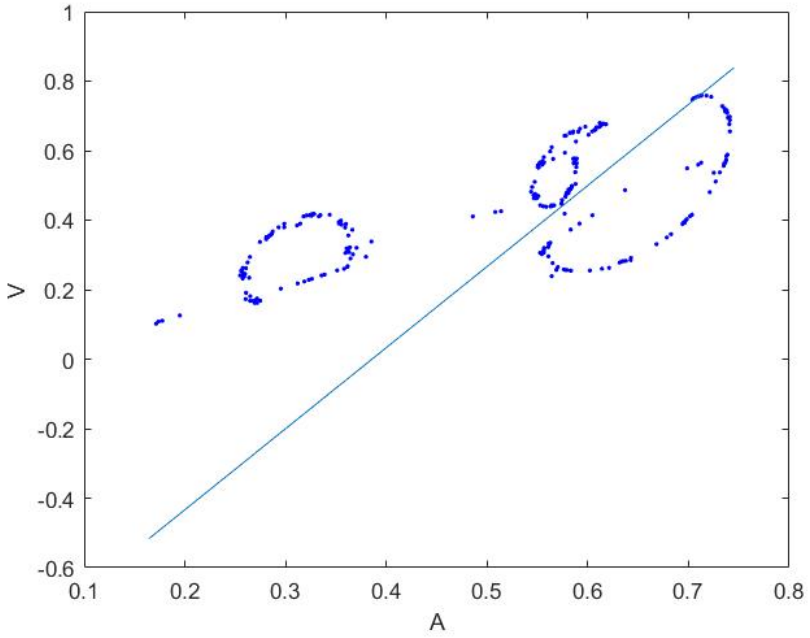

Figure 6-30: The stroboscopic map of V and A on the Omega limit cycle with $\mu_1 = 0.467$, $\omega_1 = 0.1476$, $\mu_2 = 0.72$ and $\omega_2 = 1.6180339888 \times \omega_1$ showing the formation of a different torus.

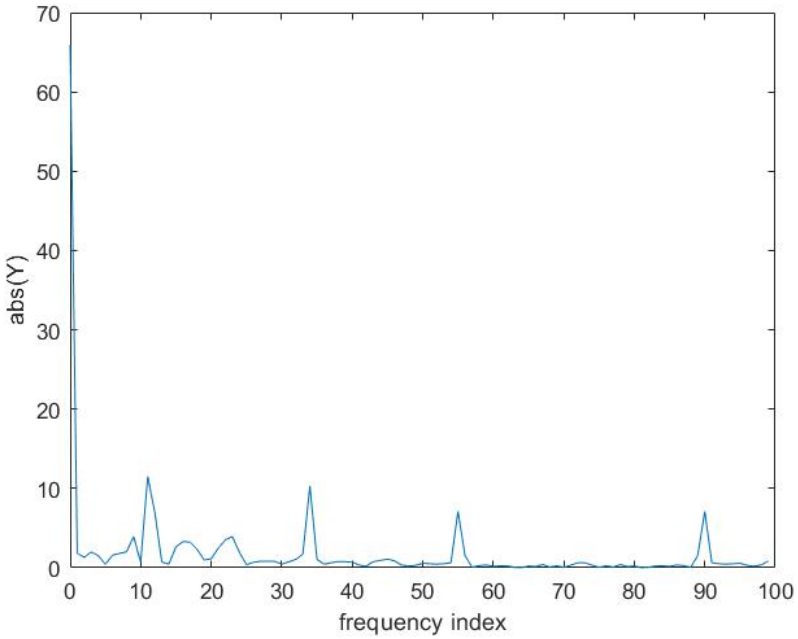

Figure 6-31: The graph showing the frequencies available in the system when $\mu_1 = 0.467$, $\omega_1 = 0.1476$, $\mu_2 = 0.72$ and $\omega_2 = 1.6180339888 \times \omega_1$.

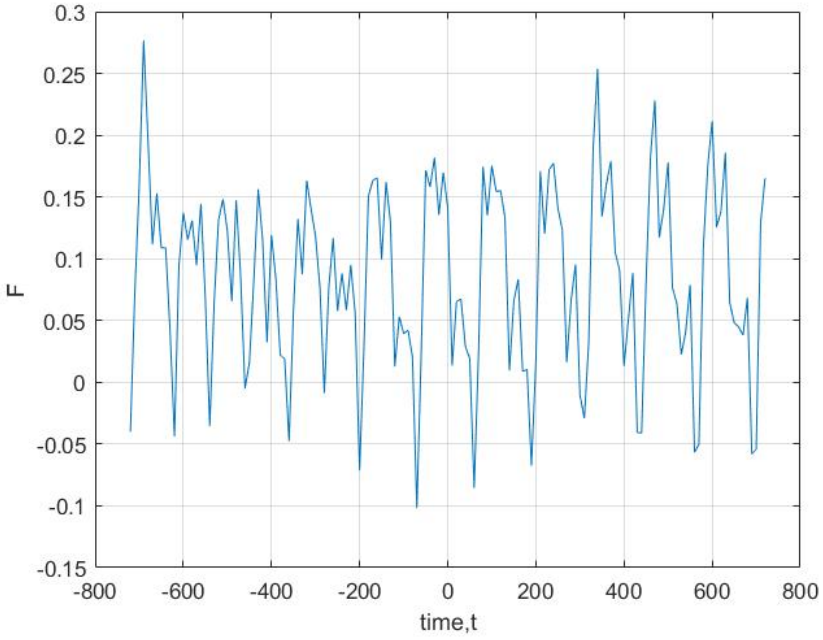

Figure 6-32: The graph showing the time series solution of F for $\mu_2 = 0.72$ and $\omega_2 = 1.6180339888 \times \omega_1$.

In considering the Fast Fourier Transform (FFT) of the solutions of the system in order to find the periods present in irrationally forced quasi-periodic system, we examined Figure 6-25, Figure 6-29 and Figure 6-31.

In Figure 6-25 we observe that the periods present are the dominant $120kyrs$ and its harmonics and also a presence or contribution of the forcing frequency at frequency index $k = 56$ which corresponds to $26kyrs$. Hence quasi-periodic solutions observed in the time solutions Figure 6-32 and Figure 6-27. As μ_2 is increased, the peaks spreads out due to the introduction of other frequency components, the growth of the peak representing the $26kyrs$ period is also clearly seen in Figure 6-29. The Figure 6-29 shows that the $120kyr$ period and the $40kyrs$ period are both driving the system.

6.3.3 Large μ_2

Now we consider the stroboscopic map of V on the Omega limit when $\mu_2 \geq 1$. The stroboscopic plot of the limit cycle in the phase plane (V, A) is plotted taking the same period of the map $T = \frac{2\,\pi}{\omega_1}$. For large μ_2, the stroboscopic plot on the Omega limits of the quasi-periodically forced model exhibits the apparent strange chaotic attractors (see Figure 6-33).

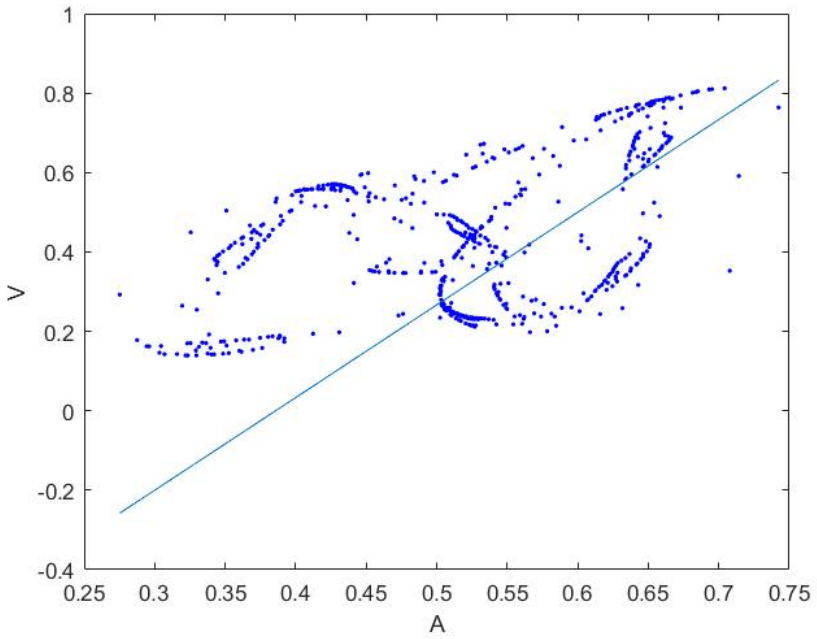

Figure 6-33: The stroboscopic map of V and A on the Omega limit cycle with $\mu_2 = 1.2$ and $\omega_2 = 1.6180339888 \times \omega_1$ showing the apparent chaotic solutions.

The presence of chaotic attractors in the quasi-periodically forced PP04 model with only two frequencies was also observed by Ashwin *et al.* [3] with similarly significant amplitude. On the other hand, the quasi-periodic time dependent solutions for the

volume of ice were observed for quasi-periodically forced smoothed system.

The full analysis of the system (6.1) is hard as it involves a long investigation of effects of a number of parameters and variables of the model. Therefore we had performed an investigation whereby we checked the effect of forcing by studying the effect of different frequencies and amplitudes. The summary of the dynamics observed in the quasi-periodic forced PP04 model with different forcing is given in Table 6.1 and shows that for small amplitudes the system exhibits quasi-periodic motion. When the frequency of the forcing is irrational and the amplitude of the forcing is increased the system exhibits chaotic motion.

Table 6.1: Table summarising the dynamics in the two mode forced quasi-periodic PP04 model

ω_1	ω_2	μ_2	Result	Figure
0.1476	$0.9 \times \omega_1$	0.2	periodic motion	Figure 6-18
0.1467	$1.6 \times \omega_1$	0.2	period motion	Figure 6-12
0.1467	$1.680339888 \times \omega_1$	0.2	quasi-periodic motion	Figure 6-24
0.1476	$1.680339888 \times \omega_1$	0.6	tori seen at $\mu_2 = 0.4$ breaks up	Figure6-26
0.1467	$1.680339888 \times \omega_1$	1.2	chaotic motion	Figure 6-33

6.3.4 Three frequency forcing

The astronomical forcing has thirty-five different modes of the astronomical forcing of which the obliquity, eccentricity and precession are dominant. Therefore Mitsui *et al.* [46] states that the three modes of $I_{65}(t)$ constitutes about seventy-five percent of the forcing and hence a good representation of the forcing. Therefore it is important to try and understand how the climate will work with this forcing by considering these three modes of forcing in order to observe their effect on the dynamics of the system.

If we consider three frequency forcing and fix $\mu_2 = 0.4$ and $\omega_2 = 1.6180339888 \times \omega_1$ with $T = \frac{2\pi}{\omega_1}$, the stroboscopic map of V on the Omega limit exhibits invariant curves when μ_3 is small which breaks when μ_3 is increased.

In Figure 6-34 we observe the invariant curves when $\mu_3 = 0.6$ and in Figure 6-35 the invariant curves are destroyed.

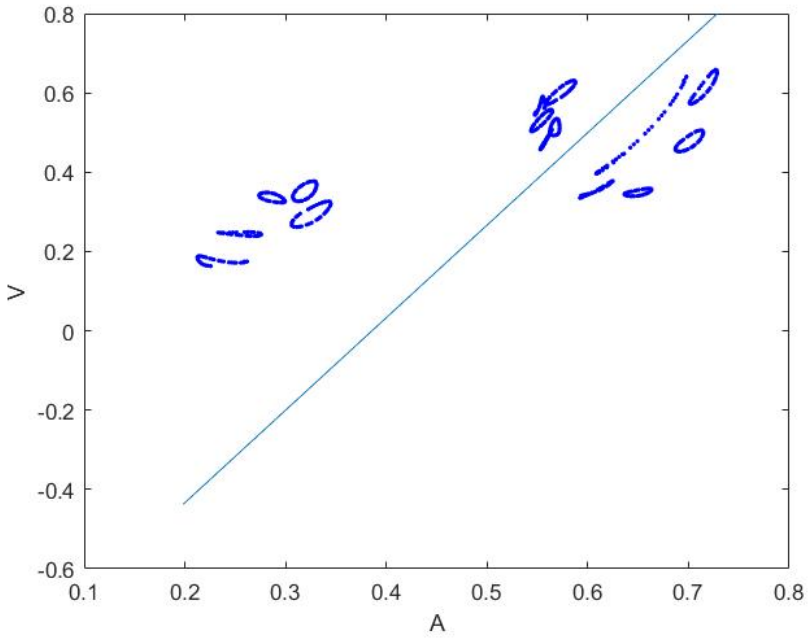

Figure 6-34: The stroboscopic map of V and A on the Omega limit cycle showing the invariant curves for $\mu_2 = 0.4$, $\omega_2 = 1.6180339888 \times \omega_1$, $\mu_3 = 0.3$ and $\omega_3 = 0.331$.

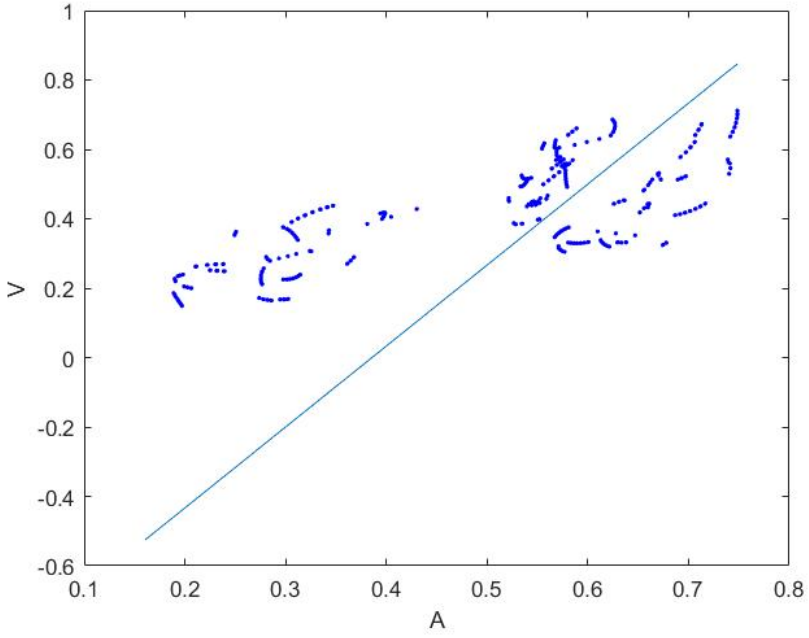

Figure 6-35: The stroboscopic map of V and A on the Omega limit cycle showing the apparent chaotic solution when invariant curves break up for $\mu_2 = 0.4$, $\omega_2 = 1.6180339888 \times \omega_1$, $\mu_3 = 0.6$ and $\omega_3 = 0.331$.

6.4 Summary

In this chapter we have established that for the quasi-periodically forced PP04 model with two modes of forcing, the system exhibits:

1. Periodic points or periodic solutions for rational forcing when using both the linear map and the stroboscopic map of the smoothed system with small forcing.
2. Tori for irrational forcing when using the linear map, or the nonlinear map for small amplitude.
3. The tori breaks down when the amplitude is increased for the full system.
4. Apparent strange chaotic attractors for large amplitude of the forcing.

Chapter 7

Grazing bifurcation, transitions and domains of attractions

In Chapter 5 we considered the periodic solutions of the periodically forced system which transversally intersects the discontinuity boundary. To extend the study of these solutions, we now look at the periodic solutions that intersects the discontinuity boundary Σ non-transversally as a parameter is varied. In this chapter, we will:

(i) Give evidence that the grazing bifurcation occurs on the period $(1, 3)$ solution

(ii) Show that this grazing bifurcation leads to a significant instability and loss of physicality of solutions.

(iii) Look at the domains of attraction of the various periodic solutions and see how these give insight into the transitions between these solution.

7.1 Grazing instability

A grazing bifurcation is said first to occur when as a parameter of the system (2.17 - 2.19) is varied the periodic orbit $\mathbf{X}$ has a point of tangency with the switching boundary Σ. That is, if we consider the orbit $\mathbf{X}$ starting from S^+ where $F(\mathbf{X}) > 0$, as a parameter is varied then there is a point X_g such that the periodic orbit touches the discontinuity boundary at a non-transversal intersection (a graze) at X_g. At this point we then have

$F(X_g) = \frac{d}{dt}F(X_g) = 0$ (see Figure 7-1). It is shown in [19] that such behaviour is highly destabilising.

The set of initial conditions that leads to a trajectory grazing is known as the grazing

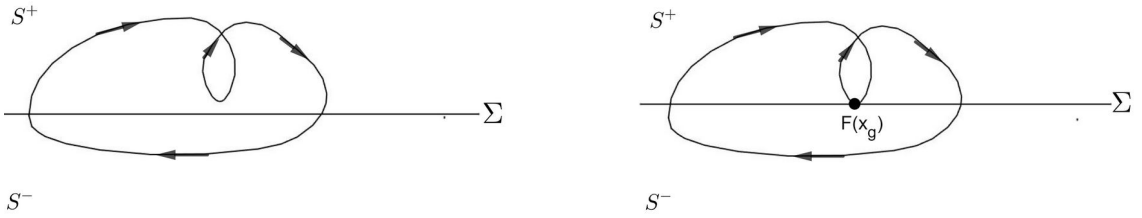

Figure 7-1: The schematic graph showing a stable periodic orbit before graze (left) and a grazing periodic orbit (right).

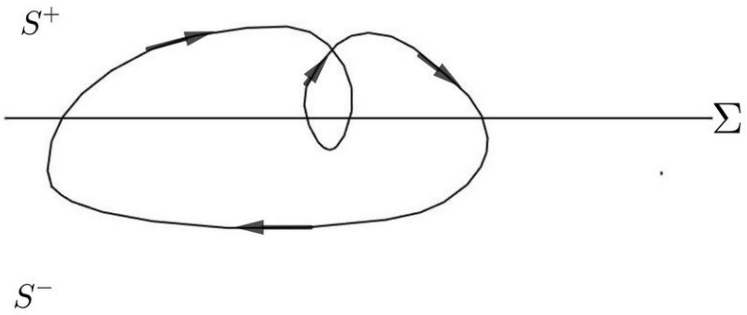

Figure 7-2: The schematic graph showing an unstable periodic orbit after graze which has an additional small excursion in S^-.

set defined as

$$G_i = \{x \in \Sigma : F(\mathbf{x}) = \frac{d}{dt}F(\mathbf{x}) = 0\}$$

These initial conditions separates the physical and the non physical solutions and hence acts as a border between the two types of solutions. The grazing bifurcation leads to sudden change in behaviour of the system as part of the orbit has a zero velocity at the switching boundary and the resulting Poincaré map has infinite stretching. Consequently the transition produce rich dynamics [49].

In Figure 5-26 and Figure 5-27 we observed that the period $(1, 3)$ solution was suddenly born or destroyed when either ω or μ are varied respectively. We also observed that the synchronised periodic solutions ceases to exist at certain values of μ when ω is constant. This behaviour of the period $(1, 3)$ solution at this certain value of μ or ω we associate with a grazing bifurcation. That is to say, for $\omega > \omega_g$ or $\mu < \mu_g$ we have a stable period $(1, 3)$ solution and for $\omega \leq \omega_g$ or $\mu \geq \mu_g$the periodic solution becomes unstable. To illustrate the grazing bifurcation of a period $(1, 3)$ solution, we fix the value of ω and vary μ until we reach the value of μ such that F changes signs while $\mathbf{x} \in S^+$ to get the value of the grazing parameter.

7.1.1 Using algebraic calculations to show grazing

We consider the non-smooth system and to find the grazing amplitude of the forcing, we solve the algebraic equations. In Figure 7-3, the solutions of the algebraic solver shows that an increase in the value of μ closer to the grazing value, the part of the periodic solution approaches the discontinuity boundary as the velocity of the trajectory at that point become smaller and smaller until the orbit grazes. This figure shows that the period $(1, 3)$ orbit grazes at $\mu \approx 0.5$ if $\omega = 0.123$ which is consistent with the solutions obtained for the smooth system in Figure 5-27.

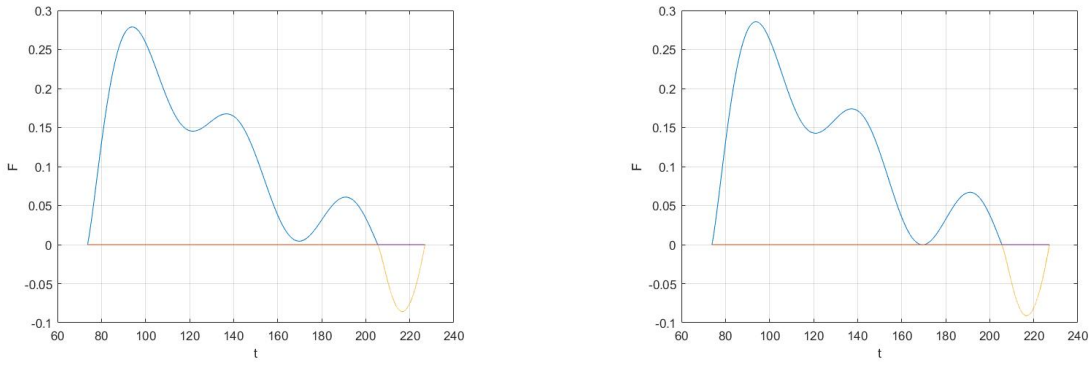

Figure 7-3: The graph showing that with an increase in the value of μ the part of the periodic solution has velocity close to zero and eventually grazes with $\omega = 0.123$ and $\mu = 0.467$ (left) and $\mu = 0.51$ (right).

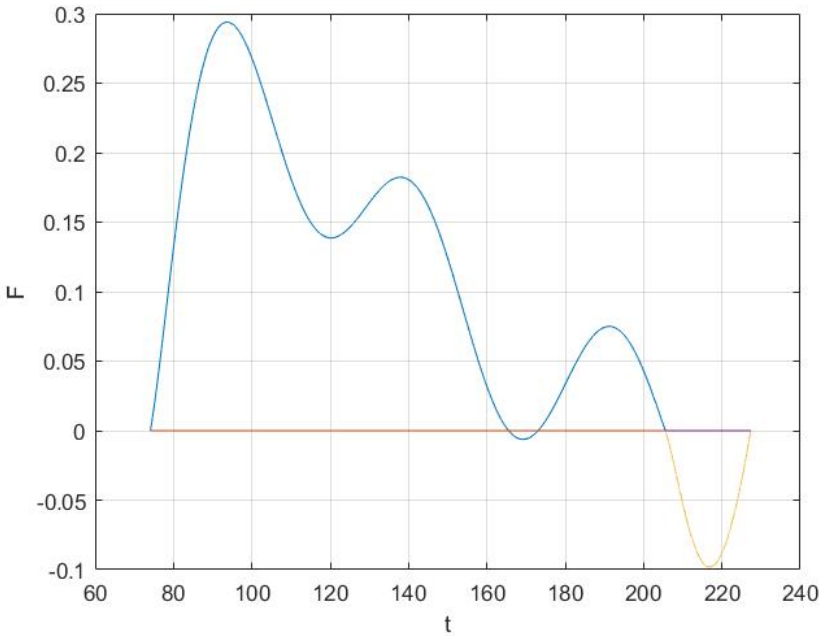

Figure 7-4: The graph showing that after the periodic solution has grazed, it loses its physicality for $\mu = 0.6$ and $\omega = 0.123$.

7.1.2 Numerical calculations showing grazing

When we consider the smoothed system, Figure 5-30 shows that when we fix $\omega = 0.126$ a period $(1, 3)$ solution is near grazing when $\mu = 0.467$. Therefore this shows that if μ is increased further, it will graze. To illustrate the grazing bifurcation of the period $(1, 3)$ solution using the smoothed system, we consider say $\omega = 0.123$ and vary μ until we reach the value of μ such that F changes signs for the orbit in S^+ in order to get the grazing value μ_g.

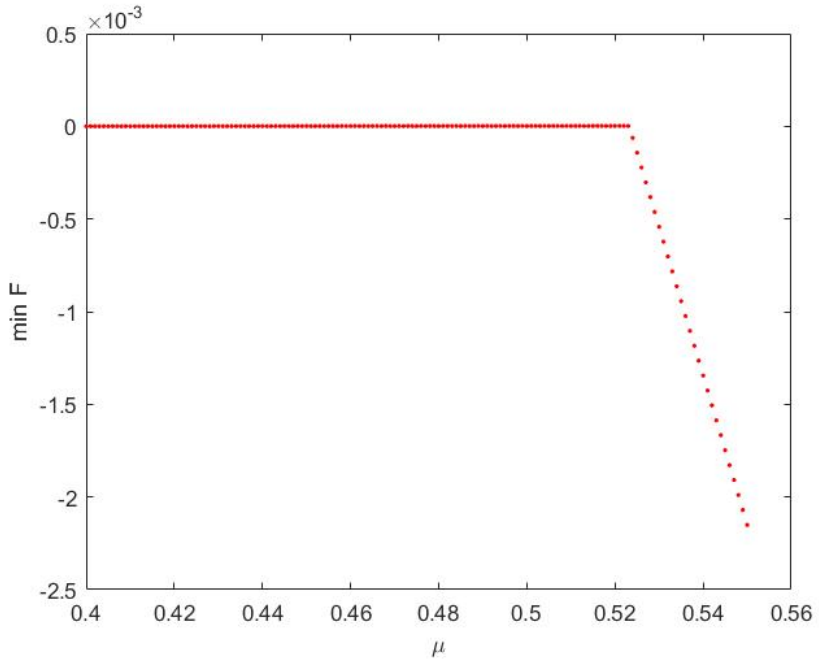

Figure 7-5: The graph showing that as μ is increased the periodic solution of the periodically forced PP04model exhibits a grazing bifurcation at $\mu = 0.525$ when $\omega = 0.123$. The graph is obtained by plotting the minimum values of F against μ.

Indeed in Figure 7-5, we observe that when solving the periodically forced smoothed system, for $\omega = 0.123$, the minimum value of F obtained for flow $\mathbf{X}$ in the region S^+, changes sign at $\mu = 0.53$. Therefore the grazing bifurcation is observed at $\mu_g = 0.53$ and similarly we observed that $\mu_g = 0.49$ for $\omega = 0.122$ agreeing with the non-smooth solution. Similar behaviour is expected for other values of ω or μ when increased and hence we can get a grazing curve (see Figure 7-12). Now we study this grazing instability.

To study the dynamics of the PP04 system in the neighbourhood of the grazing trajectory, we can use the discontinuity mapping technique. This technique was first introduced by Nordmark *et al.* [49] and then was extended to $n-$dimensional piecewise smooth systems by [19]. The normal Poincaré map P_S in the neighbourhood of the grazing trajectory is set up to describe this near grazing dynamics as trajectories near grazing will transversally cross the Poincaré section Π_N at a point near the

grazing point. If we consider the Poincaré section normal to the discontinuity boundary and to pass through the origin, then one side will be on S^+ and another on S^- and the Poincaré Discontinuity Mapping (PDM) can be constructed [20].

7.1.3 The discontinuity mapping

The discontinuity map defines the correction made to the trajectories in order to account for the presence of a discontinuity boundary in phase space [19]. This is done by considering a flow in the region S^+ close to the trajectory that contains the grazing point $\mathbf{x}_g$. The near grazing periodic orbit starting in S^+ and passing through x_0 using flow ϕ_1, intersects the boundary Σ at x_2 close to x_g and continue in S^- with flow ϕ_2 until it intersects the discontinuity boundary Σ again at x_3 and then continue to evolve in S^+ using flow ϕ_1. When we consider that grazing occur in S^+, then the discontinuity mapping is the correction to be applied only to the trajectory of the flow ϕ_1 in S^+, to account for passage through S^- [20]. Figure 7-6 is used to illustrate how this map is constructed whereby we describe the map using both flows ϕ_1 from S^+ and ϕ_2 from S^-.

When considering the flow ϕ_1, the trajectory that intersects the boundary Σ at x_2 can be continued in S^- and intersects Π_N at x_1. Similarly the orbit from x_3 can be evolved backwards in time to x_4. Suppose the flow ϕ_1 from S^+ through x_0, and intersecting the discontinuity boundary at x_2 takes $t = \delta_0$, and the flow ϕ_2 in S^- intersecting the boundary Σ at x_3 takes $t = \delta_2$. Then the flow backwards from x_3 using flow ϕ_1 intersecting Π_N at x_5 until reaching x_4 takes $t = -(\delta_0 + \delta_2)$ [19]. Where the normal Poincaré section is defined

$$\Pi_N := \{x : \frac{\partial}{\partial t} F(\phi(x)) = 0\}$$

and the Poincareé map $P_S := \Pi_N \to \Pi_N$ is through

$$\phi_1(x_1) \mapsto \phi_2(x_2) \mapsto \phi_1(x_3) \mapsto x_5.$$

Then the combination of the Poincaré map P_S and the discontinuity mapping gives insight into the behaviour of near grazing solutions [89]. The PDM map then captures the recurrent dynamics in the neighbourhood of the grazing orbit for a sufficiently small $|x - x^*|$ and $|\mu - \mu^*|$ [19]. According to di Bernardo *et al.* in [20] and [19], if the vector field is discontinuous at the grazing point the system has a square root type singularity at the grazing point. Therefore for the PP04 system which has

$$L\mathbf{X} + \mathbf{b}^+ + \mu\, \mathbf{e}\, \sin(\omega t) \neq L\mathbf{X} + \mathbf{b}^- + \mu\, \mathbf{e}\, \sin(\omega t)$$

has a square root singularity at the grazing point. Therefore the Poincaré Disconti-

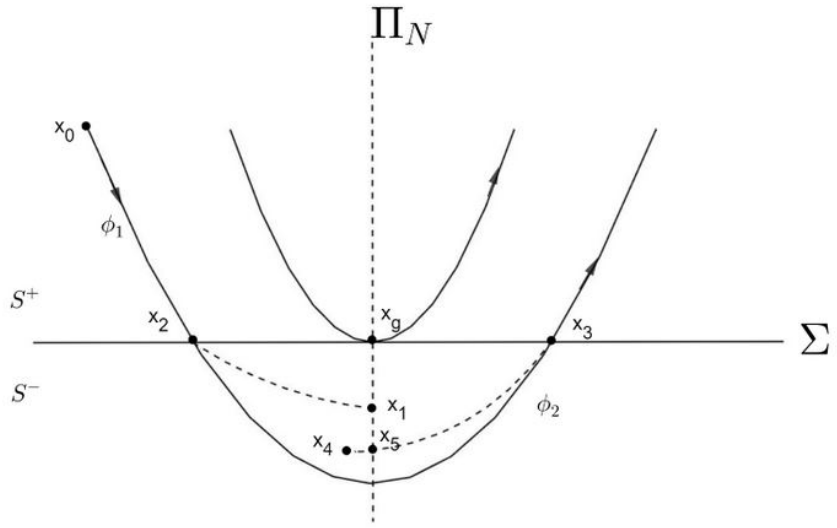

Figure 7-6: The graph used to illustrate the construction of the PDM mapping $x_1 \to x_5$

nuity mapping (PDM) which is a mapping from $x_1 \to x_5$ given by

$$PDM = \phi_1(\phi_2(\phi_1(x, \delta), \delta_2), -\delta_3)$$

for the PP04 system is given by

$$\mathbf{X}_{n+1} = \begin{cases} A\mathbf{X}_n & if \quad F(\mathbf{X}) > 0 \\ A\mathbf{X}_n + B(-F(\mathbf{X}_n))^{1/2} + \mathbf{C} & if \quad F(\mathbf{X}) < 0 \end{cases} \tag{7.1}$$

where A, B are matrices and C represents high order terms. The square root in this map leads to stretching of the phase portrait in the neighbourhood of grazing and hence resulting in an instability of the orbit (for a further reading see chapter 7 in [19]).

If $F(\mathbf{X}) > 0$ the stability is determined by A. In particular if A is a contraction matrix (as it is for the $(1, 3)$ orbit) then the fixed points of this map are stable. However if $F(\mathbf{X}) < 0$ the stretching in phase space introduced by the square-root term leads to the fixed point becoming unstable. This is the essence of the grazing bifurcation.

7.2 Stability of the $(1, 3)$ periodic solution

We consider the period $(1, 3)$ solution obtained for the smoothed system simulated for $t = -1500kyrs$ with $\omega = 0.122$ and initial values $(V, A, C) = (0.8, 0.3, 0.5)$. In Figure 7-7, we observe that for the same initial conditions, a stable period $(1, 3)$ solution

grazes at $\mu = 0.467$. When μ is increased further to $\mu = 0.4762$, the period $(1, 3)$ solution destabilises and transitions to a period $(1, 2)$ (see Figure 7-8). This shows that the grazing bifurcation has destabilised the period $(1, 3)$ solution. In Figure 7-9 a further increase in μ leads to an observed stable period $(1, 2)$ solution for $\mu = 0.6$ behaviour consistent with the behaviour observed in Figure 5-26. Furthermore, in Figure 7-10, we observe that when μ is increased and $\omega = 0.123$, the stroboscopic plots of the Omega limit set of F shows that before grazing μ_g, we have stable period $(1, 2)$ which coexists with the unstable period $(1, 3)$ solution. In Figure 7-11 when we consider $\mu > \mu_g$, that is taking $\mu > 0.525$ we observe the period $(1, 2)$ solution.

If we fix μ and ω and vary the initial conditions, we observed that we have different types of solutions. For example, in Figure 7-16, we observe a period $(1, 2)$ solution and in Figure 7-15, we observe an initial transient with close to $(1, 3)$ dynamics which then ultimately evolves to $(1, 2)$ motion. We note that there is a dramatic change in the behaviour of the system when $t \approx -500$. This occurs when there is a local minimum at which $F < 0$ which occurs for the first time in a 'glacial region'. The resulting instability is the result of a *grazing transition*. Using this observation we can now construct the domain of attraction.

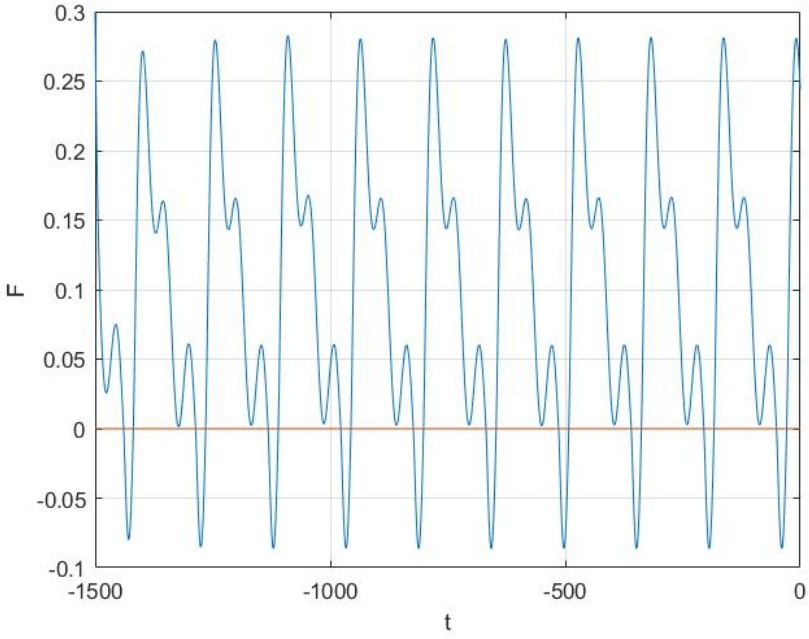

Figure 7-7: The time solution showing very near grazing orbit for $\mu = 0.467$ and $\omega = 0.122$ with initial conditions $(V, A, C) = (0.8, 0.3, 0.5)$ simulated forward in time.

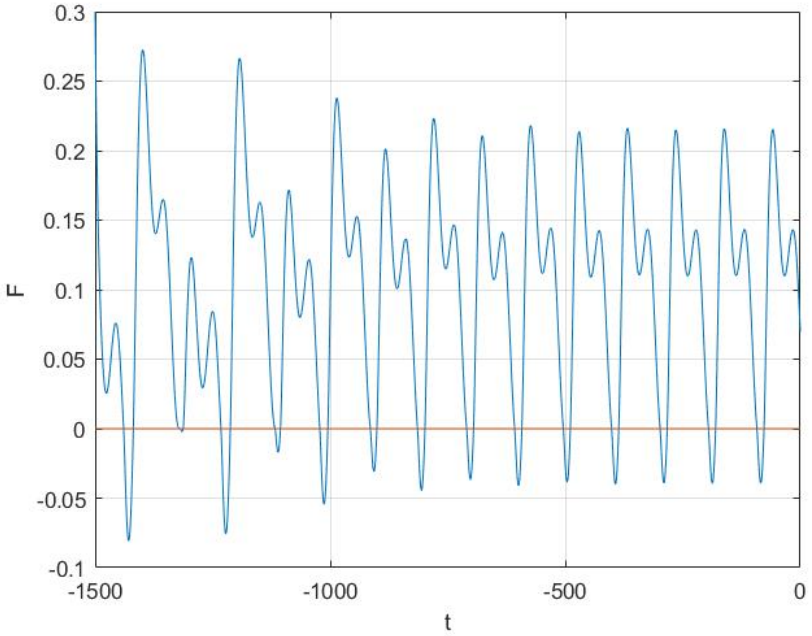

Figure 7-8: The graph showing the $(1, 3)$ solution losing stability and evolving to a period $(1, 2)$ solution for $\mu = 0.47$ and $\omega = 0.122$ with initial conditions $(V, A, C) = (0.8, 0.3, 0.5)$.

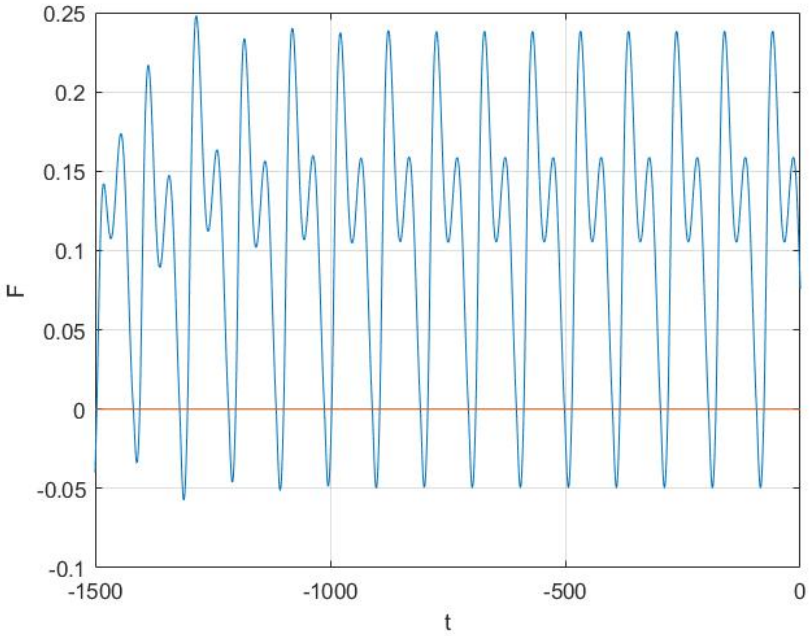

Figure 7-9: The graph showing a stable period $(1, 2)$ solution with $\mu = 0.6$, $\omega = 0.122$ and initial conditions $(V, A, C) = (0.8, 0.3, 0.5)$.

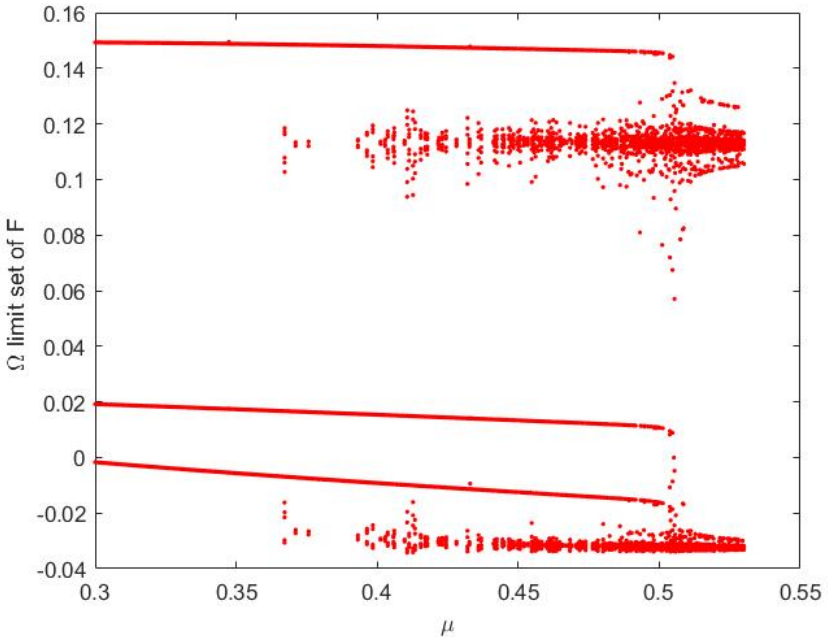

Figure 7-10: The Poincaré section points on the Omega limit set of F, as a function of μ with $\omega = 0.123$ showing the existence of different types of solutions before the grazing bifurcation at $\mu = 0.505$. The stable period $(1, 3)$ solution and the unstable $(1, 2)$ period solution as μ increases.

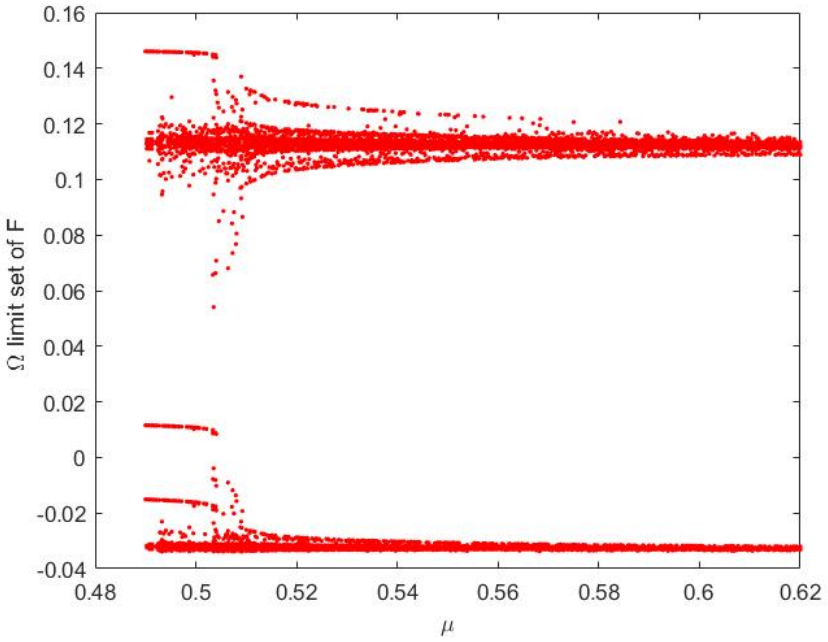

Figure 7-11: The Poincaré section of Omega limit set of F, as a function of μ with $\omega = 0.123$ showing the stable period $(1, 2)$ solutions after the grazing bifurcation at $\mu = 0.505$.

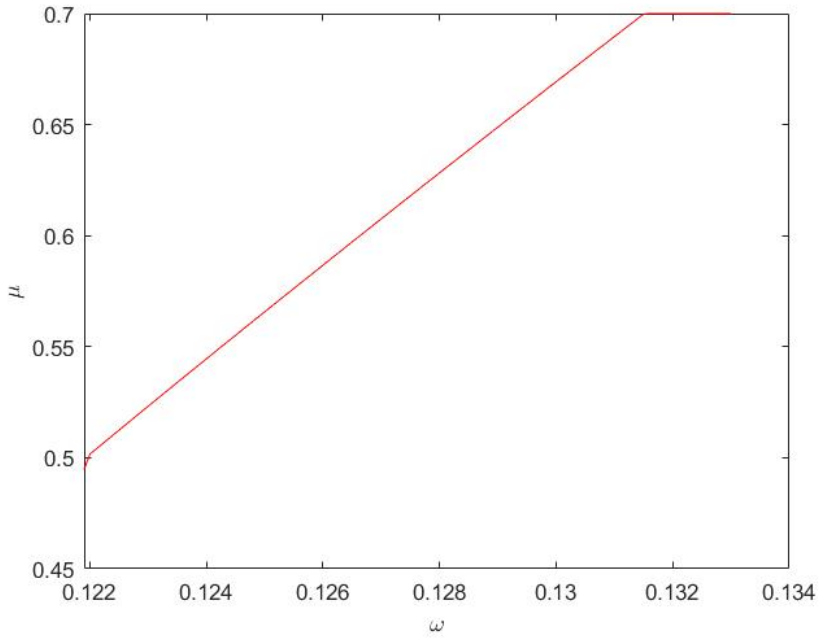

Figure 7-12: The graph showing the grazing curve of the period $(1, 3)$ orbit.

7.3 Domains of attraction

The transition from one periodic solution to the other, say from $(1, 3)$ to $(1, 2)$ implies that the period $(1, 3)$ solution will still be in existence but unstable and not dominant. Therefore there is coexistence of solutions. That is, the co-existence, for example, of the $(1, 2)$ and $(1, 3)$ solutions at the values of $\omega = 0.128$ and $\mu = 0.467$, leads to the possibility of seeing both types of behaviour for a variety of initial conditions, and indeed an evolution from one to the other for certain initial conditions. To investigate this we calculated the domains of attraction for these two orbits. These are the subsets of the three dimension phase space (V, A, C) such that the Omega-limit set of the iterations of the map P_S is either the $(1, 2)$ or the $(1, 3)$ orbit. It is problematic to find the full three dimensional sets, so for convenience we find a two-dimensional projection by fixing one of the variables say A $= 0.55$ a value used in [57]. The domain of attraction given in Figure 7-13 is obtained when we consider random initial values (V, C) for $\omega = 0.128$ and $\mu = 0.467$ and solved the smoothed PP04 model forward in time using Matlab solver ode45 for time interval $t = [-1000, 0]$. The frequencies detected when using the Matlab Fast Fourier Transform (FFT) , are used in determining the types of solutions and hence the colouring.

In Figure 7-13 we see that for the given choice of parameter values, the domain of attraction for the $(1, 3)$ orbit is much larger than for the $(1, 2)$ orbit. There is evidence, as we might expect, for more complex dynamics close to the boundary of the sets. This figure is consistent with Figure 7-15 when we explore the time evolution of the solutions for initial conditions in the green region but close to the red boundary. If we consider $\omega = 0.1275$ and the same amplitude $\mu = 0.467$, Figure 7-14

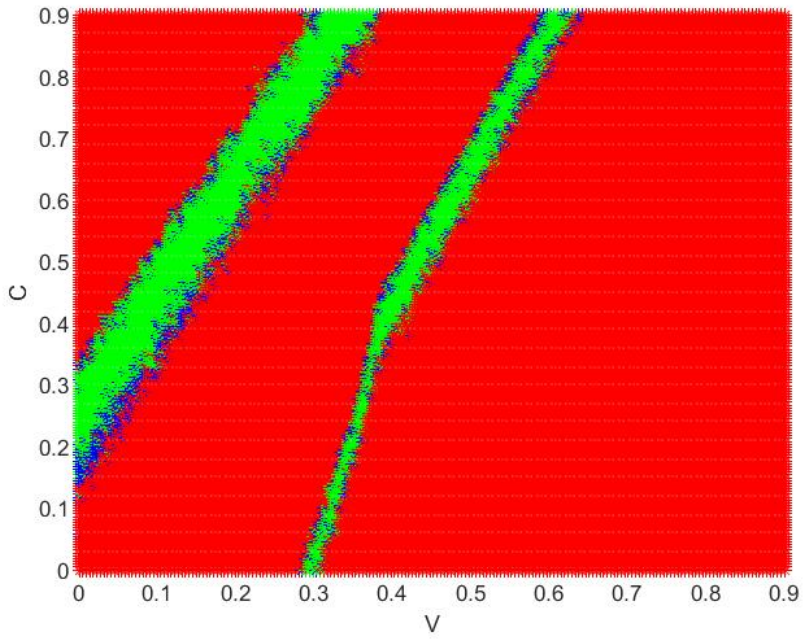

Figure 7-13: Domains of attractions for the periodic solutions with periodic forcing where $\omega = 0.128$ and amplitude $\mu = 0.467$ where the larger red region represents domain for period $(1, 3)$ solution, the smaller green region is the domain for period $(1, 2)$ solution and the very small blue regions are the domains of attraction for the other solutions.

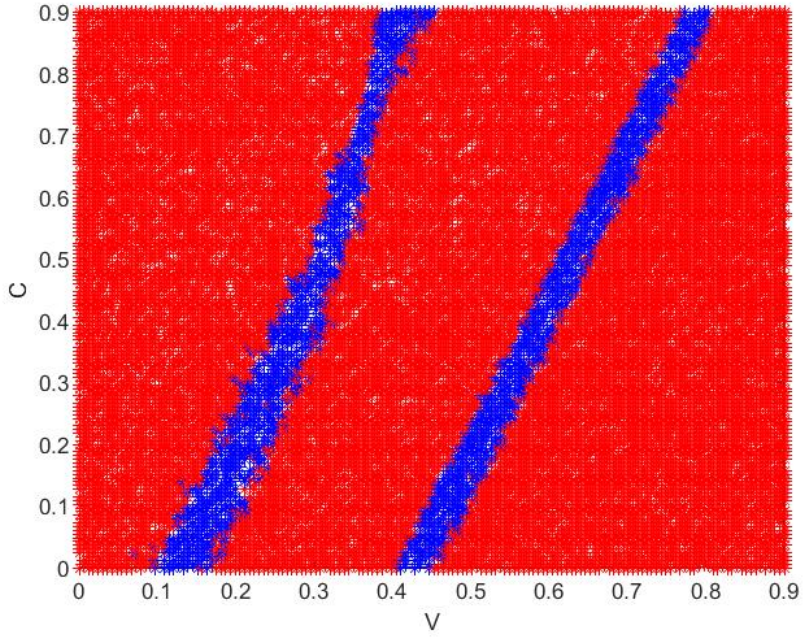

Figure 7-14: Domains of attractions for the periodic solutions with periodic forcing where $\omega = 0.1275$ and amplitude $\mu = 0.467$ where the larger red region represents domain for period $(1, 3)$ and the small blue regions are the domains of attraction for other solutions such as the period $(2, 4)$ solutions.

shows a large the domain of attraction for the $(1, 3)$ solution than for other solutions such as the $(2, 4)$ periodic solution. These results are consistent with the observed stroboscopic Omega limit sets of the F for the same frequency and amplitude in Figure 5-27.

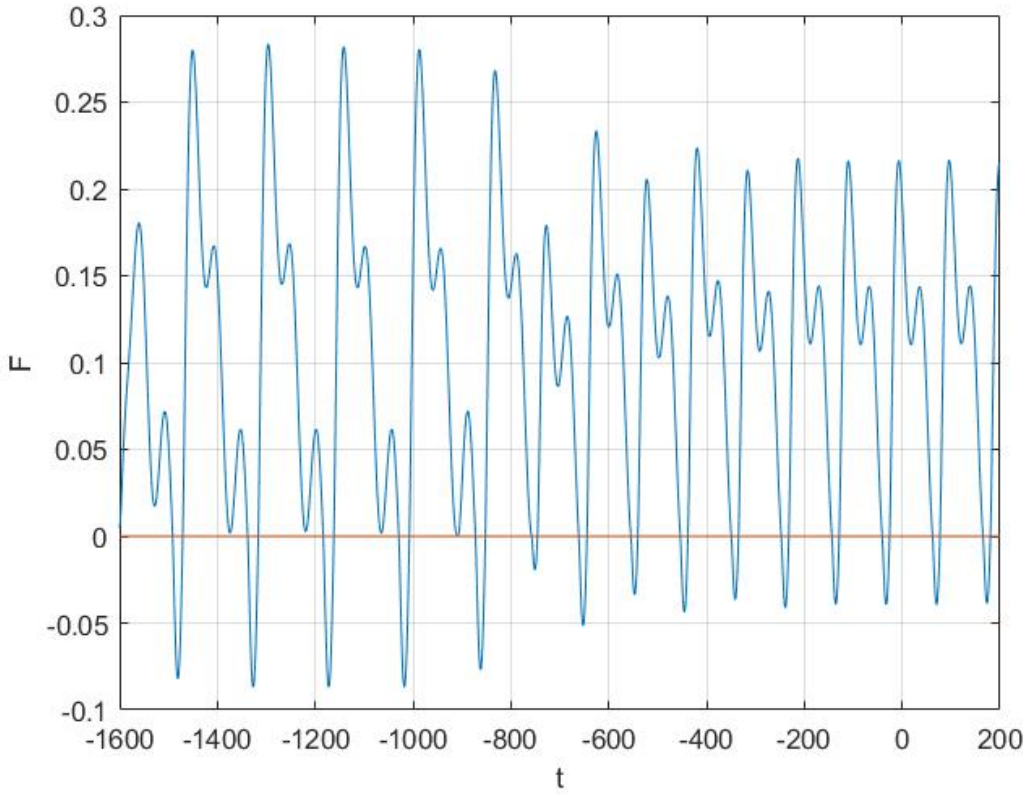

Figure 7-15: The time evolution of $F(t)$ for the system showing the slow evolution from a $(1, 3)$ orbit to a $(1, 2)$ orbit when $\omega = 0.122$ and $\mu = 0.4762$ with initial conditions $(V, A, C) = (0.4, 0.55, 0.7)$.

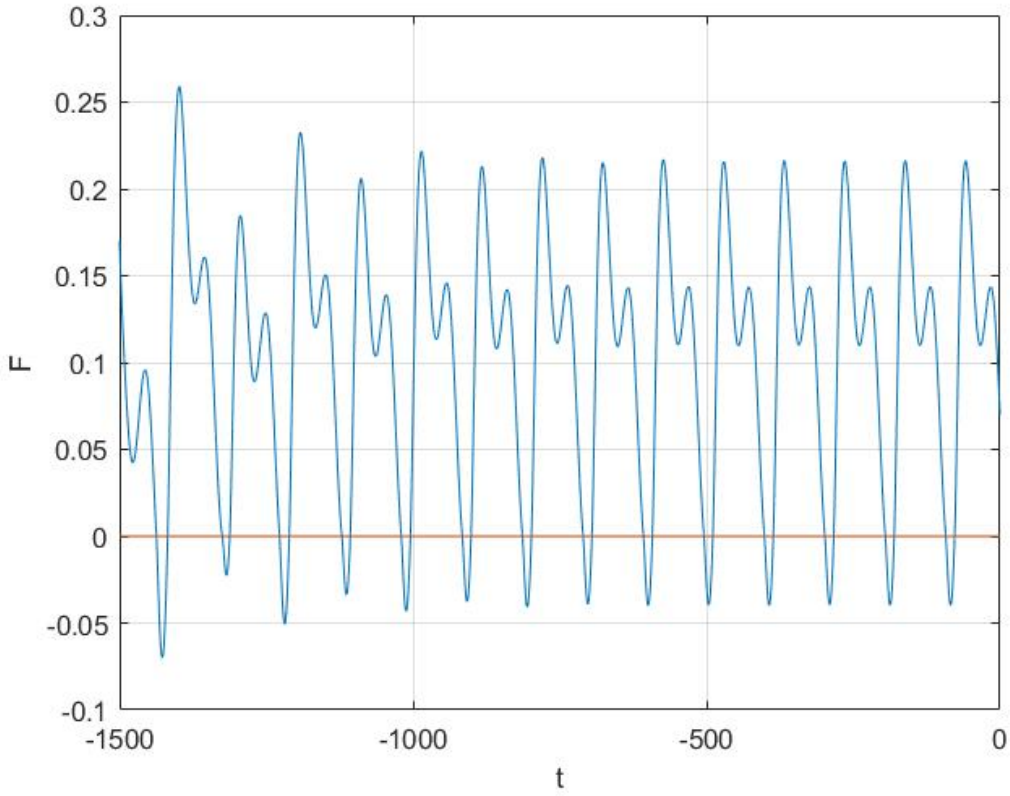

Figure 7-16: The time evolution of $F(t)$ for the system showing the evolution of a $(1, 2)$ orbit when $\omega = 0.122$ and $\mu = 0.4762$ with initial conditions $(V, A, C) = (0.6, 0.3, 0.7)$.

7.4 Summary

From this chapter we have shown that for the periodically forced PP04 model :

1. The $(1, 3)$ periodic solution experiences grazing bifurcation for a certain values of frequency and amplitude.
2. When the periodic solution grazes, the Poincaré discontinuity mapping shows that the $(1, 3)$ periodic solution destabilises and hence a transition to the $(1, 2)$ solution is possible.
3. The grazing bifurcation of the $(1, 3)$ leads to a loss of physicality of the solution .

Chapter 8

Links back to climate and conclusions

We have performed the analysis of the PP04 model with no forcing, periodic forcing and quasi-periodic forcing (with two or three modes). In this chapter, we are linking or comparing the results we observed for the analysis of the PP04 model with what has been observed in the climate.

8.1 The unforced system

From the results, the PP04 unforced system exhibits a limit cycle or a relaxation oscillator of a period about 140kyr. This result implies that the Earth's climate system if left on itself without the contribution of astronomical forcing, will oscillates successively between the two climatic states with a period of about $\frac{2\pi}{\omega} = 147.2kyrs$. We noted that this period exhibited by this system is bigger but closer to the expected or observed period of $100kyrs$, and much bigger than the previously observed $40kyrs$ period before the MPT as observed from the paleoclimate records. However the form of the orbit coincides with the expected behaviour of the system whereby the the climatic system spends most of its time on the glacial state and a little time on the interglacial states (see Figure 8-1). We have also observed that the limit cycle appears to be stable so that the unforced climate system will always experience successive glacial cycles irrespective of initial state of the climate. Nevertheless these results are observed using the constants in [57] obtained experimentally to fit the results of reconstructed climate data.

On the other hand, when varying the constant d that controls the threshold in the parameter of salty bottom water formation efficiency which induce the switch between the glacial and the interglacial states, the results shows that the system might lock into one type of climatic state. We observed that for $d = 0.32$ or $d = -0.72$, the system experiences a border collision bifurcation and therefore for $d > 0.32$ or

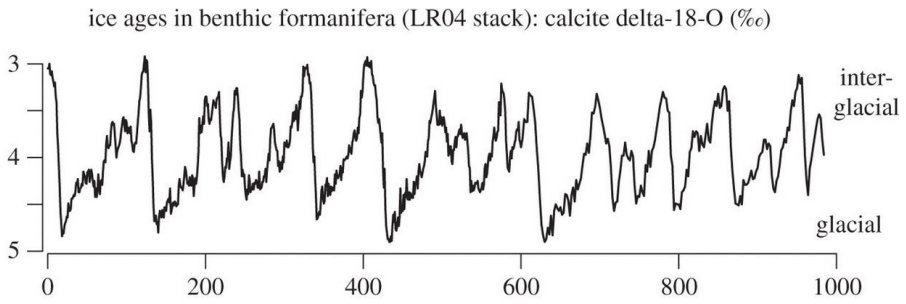

Figure 8-1: The graph showing climatic fluctuations of the Pleistocene period using the oxygen isotopic ratio of calcite shells of benthic foraminifera. (Image from Crucifix [13])

$d < -0.72$ the system has stable equilibria. This results suggests that for these values of d the climate system can get locked into one type of glacial state, that is either glacial state or inter-glacial state respectively.

8.2 The periodically forced system

The periodically forced PP04 model with forcing of the form $\mu\ sin(\omega t)$, has a range of different solutions observed depending on the strength and frequency of the forcing.

When the periodic forcing is considered for physically relevant values of $(\mu, \omega) = (0.467, 0.1476)$ that are approximately equal to the obliquity component of the forcing, only a stable $(1, 3)$ periodic orbit is observed (see Figure 5-26). The period of this periodic orbit is $\frac{3*2\pi}{\omega} = 127.7kyr$ which is slightly longer than the observed period of $100kyr$. We note that $100kyr$ would be very close to the period of the $(2, 5)$ periodic orbit. However, we have not seen any evidence of this orbit existing close to the realistic parameter values. Furthermore we also observed that the $(1, 3)$ orbit appears to be globally stable so no matter where you start you get attracted to the limit cycle. This results shows that when the astronomical forcing is solely driven by obliquity, according to the PP04 model the climate system will still experience the cyclic glacial cycles but with a reduced period of $127.7kyr$. The results further showed an introduction (addition) of the other periods into the periodic solutions of the periodically forced PP04 model due to the introduction of the Milankovitch cycle. Therefore according to this results, within one glacial cycle, the climate system will experience two glacial states of different strength. The rapid reduction of ice volume during the glacial state is also observed in real climate data records as observed in Figure 8-1.

The solutions of the periodically forced system has also exposed the existence of two different periodic solutions for each values of (μ, ω), obtained dependent on where we started in the parameter space. One of these solutions is observed to be stable while the other unstable, implying that according to the PP04 model the

type of climate observed is dependent on the amount of astronomical forcing at that particular period or time. Furthermore, the results depict that the climate system can experience the usual or previously observed climate or a slightly different but similar one for the same forcing. The starting time for periodic solutions, say t_0, was observed to change by $\frac{\pi}{n\omega*}$ within the area of existence of periodic solutions for small values of μ (small amount of forcing). This demonstrates that the phase of the response (V, A, C) to the insolation forcing, whilst locked to it for a particular periodic orbit, differs from it. This phenomenon has been observed in the record of the ice ages in which the Milankovitch cycles are not always seen to be in phase with the cooling and warming periods.

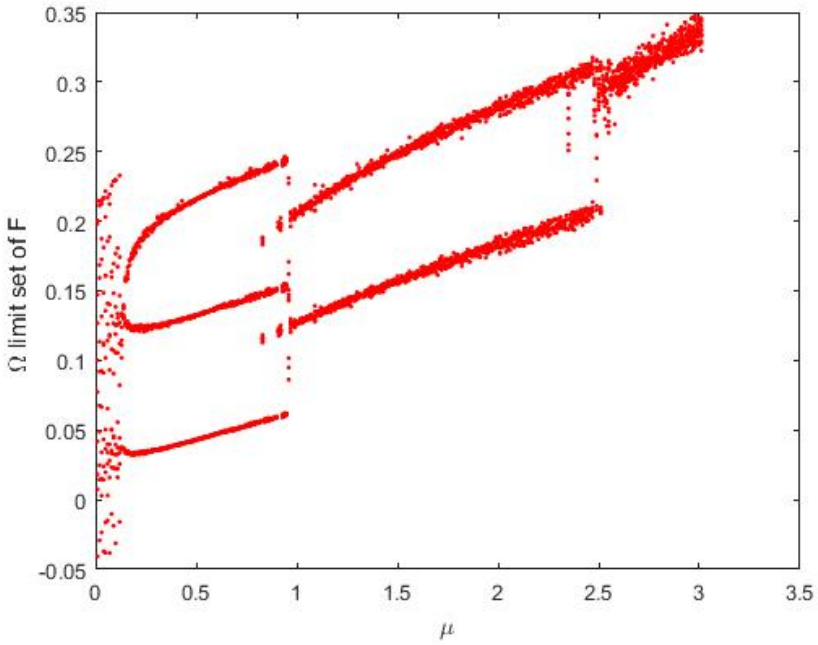

Figure 8-2: The Poincaré section points on the Omega limit set of F, as a function of μ with $\omega = 0.1476$ showing the different types of solutions as μ increases from quasi-periodic, to $(1,3)$,$(1,2)$ and then $(1,1)$ with regions of co-existence.

The 'tongues' in Figure 8-3 are observed to have regions where periodic solutions overlap for $\mu \geq 0.15$ and certain values of ω. This gives the co-existence of periodic solutions. At $\mu = 0.25$ the two types of period $(1,3)$ solutions cease to exists. These findings implies that for that certain amount of forcing that coincides with certain values of μ and ω the climate system can assume any of the periodic solutions, for instance a period $(1,3)$ or a period $(1,4)$ solution. Therefore as the value of μ or of the frequency increases, the climate system has a possibility of switching to a different type of periodic cycle.

When increasing the frequency of forcing ω or the strength of the forcing μ, we observed an abrupt existence or destruction of a period $(1,3)$ solution. However the period $(1,2)$ solution persisted for a while and ceased to exist at a period doubling. The birth of a period $(1,3)$ solution is observed as a transition from the longer period

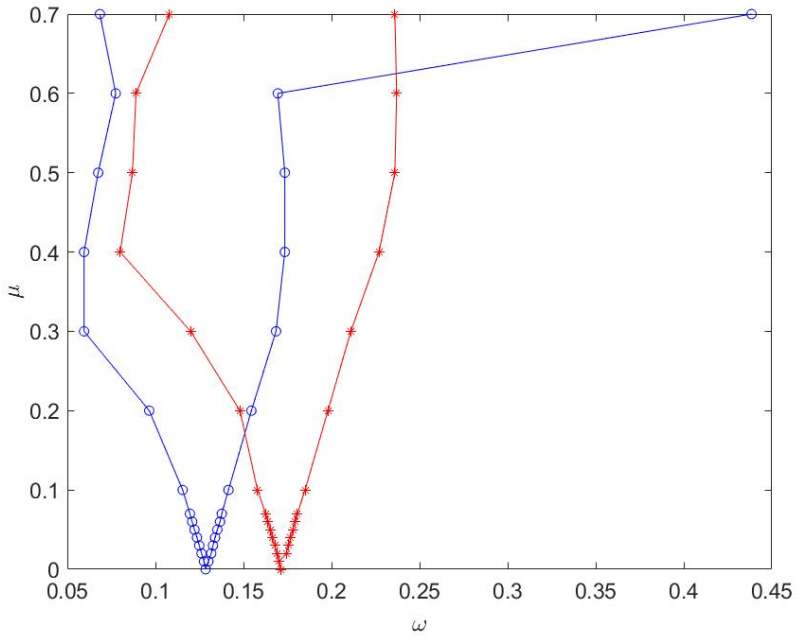

Figure 8-3: The graph showing regions of existence of period $(1, n)$ orbits when both μ and μ are varied with regions of co-existence.

$(1, 2)$ solution to a shorter $(1, 3)$ orbit, when the phase of the forcing is increased. However, when the strength of the forcing is increased, the transition from period $(1, 3)$ solution to period $(1, 2)$ solution, illustrates a similar mechanism observed at the mid-Pleistocene transition (MPT). Therefore the grazing bifurcation might be assumed to reasonably explain the MPT mainly because the transition at the MPT is from a small period to a bigger (i.e from $40kyrs$ to $100kyrs$).

8.3 The quasi-periodically forced PP04 model

The time series results we observed for the quasi-periodically forced PP04 model in Figure 8-4, showed a response behaviour of ice volume V similar to the actual response reconstructed from benthic foraminifera (see Figure 8-1). The presence of the $100kyr$ periodicity was evidently seen in the FFT plots which coincides with the peak observed at index $k = 14$. The results of this system also showed a dependence on the value of ω_2. For rational phase variable ω_2, we observe periodic solutions and invariant curves for irrational phase variable ω_2. Furthermore the size of an invariant curve increases with μ_2 that breaks up as μ_2 reaches a certain critical value. Then the results showed the existence of apparent chaotic solutions for large μ_2.

The existence of periodic solutions for rational phase implies that, according to the PP04 model, the climate system forced with forcing with rational phase will experience the period $(1, n)$ glacial cycles. The number of glacial states before the transitioning to the interglacial is dependent on the phase and the strength of the

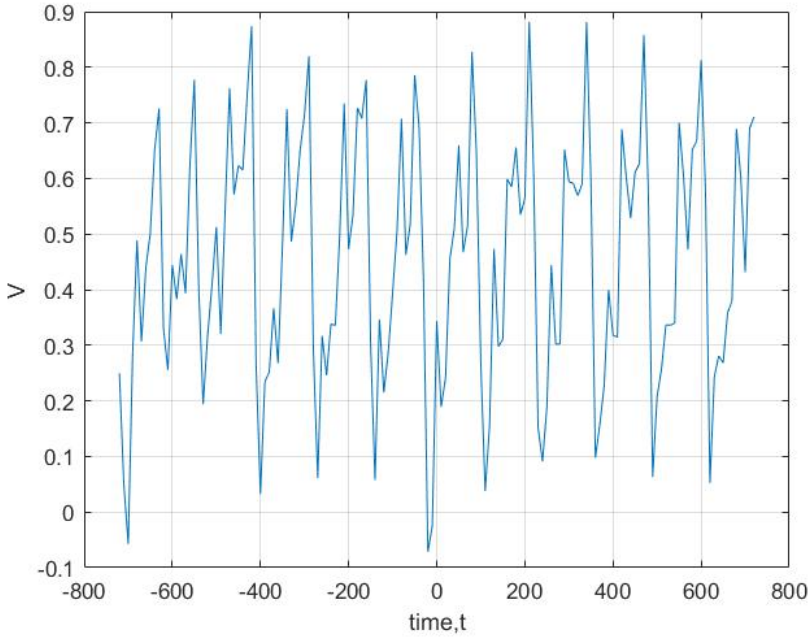

Figure 8-4: The graph showing the time series solution of V for $\mu_2 = 0.6$ and $\omega_2 = 1.6180339888 \times \omega_1$. We can compare this with Figure 8-1.

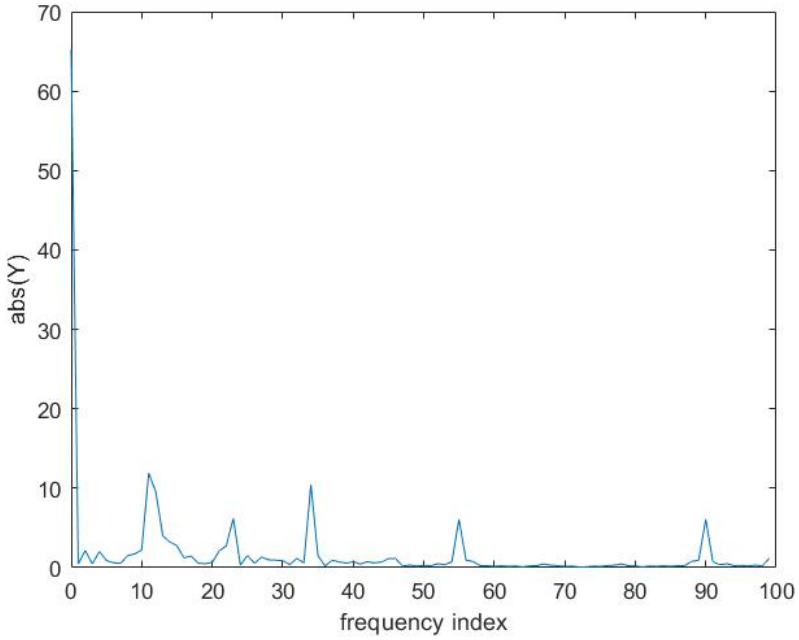

Figure 8-5: The graph showing the frequencies available in the system when $\mu_1 = 0.467$, $\omega_1 = 0.1476$, $\mu_2 = 0.6$ and $\omega_2 = 1.6180339888 \times \omega_1$. We observe the peak at $k = 14$ which is consistent with a $100kyr$ period.

forcing. However, for the irrational forcing, the solutions of the system will always be arbitrarily closer to the previous ones. This observation implies that for this type of forcing, according to the PP04 model the climate system will experience cyclic oscillations of volume of ice with some abrupt changes during the entire glacial states period. These abrupt changes were also observed in the reconstructed data of past climate (see Figure 8-1) and has been associated with the Heinrich and or Dansgaard Oeschger events[13]. The existence of apparent chaotic solutions in the quasi-periodically forced PP04 model for large μ_2, suggest that the climate system might become chaotic if the astronomical forcing is very strong. However these large values of the forcing might not be relevant to the Pleistocene glacial cycles. Ashwin et al [3] also observed the same solutions and came to the conclusion that, chaotic solutions for large amplitude might be observed in regions of the phase space that may not be relevant to the late Pleistocene glacial cycles.

8.4 Conclusion and remarks

We conclude the contents of this thesis by stating the new results stated in this thesis and present the ideas for further research.

In Chapter 4 we studied the unforced PP04 model

$$\dot{\mathbf{X}} = L\mathbf{X} + \mathbf{b}^{\pm}$$

with dynamics defined in $S^{\pm}$ and the discontinuity boundary $\Sigma = \{\mathbf{X} : \mathbf{c}^T\mathbf{X} + d = 0, \}$. This system showed existence of two virtual fixed points and a periodic solution between them. This periodic solution is observed to exists when the parameter d of the ocean stratification is within the interval $-0.72 < d < 0.32$, however at either $d = 0.32$ or $d = -0.72$, the system experiences a Border Collision Bifurcation.

In Chapter 5, we studied the periodically forced PP04 model of climate change defined

$$\dot{\mathbf{X}} = L\mathbf{X} + \mathbf{b}^{\pm} + \mu \sin(\omega t)$$

so that the period of the forcing is given by

$$T = \frac{2\pi}{\omega}.$$

We have first made a mathematical study of this model, which revealed the existence of stable and unstable periodic orbits marked by saddle node bifurcation, with subtle domains of attraction for small forcing. However, when the values of μ and ω were increased, the grazing bifurcation was observed which consequently lead to unstable periodic solutions. These values of μ and ω, marked the boundary between

the physical and non-physical solutions. The increase in the phase of the forcing exhibited the period doubling transition from period (m, n) solutions to period $(2m, 2n)$ solutions.

In Chapter 6 the derivation of the linear map motivated the study of the quasi-periodically forced PP04 model given by

$$\dot{\mathbf{X}} = L\mathbf{X} + \mathbf{b}^{\pm} + \mu_1 \sin(\omega_1\, t) + \mu_2\ \sin(\omega_2\, t).$$

It was observed that under small additional quasi periodic forcing forcing, the stable periodic orbits calculated for physically realistic values of the parameters persisted and have a similar form to those of the observed glacial cycles. Therefore the quasi-periodically forced system was studied as a perturbation of the periodically forced one using linear map and stroboscopic plots of Poincaré map with sampling period $T = \frac{2\pi}{\omega_1}$. The study through both maps showed the existence of period n cycle solutions when the forcing is rational and invariant curves or tori when irrationally forced. The time evolution solutions showed quasi-periodic solutions. However, for large amplitudes, the stroboscopic map showed apparent chaotic solutions on the phase plane.

In Chapter 7 we further studied the periodically forced PP04 model and our main focus was in showing evidence of grazing bifurcation of the period $(1, 3)$ solution. We studied the grazing bifurcation of the PP04 model using discontinuity mapping and then showed the domains of attraction of different solutions. We observed that at the grazing bifurcation, the discontinuity mapping has a square-root singularity and that periodic solution loses stability and physicality.

However other researchers who studied the climate models have observed a Hopf bifurcation in their system [67, 68] and associated the MPT with this bifurcation. Other researchers such as as Mitsui *et al.* [46, 47], Crucifix [13] and Ashwin *et al.* [3] who studied the PP04 model, also observed the Hopf bifurcation as parameter is varied and associated this bifurcation with the MPT. In our study of the PP04 model, in Figure 5-26 we observed a sudden transition from a $(1, 3)$ periodic solution to a $(1, 2)$ periodic solution when a parameter is varied which depicts a transition from a bigger period to a smaller one, the opposite way round from the MPT. However Figure 5-27 shows a transition from a $(2, 4)$ periodic solution to a $(1, 3)$ periodic solution which closely resemble the MPT. Therefore we suggest that the MPT can be explained using the grazing bifurcation as all these are sudden transitions.

A further study is needed to understand better the importance of including additional climatic terms into the PP04 model. Much more work needs to be done to fully develop the discontinuity mapping in order to do a thorough study of the grazing transition. The study of the of all other transitions in the whole of the parameter space under the effect of additional larger terms in the quasi periodic forcing also needs be done. Furthermore, the investigation of strange non-chaotic attractors and

calculation of Lyapunov exponents should be done. However, the PP04 model as a simple model of climate change has a rich structure as a discontinuous dynamical system, and is a plausible explanation of the glacial cycles. Nevertheless, the study of more advanced models of climate change and other models of climate with discontinuities such as Paillard and Parrenin model of 2012 [58] and the Stommel model of thermohaline circulation [21, 80] are needed.

Appendix A

Matlab codes used

The sample of the matlab codes used in this thesis are:

A.1 The Matlab codes for solving the smoothed PP04 model

This is the code that provides the PP04model: function [Vdot] = paillard04int(t, VAC)

Vdot = zeros(3, 1);
global e alpha y c a b d h eta delta;

$x = 1.3$; $z = 0.8$; beta = 0.5; gamma = 0.7;

$\tau_V = 15$;
$\tau_A = 12$;
$\tau_C = 5$;
insolNorth = insol65Nperiodc(t,e); insolS = insol60(t,e);

F = a*VAC(1) - b*VAC(2)-c*insolS + d;

Vr = -x*VAC(3)-y*insolNorth + z;

discont = swich(F,eta);

Cr = alpha*insolNorth - beta*VAC(1) + gamma*discont + delta;
Vdot(1) = (Vr-VAC(1))/τ_V;
Vdot(2) = (VAC(1)-VAC(2))/τ_A;
Vdot(3) = (Cr - VAC(3))/τ_C;
Vdot = [Vdot(1); Vdot(2); Vdot(3)];
end

function [t, V, A, C] = $pp041pdcforcededit(tf, V_{init}, A_{init}, C_{init})$
global omega $t_{initial}$;
$TT = (2 * pi)$/omega;
options=odeset('AbsTol',1e-12,'RelTol',1e-12);
$[t, VAC]$ = ode45(@paillard04pdcforced, [$t_{initial}$: TT: tf], [$V_{init}, A_{init}, C_{init}$],options);
V = VAC(:, 1);
A = VAC(:, 2);
C = VAC(:, 3);
end

A.1.1 Function to regularise the model

This is the code that represents the Heaviside function as a *tanh* function and hence providing the regularization of the PP04 model:

function [discont] =swich (F,eta)
discont= (1+tanh(-F*eta))/2;
end

A.1.2 Script file for solving the system

This is the code to solves the smoothed PP04 model as an initial value problem:

close all
clc
global alpha y c a b d eta amp omega e delta $t_{initial}$

eta=1000;
y =0.5;
alpha =0.15;
c = 0;
e = 23.58;
omega = 0.121;
amp = 0.467;
a = 0.3;
b =0.7;
d = 0.27;

delta = 0.4;
V_{init} = 0.1;
A_{init} = 0.55;
C_{init} = 0.2;
$t_{initial}$ = -15000;
tf = 0;

[t, V, A, C] = pp041pdcforcededit(tf,V_{init}, A_{init}, C_{init});
insolNorth = insol65Nperiodicbifurc(t);
F = a*V-b*A+d;
figure(2)
plot(A,V);
hold on;
plot(A,1/a*(b*A-d));hold off;
xlabel('A');
ylabel('V');hold on;
figure(3) plot(t,C,'b'); hold on;
xlabel('t');

figure(4) plot(t,V,'r'); hold on;
xlabel('t,in Kyrs');

figure(5) plot(t,A,'g'); hold on;
xlabel('t,in Kyrs');

figure(7) plot(t,F)
hold on;
plot(t,0*t)
hold off;
xlabel('t');
ylabel('F');hold on;
grid on

This is the code that provides the function for astronomical forcing:

function [insolNorth] = insol65Nperiodicbifurc(t)
global omega amp
insolNorth= amp*sin(omega*t);
end

A.2 Matlab codes for solving the non-smooth PP04 system

This is the code that solves the non-smooth PP04 model using the tabulated values given in the paper

function f = algcal(x)

global mu om nn

x0 = x(1:3)'; t0 = x(4); t1 = x(5);

L = [-1/15 0 -1.3/15;1/12 -1/12 0;-0.5/5 0 -1/5];
e = [-0.5/15 0 0.15/5]';
bp = [0.8/15 0 0.4/5]';
bm = [0.8/15 0 1.1/5]';

cc = [0.3 -0.7 0];
dd = 0.27;

T = 2*pi*nn/om; t2 = t0+T;

```
Lbp = L\bp;
```

```
Lbm = L\bm;
```

$L2 = L * L + om^2 * eye(3);$

```
a = L2\(-om*mu*e);
```

$b = L * a/om;$

x1 = $expm(L * (t1 - t0)) * (x0 + Lbp - a * \cos(om * t0) - b * \sin(om * t0)) - Lbp + a * \cos(om * t1) + b * \sin(om * t1);$
x2 = $expm(L * (t2 - t1)) * (x1 + Lbm - a * \cos(om * t1) - b * \sin(om * t1)) - Lbm + a * \cos(om * t2) + b * \sin(om * t2);$
f1 = dot(cc,x1) + dd;
f2 = dot(cc,x2) + dd;
r1 = x2 - x0;
f = [r1' f1 f2]';
end

A.2.1 The script file to solve the system of algebraic equations

```
close all;
clear all;
clc;
global mu om nn


nn = 3;
om = 0.132;
zero = zeros;
timeone = zeros;
mu = 0.3;
x = [0.1102 0.4329 0.9405 1.6829 100];


[x,fval]=fsolve(@algcal,x);
x0 = x(1:3)';
V0 = x0(1);
t0 = x(4);
t1 = x(5);
L = [-1/15 0 -1.3/15;1/12 -1/12 0;-0.5/5 0 -1/5];
e = [-0.5/15 0 0.15/5]';
bp = [0.8/15 0 0.4/5]';
bm = [0.8/15 0 1.1/5]';
cc = [0.3 -0.7 0];
dd = 0.27;


T = 2*pi*nn/om;
t2 = t0+T;


 Lbp = L\bp;

Lbm = L\bm ;

L2 = L * L + om^2 * eye(3);


a = L2\(-om*mu*e);

b = L*a/om;

N = 100;

dtp = (t1 - t0)/N; dtm = (t2 - t1)/N; tp = [t0:dtp:t1];
```

```
tm = [t1:dtm:t2];

for n = 1:N+1

tpn = tp(n);
x1 = expm(L*(tpn-t0))*(x0+Lbp-a*cos(om*t0)-b*sin(om*t0))-Lbp+a*cos(om*tpn)+
b*sin(om*tpn);
Fp(n) = dot(cc,x1) + dd;
Vp(n) = x1(1);
Ap(n) = x1(2);
Cp(n) = x1(3);
end
x11 = expm(L*(t1-t0))*(x0+Lbp-a*cos(om*t0)-b*sin(om*t0))-Lbp+a*cos(om*t1) +
b*sin(om*t1);
for n = 1:N+1
tmn = tm(n);
x2 = expm(L*(tmn-t1))*(x11+Lbm-a*cos(om*t1)-b*sin(om*t1))-Lbm+a*cos(om*tmn)+
b*sin(om*tmn);
Fm(n) = dot(cc,x2) + dd;
Vm(n) = x1(1);
Am(n) = x1(2);
Cm(n) = x1(3);
end

x22 = expm(L*(t2-t1))*(x11+Lbm-a*cos(om*t1)-b*sin(om*t1))
- Lbm+a*cos(om*t2)+b*sin(om*t2);
T = 2*pi*nn/om;
hold on
plot(tp+T,Vp,'r',tm + T,Vm,'r')
plot(tp,Ap,'b',tm,Am,'b')
plot(tp+T,Ap,'b',tm+T,Am,'b')
plot(tp,Cp,'m',tm,Cm,'m')
plot(tp+T,Cp,'m',tm+T,Cm,'m')
plot(tp,Fp,'k',tm,Fm,'k',tp,Fp==0,'g')
plot(tp+T,Fp,'k',tm+T,Fm,'k',tm,Fm==0,'b')
plot(tp,mu*sin(om*tp),'g',tm,mu*sin(om*tm),'g')
plot(tp+T,mu*sin(om*tp),'g',tm+T,mu* sin(om*tm),'g')
hold off
```

Bibliography

[1] R.B. Alley. Ice-core evidence of abrupt climate changes. *Proceedings of the National Academy of Sciences*, 97(4):1331–1334, 2000.

[2] P. Ashwin and P. Ditlevsen. The middle pleistocene transition as a generic bifurcation on a slow manifold. *Climate dynamics*, 45(9-10):2683–2695, 2015.

[3] P. Ashwin, C. David Camp, and A.S. von der Heydt. Chaotic and non-chaotic response to quasiperiodic forcing: Limits to predictability of ice ages paced by milankovitch forcing. *Dynamics and Statistics of the Climate System*, 3(1): dzy002, 2018.

[4] A.M. Barry, E. Widiasih, and R. Mcgehee. Non-smooth frameworks for an extended budyko model. *Discrete & Continuous Dynamical Systems-B*, 22(6): 2447, 2017.

[5] N. Bouttes, D. Paillard, and D.M.V.A.P. Roche. Impact of brine-induced stratification on the glacial carbon cycle. *Climate of the Past*, 6(5):575–589, 2010.

[6] M.I. Budyko. The effect of solar radiation variations on the climate of the earth. *tellus*, 21(5):611–619, 1969.

[7] R. Calov and A. Ganopolski. Multistability and hysteresis in the climate-cryosphere system under orbital forcing. *Geophysical research letters*, 32(21), 2005.

[8] A.S. Cassol, F.L.S. Veiga, and M.H.R. Tragtenberg. Strange nonchaotic attractor in a dynamical system under periodic forcing. *arXiv preprint cond-mat/0002329*, 2000.

[9] T.B. Chalk, M.P. Hain, G.L. Foster, E.J. Rohling, P.F. Sexton, M.P.S. Badger, S.G. Cherry, A.P. Hasenfratz, G.H. Haug, S.L. Jaccard, et al. Causes of ice age intensification across the mid-pleistocene transition. *Proceedings of the National Academy of Sciences*, 114(50):13114–13119, 2017.

[10] A. Colombo and F. Dercole. Discontinuity induced bifurcations of nonhyperbolic cycles in nonsmooth systems. *SIAM Journal on Applied Dynamical Systems*, 9 (1):62–83, 2010.

[11] A. Colombo, M. di Bernardo, S.J. Hogan, and M.R. Jeffrey. Bifurcations of piecewise smooth flows: Perspectives, methodologies and open problems. *Physica D: Nonlinear Phenomena*, 241(22):1845–1860, 2012.

[12] J. Cortes. Discontinuous dynamical systems. *IEEE Control systems magazine*, 28(3):36–73, 2008.

[13] M. Crucifix. Oscillators and relaxation phenomena in pleistocene climate theory. *Phil. Trans. R. Soc. A*, 370(1962):1140–1165, 2012.

[14] M. Crucifix. Why could ice ages be unpredictable? *arXiv preprint arXiv:1302.1492*, 2013.

[15] M. Crucifix, G. Lenoir, and T. Mitsui. Challenges for ice age dynamics: a dynamical systems perspective. *arXiv preprint arXiv:1512.03557*, 2015.

[16] B. De Saedeleer, M. Crucifix, and S. Wieczorek. Is the astronomical forcing a reliable and unique pacemaker for climate? a conceptual model study. *Climate Dynamics*, 40(1-2):273–294, 2013.

[17] M. di Bernardo and S.J. Hogan. Discontinuity-induced bifurcations of piecewise smooth dynamical systems. *Philosophical Transactions of the Royal Society of London A: Mathematical, Physical and Engineering Sciences*, 368(1930): 4915–4935, 2010.

[18] M. di Bernardo, M.I. Feigin, S.J. Hogan, and M.E. Homer. Local analysis of c-bifurcations in n-dimensional piecewise-smooth dynamical systems. *Chaos, Solitons and Fractals: the interdisciplinary journal of Nonlinear Science, and Nonequilibrium and Complex Phenomena*, 11(10):1881–1908, 1999.

[19] M. di Bernardo, C. Budd, A. R. Champneys, and P. Kowalczyk. *Piecewise-smooth dynamical systems: theory and applications*, volume 163. Springer Science & Business Media, 2008.

[20] M. di Bernardo, C.J. Budd, A.R. Champneys, P. Kowalczyk, A.B. Nordmark, G.O. Tost, and P.T. Piiroinen. Bifurcations in non-smooth dynamical systems. *SIAM review*, 50(4):629–701, 2008.

[21] H.A. Dijkstra. *Nonlinear climate dynamics*. Cambridge University Press, 2013.

[22] M. Ding, C. Grebogi, and E. Ott. Evolution of attractors in quasiperiodically forced systems: From quasiperiodic to strange nonchaotic to chaotic. *Physical review A*, 39(5):2593, 1989.

[23] S. Easterbrook. *Hierachy of climate models*, (accessed 06 June 2020). URL `http://www.cs.toronto.edu/~sme/PMU199-climate-computing/pmu199-2011/modelhierarchy.jpg`.

[24] A. Farokhniaee and E.W. Large. Mode-locking behavior of izhikevich neurons under periodic external forcing. *BMC neuroscience*, 16(1):P140, 2015.

[25] M.I. Feigin. Doubling of the oscillation period with c-bifurcations in piecewise-continuous systems: Pmm vol. 34, no 5, 1970, pp. 861–869. *Journal of Applied Mathematics and Mechanics*, 34(5):822–830, 1970.

[26] M.I. Feigin. On the structure of c-bifurcation boundaries of piecewise-continuous systems: Pmm vol. 42, no. 5, 1978, pp. 820–829. *Journal of Applied mathematics and Mechanics*, 42(5):885–895, 1978.

[27] S. Foale and S.R. Bishop. Dynamical complexities of forced impacting systems. *Philosophical Transactions of the Royal Society of London. Series A: Physical and Engineering Sciences*, 338(1651):547–556, 1992.

[28] A. García-Olivares and C. Herrero. Simulation of glacial-interglacial cycles by simple relaxation models: consistency with observational results. *Climate dynamics*, 41(5-6):1307–1331, 2013.

[29] P. Glendinning. Classification of boundary equilibrium bifurcations in planar filippov systems. *Chaos: An Interdisciplinary Journal of Nonlinear Science*, 26 (1):013108, 2016.

[30] C. Grebogi, E. Ott, S. Pelikan, and J.A. Yorke. Strange attractors that are not chaotic. *Physica D: Nonlinear Phenomena*, 13(1-2):261–268, 1984.

[31] M. Guardia, T.M. Seara, and M.A. Teixeira. Generic bifurcations of low codimension of planar filippov systems. *Journal of Differential Equations*, 250 (4):1967–2023, 2011.

[32] J.D. Hays, J. Imbrie, N.J. Shackleton, et al. Variations in the earth's orbit: pacemaker of the ice ages. *Science*, 194(4270):1121–1132, 1976.

[33] I.M. Held. Climate models and the astronomical theory of the ice ages. *Icarus*, 50(2-3):449–461, 1982.

[34] S.J. Hogan, M.E. Homer, M.R. Jeffrey, and R. Szalai. Piecewise smooth dynamical systems theory: the case of the missing boundary equilibrium bifurcations. *Journal of Nonlinear Science*, 26(5):1161–1173, 2016.

[35] P.J. Holmes. The dynamics of repeated impacts with a sinusoidally vibrating table. *Journal of Sound and Vibration*, 84(2):173–189, 1982.

[36] J. Imbrie, A. Berger, E.A. Boyle, S.C. Clemens, A. Duffy, W.R. Howard, G. Kukla, J. Kutzbach, D.G. Martinson, A. McIntyre, et al. On the structure and origin of major glaciations cycles. pt. ii., the 100000 cycle year. *Paleoceanography*, 8:699–785, 1993.

[37] A.Y. Jalnine and A.H. Osbaldestin. Smooth and nonsmooth dependence of lyapunov vectors upon the angle variable on a torus in the context of torus-doubling transitions in the quasiperiodically forced hénon map. *Physical Review E*, 71(1):016206, 2005.

[38] M.R. Jeffrey. Hidden dynamics in models of discontinuity and switching. *Physica D: Nonlinear Phenomena*, 273:34–45, 2014.

[39] D. Jordan, P. Smith, and P. Smith. *Nonlinear ordinary differential equations: an introduction for scientists and engineers*, volume 10. Oxford University Press on Demand, 2007.

[40] J. Jouzel, C. Lorius, J.R Petit, C. Genthon, N.I Barkov, V.M Kotlyakov, and V.M Petrov. Vostok ice core: a continuous isotope temperature record over the last climatic cycle (160,000 years). *Nature*, 329(6138):403, 1987.

[41] H. Kaper and H. Engler. *Mathematics and climate*, volume 131. SIAM, 2013.

[42] L.E. Lisiecki and M.E. Raymo. A pliocene-pleistocene stack of 57 globally distributed benthic δ18o records. *Paleoceanography*, 20(1):1–7, 2005.

[43] Arianna Marchionne, Peter Ditlevsen, and Sebastian Wieczorek. Synchronisation vs. resonance: Isolated resonances in damped nonlinear oscillators. *Physica D: Nonlinear Phenomena*, 380:8–16, 2018.

[44] M. Maslin. In retrospect: Forty years of linking orbits to ice ages. *Nature*, 540 (7632):208, 2016.

[45] M. Milankovitch. Canon of insolation of the ice age theory. *Israel Program of Scientific Translation*, page 484, 1969.

[46] T. Mitsui and K. Aihara. Dynamics between order and chaos in conceptual models of glacial cycles. *Climate dynamics*, 42(11-12):3087–3099, 2014.

[47] T. Mitsui, M. Crucifix, and K. Aihara. Bifurcations and strange nonchaotic attractors in a phase oscillator model of glacial–interglacial cycles. *Physica D: Nonlinear Phenomena*, 306:25–33, 2015.

[48] F. Montoya, M. Rivera, J. Escalona, and P. Parmananda. Construction of arnold tongue structures for coupled periodic oscillators. *Physics Letters A*, 377(43): 3124–3127, 2013.

[49] A.B. Nordmark. Non-periodic motion caused by grazing incidence in an impact oscillator. *Journal of Sound and Vibration*, 145(2):279–297, 1991.

[50] A.B. Nordmark. Existence of periodic orbits in grazing bifurcations of impacting mechanical oscillators. *Nonlinearity*, 14(6):1517, 2001.

[51] H.E. Nusse and J.A. Yorke. Border-collision bifurcations including period two to period three' for piecewise smooth systems. *Physica D: Nonlinear Phenomena*, 57(1-2):39–57, 1992.

[52] J. Oerlemans. Model experiments on the 100,000-yr glacial cycle. *Nature*, 287 (5781):430, 1980.

[53] H. Osinga, J. Wiersig, P. Glendinning, and U. Feudel. Multistability and non-smooth bifurcations in the quasiperiodically forced circle map. *International Journal of Bifurcation and Chaos*, 11(12):3085–3105, 2001.

[54] D. Paillard. The timing of pleistocene glaciations from a simple multiple-state climate model. *Nature*, 391(6665):378, 1998.

[55] D. Paillard. Glacial cycles: toward a new paradigm. *Reviews of Geophysics*, 39 (3):325–346, 2001.

[56] D. Paillard. Climate science: Predictable ice ages on a chaotic planet. *Nature*, 542(7642):419, 2017.

[57] D. Paillard and F. Parrenin. The antarctic ice sheet and the triggering of deglaciations. *Earth and Planetary Science Letters*, 227(3-4):263–271, 2004.

[58] F. Parrenin and D. Paillard. Terminations vi and viii (530 and 720 kyr bp) tell us the importance of obliquity and precession in the triggering of deglaciations. *Climate of the Past*, 8(6):2031, 2012.

[59] F. Peterka and J. Vacik. Transition to chaotic motion in mechanical systems with impacts. *Journal of Sound and Vibration*, 154(1):95–115, 1992.

[60] Jean-Robert Petit, J. Jouzel, D. Raynaud, N.I. Barkov, J.M. Barnola, I. Basile, M. Bender, J. Chappellaz, M. Davis, G. Delaygue, et al. Climate and atmospheric history of the past 420,000 years from the vostok ice core, antarctica. *Nature*, 399(6735):429, 1999.

[61] P.T. Piiroinen and Y.A. Kuznetsov. An event-driven method to simulate filippov systems with accurate computing of sliding motions. *ACM Transactions on Mathematical Software (TOMS)*, 34(3):13, 2008.

[62] A. Pikovsky, M. Rosenblum, J. Kurths, and J. Kurths. *Synchronization: a universal concept in nonlinear sciences*, volume 12. Cambridge university press, 2003.

[63] A.S. Pikovsky and U. Feudel. Correlations and spectra of strange nonchaotic attractors. *Journal of Physics A: Mathematical and General*, 27(15):5209, 1994.

[64] M.V. Pozdnyakov, A.V. Savin, and D.V. Savin. A nonlinear system with weak dissipation under external force on incommensurate frequency: coexistence of attractors. *arXiv preprint arXiv:1602.02548*, 2016.

[65] A. Prasad, S.S. Negi, and R. Ramaswamy. Strange nonchaotic attractors. *International Journal of bifurcation and Chaos*, 11(02):291–309, 2001.

[66] M.E. Raymo and P. Huybers. Unlocking the mysteries of the ice ages. *Nature*, 451(7176):284, 2008.

[67] B. Saltzman and K.A. Maasch. A first-order global model of late cenozoic climatic change. *Earth and Environmental Science Transactions of the Royal Society of Edinburgh*, 81(4):315–325, 1990.

[68] B. Saltzman and K.A. Maasch. A first-order global model of late cenozoic climatic change ii. further analysis based on a simplification of co 2 dynamics. *Climate Dynamics*, 5(4):201–210, 1991.

[69] M.J. Schaus and J. Moehlis. On the response of neurons to sinusoidal current stimuli: phase response curves and phase-locking. In *Proceedings of the 45th IEEE Conference on Decision and Control*, pages 2376–2381. IEEE, 2006.

[70] K.G. Schulz and R.E. Zeebe. Pleistocene glacial terminations triggered by synchronous changes in southern and northern hemisphere insolation: The insolation canon hypothesis. *Earth and Planetary Science Letters*, 249(3-4): 326–336, 2006.

[71] W.D. Sellers. A global climatic model based on the energy balance of the earth-atmosphere system. *Journal of Applied Meteorology*, 8(3):392–400, 1969.

[72] S.W. Shaw and P.J. Holmes. A periodically forced piecewise linear oscillator. *Journal of sound and vibration*, 90(1):129–155, 1983.

[73] D.M. Sigman and E.A. Boyle. Glacial/interglacial variations in atmospheric carbon dioxide. *Nature*, 407(6806):859, 2000.

[74] D.J.W. Simpson. *Bifurcations in piecewise-smooth continuous systems*, volume 70. World Scientific, 2010.

[75] D.J.W. Simpson and J.D. Meiss. Simultaneous border-collision and period-doubling bifurcations. *Chaos: An Interdisciplinary Journal of Nonlinear Science*, 19(3):033146, 2009.

[76] D.J.W. Simpson, S.J. Hogan, and R. Kuske. Stochastic regular grazing bifurcations. *SIAM Journal on Applied Dynamical Systems*, 12(2):533–559, 2013.

[77] I. Sliwa, P. Szlachetka, and K. Grygiel. Coexisting solutions and their neighbourhood in the dynamical system describing second-order optical processes. *arXiv preprint nlin/0604074*, 2006.

[78] M.S. Soliman. Global stability properties of equilibria, periodic, and chaotic solutions. *Applied mathematical modelling*, 20(7):488–500, 1996.

[79] J.C. Sprott and A. Xiong. Classifying and quantifying basins of attraction. *Chaos: An Interdisciplinary Journal of Nonlinear Science*, 25(8):083101, 2015.

[80] H. Stommel. Thermohaline convection with two stable regimes of flow. *Tellus*, 13(2):224–230, 1961.

[81] S.H. Strogatz. *Nonlinear dynamics and chaos: with applications to physics, biology, chemistry, and engineering*. CRC Press, 2018.

[82] R. Szalai and H.M. Osinga. Arnol'd tongues arising from a grazing-sliding bifurcation. *SIAM Journal on Applied Dynamical Systems*, 8(4):1434–1461, 2009.

[83] R.L.V. Taylor. Attractors: Nonstrange to chaotic. *Society for Industrial and Applied Mathematics, Undergraduate Research Online*, pages 72–80, 2010.

[84] J.M.T. Thompson and H.B. Stewart. *Nonlinear dynamics and chaos*. John Wiley & Sons, 2002.

[85] E. Walsh, J.and Widiasih, J. Hahn, and R. McGehee. Periodic orbits for a discontinuous vector field arising from a conceptual model of glacial cycles. *Nonlinearity*, 29(6):1843, 2016.

[86] B. White. Physics in the current climate. *Physics Education-London*, 42(4):327, 2007.

[87] E.R. Widiasih. Dynamics of the budyko energy balance model. *SIAM Journal on Applied Dynamical Systems*, 12(4):2068–2092, 2013.

[88] R.C.L. Wilson, S.A. Drury, J.L. Chapman, and J.A. Chapman. *The Great Ice Age: climate change and life*. Psychology Press, 2000.

[89] X. Zhao. Discontinuity mapping for near-grazing dynamics in vibro-impact oscillators. In *Vibro-Impact Dynamics of Ocean Systems and Related Problems*, pages 275–285. Springer, 2009.

[90] T. Zhou. Relaxation oscillation. In *Encyclopedia of Systems Biology*, pages 1844–1844. Springer, 2013.